JUICE - 2024
"Striving for Excellence"

www.juice.jfn.ac.lk

Under the Sphere of

Years of Academic Pursuits

Jaffna University International Research Conference - 2024

TechInn-2024

2nd Conference On
Technological Advance and Innovation - 2024

"Harnessing Cutting Edge Technologies for Economic Resilience"

CONFERENCE PROCEEDING

Volume 02

23 rd October 2024

Faculty of Technology
University of Jaffna
Ariviyalnagar, Kilinochchi, Sri Lanka

Tech*Inn* – 2024

Second Conference on Technological Advances and Innovations - 2024
https://www.tech.jfn.ac.lk/techinn-2024/

Organized by Faculty of Technology, University of Jaffna, Sri Lanka
23rd of October 2024

ISBN: 978-624-6150-42-6

Tech*Inn* 2024 offers a platform for academics to disseminate their research findings and encourage novel ideas. Particularly, the conference offers chances for academics from several disciplines of study. Scientific papers from six primary tracks contribute to the schedule. It promotes academics to discuss the latest developments, technologies, skills, information, and knowledge in their fields of study as well as to consider regional and global trends in those areas of study.

Editor-in-Chief: Mr. S. Vinujan

Disclaimer:

The content in this publication has been contributed by writers, and the opinions stated are still the authors' own. The editorial team and the University of Jaffna might not always concur with the points of view and thoughts expressed in this publication. The University of Jaffna and the Editorial Board disclaim any liability for the veracity and applicability of any information included in the text and pictures.

Without a prior authorization from the Editorial Board and University of Jaffna, no portion of this publication may be copied, stored, transmitted, or distributed for educational or other charitable uses in any format or by any means, as long as the source is properly credited. The University of Jaffna prohibits the reproduction of this book for reselling or for profit-making purposes unless prior written consent.

Published by: Faculty of Technology, University of Jaffna, Sri Lanka

Contact: techinn@tech.jfn.ac.lk

Message from the Vice Chancellor

Dear Distinguished Guests, Participants, and Innovators,

It gives me immense pride and joy to offer my warmest blessings to all those gathered for the Technological Advances and Innovations - 2024 conference. The theme for this year, "Harnessing Cutting-Edge Technologies for Economic Resilience," reflects both the urgency and the opportunity before us, as we navigate a world of rapidly evolving challenges and unprecedented potential.

As the Vice Chancellor of the University of Jaffna, I wholeheartedly recognize the importance of technological innovation as a cornerstone for building stronger, more resilient economies. This conference represents a vital platform for researchers, scientists, and thought leaders to come together, share their insights, and inspire new ways of thinking about the role of technology in shaping our collective future.

May your efforts during this event lead to meaningful discoveries and foster collaborations that contribute to the advancement of knowledge, the well-being of society, and the betterment of humanity as a whole. Let this gathering be a beacon of hope and progress, uniting us in our shared commitment to harness the power of technology to address today's challenges and to create a more prosperous and resilient tomorrow.

With heartfelt blessings, I wish all of you a fruitful, inspiring, and successful conference.

Prof. S. Srisatkunarajah
Vice Chancellor
University of Jaffna

Message from the Dean

Dear Esteemed Participants, Innovators, and Distinguished Guests,

It is with immense pleasure that I extend my warmest greetings and heartfelt best wishes to all who are attending the Technological Advances and Innovations – 2024 conference. This prestigious gathering, under the insightful theme of "Harnessing Cutting-Edge Technologies for Economic Resilience," could not be timelier. The world today is navigating complex challenges—economic uncertainties, environmental crises, and rapid technological shifts—and it is through our collective ingenuity that we can unlock solutions to build a more resilient and sustainable future.

Innovation stands at the core of progress. It is the driving force that propels us toward new horizons of possibility and promise. As you convene to share groundbreaking ideas, explore transformative technologies, and deliberate on how best to harness these innovations for the betterment of society, I am confident that your efforts will spark advancements that not only address today's challenges but also fortifyour economies for generations to come.

This conference is a testament to the power of collaboration and shared vision. As you exchange knowledge, form new partnerships, and engage in spirited discussions, I encourage each of you to think boldly and to push the boundaries of what is possible. Technological innovation is not merely about solving problems but about envisioning new futures—ones that are more equitable, sustainable, and prosperous for all.

May the insights gained and the networks formed at this event pave the way for pioneering breakthroughs that leave a lasting impact, both within your respective industries and across the global economy. Your work has the potential to inspire profound change, driving us closer to a world where economic resilience is not just an aspiration but a reality.

Wishing you all a deeply enriching, productive, and successful conference, filled with inspiration, collaboration, and the seeds of transformative innovation.

Dr. T. Ketheesan
Dean, Faculty of Technology
University of Jaffna

Message from the Convener

As the convener, it is my great pleasure to well come all the participants to the Second Conference on Technological Advances and Innovations (TechInn - 2024) organized by the Faculty of Technology, University of Jaffna as one of the satellite conferences of JUICe – 2024. TechInn –2024 is a multi-disciplinary conference under the theme of “Harnessing Cutting-Edge Technologies for Economic Resilience”. With the aim of disseminating innovative and sustainable research outcomes to the future development of the country. To fulfil the aim, we have collected research works from six specific themes including Automobile Technology, Construction Technology, Electro Technology, Commercial Green Farming Technology, Food Production Technology and Science and Technology. Conference will provide a platform not only to promote the research finding but also to share knowledge of academics, industry experts and graduate students. All the full papers were carefully peer reviewed and accepted papers will be published in the conference proceeding.

I would like to express my sincere thanks to the keynote speaker for accepting our invitation and joining with us to make this event meaningful. Also, I would like to express my sincere appreciation for all the authors for their great contribution to the success of the conference. My special thanks go to the all the reviewers, sponsors, conference organizing committee and all the academic and non-academic staff members of the Faculty of Technology for their dedicative, hard work from the beginning to the end to make this event success. I hope all the participants enjoy the conference and will be with us for future conferences.

Dr (Ms.) T. H. K. Nawarathna
Convener,
Tech*Inn* 2024 Proceedings

Message from Editor-in-Chief

We are excited, humbled, and very happy to commemorate the second edition of the Faculty of Technology, University of Jaffna Conference on Technological Advances and Innovations. Once again, our conference has been an exemplary instance of intellectual collaboration, providing a forum for the convergence of cutting-edge research, creative concepts, and a wide range of perspectives.

As the editor-in-chief, it gives me a great pleasure and honour to deliver my remarks at our second conference, which has laid under the theme of "Harnessing Cutting-edge Technologies for Economic Resilience". To ensure the standard of our conference, all the research findings were subjected to a thorough review procedure, as is customary. At this conference, scientists, academics, and researchers get the chance to share their research findings and professional knowledge with other stakeholders and the scientific community. Acknowledging the advantages of national experts and researchers in the domains of engineering, technology, and green farming, this conference promises to be a unique event, offering additional beneficial chances on excellent research and presenting creative and problem-based studies in the multidisciplinary approach.

I would want to use this moment to extend a warm welcome and express my sincere appreciation to each and every participant for participating. I convey my heartfelt thanks to all the track coordinators for their outstanding work in expeditiously reviewing the papers and bringing together in the proceeding. I also like to express my heartfelt gratitude to all of the reviewers and session chairs for their lightning-fast and committed assistance in making this successful event. I exhort each and every participant to keep up the good work of encouraging teamwork, expanding the horizons of knowledge, and striving for greatness in their fields.

Mr. S. Vinujan
Editor-in-Chief

Table of Contents

1. An investigation into the impact of blade pitch on the hydrodynamic characteristics of a variable pitch propeller using computational fluid dynamics (CFD)….. 1
2. Influence of TiO2 and fullerene-C60 nanoparticles content on Thermos- physical properties of lubricant oil 13
3. Effect of type and content of fine soils on compaction characteristics …............................. 19
4. Investigation and evaluation of a probable tsunami event near Sri Lanka 26
5. Automatic vehicle classification system for estimating the traffic density............................. 33
6. Experimental analysis of performance enhancement in polycrystalline photovoltaic panels incorporated with closed-loop active water-cooling system 43
7. Implementation of programmable logic controller in machine operations with product sorting based on metal detection ….….. 52
8. Investigation of the electronic structure and interactions at the interface between L-cysteine and silver surfaces ……….. 60
9. Thermo-physical characteristics of reduced graphene oxide incorporated enhanced transformer oil nanofluids 67
10. Low Cost IoT-Based Home Remote Monitoring and Controlling System 75
11. Helmet and Mask Detection for ATM's Surveillance via Deep Learning for Entrance Verification 83
12. Detecting of Tomato Leaf Diseases using Machine Learning 91
13. IoT Based Underground Power Cable Fault Monitoring System 98
14. IoT-Based LPG Leakage Alert System 107
15. Evaluate the effect of edible coating and packaging to improve the shelf- life of sugarcane jaggery 112
16. Incorporation of sesame flour as a substitute for chicken fat in the manufacturing of chicken sausages 117
17. Study the effect of post-harvest quality of sugarcane juice in the jaggery production …….124
18. Study on synbiotic salad dressing based on the addition of *Lacticaseibacillus rhamnosus*... 129
19. Detection of GMOs in some imported seed consignments to Sri Lanka 136
20. Formulation and evaluation of natural hair dyeing cream 144
21. Formulation and quality assessment of herbal hair dyeing oil 151
22. Investigation on impacts of mosquito fern (*Azolla pinnata*) liquid fertilizer ……………... 158
23. Optimization of an RNA extraction method for *Aglaonema*. Spp for improving RNA yield and quality 166

An investigation into the impact of blade pitch on the hydrodynamic characteristics of a variable pitch propeller using computational fluid dynamics (CFD).

Samarathunga Vidana Arachchige Amalka Indupama[1,2,3], Happawana Vithanage Vimukthi Priyadarshana[1,2,3], Galpayage Don Chanaka Pradeep Galpaya[1], Dingiriappu Kankanamlage Ashan Induranga[1,2] Watagoda Gedara Chathura Madusanka Kulasooriya[2], and Kaveenga Rasika Koswattage[1,2]*

[1]*Centre for Nanodevices Fabrication and Characterization, Faculty of Technology, Sabaragamuwa University of Sri Lanka, Belihuloya, Sri Lanka.*
[2]*Department of Engineering Technology, Faculty of Technology, Sabaragamuwa University of Sri Lanka, Belihuloya, Sri Lanka.*
[3]*Faculty of Graduate Studies, Sabaragamuwa University of Sri Lanka, Belihuloya, Sri Lanka.*

* koswattagekr@appsc.sab.ac.lk

Abstract

This research study outlines the Computational Fluid Dynamics (CFD) analysis of a Controllable Pitch Propeller (CPP), which is emerging in the maritime industry. This project aimed to comprehensively investigate the hydrodynamic properties and operational parameters of a four-bladed controllable pitch naval propeller. A scaled-down propeller was used for both structural and fluid simulations to evaluate its thrust generation, power consumption, and mass flow rate across various positive and negative pitch angles. The Ansys fluent 16 simulation platform was used to simulate the hydrodynamic characteristics of the NACA 6612 aerofoil based propeller, which was designed using SolidWorks 2022 designing software. The scaled down propeller with 150 mm hub diameter and 480 mm blade tip to tip diameter was analyzed for -40° to 40° degrees of pitch angle for an interval of 10°. The results proved that the designed propeller shows higher hydrodynamic properties in positive pitch angles compared to negative angles. Additionally, a propeller with positive pitch angles consumes less power to achieve a high mass flow rate compared to negative pitch angles. Among the analyzed positive pitch angles set, the propeller with 10° blade pitch shows the minimum power-to-thrust ratio of 1.5. Hence the propeller with a 10° blade pitch was considered as the optimum propeller under assigned working conditions. Similarly, the propeller with -20° of negative pitch angle shows a minimum power to thrust ratio of 2.3. Hence that propeller was considered as the optimum propeller under assigned working conditions. The findings may lead to performance enhancement and design optimization for future design modifications and manufacturing of more efficient naval propulsion systems by utilizing Computational Fluid Dynamics (CFD) as a simulation tool.

Keywords: Controllable Pitch Propellers, CFD, Naval Propeller, Propeller efficiency, Finite Element Analysis

---

1.Introduction

The propeller is one of the major components in the naval propulsion system which is used to pull and push the water flow to generate the required thrust to move forward. The amount of thrust generated directly depends on the propeller diameter, number of blades, spinning speed, and pitch angle(Li *et al.*, 2022). Generally, a propeller consists of several sun parts named propeller hub, bearings, and propeller blades. Propeller blades are configured in an angle called pitch angle where the angle between the blade root middle axis and the propeller mid axis. In modern fixed pitch propellers, the blade has been twisted from root to tip to achieve optimized hydrodynamic characteristics. The main disadvantage of a fixed-pitch propeller is it cannot be adjusted according to the shipping conditions. Therefore, the only propulsion-controlling method is changing propeller speed, which generates lots of difficulties during precise maneuvering. In naval propulsion, a controllable pitch propeller proves superior in efficiency and effectiveness when compared to fixed-pitch propellers(Lam, Hamill and Robinson, 2013). Marine propulsion system optimization is essential for improving ship performance, fuel economy, and environmental sustainability. As a major development in maritime propulsion technology, variable pitch propellers (VPPs) allow blade angles to be dynamically adjusted to maximize performance and efficiency under a variety of operating situations. In order to analyze the intricate fluid dynamics surrounding VPPs, computational fluid dynamics (CFD) has become an essential technique. It offers important insights into structural integrity, cavitation behavior, and hydrodynamic performance. In the context of ship propulsion, this literature review seeks to explore recent developments and significant discoveries in CFD analysis of variable pitch propellers.

Adjustable pitch propeller technology has emerged in both the aerospace and naval industries due to its wide applicability, and high thrust to power ratio. Further, the same propulsion system could be used to generate various thrust values with minimal operational changes. A research group from Lodz University of Technology, Poland has experimentally and numerically analysed the aerodynamic properties of scaled-down two-bladed propellers at different spinning rates. The study has revealed that the generated maximum thrust was measured at 12.4 degrees of blade angle. Further coefficient of thrust (CT), coefficient of power (CP), and motor efficiency were analyzed to obtain the best-suited propeller geometry.(Podsędkowski *et al.*, 2020) The factors affecting on blade design of a variable pitch naval propeller should be analysed such as root and size of the boss, type, and number of blades, and balancing of hydrodynamic and centrifugal forces acting on the propeller to ensure that the designed blade is capable of achieving high propulsion characteristics.(Kim, Ha and Paik, 2020) The comprehensive numerical study on full scale controllable pitch propellers (CPP) for electric combat naval combatants conducted by Devin L. Witt et.al reveals that CPPs have the advantage of avoiding or reducing of propeller cavitation compared to fixed pitch propellers at the full range of speeds.(Witt *et al.*, 2012)

(CFD) has been extensively used for optimizing naval propellers to obtain maximum efficiency. Several investigations have been carried out to examine the impact of the Reynolds number on diverse full-scale performance predictions employing viscous solvers. For instance, Yoon et al. conducted a comparative analysis of the wake patterns between a model ship and a full-scale ship using (CFD) (Jang *et al.*, 2020). In a separate study, Jasak et al. (2019) explored the sensitivity of grid size selection for a full-scale ship operating in a self-propulsion state (Jasak *et al.*, 2019; Castro et al. (2011). employed a discretized propeller to conduct a comprehensive analysis of full-scale self-propulsion.(Castro, Carrica and Stern, 2011)

The way how torque output, overall efficiency, and amount of thrust generation were obtained by Zhang et al. through a comprehensive analysis based on a (CFD) model (Taylor, 1946). Further, how pitch angle and pitch ratio effect on above parameters were also analysed based on a CFD model of a variable pitch propeller. Further, how those factors effect on overall efficiency and optimum blade pitch angles was discovered by Nadery and Ghassemi, (2020) through CFD analysis. These two studies have been a turning point in investigating the complex relationship between blade characteristics and propeller efficiency under different working conditions to direct future research works. According to the literature it has been proven that using variable pitch propellers are emerging in the maritime filed. This research aims to evaluate the efficiency of using reverse pitch angles for reverse thrust operations while maintaining forward thrust generation of available propellers.

2. Materials and Methods

2.1 Mechanical Design of four bladed naval propeller – Prototype

The scaled down variable pitch propeller with 150 mm hub diameter, and 300 mm overall diameter was designed using SolidWorks 2022 design software. Further, the propeller was in cooperating 4 blades made of stainless steel (Witt *et al.*, 2012) with an initial pitch angle of zero degrees measured at the maximum chamber and can be varied up to 40 degrees NACA 6612 profile was used to develop the twisted marine propeller blade with 100 mm of the maximum chamber. NACA 6612 is a moderately thick chamber type aerofoil that is commonly used in aircraft propellers, marine propellers, and wind turbines. National Advisory Committee for Aeronautics (NACA) has defined the specific geometry as a series of coordinates that generates the profile of the aerofoil

For ease of analysis, the pitch angle of each propeller geometry was defined. According to the literature, blade pitch angle refers to the angle between the chord line of the propeller blade to the plane of rotation. For the analysis, a twisted propeller blade was selected. Therefore, the angle was measured at the root of the propeller. Generally, propellers are twisted to obtain maximum fluid dynamic properties where the pitch angle is maximum at the hub and minimum at the tip. These modifications are necessary for maintaining a higher thrust-to-power ratio and also it directly affects the structural strength as well. The designed solid model is capable of having any pitch angle between -40 degrees to 40 degrees.

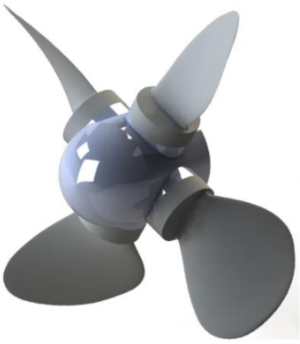

Figure 1. 3D model of the propeller

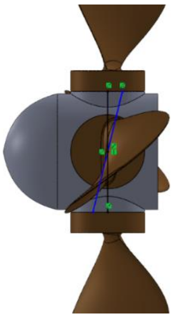

Figure 2. Pitch angle definition

2.2 Computational Fluid Dynamics (CFD) Analysis

The effect on the pitch angle was analysed using ANSYS-Fluent 2016 software platform with fundamental continuity equations and Reynolds equations. Initially, it was decided to carry out the transient flow simulation to obtain torque on the propeller shaft, the thrust generated, and the flow rate for zero (0) pitch angle because it could be used as the base model for results analysis. After importing the solid model in .STEP format of the 4-bladed propeller to the Design Modler software, several tools were used to create and define the computational domain.

The near domain of the propeller is defined as a cylindrical rotating domain with a diameter of 310 mm with 1000 mm cylindrical fixed surrounding. The fluid domain around the propeller was divided into two sections where the cylindrical fluid portion near the propeller was defined as the rotating domain, and the rest of the fluid section was defined as the surrounding for ease of analysis.

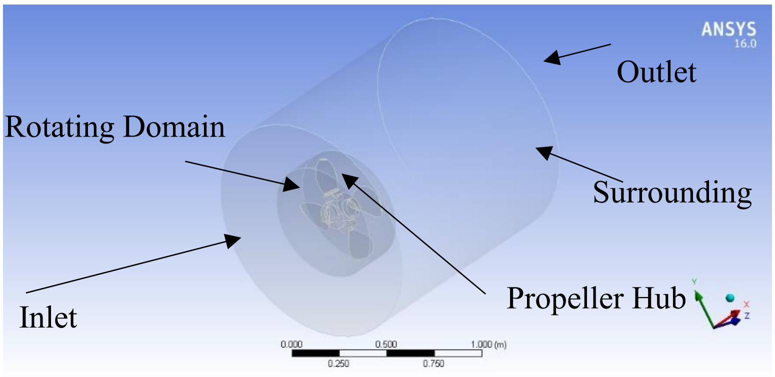

Figure 3. Boundary Conditions

Since the simulation is conducted for a rotating propeller with different pitch ratios, a sliding mesh method was used. To enhance the accuracy of the results the downstream length was increased as much as possible considering available computational power. The front face of the computational domain was renamed as “inlet” and the boundary type was set as pressure inlet. The reason behind that was, then the computational system would automatically set the velocity with the computational parameters during the calculation.

Table 1. Boundary Properties

No	Boundary	Type
1	Inlet	Pressure Inlet
2	Outlet	Pressure Outlet
3	Rotating Domain	Rotating around axis (120rpm)
4	Surrounding	Fixed wall

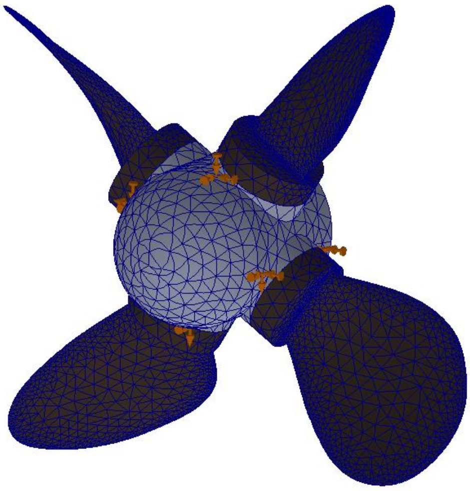

Figure 4. Mesh

A tetrahedral mesh (Figure 3) was obtained to conduct the sliding mesh analysis with the parameters mentioned in below. To obtain results with better accuracy, the initial mesh was modified following below steps.

The minimum face size was set to: 0.003 mm
The maximum face size was set to: 0.00054 mm
Nodes: 103556
Elements: 566363

3. Results and Discussion

3.1.CFD - Forward operation of Variable Pitch Propeller (VPP - Forward)

To analyze the flow pattern and turbulence at downstream, the following figures and plots were generated.

- Velocity contour at the mid-section
- Streamlined plot throughout the fluid domain: 300 nos of starting points
- Vector plot for the entire fluid domain

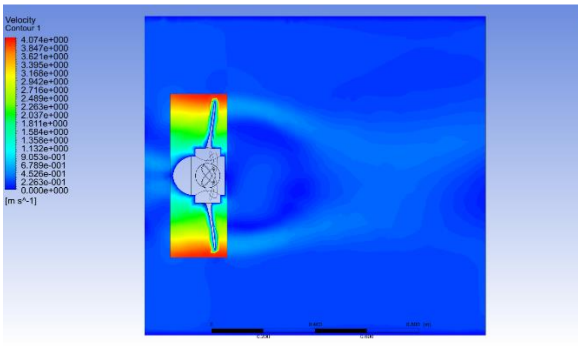

Figure 5.a. Pitch angle 0 degrees

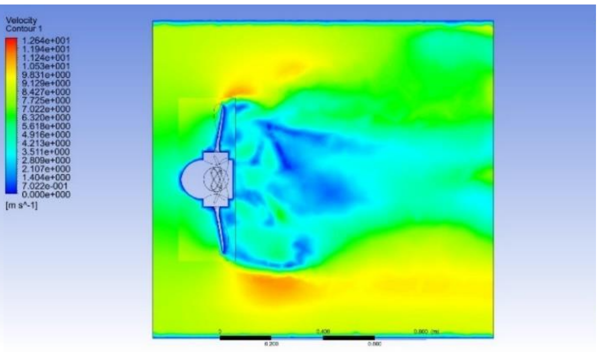

Figure 5.b. Pitch angle 10 degrees

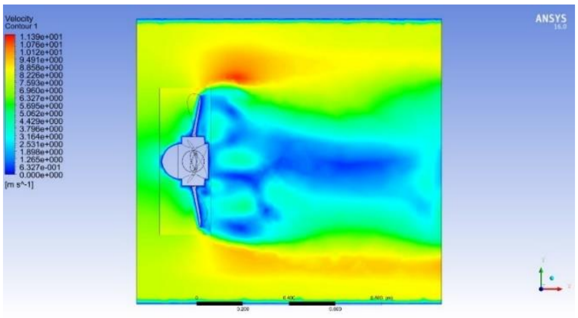

Figure 5.c. Pitch angle 20 degrees

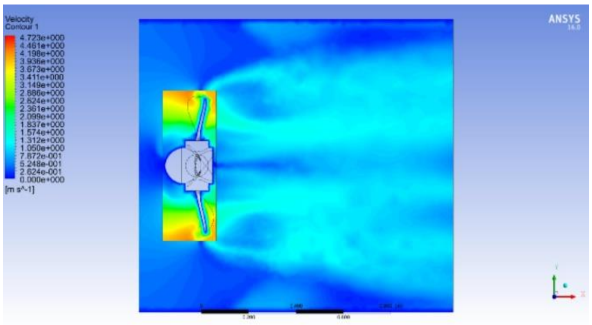

Figure 5.d. Pitch angle 30 degrees

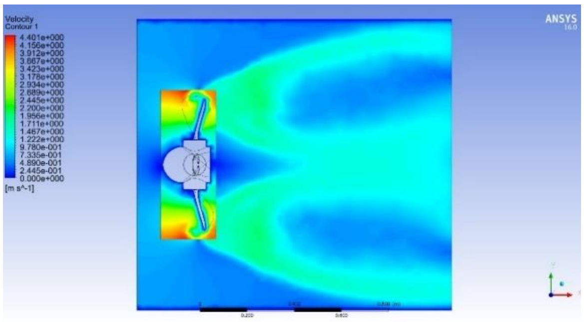

Figure 5.e. Pitch angle 40 degrees

When comparing velocity plots (figure 5.a -5.e), it is clear that when the pitch angle increases, the flow becomes more turbulent and leads to flow separations and wakes in downstream. Further at 0 degrees of pitch angle, flow becomes more laminar, and flow near the spinning propeller has more velocity. This means there is less mass flow rate compared to other flows which represents higher pitch angles.

Streamlined plots and vector plots (Forward pitch + ve)

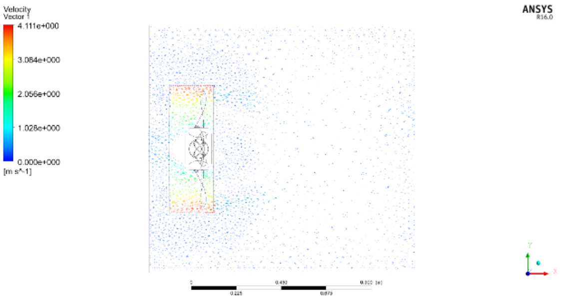

Figure 6.a . Vector plot at mid section : 0 degrees pitch

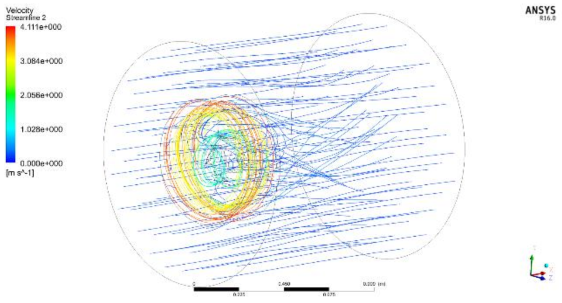

Figure 6.b. Streamline plot : 0 degrees pitch

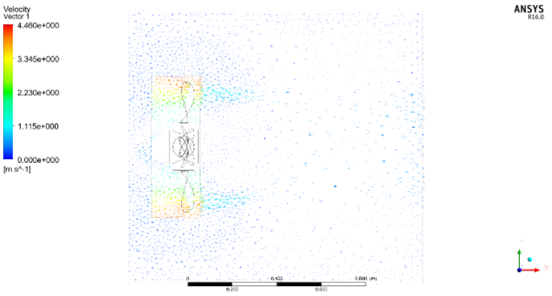

Figure 6.c. Vector plot at mid section :10 degrees pitch

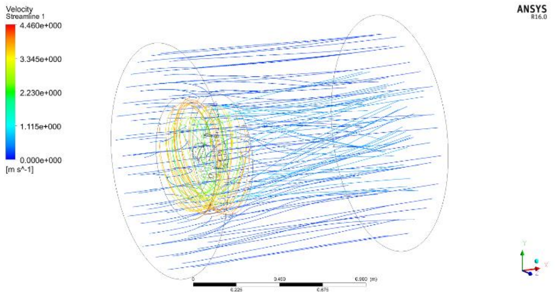

Figure 6.d. Streamline plot : 10 degrees pitch

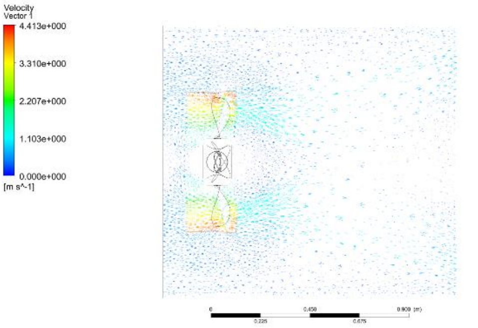

Figure 6.e. Vector plot at mid-section: 20 degrees pitch

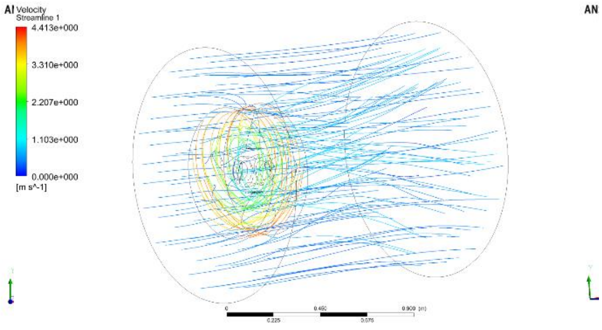

Figure 6.f. Streamline plot : 20 degrees pitch

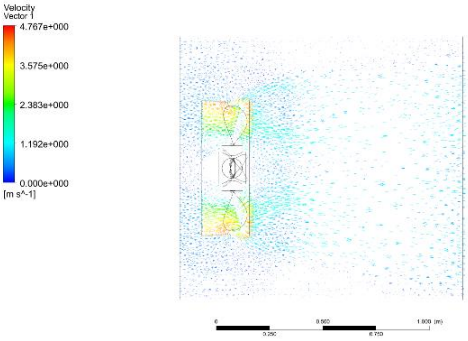

Figure 6.g. Vector plot at mid section : 30 degrees pitch

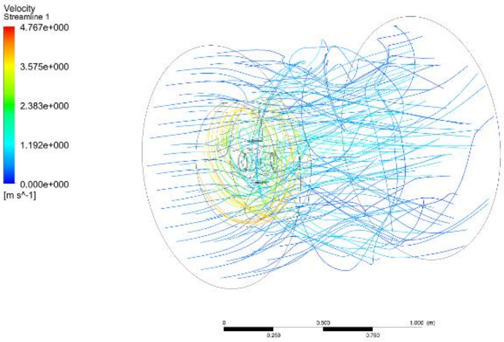

Figure 6.h. Streamline plot : 30 degrees pitch

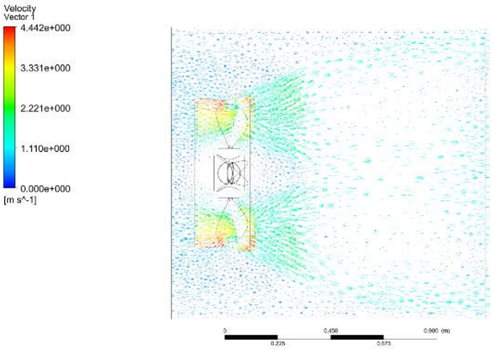

Figure 6.i. Vector plot at mid section : 40 degrees pitch

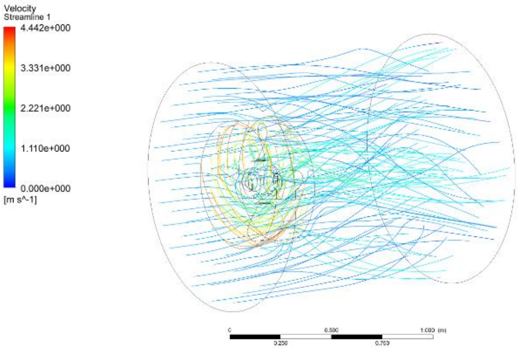

Figure 6.j. Streamline plot : 40 degrees pitch

According to the obtained streamlined plots, it is clear that the downstream tends more turbulent at higher pitch angles which may lead to higher power consumption and thrust generation. Anyway, it is better to check the numerical results for thrust generated, torque on the shaft, and flow rate to validate the above finding.

Table 2. Results

Parameter	Units	Forward Pitch				
	Degrees	0	10	20	30	40
Torque	Nm	2.35	6.99	15.62	41.32	49.89
Thrust	N	4.58	57.82	123.95	239.24	223.69
Mass Flow rate	kg/s	248.82	331.19	561.43	548.01	747.59
Power Consumed	W	29.53097	87.83893	196.2867	519.2424	626.9362

Power/Thrust	6.4	1.5	1.6	2.2	2.8

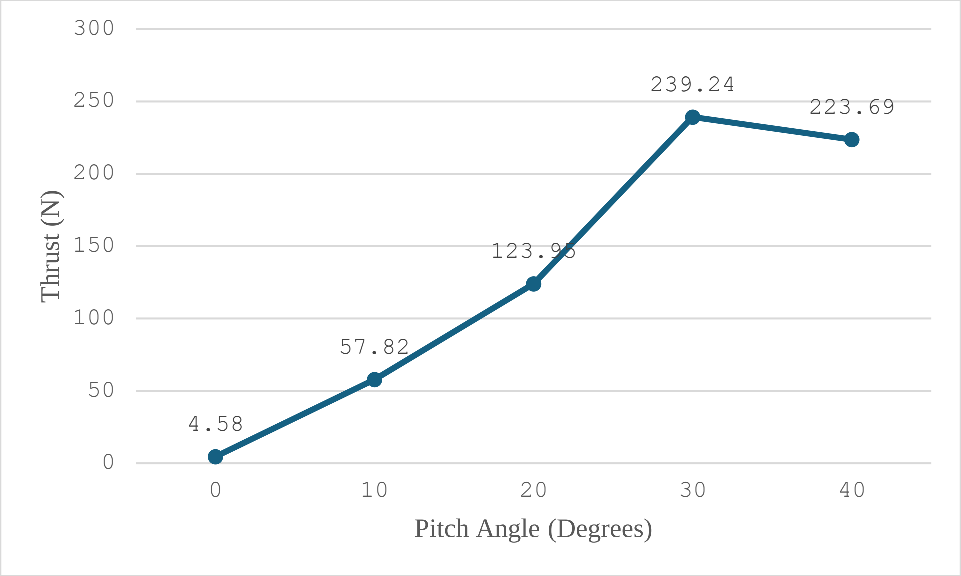

Figure 1.0. Thrust Generated vs. pitch angle

According to the thrust vs pitch angle graph, there is a positive slope up to 30 degrees of pitch angle. This means the amount of thrust generated is gradually increasing with the pitch angle. At 30 degrees propeller shows a maximum thrust generation of 239. 24 N. Further increment of pitch angle will lead to a reduction in generated thrust.

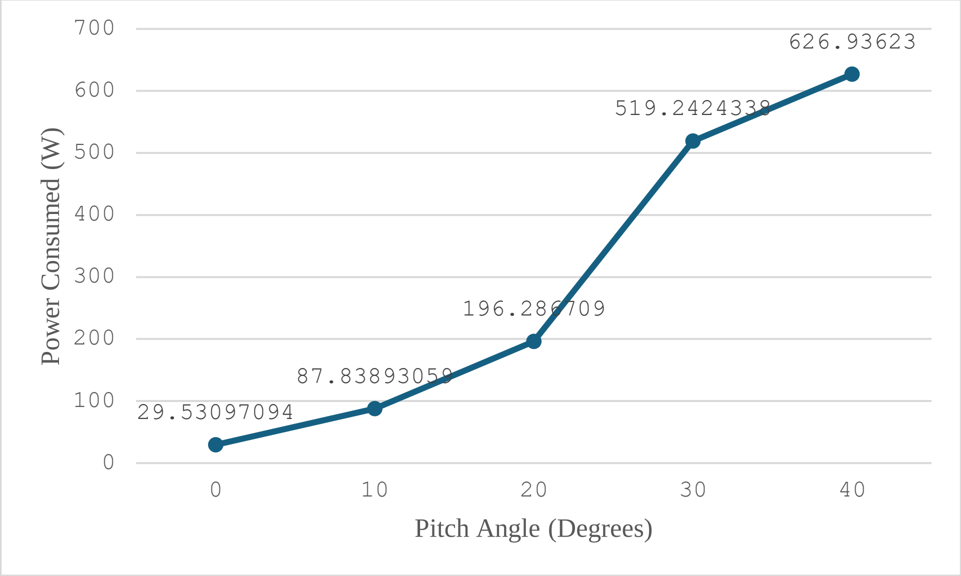

Figure 2.1. Power consumed vs pitch angle

When it comes to the power consumed vs pitch angle graph it is clear that when pitch angle increases, the total consumed power to maintain the required inertia of the propeller assembly increases. However, it is difficult to find a liner relationship with the obtained results.

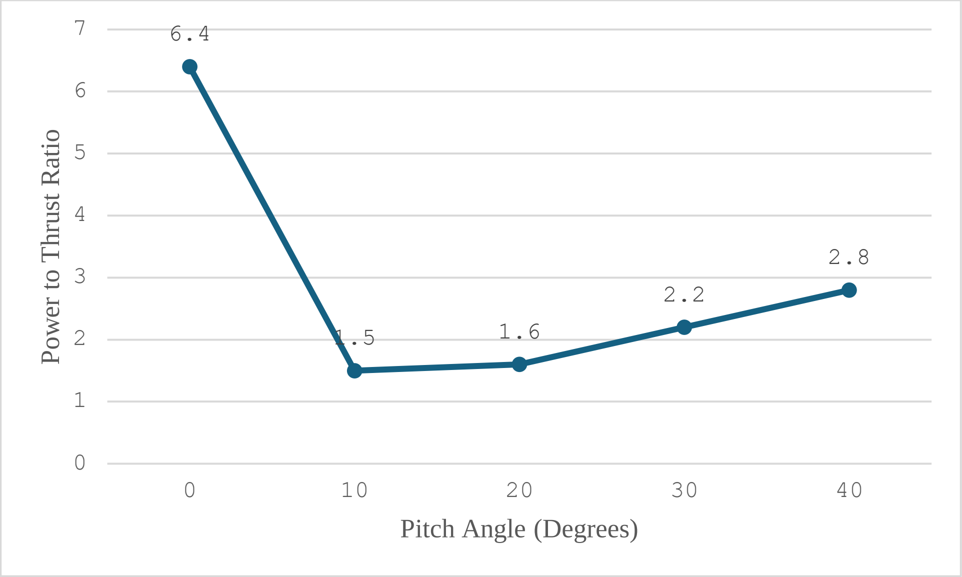

Figure 2.2. Power to thrust ratio vs pitch angle

According to the results obtained after the analysis for different pitch angles, it is clear that the generated thrust has been gradually increased with the forward pitch angle up to 30 degrees of pitch angle. Further increment of pitch angle has been a cause for the decrement of generated thrust. Therefore, the maximum generated thrust for 120 rpm of spinning speed is approximately 240 N. Furthermore, the torque on the shaft has been gradually increased without any variation. When it comes to mass flow rate there is a slight change than expected. From 0 degrees to 40 degrees of pitch angle, generally, mass flow rate has been increased and at 40 degrees of pitch angle it shows the maximum mass flow rate of 745 kg/s. There is a slight deviation at 30 degrees pitch angle. Accordingly, the power consumption is also calculated using the the standard power transmission equations.

$P = T \times \omega$ Eq.1

Where P : Power Consumed
T : Torque Generated
ω: Spining velocity of the propeller in rad/sec

The power to thrust ratio is an effective parameter for comparing such aerodynamic profiles. It is clear that minimum power to thrust has been obtained at 10 degrees of pitch angle. Anyway, it should be concluded that at zero pitch angle, the propeller generates very little thrust compared to other pitch angles.

3.2.CFD - Reverse operation of Variable Pitch Propeller (VPP - Reverse)

The force report, thrust, and mass flow rate was obtained using the ANSYS Fluent post processor. The following data set shows the force report which was obtained for negative ten (-10) degrees of pitch angle.

Table 3 - Force, Moment, and Flow rate results

	Units	Reverse Pitch			
Parameter	Degrees	10 degrees	20 degrees	30 degrees	40 degrees

Torque	Nm	2.4	2.56	3.95	4.69
Thrust	N	5.45	87.56	45.94	2.63
Mass Flow rate (Reverse)	kg/s	235.36	128.91	17.32	20.8
Power Consumed	W	30.15	32.16	49.63	58.93
Power/Thrust		5.5	0.4	1.1	22.4

4. Conclusion

The objective of this research project was to analyze the hydrodynamic characteristics of a ship (naval) propeller considering different working conditions, such as different speeds and pitch angles of the blades. The goal was to analyze the propeller's efficiency, generation of hydrodynamic thrust, and power consumption, and give recommendations for future design modifications. According to the Finite Element Analysis (FEA) results, the designed propeller is capable of both forward and reverse operation. According to the CFD analysis that was carried out for the designed propeller, it performed better at moderate pitch angles, producing a higher thrust with less power consumption. The efficient fluid flow around the blades was indicated by the streamlined laminar and uniform flow patterns displayed by the flow visualization. Further, considering the power-to-thrust ratio, it was clear that during the forward operation of the 10 degrees of pitch angle propeller works at maximum efficiency among the compared pitch angles. According to the obtained results, the 20 degrees of pitch angle propeller generates 57. 82 N of thrust using 87.83 W power. Similarly, at the reverse operation -20 degrees of pitch angle the propeller works at maximum efficiency among the compared pitch angles. According to the obtained results, at the -20 degrees of pitch angle propeller generates 47.86 N of thrust using 110.33 W power.

In addition to that future investigations on naval variable pitch propellers should concentrate on carrying out of parametric studies to look into how different blade shapes, number of blades, blade materials, and manufacturing processes affect propeller performance. Furthermore, integrating SolidWorks or any other structural simulations with computational fluid dynamics analysis may be helpful in improving the propeller's durability and structural stability under various operating conditions. In conclusion, the carried out finite element analysis has revealed and validated important details about the hydrodynamic performance of the ship or marine propeller. The above findings may lead to performance enhancement and design optimization of four-bladed propellers. As the final outcome designers and engineers could design more powerful and efficient naval propulsion systems by utilizing CFD as a virtual prototyping tool.

5. Acknowledgement

This work was supported by the Science and Technology Human Resource Development Project, Ministry of Education, Sri Lanka, funded by the Asian Development Bank (Grant number CRG-R3-SB-4).

6. References

Nadery, A and Ghassemi, H. (2020). Numerical Investigation of the Hydrodynamic Performance of the Propeller Behind the Ship with and Without Wed. Polish Maritime Research 27(4):50-59 Available at: https://www.researchgate.net/publication/348477385_Numerical_Investigation_of_the_Hydrodynamic_Performance_of_the_Propeller_Behind_the_Ship_with_and_Without_Wed (Accessed: 19 August 2024).

Castro, A.M., Carrica, P.M. and Stern, F. (2011) 'Full scale self-propulsion computations using discretized propeller for the KRISO container ship KCS', *Computers & Fluids*, 51(1), pp. 35–47. Available at: https://doi.org/10.1016/j.compfluid.2011.07.005.

Jang, Y.-H. *et al.* (2020) *A NUMERICAL STUDY ON THE OPEN WATER PERFORMANCE OF A PROPELLER WITH SINUSOIDAL PITCH MOTION. | Brodogradnja | EBSCOhost*. Available at: https://doi.org/10.21278/brod71105.

Jasak, H. *et al.* (2019) 'CFD validation and grid sensitivity studies of full scale ship self propulsion', *International Journal of Naval Architecture and Ocean Engineering*, 11(1), pp. 33–43. Available at: https://doi.org/10.1016/j.ijnaoe.2017.12.004.

Kim, D.-Y., Ha, J.-Y. and Paik, K.-J. (2020) 'Numerical Study on the Extrapolation Method for Predicting the Full-scale Resistance of a Ship with an Air Lubrication System', *Journal of Ocean Engineering and Technology*, 34. Available at: https://doi.org/10.26748/KSOE.2020.008.

Lam, W.H., Hamill, G.A. and Robinson, D.J. (2013) 'Initial wash profiles from a ship propeller using CFD method', *Ocean Engineering*, 72, pp. 257–266. Available at: https://doi.org/10.1016/j.oceaneng.2013.07.010.

Li, S. *et al.* (2022) 'Ship maneuverability modeling and numerical prediction using CFD with body force propeller', *Ocean Engineering*, 264, p. 112454. Available at: https://doi.org/10.1016/j.oceaneng.2022.112454.

Podsędkowski, M. *et al.* (2020) 'Variable Pitch Propeller for UAV-Experimental Tests', *Energies*, 13(20), p. 5264. Available at: https://doi.org/10.3390/en13205264.

Taylor, J.L. (1946) 'The Variable-pitch Marine Propeller', *Proceedings of the Institution of Mechanical Engineers*, 155(1), pp. 211–231. Available at: https://doi.org/10.1243/PIME_PROC_1946_155_031_02.

Witt, D.L. *et al.* (2012) 'Analysis of Controllable Pitch Propellers for an All-Electric Naval Combatant', in. *SNAME Maritime Convention*, OnePetro. Available at: https://doi.org/10.5957/SMC-2012-S4.

Influence of TiO_2 and fullerene-C_{60} nanoparticles content on thermo-physical properties of lubricant oil

Galpayage Don Chanaka Pradeep Galpaya[1], Happawana Vithanage Vimukthi Priyadarshana[1,2,3], Dingiriappu Kankanamlage Ashan Induranga[1,2], Samarathunga Vidana Arachchilage Amalka Indupama[1,2,3] and Kaveenga Rasika Koswattage[1,2]*

[1]*Centre for Nanodevices Fabrication and Characterization, Faculty of Technology, Sabaragamuwa University of Sri Lanka, Belihuloya, Sri Lanka.*
[2]*Department of Engineering Technology, Faculty of Technology, Sabaragamuwa University of Sri Lanka, Belihuloya, Sri Lanka.*
[3]*Faculty of Graduate Studies, Sabaragamuwa University of Sri Lanka, Belihuloya, Sri Lanka.*

* koswattagekr@appsc.sab.ac.lk

Abstract

Nanofluids enhance thermo-physical properties in many applications, such as automotive industry, electronic and microelectronic, energy sector, manufacturing and material processing, etc. Nanofluids in automotive industry help to maintain and enhance the lubricating and cooling properties, especially in engines. This study reports the effect on thermo-physical properties of 10W30 CALTEX engine oil suspended TiO_2 and fullerene-C_{60} nanoparticles. Two different weight ratios (0.05 wt.% and 0.1 wt.%) of nanoparticles in the base fluid are used for the analysis within the temperature range of 30-120 °C. The scanning electron microscope (SEM) images were used to obtain nanoparticles size, shape and surface morphology. The two-step direct mixing method was used to prepare nanofluid samples under both magnetic stirring and ultrasonication conditions. Thermal conductivity, flash point, and dynamic viscosity measurements were conducted using a LAMBDA thermal conductivity meter, Anton Paar PMA 500 flash point tester, and SVM 3001 viscometer respectively, for each nanofluid sample and base fluid. The results indicate that thermal conductivity and flash point of TiO_2 added nanofluid showed the highest enhancement ratio 6.0% and 5.4% respectively at 0.1 wt.% while maintaining the dynamic viscosity values constantly. However, the experimental results proved that the TiO_2 added nanofluids enhanced both thermal properties while fullerene-C_{60} added nanofluid only enhanced flash point values. The results of this study provide valuable information regarding the two different nanoparticle effects on thermo-physical properties of engine oil-based nanofluid which can lead to the overall performance of vehicles.

Keywords: Nanoparticles, Lubricant oil, Thermal conductivity, Flashpoint, Dynamic Viscosity

1. Introduction

Thermal and physical properties of heat transfer fluids are one of the main topics that have been discussed among researchers over the past few decades and they are still working on enhancing the thermal properties of engine oils by adding different additives. Oil based nanofluids are a popular modification and there are several studies regarding the nanofluids, preparation methods, and their properties.

The engine oils are used in a motor engine to reduce the friction, clean the system, prevent corrosion, and cool the engine (Jatti & Singh, 2015). By taking into the account, thermal conductivity is one of the main properties which needs to be considered as the base oils are not able to fulfil the cooling requirement of modern high-power engines. The flashpoint of engine oil depends on several parameters such as additives, temperature and pressure. Furthermore, flashpoint of engine oil should be maintained at greater than 100°C due to lower flashpoint can cause to engine fires or oil vaporizations. In physical properties of engine oil, viscosity can be considered as the main property, and it mainly depends on temperature, when increasing the temperature it decreases the viscosity value.

Additives enhance the desired properties of base oils (Wu, et al., 2007; Induranga, et al., 2024; Chanaka, et al., 2024). Therefore, to enhance the properties of base oils, adding nano-particles to the base oil as an additive is becoming the most integral method and on the other hand the cost of the final product is still the dominant factor in determining the feasibility of such production processes (Liu, et al., 2011; Peng, et al., 2007). Mainly, there are two types of nanoparticles which are metal-based and carbon-based nanoparticles. The metal-based nanoparticles can be divided in to two groups and they are metal and metal-oxide. From all the metal oxide nanoparticles, TiO_2 is the most attractive nano additive in formulation of nanofluids due to its versatile properties which can be utilized in applications such as: antibacterial agent (Cui, et al., 2012), self-cleaning coating (Smits, et al., 2013), solar cells (Meng, et al., 2014), gas sensors (Ananth, et al., 2014) and dentistry (Sun, et al., 2011). On the other hand, the high availability and low production cost of TiO_2 nanoparticles is a considerable advantage. When coming to the fullerene-C_{60} is one of the best carbon-based nano material due to its unique properties such as high surface area to volume ratio, shape, symmetry, etc.

For this study, the anatase-type TiO_2 and Fullerene-C_{60} nanoparticles were used with two different weight fractions, 0.05% and 0.1%. In addition, more investigations were performed using a FLUCON Lambda thermal conductivity meter, Flashpoint analyzer, Viscosity meter and SEM, to correlate the physicochemical properties with thermo-physical properties.

2. Materials and Methods

2.2 Preparation of Nanofluids

In this research, the base oil CALTEX 10W30 engine oil and nanoparticles, commercially purchased anatase-type TiO_2 (particle size 30-60 nm) and fullerene-C_{60} (particle size 100-200 nm) were used with the weight fractions 0.05% and 0.1%. The two-step direct mixing method was used to prepare nanofluids in different weight fractions with two different nanoparticles. The measured nanoparticles were mixed with the base fluid and kept for 2 hours under magnetic stirring at 50 °C, followed by ultrasound treatment for 3 hours at 50 °C in order to obtain stable and homogenous blends.

2.3 Thermo-physical properties of nanofluids

The thermo-physical properties: thermal conductivity, flashpoint and viscosity were measured for each nanofluid and base fluid. The thermal conductivity was measured using TECHNE UCAL 400+ dry-block calibrator (FLUCON Lambda thermal conductivity meter) in the temperature range 30-120°C, flashpoint tester (Anton Paar PMA500, Germany) was used to measure the flashpoints, while viscosity meter (Anton Paar 3000, Germany) was used to measure viscosity in the temperature range 20-100°C of nanofluids and base fluid.

3. Results and Discussion

3.1 Characterization of nanoparticles

The surface topography and composition of the nanoparticles were investigated using scanning electron microscope tests. Fig. 1, represents the obtained SEM images of fullerene-C_{60} and TiO_2 nanoparticles.

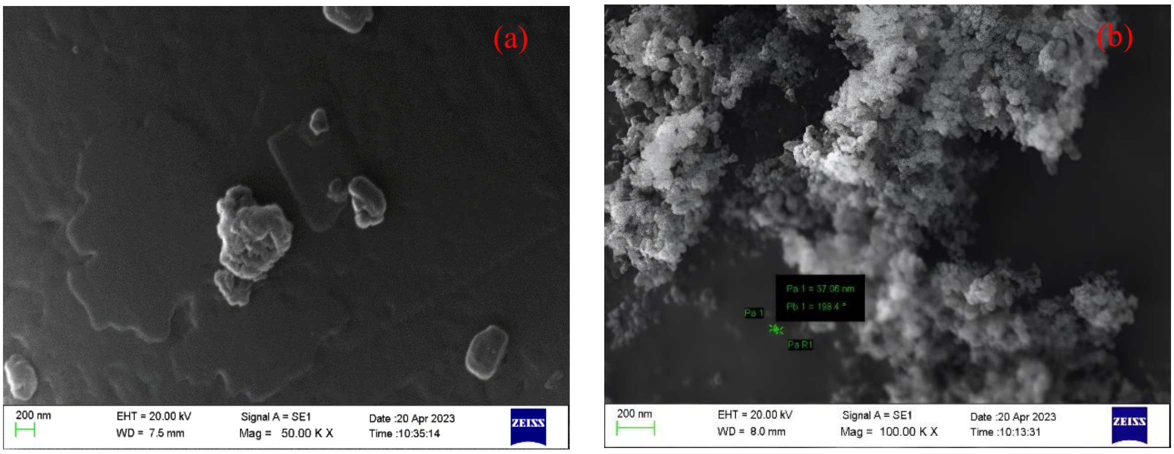

Figure 2: Scanning Electron Microscope images of nanoparticles (a) Fullerene-C_{60} and (b) TiO_2

3.2 Thermal conductivity

The thermal conductivity of base fluid and nanofluids were measured in the temperature range 30-120 °C and the comparisons are represented from Fig. 2. According to the graphs the thermal conductivity of TiO_2 based nanofluids shows considerable enhancement when comparing with base fluid, but fullerene-C_{60} based nanofluids did not show such enhancement. As can be seen obviously, the enhancement of the thermal conductivity was a linearly correlated relationship with increase in temperature.

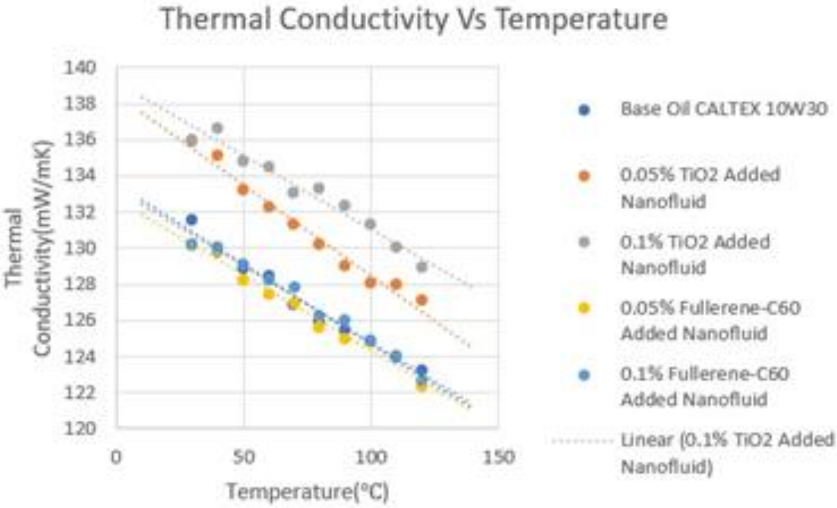

Figure 3: Thermal conductivity comparison of nanofluids and base fluid

3.3 Flash point

The term flash point of a liquid represents the temperature of the oil at which its vapour will ignite. The trends of changes in flash point as a function of nanoparticle volume fraction and nanoparticle type is shown in Fig.3. It can be observed that the type of nanoparticle and their volume fractions cause an increase in the flash point. As it is observed, the TiO_2 added nanofluids show significant enhancement compared to base fluid and increasing the volume ratios of nanoparticles also cause the increment of flash points.

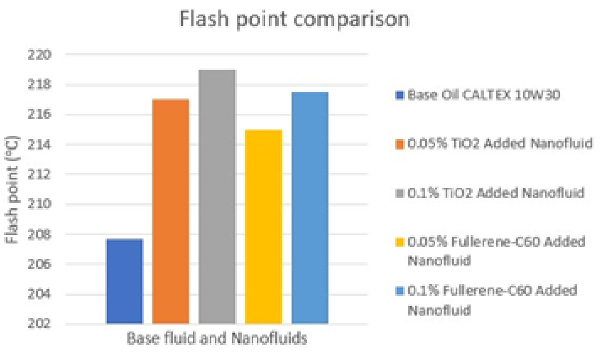

se fluid

3.4 Viscosity

The viscosity of oil can be recognized as a resistance of flow or continuous flow circulation. In a vehicle engine, the lubricating oil should flow at a constant speed to maintain the engine requirements especially, cleaning and cooling. The engine oils have specific viscosity values at different temperature values and they are graded according to viscosity values in standard grading system. The nanoparticles added engine oil helps to maintain viscosity values in required range while increasing thermal properties. Fig. 4, represents the viscosity values of nanofluids and base fluid at temperature range of 20-100℃; nanoparticles added engine oils viscosity does not change considerably in contrast to base fluid at temperature range.

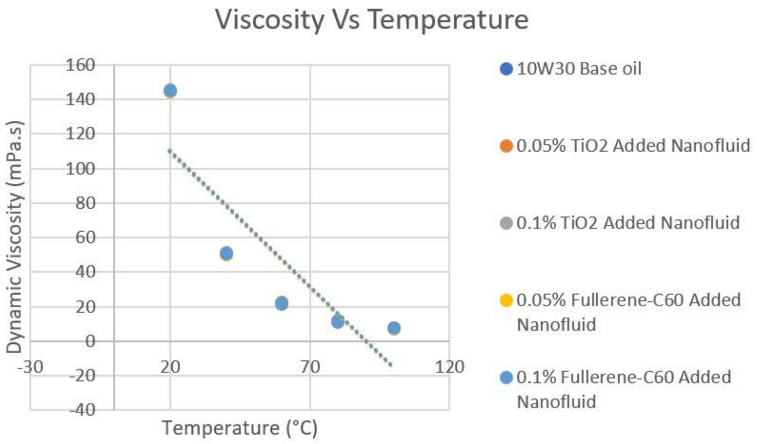

Figure 5: Viscosity comparison of nanofluids and base fluids

The highest percentage of thermal conductivity ratios of nanofluids at particular temperatures and comparison of the increment percentage of flash point ratios are represented in Table 1.

Table 1: Maximum thermal conductivity and Flashpoint ratios at particular temperature values of nanofluids

Nanofluids	**Thermal conductivity ratio (%)**	**Flashpoint ratio (%)**
0.1% TiO_2/Engine Oil	6 at 80 ℃	5.44
0.05% TiO_2/Engine Oil	4 at 40 ℃	4.47
0.1% Fullerene-C_{60}/Engine Oil	-	4.71
0.05% Fullerene-C_{60}/Engine Oil	-	3.51

4. Conclusion

In this research, the behavior of TiO_2/10W30 oil and fullerene-C_{60}/10W30 oil nanofluids were observed under three thermo-physical properties, thermal conductivity, flashpoint, and viscosity through an experimental procedure. It is observed that the thermal conductivity of 10W30 engine oil-based nanofluids increases with the nanoparticle concentration where 0.1% TiO_2/10W30 Oil showed the highest thermal conductivity ratio of 6% and a flash point ratio of 5.44% and no considerable enhancements noted in viscosity values from the tested samples. It can be concluded that TiO_2 nanoparticles, which is a metal-based nanomaterial, show comparatively better thermal properties than fullerene-C_{60}, a carbon-based nanomaterial, with 10W30 engine oil base fluid without notably changing viscosity values with temperature.

5. Acknowledgement

This work was supported by the Science and Technology Human Resource Development Project, Ministry of Education, Sri Lanka, funded by the Asian Development Bank (Grant number CRG-R2-SB-1).

6. References

Ananth, P., V., T., A. & P, M., 2014. Natural dye extract of lawsonia inermis seed as photo sensitizer for titanium dioxide-based dye sensitized solar cells. *Spectrochim. Acta Part A Mol. Biomol. Spectrosc.,* Volume 128, pp. 420-426.

Chanaka, G. et al., 2024. Comparative Study on the Thermal Properties of Engine Oils and Their Nanofluids Incorporating Fullerene-C60, TiO2 and Fe2O3 at Different Temperatures. *Energies,* Volume 17, p. 732.

Cui, et al., 2012. Microstructure and antibacterial property of in situ TiO2 nanotube layers/titanium biocomposites. *J. Mech. Behav. Biomed. Mater.,* Volume 8, pp. 178-183.

Induranga, A., Galpaya, C., Vithanage, V. & Koswattage, K. R., 2024. Thermal Properties of TiO2 Nanoparticle-Treated Transformer Oil and Coconut Oil. *Energies,* Volume 17, p. 49.

Jatti, V. S. & Singh, T. P., 2015. Copper oxide nano-particles as friction-reduction and anti-wear additives in lubricating oil. *Journal of Mechanical Science and Technology,* Volume 29(2), pp. 793-798.

Liu, L., Fang, Z., Gu, A. & Guo, Z., 2011. Lubrication effect of the paraffin oil filled with Functionalized Multiwalled Carbon Nanotubes for Bismaleimide Resin. *Tribology Letters,* Volume 42, pp. 59-65.

Meng, T., Y. & T, K., 2014. Preparation and gas sensing properties of undoped and Pd-doped TiO2 nanowires. *Sens. Actuators B Chem.,* Volume 190, p. 838–843.

Peng, Y., Hu, Y. & Wang, H., 2007. Tribological behaviours of surfactant-functionalized carbon nanotubes as lubricant additive in water. *Tribology Letters,* Volume 25(3), pp. 247-253.

Smits, et al., 2013. Photocatalytic degradation of soot deposition: self-cleaning effect on titanium dioxide coated cementitious materials. *Chem. Eng.,* Volume 222, pp. 411-418.

Sun, et al., 2011. Improving performance of dental resins by adding titanium dioxide nanoparticles. *Dent. Mater.,* Volume 27, p. 972–982.

Wu, Y., Tsuia, W. & Liub, T., 2007. Experimental analysis of tribological properties of lubricating oils with nanoparticle additives. *Wear,* Volume 262, p. 819–825.

Effect of type and content of fine soils on compaction characteristics

H.W.M.V. Weligala[1]*, G.I. Wanasinghe[1]

[1] *Department of Construction Technology, Faculty of Technology, Wayamba University of Sri Lanka, Kuliyapitiya, Sri Lanka.*

* milanvishmitha@gmail.com

Abstract

The gradation of a soil sample is a leading factor which influences the compaction characteristics of the soil mixture. This study was performed to investigate the impact of the type and the content of fine soils on compaction properties of the soil. The gravel soil was used as coarse soil and fine gravel soil, termite mound soil and kaolin were used as the different types of fine soils. Standard proctor compaction test was used during the study and the samples were generated such that the particle size distribution curve of the coarse soil is constant for all the samples. This was maintained by selecting a fixed weight of gravel soil from different sieve sizes while different fine percentages were used from each type of fine soil. The maximum dry density and the optimum moisture content corresponding to the maximum dry density of each sample were compared within the analysis of the results. The results revealed that a 10% fines content yielded the highest maximum dry density and lowest optimum moisture content across all soil types, suggesting it as the optimum fine content. Notably, kaolin soil at 10% fine content demonstrated superior compaction properties, exhibiting the highest maximum dry density at the lowest water level compared to other soils. This optimal compaction was attributed to fine particles filling voids within the coarse-grained matrix, forming a densely packed structure. The study underscores the significant impact of fines content and soil type on compaction behavior, with kaolin at the optimum fine content offering the best compaction characteristics. This research contributes valuable insights for soil compaction practices in engineering applications.

Keywords: compaction characteristics, kaolin, Proctor compaction test, Termite mound soil, Fine content

1. Introduction

Soil compaction is the process of increasing the density of soil by reducing the volume of air within the soil mass through the application of mechanical energy. Understanding the compaction characteristics of different soil types is paramount for ensuring the efficacy and longevity of such projects. Fine soils, which include clay, silt, and various mixtures thereof, play a significant role in this regard due to their prevalence in construction sites and their diverse mechanical properties. This research aims to delve into the nuanced relationship between fine soil types and their compaction characteristics:

- Optimum moisture content
- Maximum dry density
- Compaction Curve
- Soil type

While compaction is a common practice in construction, the behavior of fine soils under compaction processes varies significantly based on their mineralogical composition, particle size distribution, moisture content, and other intrinsic factors. Therefore, it becomes imperative to investigate how different types of fine soils respond to compaction efforts.

The study will focus on systematically analyzing and comparing the compaction characteristics of various fine soil types, considering factors such as optimum moisture content, maximum dry density. By examining two types of fine soils that can be seen from the environment around us, this research seeks to provide valuable insights into the compaction behavior of these materials.

Understanding the effect of fine soil types on compaction characteristics not only enhances our theoretical knowledge but also holds practical implications for construction practices. Engineers and practitioners can use the findings to optimize compaction techniques, soil stabilization methods, and mitigate potential risks associated with inadequate compaction. Additionally, insights gained from this research can contribute to the development of more accurate predictive models and guidelines for soil compaction in diverse engineering applications.

In summary, this research endeavors to shed light on the intricate relationship between fine soil types and their compaction characteristics.

Aim:
Comprehensively understand the compaction behavior of fine-grained soils, specifically termite mound soil and kaolin, utilizing the Proctor compaction test as a key analytical tool.
Objectives:
To determine the soil classification of gravel soil and both fine soils.
To determine the compaction characteristics (MDD & OMC) on changes of fine percentage.
To determine the compaction characteristics (MDD & OMC) for termite mound soil and kaolin in respective fine percentages with coarse-grained (graded gravel soil) using the Proctor compaction test.
To compare the compaction characteristics between termite mound soil and kaolin under varying mix proportions.

2. Materials and Methods

2.1 Sample Collection

Selection of gravel soil is done at the construction site which is located in Wayamba university. Referring literature reviews about the fine soil types and soil specifications (B.B. Mujinya, 2013), I have selected the fine soil type and sample preparation using coning and quartering method. Kaolin soil is collected to ensure that the samples accurately represent

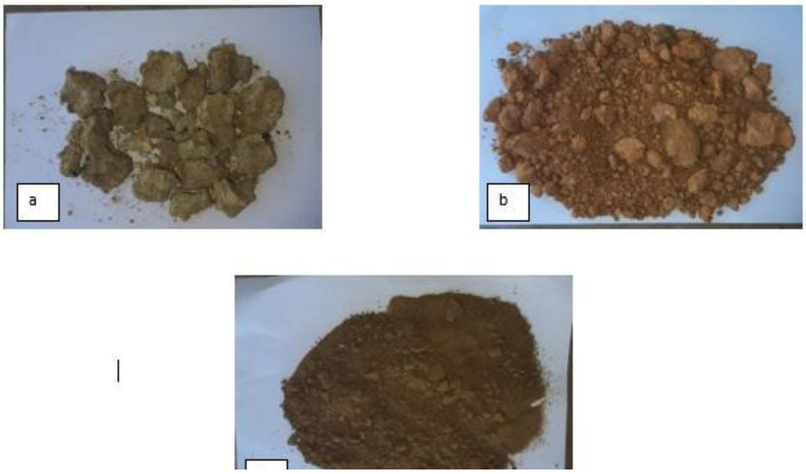

Figure 2.1 Soil sample: (a) Kaolin soil (b) Gravel soil (c) Termite mound soil

the in-situ conditions from Narangalla construction site. Termite mound soil with good variation of composition was found in land near Kuliyapitiya university premises.

2.2 Sample Preparation

Firstly, the bulk samples (Gravel soil) were divided in to laboratory sample fraction by coning and quartering method. Coning and quartering improve the precision of the sampling process. This is especially important in quality control and regulatory compliance where precise measurements are required. The samples were air-dried and lumps of soils were broken up with fingers or the mortar and pestle. The completed soil samples were put in to the oven and that were dried at 105^0C to 110^0C temperature. Especially if the samples have organic matter contain is high the oven temperature should reduce because the matters can be burned. After the oven dried samples were cooled down. The kaolin and termites mound soil were again broken up to fine type using rubber hammer make the sample as previous method.

Figure 2.2 Gravel soil sieving by 37.5mm sieve

2.3 Proctor Compaction Test Procedure

First, the entire gravel sample is sieved using a 37.5mm sieve to remove any large particles and other waste (Figure 2.2). The gravel soil sample is then poured onto the top sieve, and a cover plate is added to prevent dust and the loss of particles during shaking. The stack of sieves is placed on a mechanical shaker, which is then operated horizontally for approximately 3 minutes or until additional shaking no longer results in significant changes in the amount of material retained on each sieve. The fraction retained on each sieve is weighed. Using the weight of the sieves, a particle size distribution curves is drawn (Figure 2.3). Similarly, fine soil samples are sieved and the fraction retained on each sieve is weighed, with the data used to illustrate a graph for the obtained sieve analysis (Figure 2.4). Following this, the entire gravel soil and fine soils are sieved to separate each particle into containers, which are then labeled according to particle size.

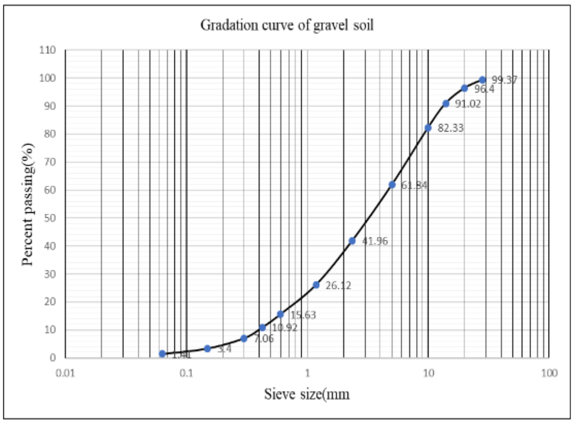

Figure 2.4 Gradation curve of Gravel soil

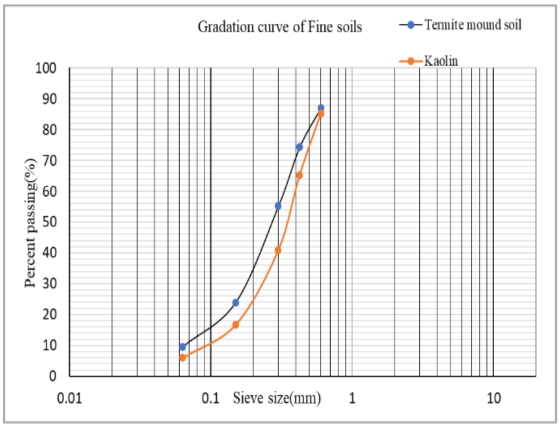

Figure 2.3 Gradation Curves of Fine soils

The proctor compaction apparatus is first ensured to be clean, calibrated and functioning properly. The ASTM standard proctor compaction test method B (John T. Germaine, Amy V. Germaine, 2009)is followed to conduct the proctor compaction test. The compaction mold and hammer are confirmed to be in good condition. New samples are prepared by adding selected sieved particles of the gravel soil according to the gravel gradation.

The Graded sample was prepared to maintain a constant gravel gradation according to the ASTM Standard Proctor Test Method B. Next, the fine types (Figure 2.5) and fine percentage are changed in constant gravel percentage of graded sample during the test. The fine percentage was changed to 5%,10% and 20% with each type. The above-mentioned graded gravel sample with one fine content is taken and equal weights are obtained to create the testing sample. The sample is then mixed thoroughly to achieve homogeneity. The moisture content is incrementally adjusted by adding a specific amount of water and thoroughly mixing it with the sample.

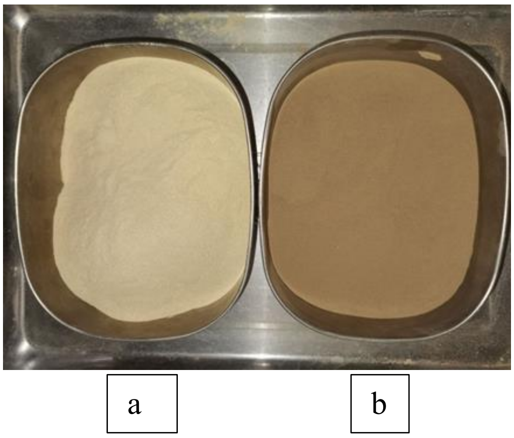

Figure 2.5 Fine particle of fine soils: (a) kaolin fine. (b)Termite mound soil fine

Assemble the compaction mold to the base, place a specified weight of the prepared sample into the compaction mold in 3 layers. Compact each layer using the compaction hammer with 25 blows per layer. The drops should be applied at a uniform rate and hammer should provide uniform coverage of the specimen surface. Fill the moisture cans with soil and determine the water content. As mentioned above, the selected fine soil is mixed with the gravel soil and proctor tests are done. There, the fine particles of the fine soil reserved from the sieve analysis test were tested fine content at 5%,10 % and 20%. Proctor test for one fine content is done five times in different moisture content and ρ_d and ω_c values are obtained. Measure and record the dry density and moisture content after each compaction.

3. Result & discussion

The proctor compaction test is done with graded gravel sample under fine particles of gravel soil, kaolin and termite mound soil that all fine particle with different fine content such as 5%,10% and 20%. Mainly all gravel samples are kept constant gradation to find the effect of fine types on compaction characteristics.

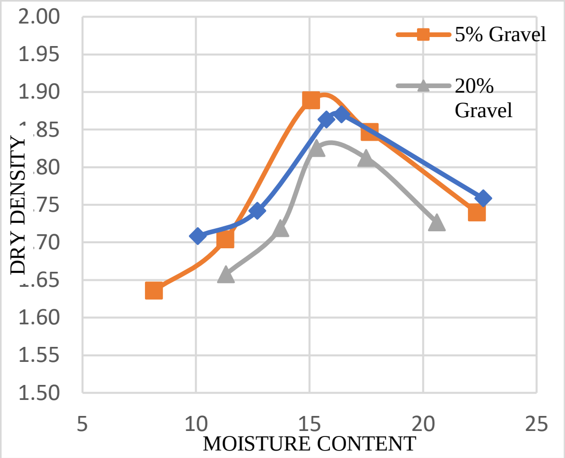

Figure 3.1 Compaction curve of Gravel soil with graded gravel sample

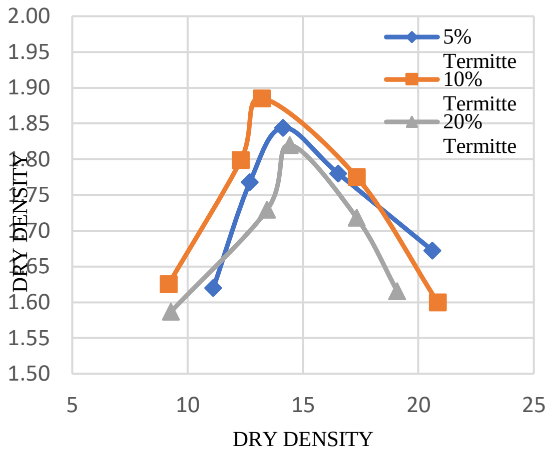

Figure 3.2 Compaction curve of Termite mound soil with graded gravel sample

The graph (fig 3.1) indicates all compaction curves with different gravel FC using obtained ω values and ρ_d values. Each compaction curve is indicated OMC (ω_{opt}) corresponding to the MDD(ρ_{dmax}). The ρ_d increases with ω when $\omega < \omega_{opt}$ .And the ρ_d decreases with ω when $\omega > \omega_{opt}$.As FC increases, water holding capacity of the gravel sample is increased.

10% FC gravel sample have largest ρ_{dmax} and minimum ω_{opt} compared to other gravel FCs. 5% FC gravel sample has ρ_{dmax} than 20% FC gravel sample. According to the result of the graded gravel sample with gravel fines particle, ρ_{dmax} will decreases and ω_{opt} will increases when the FC of gravel soil is increased to more than 10%.

According to the result of the graded gravel sample with the termite mound soil fines particles, ρ_{dmax} will decreases and ω_{opt} will increases when the FC of graded gravel soil is increased to more than 10%.

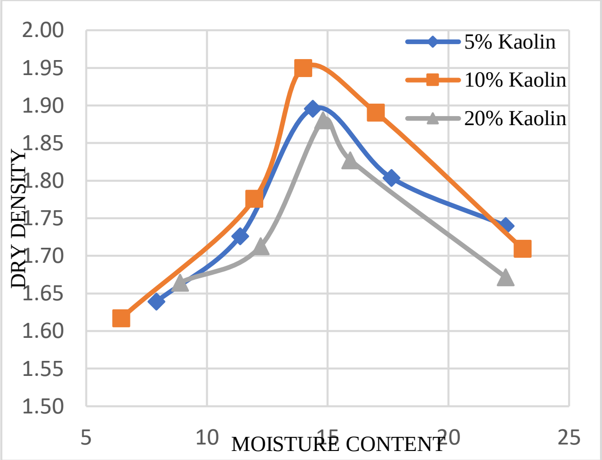

Figure 3.3 Compaction curve of Kaolin soil with graded gravel sample

The data indicates that the 10% FC with fine particles of Kaolin soil yields the largest $\boldsymbol{\rho_{dmax}}$ and the lowest $\boldsymbol{\omega_{opt}}$compared to other kaolin FCs (fig 3.3). Based on the results, it is evident that as the kaolin FC of the graded gravel soil increases beyond 10%, the $\boldsymbol{\rho_{dmax}}$ decreases while the $\boldsymbol{\omega_{opt}}$ increases. This trend suggests that a higher fines content results in a reduced maximum dry density and a higher optimum moisture content. When comparing the effects of kaolin soil fines on compaction characteristics, the 10% FC shows higher value for $\boldsymbol{\rho_{dmax}}$ than other types of soil. Nevertheless,10% Kaolin FC have middle value for $\boldsymbol{\omega_{opt}}$ than other soil fines (termite $\boldsymbol{\omega_{opt}}$ < kaolin $\boldsymbol{\omega_{opt}}$ < gravel $\boldsymbol{\omega_{opt}}$). Considering all 10% FC of soil types, $\boldsymbol{\rho_{dmax}}$ shows a law value and $\boldsymbol{\omega_{opt}}$ shows a law value of termite mound soil than other soil types. Compared to other soils, the graded gravel sample mixed with kaolin soil fines demonstrates superior compressibility at lower moisture levels. This characteristic allows for effective compaction even with minimum water content.

4. Conclusion

The Proctor compaction test was conducted using a graded gravel sample mixed with various fine particles, including fine gravel soil, kaolin, and termite mound soil. These fine particles were incorporated at different fines contents of 5%, 10%, and 20%. Throughout the testing process, the gradation of the gravel samples was kept constant to isolate and evaluate the effect of different fine types on the compaction characteristics. By maintaining a consistent gradation, the study aimed to provide a clear comparison of the impact of fine particle variations on the compaction behavior of the gravel samples. At 10%FC maximum $\boldsymbol{\rho_{dmax}}$ and minimum $\boldsymbol{\omega_{opt}}$ were found in all the three soil types. So that 10%FC is denoted as optimum fine content. Among them, in optimum fine content(10%FC) of kaolin soil, higher$\boldsymbol{\rho_{dmax}}$ was observed at minimum water level compared to other soil. In other word kaolin soil can reach well compaction characteristics than other soils.

When the FC is maintained at the optimum value, the fine particles are moved to the voids formed by coarse-grained sample. This happened in a densely packed soil structure that facilitate optimum compaction. In monitoring the previous investigations, it has been found that the chemical composition of the kaolin affects the adhesion between the particles (Badee Alshameri,, 2020). However, the optimum FC of kaolin fill that kind of voids formed by graded gravel sample. Optimum compaction of the soil represents better compaction characteristics than other soils. Finally, considering all results and discussion, the effect of fine soil types on compaction characteristics was observed through this experiment.

5. Acknowledgement

I want to express my sincere gratitude to Mr. Gayan Wanasinghe for his important contributions and constant assistance during this research project. Eng. Wanasinha's expertise in the field of civil engineering and directed me do this research about geo mechanics. I extend my heartfelt appreciations to him for his great supervision which has played an indispensable role in refining the vision and goals of this study. I also wish to express my deepest thanks to Dr. Dilani Dassanayake, the department coordinator. Her commitment to fostering innovative solutions within our department is a testament to her dedication. And I should acknowledge the rich history of geotechnical research that came before this investigation. Through a well-designed experimental program supplemented by in-depth analysis, the goal of the experiment is to shed light on the complex interactions between moisture content and dry density.

6. References

Badee Alshameri,, 2020. *Maximum dry density of sand–kaolin mixtures predicted by using fine,* Switzerland AG: Springer Nature.

B.B. Mujinya, F. H. M. G., 2013. Geoderma. *Clay composition and properties in termite mounds of the Lubumbashi area, D.R. Congo,* Geoderma(Belgium), pp. Pages 304-315.

John T. Germaine, Amy V. Germaine, 2009. Compaction Test Using Standard Effort. In: *Geotechnical Laboratory.* Hoboken, New Jersey: Published by John Wiley & Sons, Inc., pp. 210-223.

Investigation and evaluation of a probable tsunami event near Sri Lanka

L.H. Heshan Kavinda[1*], K. B. A. Silva[1]

[1] *Department of Construction Technology, Faculty of Technology, Wayamba University of Sri Lanka.*

* heshankavinda570@gmail.com

Abstract

The purpose of this study is to provide insights for risk mitigation and disaster preparedness by examining the possible effects of future tsunami events close to Sri Lanka. Underwater disturbances such as earthquakes can trigger tsunamis, which are a serious hazard to coastal communities worldwide, with Sri Lanka being especially vulnerable. The goals include gathering and evaluating past seismic data, pinpointing areas of risk, modelling tsunami waves mathematically and their propagation, and interpreting model outputs to comprehend how the tsunami interacts with Sri Lanka's coastline. Methodologically, the US Geological Survey database's earthquake parameters and bathymetry data from the GEBCO_08 grid are used. In order to determine probable tsunami origins, seismic factors are examined, and sophisticated mathematical modelling methods are used to mimic the creation and spread of tsunamis. Okada's equations are employed to simulate surface deformation, while, the Delft3D Flow module is used to simulate the wave propagation. The association between inundated waters and tsunami magnitude is revealed by the analysis, with observation stations along Sri Lanka's coastline exhibiting varied degrees of susceptibility. Places like Galle, Matara, Hambantota, and Colombo are more vulnerable to intrusion and the possibility of infrastructure and community damage. In order to increase resilience and lessen the effects of future tsunamis, the study highlights the significance of taking preemptive steps. The results point to the necessity of focused initiatives and community involvement for improving the local awareness on the probable threat of tsunami.

Keywords: Tsunami, Delft3D Flow, Earthquake, Mathematical Modelling, Sri Lanka

1. Introduction

A tsunami is a sequence of ocean waves with long wavelengths, triggered by disturbances like undersea earthquakes, volcanic eruptions, or landslides (Silva & Araki, 2018). Undersea earthquakes are the primary cause (Shuto, 2015). This research assesses the potential impact of a tsunami on Sri Lanka's coastal regions using mathematical modelling. By analyzing historical earthquake data, vulnerable areas are identified, and parameters for tsunami generation are determined. Sophisticated models simulate tsunami wave generation and propagation (Silva & Araki, 2018). The results are critically analyzed to provide valuable insights for disaster preparedness, risk mitigation, and protection of lives and property in Sri Lanka.

2. Data Collection

2.1. Bathymetry Data

Bathymetry data refers to underwater topography, collected using sonar to map seafloor depth (Hell et al., 2011). It is vital for navigation, marine research, and environmental monitoring (Ensign et al., 2004). For this study, bathymetry data was sourced from the GEBCO_08 grid, a global bathymetric grid with 30 arc-second spacing, providing precise underwater terrain representation (Figure 1) (Becker et al., 2009).

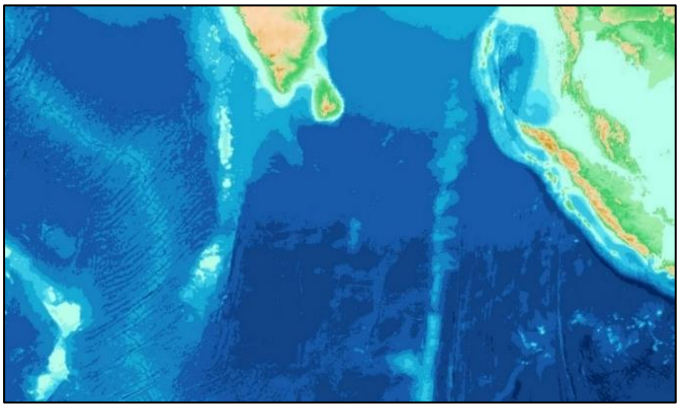

Figure 1. Bathymetry Data

2.2. Earthquake Data

Tectonic plate boundaries, where Earth's plates meet, cause earthquakes and volcanic activity (Le Pichon et al., 1982). Identifying these boundaries is crucial for collecting earthquake data from the US Geological Survey (USGS). This study collected earthquake data with magnitudes between 5 and 10 from 1950 to 2024, including 150 events near Sri Lanka (Silva & Araki, 2018), as shown in Figure 2.

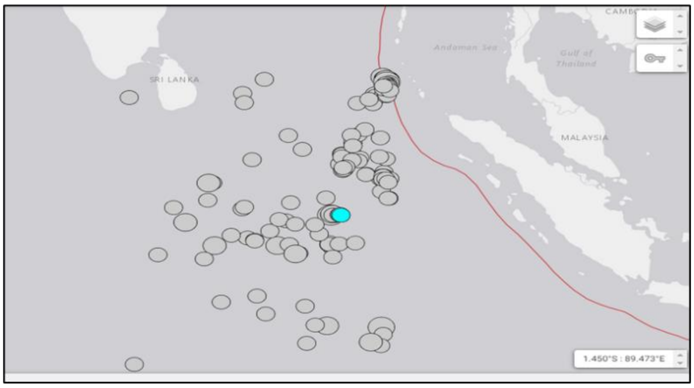

Figure 2. Earthquake location on the USGS map

2.3. Identifying a Significant Zone

From the obtained earthquake data, a suitable cluster of earthquakes that happened near Sri Lanka was selected as shown in Figure 3. That cluster consists of 10 earthquakes. All the details of those 10 earthquakes are listed in Table 1.

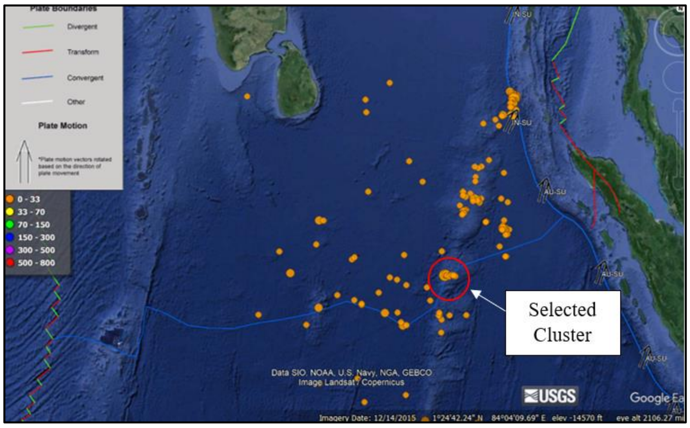

Figure 3. Selected cluster of earthquakes

Table 1. Details of Selected Cluster of Earthquakes

Date & Time	Place	Latitude (ºS)	Longitude (ºE)	Magnitude	Depth (km)
1987-04-01 20:19	South Indian Ocean	1.349	89.515	5	10
2023-04-12 13:59	South Indian Ocean	1.297	89.465	5	10
2007-04-09 20:48	South Indian Ocean	1.317	89.419	5	10
1972-12-14 20:49	South Indian Ocean	1.297	89.325	5.5	15
1999-11-28 10:17	South Indian Ocean	1.380	89.218	5.4	10
1999-11-29 03:55	South Indian Ocean	1.343	89.099	5.3	10
2000-01-28 22:42	South Indian Ocean	1.347	80.083	5.5	10
1999-11-29 03:46	South Indian Ocean	1.275	89.043	6.4	10
1999-11-15 05:42	South Indian Ocean	1.339	88.976	7	10
1999-11-28 10:17	South Indian Ocean	1.296	88.9	5.4	10

3. Methodology

3.1. Locating the Observation Points.

Observation points (Silva & Araki, 2018) are used to collect data on water levels, velocities, and wave heights. In this simulation, six observation points were established in Galle, Matara, Hambantota, Colombo, Trincomalee, and Jaffna using Delft Dashboard software to gather water level parameters during the tsunami simulation.

3.2. Generating the Initial Conditions

The initial tsunami wave was generated using the Delft Dashboard software (Van Ormondt et al., 2020) based on the selected cluster of earthquakes. First, a grid outline was defined on the earth map to cover the area, including Sri Lanka and the earthquake cluster, as shown in Figure 4. The fault line was then positioned to intersect the earthquake cluster. The initial tsunami wave was created and is illustrated in Figure 5. Four different tsunami scenarios were set up in Delft Dashboard by varying the wave magnitudes to 8, 8.5, 9, and 9.5 to produce various test results.

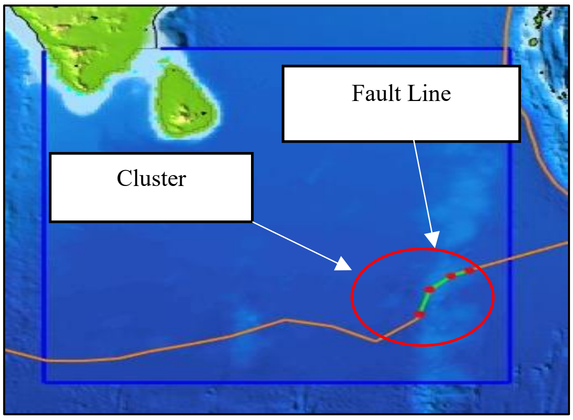

Figure 4. Selecting the grid outline on Delft Dashboard

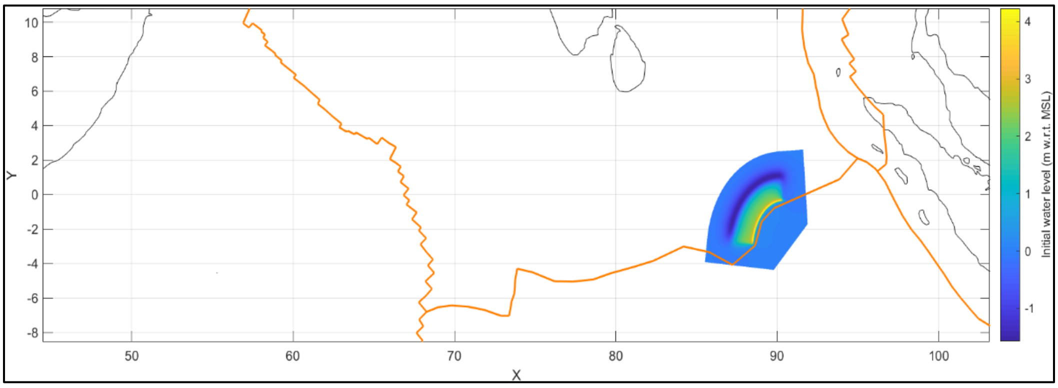

Figure 5. Initial tsunami wave

3.3 Simulating the Tsunami Wave Propagation

The propagation of a tsunami wave was simulated by using Delft3D software. Delft3D flow module is a modelling toolkit for simulating morphological processes, sediment transport, and hydrodynamics in aquatic environments, such as rivers and coastal regions (Delft 3D, 2011). The simulation did not account for wind waves, salinity, temperature, or dissolved sediments. A time step of 0.5 minutes was used to satisfy courant number criteria, and open boundary conditions were set to Riemann type (Delft 3D, 2011) for greater hydrodynamic variability with minimal reflection. Manning's roughness coefficient was set uniformly at 0.02. The simulation ran for 3 hours, employing the cyclic method for momentum advection. The acceleration of gravity and density of seawater were taken as 9.81 m/s^2 and 1020 kg/m^3 respectively.

4. Results and Discussion

4.1. Simulation No-1 - (Magnitude – 8)

According to the results from the mathematical model for a magnitude 8 tsunami (Figure 7), the highest maximum water levels are projected to reach 1.6 meters in Galle and 0.8 meters in Hambantota as shown in Figure 6. Moderate water levels are expected in Colombo and Matara, with heights of 0.65 meters and 0.46 meters, respectively. These areas may experience risks such as coastal flooding, saltwater intrusion, and erosion. In contrast, Trincomalee and Jaffna are projected to have no measurable water level rise, with recorded heights at 0 meters.

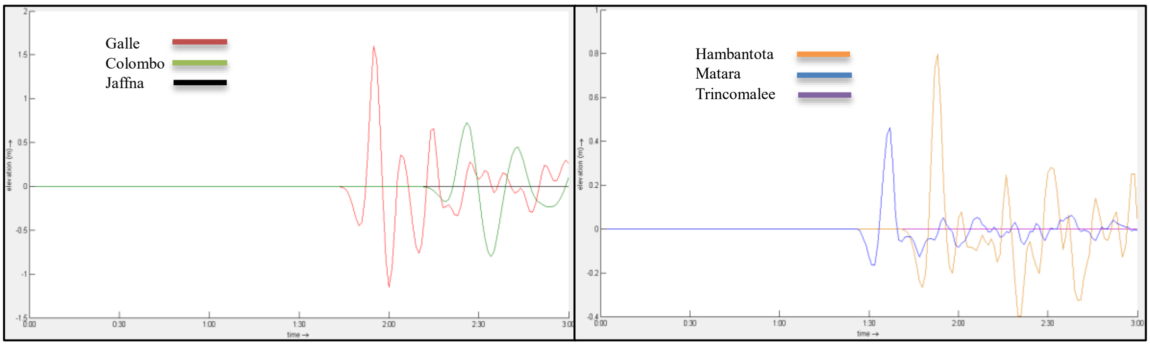

Figure 6. Water level variations at Matara, Galle, Colombo, Hambantota, Jaffna, Trincomalee

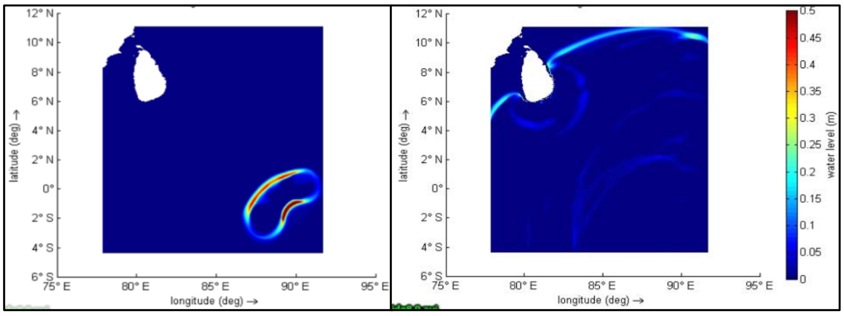

Figure 7. Simulations of tsunami wave

4.2. Simulation No-2 - (Magnitude – 8.5)

For an earthquake with a magnitude of 8.5 (Figure 9), the highest water levels reach 2.5 meters in Galle and 1.8 meters in Colombo as shown in Figure 8, indicating greater vulnerability to tsunami flooding. Hambantota and Matara show moderate levels of 1.2 meters and 0.85 meters, respectively, posing risks like coastal flooding. Trincomalee and Jaffna recorded no measurable rise.

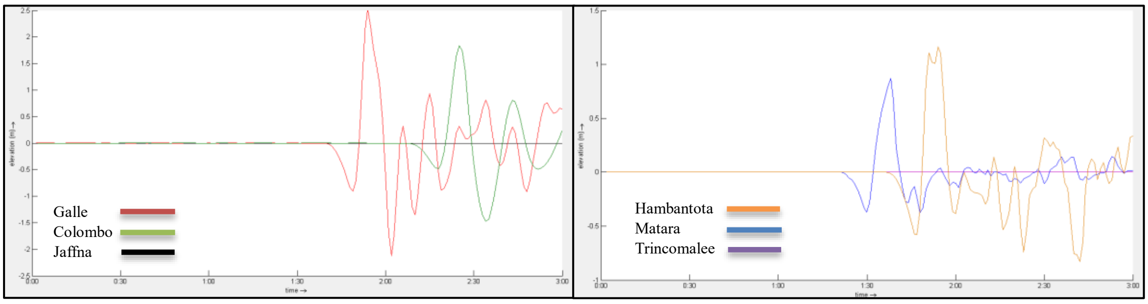

Figure 8. Water level variations at Matara, Galle, Colombo, Hambantota, Jaffna, Trincomalee

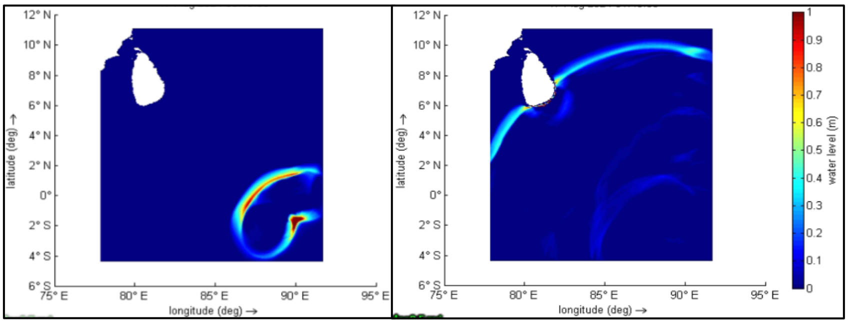

Figure 9. Simulations of tsunami wave

4.3. Simulation No-3 - (Magnitude – 9)

For a magnitude 9 earthquake (Figure 11), the highest water levels reach 3.8 meters in Galle and 2.9 meters in Colombo as shown in Figure 10, indicating severe vulnerability to tsunami flooding and damage. Hambantota and Matara show moderate levels of 1.6 meters and 1.1 meters, posing some risk. Trincomalee and Jaffna recorded no measurable rise.

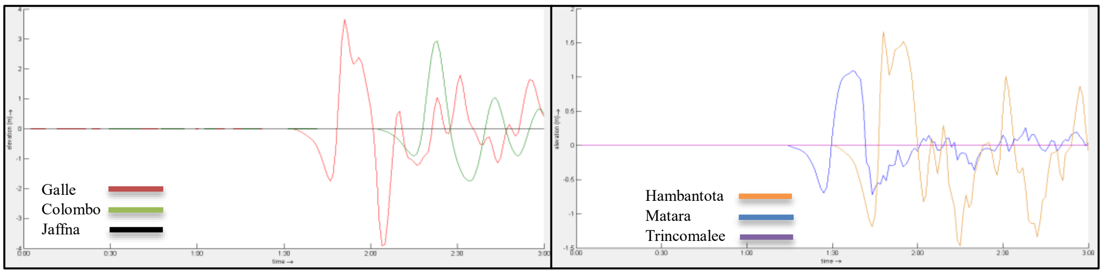

Figure 10. Water level variations at Matara, Galle, Colombo, Hambantota, Jaffna, Trincomalee

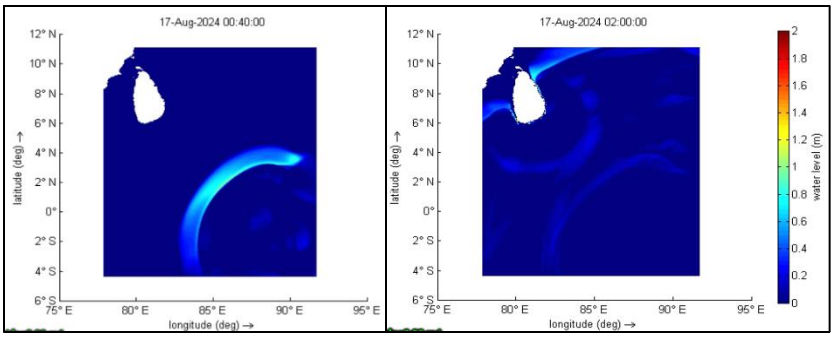

Figure 11. Simulations of tsunami wave

4.4. Simulation No-4- (Magnitude – 9.5)

For a magnitude 9.5 earthquake (Figure 13), the highest water levels reach 6.1 meters in Galle and 5.0 meters in Colombo as shown in Figure 12, indicating severe risk of tsunami-induced damage. Hambantota and Matara have moderate levels of 3.0 meters and 2.3 meters, respectively, posing additional risk. Trincomalee and Jaffna recorded no measurable rise.

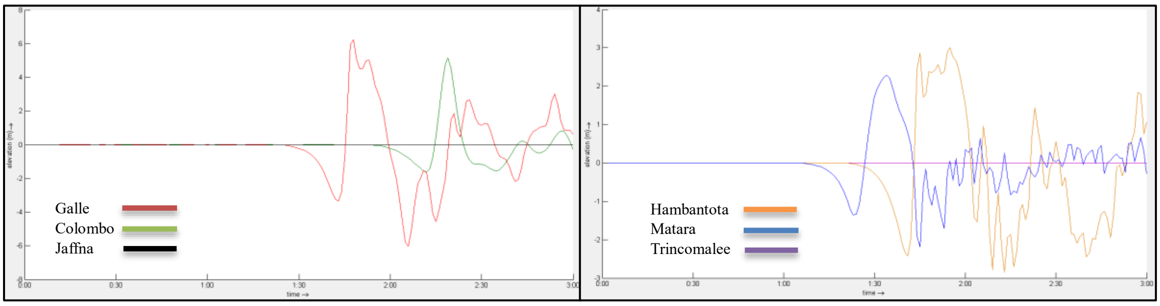

Figure 12. Water level variations at Matara, Galle, Colombo, Hambantota, Jaffna, Trincomalee

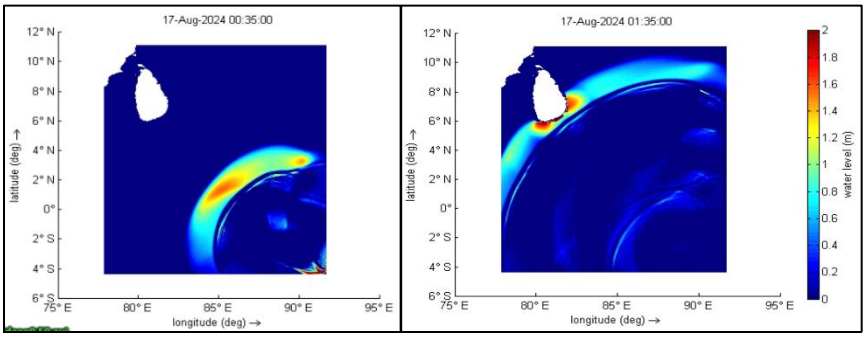

Figure 13. Simulations of tsunami wave

Figure 14 compares water level elevations for tsunami magnitudes 8.0, 8.5, 9.0, and 9.5.

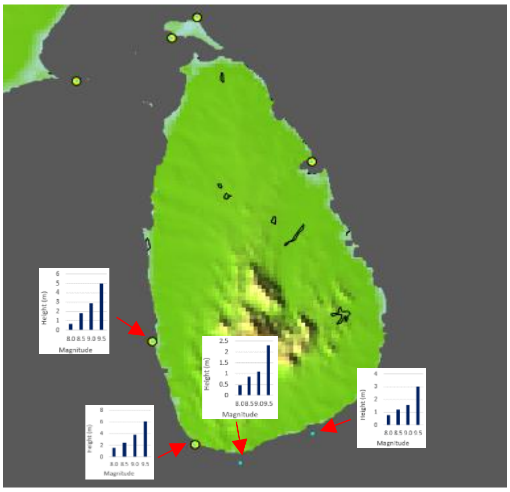

Figure 14. Water level variations at observation points for each simulation case (Earthquake magnitude 8.0, 8.5, 9.0, and 9.5)

5. Conclusion

The evaluation of tsunami magnitudes shows a clear link between tsunami size and water level extent. Galle, Matara, Hambantota, and Colombo are highly vulnerable, highlighting the need for targeted risk assessments and mitigation. Due to limited simulation time, the derived water level variations at Trincomalee and Jaffna do not show tsunami induced variations, however, those cities can also remain at risk from strong tsunamis. Proactive measures are crucial for enhancing resilience and reducing tsunami impacts. Integrating scientific data with community engagement will improve coastal protection and inform future coastal construction and displacement planning.

6. Acknowledgment

I would like to express my heartfelt gratitude to my esteemed research supervisor, Dr. Akalanka Silva, whose guidance, expertise, and unwavering support have been instrumental in shaping the direction of this research. In addition, I would like to express my gratitude to the individuals and organizations that I am willing to acquire resources, data, and information necessary for this research.

Reference

Becker, J.J. *et al.* (2009) ‘Global Bathymetry and elevation data at 30 arc seconds resolution: SRTM30_PLUS’, *Marine Geodesy,* 32(4), pp. 355–371.

Delft3D-FLOW, (2011). “User Manual, Simulation of multi-dimensional hydrodynamic flows and transport phenomena, including sediments,” Deltares, 3.15, 14499.

Ensign, S.H., Halls, J.N. and Mallin, M.A., (2004) ‘Application of digital bathymetry data in an analysis of flushing times of two large estuaries’. *Computers & Geosciences*, *30*(5), pp.501-511.

Hell, B. *et al.* (2011) ‘The use of bathymetric data in society and science: A review from the Baltic Sea’, *AMBIO,* 41(2), pp. 138–150.

Le Pichon, X., Angelier, J. and Sibuet, J. (1982) ‘Plate boundaries and extensional tectonics’, *Tectonophysics*, 81(3–4), pp. 239–256.

Shuto, N. (2015) ‘Tsunamis — their coastal effects and defense works’. *International Compendium of Coastal Engineering*, pp. 55–84.

Silva, A. and Araki, S. (2018) ‘Tsunami Interaction with Bay Beaches and Associated Headlands-A Numerical Case Study Based on 2004 and 2011 Tsunami Disasters’. *ISOPE International Ocean and Polar Engineering Conference* (pp. ISOPE-I). ISOPE.

Silva, A. and Araki, S. (2020) ‘Investigating the behavior of an onshore wall and trench combination ahead of a tsunami-like wave’. *Geosciences*, 10(8), p. 310.

Tsunami Le Pichon, X., Angelier, J. and Sibuet, J. (1982) ‘Plate boundaries and extensional tectonics’, *Tectonophysics*, 81(3–4), pp. 239–256.

Van Ormondt, M., Nederhoff, K. and van Dongeren, A., (2020). ‘Delft Dashboard: a quick set-up tool for hydrodynamic models’. *Journal of Hydroinformatics*, *22*(3), pp.510-527.

Automatic vehicle classification system for estimating the traffic density

Rajkumar Thilaksani[1], Kaleel Mohammethu Nubair[1], H.D.T Karunarathna[1], Mrs. K. Saikrisha[1]

[1] *Department of Engineering Technology, Faculty of Technology, University of Jaffna, Kilinochchi, Sri Lanka*

* rajkumardilakshi@gmail.com

Abstract

Traffic congestion is a common urban issue that increases passenger stress and leads to significant fuel waste due to prolonged waiting times at traffic junctions. Currently, traffic lights operate on preset timing systems that do not adjust based on real-time traffic conditions, failing to prioritize roads with higher vehicle density. To address this issue, recent years researchers focused to prioritize the vehicle movement on each road based on real time vehicle density measurement. In this paper, we focused on popular pre trained models such as convolutional neural network (CNN), YOLOV8 algorithm, KNN, and MOG2 are selected to identify the traffic congestion through the video frames and images received by cameras. The experiment was carried out using the popular traffic areas in northern area dataset, which has 7000 image samples of different traffic roads with 7 classes of vehicles. The dataset is split into two subset such as training and testing. 6222 images were used for training and 778 images were used for testing the system. The detection component of the system includes the elimination of background and the retrieval of data to determine the number of vehicles spotted. The models performance was evaluated using classification accuracy, sensitivity and specificity. Based on this vehicle classification, traffic density is calculated. The experiments proved that DenseNet-121 achieved 98% higher classification accuracy, and 67.63% for MOG2, 88.64% for KNN, 96% for YOLOV8 and 97.3% for CNN.

Keywords: Computer Vision, Real-Time System, Smart Traffic Lights, Traffic Congestion, Vehicle Detection.

1.Introduction

This project aims to design and implement a smart traffic control system that integrates machine learning (ML) to optimize traffic density in real time. Traditional traffic control methods, such as hand signals, were limited in their ability to adapt to fluctuating traffic patterns, leading to congestion, increased fuel consumption, and environmental pollution. The system developed in this project addresses these limitations by utilizing cameras to collect real-time data on traffic density, allowing continuous monitoring and analysis. Based on this data, AI algorithms will analyze traffic density and optimize traffic density accordingly. This project focuses on making traffic management smarter, more efficient, and eco-friendly through advanced technology.

2. Literature review

Researchers Rashi et al. [4] was based on smart control of traffic light systems using image processing. The main objective of this research paper was to change the traffic light according to traffic density and traffic count. The researchers mainly used MATLAB code and Arduino UNO.

Hosur et al. [6] describes a smart density-based traffic light system. This paper was developed to automatically adjust the timing based on traffic density using an Arduino UNO

AT Mega 328 microcontroller and infrared sensors. The traffic signal was designed using LEDs. The IR sensors detect vehicles by sensing the light reflected from them. The Arduino UNO, serving as the system's brain to continuously reads data from the IR sensors.

Arul et al. [8] used image processing, specifically the YOLO (You Only Look Once) algorithm and OpenCV, to analyze images and determine vehicle density in each lane, as well as detect the presence of emergency vehicles. Based on this information, the system optimizes the traffic lights, reducing unnecessary waiting times by giving green lights to lanes with higher vehicle density or emergency vehicles.

Upadhyay et al. [9] proposed using the YOLO v3 algorithm, a deep learning model, for real-time traffic monitoring. YOLO v3 is effective for object detection, including vehicle detection, making it valuable for traffic management. By accurately monitoring traffic flow, it can help optimize the timing of traffic signals, improving overall traffic management.

Kataria et al. [10] introduces a Traffic Light Management System with Manual Control, featuring three components: Vehicle Counting via Image Classification, a decision-making algorithm, and Manual Control. It analyzes traffic in real-time, adjusts green light timings based on vehicle counts, and allows manual adjustments. The system performs 75% better than the existing systems.

Chandra et al. [11] highlights the critical role of accurate Passenger Car Unit (PCU) values in traffic analysis, including applications like level of service, signal design, and traffic flow models. It notes that while many methods for estimating PCU values have been developed, those from developed countries aren't fully suitable for mixed traffic conditions due to the diversity of vehicle types, lack of lane discipline, and variability in vehicle behavior.

Yusefi et al. [12] proposes a new traffic light control method using an image processing model that counts vehicles and people at signals. The system uses the KNN classification technique to adjust the traffic lights based on the data collected. Tested with MATLAB, the method showed positive results, but its main limitation is the ability to identify only 30 inputs at a time.

3. Data collection

In this research we gathered a total of 8,000 images from three different locations to ensure a diverse set of traffic conditions and scenarios.

- Vavuniya: A dataset of 2,000 images was collected from key intersections and streets in Vavuniya. This location provided insight into traffic patterns in a smaller urban setting with moderate congestion levels.

- Colombo City: A larger dataset of 3,000 images was gathered from high-traffic areas in Colombo City, capturing diverse traffic situations, including peak hour congestion, pedestrian movements, and vehicle types. This dataset allowed the system to adapt to more complex and crowded urban environments.

- Kaggle Dataset: Additionally, we sourced 5,000 images from Kaggle [Kaggle: Your Home for Data Science], an open-source data platform. These images were used to further train the machine learning models with a variety of traffic conditions from global datasets, providing a broader context for understanding different traffic behaviors across multiple regions.

By incorporating these diverse datasets, the AI algorithms were trained to recognize traffic density and patterns in both local (Sri Lankan) contexts and generalized global conditions.

This ensured that the system is robust, capable of making accurate decisions in varying environments, and adaptable to other regions with similar traffic challenges.

Figure 1: Capture of road area [Colombo city]

4. Model implementation

4.1. Road area detection

Road area detection is an essential part of a smart traffic light system. Such a system is made more effective, safe, and efficient by incorporating road area detection.

4.1.1 Gray scale

Color images consist of RGB channels, with each channel representing a pixel's hue's depth. Grayscale conversion simplifies these channels, allowing each pixel to express brightness or depth. This simplifies photo processing tasks like location identification and movement monitoring. Background subtraction separates foreground objects from static backgrounds [2].

Figure 2: Gray scale image

Figure 3: Background subtraction

4.1.2 Point selection

Points on the road surface are marked on the video frame and the mouse callback function is set for the video window, allowing interactive recording of the coordinates of clicked spots while viewing the video.

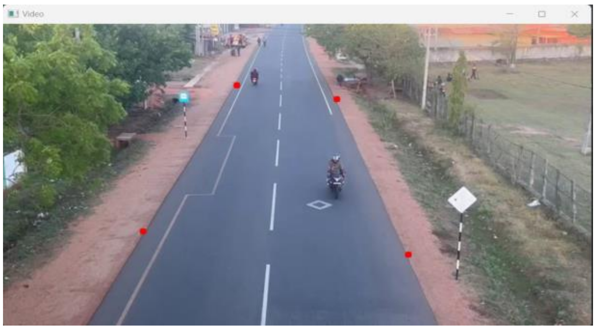

Figure 4: Points of the road area surface

Coordination of road area surface are Top left- (308, 146), Bottom left- (188, 362), Top right- (580, 359), Bottom right- (490, 147)

4.1.3 Masking

A Region of Interest (ROI) is selected by specifying a polygonal area using masking techniques [3]

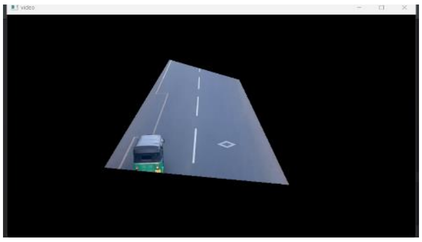

Figure 5: Masking

4.2 Vehicle detection using machine learning

4.2.1 KNN

K-Nearest Neighbors (KNN) is used to classify data by comparing new cases to similar past cases stored in its "memory" [4]. It uses parameter tuning, like adjusting the value of K, to improve accuracy. Small K values work well for noisy or small datasets, while larger K values provide better accuracy by considering more data points, reducing noise and outliers.

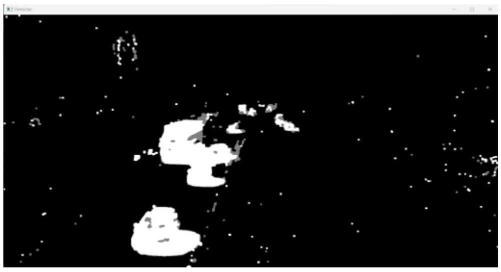

Figure 6. KNN Background subtraction

4.2.2 MOG2

MOG2 (Mixture of Gaussians 2) is a background subtraction algorithm in computer vision that detects moving objects by modeling the background with two Gaussian distributions [5]. It reviews each pixel to create a mask, separating the background from moving objects, making it useful for object detection, tracking, and surveillance

Figure 7: MOG2 Background subtraction

4.3 vehicle detection using deep learning methods

4.3.1 Data set collection and data processing

A total of 291 images were used for algorithmic testing and evaluation, while 2,553 images were utilized for training validation. To ensure accuracy during segmentation, the sample categories in both the training validation and test sets is balanced.

Figure 8: Training data [Local area]

4.3.2 YOLOV8 algorithm

YOLO set of rules works the use of the following 3 strategies [6]:

1. Residual blocks
   Images are divided into equal-sized grid cells (S x S), each responsible for detecting objects within its area, focusing on those at the center. This setup assigns each part of the image its own "detective" for spotting objects.

2. Bounding box regression
   The bounding box as a frame around something important in a picture. It's like drawing a border around a thing you want to pay attention to. Inside the photo, each bounding box has special info about what it's framing and it has spitted as Width (bw), Height (bh) and bounding box middle (bx,by)

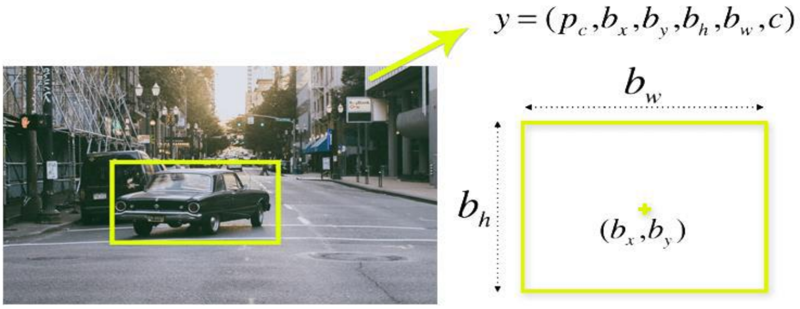

Figure 9: Bounding box [6]

3. Intersection Over Union (IOU)
   Intersection over Union (IOU) measures how much two overlapping boxes one drawn by a person and the other by a computer coincide in object detection. In YOLO, IOU helps refine object outlines by ensuring grid cells keep only the boxes that perfectly match the real objects, with an IOU of 1 indicating perfect overlap.

4.3.3 CNN

CNN is used to classify images in five stages: input, convolution, pooling, fully-connected, and output. The first three stages extract features, resizing, filtering, and condensing the image. The last two stages classify the image by combining extracted features and delivering the final classification result.
F1 score is given by the formula by [8],
$F\ 1=2t\ p\ 2t\ p+f\ n+f\ p$.
True positives (tp), false positive (fp), and false negative (fn).

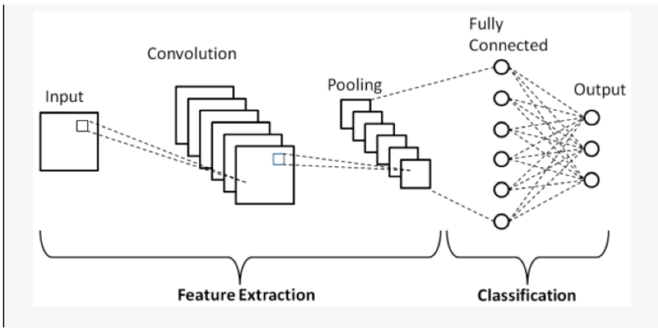

Figure 10: Schematic diagram of basic convolutional neural network [8]

5. Result

5.1. KNN and MOG2

The error percentage calculated by using below formula [7],
Error percentage%=|system counting−actual counting| / actual counting
Accuracy = 100% - error percentage

Table 1. Comparison between KNN and MOG2

No of video	**Actual no of vehicles**	**MOG2**		**KNN**	
		Counting	%	Counting	%
1	26	35	65.38	28	92.31
2	35	48	62.86	38	91.43
3	28	32	85.71	29	96.43
4	31	38	77.42	33	93.55
5	19	28	52.63	23	78.95
6	38	50	68.42	39	97.37
7	25	40	40.00	27	92.00
8	19	35	15.79	19	100.00
9	38	51	65.79	40	94.74
10	24	36	50.00	28	83.33
Accuracy			67.63		88.64

5.2. YOLOV8

Below figure 11 class "auto" has 0.46 cases or 46% of its detections assigned to class "background". This information can be useful for further analysis and improvements.

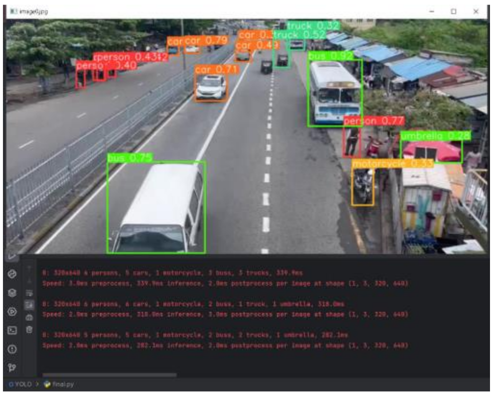

```
0: 320x640 4 persons, 5 cars, 1 motorcycle, 3 buss, 3 trucks, 339.9ms
Speed: 3.0ms preprocess, 339.9ms inference, 2.0ms postprocess per image at shape (1, 3, 320, 640)

0: 320x640 6 persons, 4 cars, 1 motorcycle, 2 buss, 1 truck, 1 umbrella, 318.0ms
Speed: 2.0ms preprocess, 318.0ms inference, 3.0ms postprocess per image at shape (1, 3, 320, 640)

0: 320x640 5 persons, 5 cars, 1 motorcycle, 2 buss, 2 trucks, 1 umbrella, 282.1ms
Speed: 2.0ms preprocess, 282.1ms inference, 2.0ms postprocess per image at shape (1, 3, 320, 640)
```

Figure 11: Automatically vehicle

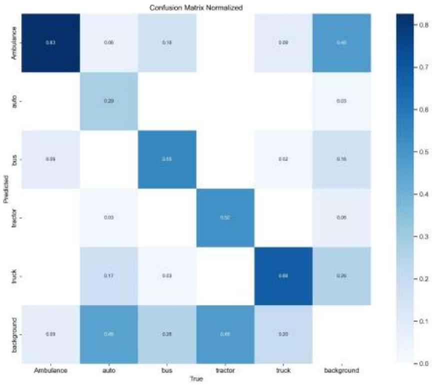

Figure 12: Confusion Matrix of YOLOV8

5.3. CNN

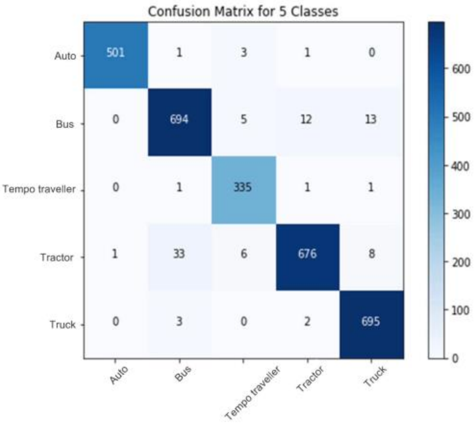

Figure 13: Automatically vehicle classification Figure 14: Confusion matrix of CNN

6. Density calculation

The YOLOV8 method to detect its vehicle classification and calculate each vehicle body area. Calculate the sum of all the vehicle areas in video frame.

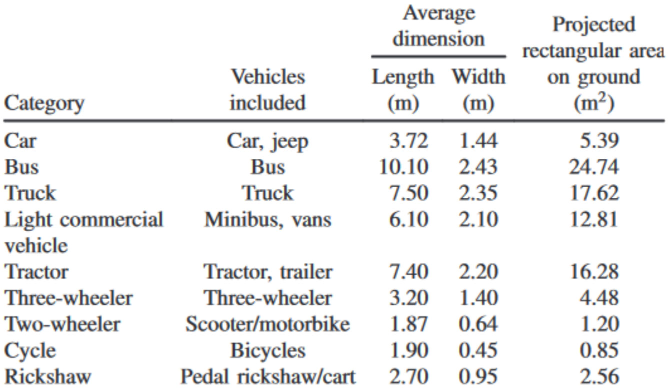

		Average dimension		Projected rectangular area on ground
Category	Vehicles included	Length (m)	Width (m)	(m^2)
Car	Car, jeep	3.72	1.44	5.39
Bus	Bus	10.10	2.43	24.74
Truck	Truck	7.50	2.35	17.62
Light commercial vehicle	Minibus, vans	6.10	2.10	12.81
Tractor	Tractor, trailer	7.40	2.20	16.28
Three-wheeler	Three-wheeler	3.20	1.40	4.48
Two-wheeler	Scooter/motorbike	1.87	0.64	1.20
Cycle	Bicycles	1.90	0.45	0.85
Rickshaw	Pedal rickshaw/cart	2.70	0.95	2.56

Figure 15: Estimation of passenger car unit [6]

Table 2: Total vehicle area

Type of the vehicle	**No of vehicle**	**Area of the per vehicle(m2)**	**Total area of the vehicle(m2)**
Car	1	5.39	5.39
Motorcycle	1	1.20	1.20
Track	1	24.74	24.74
Total vehicle area		31.33	

Coordination of road area surface mention in above figure Top left- (308, 146), Bottom left- (188, 362), Top right- (580, 359), Bottom right- (490, 147)
Area =61403m^2
By using below formula, the traffic density was calculated [6],

$$\text{Traffic density} = \frac{\text{Area covered by the vehicle}}{\text{area of the total region}}$$

$$\text{Traffic density} = \frac{31.33}{61403}$$

$$= 0.05\%$$

7. Discussion

The results of this research show clear differences in the performance of various algorithms used for vehicle detection and classification. By comparing the results of KNN, MOG2, CNN, and YOLOv8.

1. KNN vs MOG2

The comparison between KNN and MOG2 reveals that KNN significantly outperforms MOG2, achieving an average accuracy of KNN’s 88.64% vs MOG2's 67.63%. MOG2's higher error rates stem from its reliance on background subtraction, which struggles in complex urban environments with changing lighting and dynamic backgrounds. In contrast, KNN, as a supervised learning algorithm, classifies vehicles more accurately using labeled data, making it more robust under varying conditions. However, KNN's computational demands and slower processing speed make it less suitable for real-time applications compared to more advanced deep learning techniques.

2. CNN vs. YOLOv8

In the results, CNN performed slightly better than YOLOv8 in terms of accuracy, achieving an IOU score of 97.3% for CNN compared to 96% for YOLOv8. Several factors may include this higher accuracy:

1. Detection Conditions: Depending on the specific conditions of the data (such as lighting, angle, and occlusions), CNN may have performed better in accurately classifying objects.
2. Training Data: CNN was trained on a more comprehensive dataset, it might have learned to distinguish between classes more effectively, resulting in higher accuracy.

3. Traffic Density Estimation

Using YOLOv8 and CNN for vehicle detection enabled accurate calculation of traffic density, based on the total area occupied by vehicles in a given video frame. With a traffic density of 0.05% calculated from one of the observed frames.

8. Conclusion

In this research, we developed a system to classify vehicles and estimate vehicle density, divided into three key tasks: road detection, vehicle detection, and density calculation. The system utilized a dataset of 70,000 images and several videos collected from Colombo City, Vavuniya, and an external website. 80% of the data was used for training, while the remaining was set aside for testing and validation.

We compared multiple algorithms, including K-Nearest Neighbors (KNN), Mixture of Gaussians (MOG2), Convolutional Neural Networks (CNN), and the YOLOv8 deep learning model. The results showed that KNN achieved an accuracy of 88.64%, while MOG2 performed lower, with an accuracy of 67.63%. For deep learning-based approaches, YOLOv8 achieved an accuracy of 96%, outperforming CNN, which achieved 97.3% in terms of IOU (Intersection Over Union) score.

The superior performance of YOLOv8 can be attributed to its advanced architecture and real-time object detection capabilities. YOLOv8 leverages improved bounding box predictions, faster processing speeds, and higher accuracy, making it more suitable for real-time applications like traffic monitoring. Its ability to detect and classify multiple objects within a frame efficiently allowed for more accurate vehicle detection and, consequently, better vehicle density estimation.

By utilizing YOLOv8, the system was able to estimate vehicle density accurately in a single frame, making it ideal for use in traffic management systems where real-time data is essential for making rapid decisions. In summary, the superior performance of YOLOv8 over other algorithms demonstrates its effectiveness in enhancing traffic management by providing more reliable and efficient vehicle detection.

References

Arul, S.J., Mithilesh, B.S., Shreyas, L., Kaliyaperumal, G. and KA, J.K., 2023, February. Modelling and Simulation of Smart Traffic Light System for Emergency Vehicle using Image Processing Techniques. In 2023 3rd International Conference on Innovative Practices in Technology and Management (ICIPTM) (pp. 1-4). IEEE.

Ashwin, S., Vasist, R.A., Hiremath, S.S. and Lakshmi, H.R., 2017, August. Automatic control of road traffic using video processing. In 2017 International Conference On Smart Technologies For Smart Nation (SmartTechCon) (pp. 1580-1584). IEEE.

Bhatti, J.A., Asif, M., Hussain, S., Wasi, S. and Rajab, T., 2022, February. Smart street light for energy saving based on vehicular traffic volume. In 2022 Global Conference on Wireless and Optical Technologies (GCWOT) (pp. 1-4). IEEE

Bhavani, A., Verma, S., Singh, S.V. and Yadav, S.A., 2022, April. Smart Traffic Light System Time Prediction Using Binary Images. In 2022 3rd International Conference on Intelligent Engineering and Management (ICIEM) (pp. 367-372). IEEE. 51

Chandra, S. and Kumar, U., 2003. Effect of lane width on capacity under mixed traffic conditions in India. Journal of transportation engineering, 129(2), pp.155-160.

Firdous, A. and Niranjan, V., 2020, June. Smart density based traffic light system. In 2020 8th International Conference on Reliability, Infocom Technologies and Optimization (Trends and Future Directions)(ICRITO) (pp. 497-500). IEEE.

Hosur, J., Rashmi, R. and Dakshayini, M., 2019, March. Smart Traffic light control in the junction using Raspberry PI. In 2019 3rd International Conference on Computing Methodologies and Communication (ICCMC) (pp. 153-156). IEEE.

Kataria, P. and Rani, A., 2019, October. Real-time traffic light management system with manual control. In 2019 3rd international conference on recent developments in control, automation & power engineering (rdcape) (pp. 419-424). IEEE.

Khushi, 2017, September. Smart Control of Traffic Light System using Image Processing. In 2017 International Conference on Current Trends in Computer, Electrical, Electronics and Communication (CTCEEC) (pp. 99-103). IEEE.

Upadhyay, V. and Sivakumar, N., 2023, May. Traffic Monitoring System using YOLOv3 Model. In 2023 7th International Conference on Intelligent Computing and Control Systems (ICICCS) (pp. 1041-1048). IEEE.

Yusefi, A., Altun, A.A. and Sungur, C., 2020. Data Mining in A Smart Traffic Light Control System Based on Image Processing and KNN Classification Algorithm. Avrupa Bilim ve Teknoloji Dergisi, pp.461-465.

Experimental analysis of performance enhancement in polycrystalline photovoltaic panels incorporated with closed-loop active water-cooling system

H.V.V. Priyadarshana [1,2,3], N.M.Weerakkodi [2], M.G.K. Subodha [2], P.A.M. Gunathilaka [2], D.M.S.K. Deniyawaththa [2], P.L.L.P.U. Alwis [2], G.D.C.P Galpaya [1,2,3], D.K.A Induranga [1,2,3], S.V.A.A. Indupama[1,2,3], K.R Koswattage*[2,3]

[1] *Faculty of Graduate Studies, Sabaragamuwa University of Sri Lanka, Belihuloya, Sri Lanka.*
[2] *Department of Engineering Technology, Faculty of Technology, Sabaragamuwa University of Sri Lanka, Belihuloya, Sri Lanka.*
[3] *Centre for Nanodevices Fabrication and Characterization, Faculty of Technology, Sabaragamuwa University of Sri Lanka, Belihuloya, Sri Lanka.*

* koswattagekr@appsc.sab.ac.lk

Abstract

Solar photovoltaic technology is emerging as the most popular renewable energy source globally due to its environmental benefits, low operation and maintenance costs, modularity, flexibility, and energy independence. However, despite many advancements in the past few decades, the efficiency of commercially used solar photovoltaic panels remains relatively low due to reasons such as material limitations, temperature sensitivity, reflective losses, spectral mismatch, internal resistance, etc. Among these reasons, the operating temperature of the PV panel is a major factor that negatively affects the efficiency of the solar panel as a result of its temperature sensitivity. This study investigates the performance of a commercially used polycrystalline solar panel incorporated with a closed-loop active water-cooling system through an experimental procedure. The indoor experiment utilized an aluminum tube cooling panel integrated with a 260W commercial-grade polycrystalline PV panel. The performance measurements were taken under two main operating conditions, with and without the closed-loop water cooling system. Data for different parameters such as open circuit voltage (V_{oc}), short circuit current (I_{sc}), average panel temperature, coolant temperatures, ambient temperature and flow rate were collected for a period of 75 minutes at 5-minute intervals. The polycrystalline PV panel operated with the water-cooling system showed an average electrical power output increment of 12.72 W and an average decrease in operating temperature of 6.3% on the bottom surface. The results demonstrate that the operating temperature of the PV panel can be effectively controlled through closed-loop water cooling systems, leading to an increase in the electrical power output of the solar panel.

Keywords: Polycrystalline photovoltaic panels, PV cooling, efficiency enhancement, active water cooling, performance enhancement

1. Introduction

Solar PV technology has gained a great demand throughout the world. As a result of higher demand, solar PV technology is rapidly developing with the latest technologies to achieve the requirements of the energy industry. The main objective of a solar photovoltaic panel is to provide an optimum electrical energy output by converting a maximum amount of solar irradiance received by the solar panel with a minimum energy loss. However, the low energy conversion efficiency, which is generally around the 13%-20% range, is the main challenge faced by solar PV technology [1]-[3]. Apart from the type of solar PV panel used, there are several external parameters that affect the efficiency of a solar panel such as installation parameters of the solar system, operating temperature, solar irradiance level, wind speed, shading, dust accumulation, humidity, etc. [4]-[7]. Even though these commercially used solar photovoltaic panels are generally designed to withstand a wide range of operating temperatures, the increase in the operating temperature of the panel is a major factor that negatively affects the efficiency of the solar panel. The recent research findings suggest that a 1°C increase in operating temperature in a solar panel decreases its efficiency by 0.4% to 0.65% [7]-[10]. There have been several of research studies conducted on different technologies to control the increasing temperature of solar PV modules such as water spray cooling, forced air cooling, heat pipe cooling systems, water immersion cooling, floating solar systems, nanofluid-based cooling systems, heat sinks, phase change material-based cooling, etc. [11]-[17]. Many of these cooling technologies face financial challenges and practical limitations, making them difficult to implement in commercial solar PV systems. Among these technologies, closed-loop water cooling systems are significant as they can be developed as a commercial product due to high design flexibility and ability to utilize heat output for HVAC applications which can increase the energy efficiency considerably [18][19]. There have been some similar experiments conducted with active water-cooling methods proposing solutions for controlling the operating temperature of PV panels. Ali Sohani et al. have conducted a study on the energy efficiency and exergy increase of polycrystalline PV panels with a water-flow cooling system, which resulted in an increase in exergy efficiency of 13.0%-19.6% range [20]. Muhammad Faizan Younas et al. have conducted an experimental analysis on polycrystalline PV panels with water cooling systems which resulted in a 1.61% overall efficiency increase [21]. There are several other studies conducted by E. Roslan et al. [22], Laith Jaafer Habeeb et al. [23], Winston Woon Lee Meng et al. [24], Ilaf N. Rasool et al. [25] which studied the performance of solar PV panels with active water-cooling systems. Ateekh Ur Rehman has conducted a solar panel cooling system evaluation using a multi-criteria decision-making procedure which shows heat pipe cooling systems are the third best solar system cooling method considering a number of criteria [26]. Most of the similar research studies have been conducted with outdoor experimental setups where the operating temperature of the PV panel can be affected by a number of other environmental parameters like wind, humidity, irradiance, reflections, shadings, etc. This study was conducted in an indoor premises that controlled all of the above parameters which helped to identify the real effect of a closed-loop water cooling system on the PV panel. The objective of the research is to study the behaviors of the operating temperature and electrical efficiency of a polycrystalline solar panel provided by a closed loop water cooling system. The experiment was conducted using an indoor experimental setup built in the Faculty of Technology, Sabaragamuwa University of Sri Lanka. In this article, the study is presented under four sections. Section 1 discusses the solar PV cell model. Section 2 details development of the experimental setup and measuring equipment. Section 3 discusses the experimental results. Section 4 discusses the final conclusions of this study.

2. Methodology

The experiment was conducted using an indoor laboratory setup in Sabaragamuwa University of Sri Lanka, Belihuloya, (6.7184° N, 80.7741° E) in January, 2024. This experimental setup comprises a 260W polycrystalline solar PV panel, 500W halogen lamps (230V, AC), an Aluminium tube water cooling panel, a DC power supply unit (GW INSTEK GPS-4303), temperature sensors, an Arduino microcontroller unit, flow sensor, multimeters (Amprobe AM-570), a lux meter (LUX-29), a diaphragm water pump, a heat exchanger unit, and valves. The setup was built using galvanized box bars and placed within an enclosed chamber. Initially, the basic arrangement of the experimental setup and the cooling panel were designed using SolidWorks 2020 software as shown in Figure 01 and Figure 02.

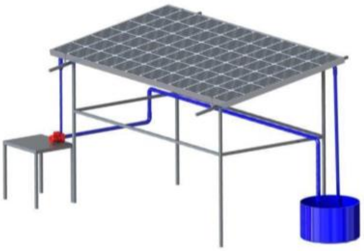

Fig 01: Closed-loop water circulating system design design

Fig 02: Layout of the water-cooling panel

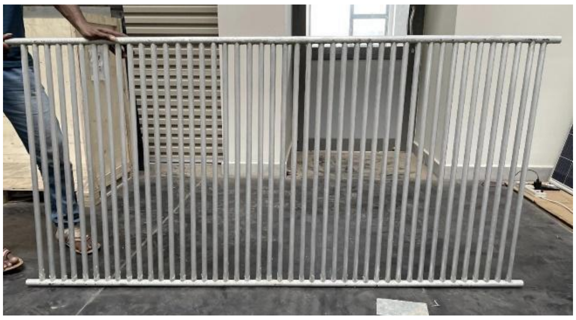

Fig 03: Aluminium tube cooling panel

Fig 04: 260 W polycrystalline PV panel

DC diaphragm water pump (TAIYOU TY-44520,12V DC), shown in figure 05 was used to circulate water through the cooling system. It has a maximum flow rate of 4 L/min and a 1.5m vertical suction lift. A sensor system was installed to monitor the flow rate and temperature of several components, including the tempered glass of the solar panel, its back sheet, frame, input and output water flow to the cooling panel. Additionally, the system tracks the ambient temperature. KY-028 digital temperature sensors (Fig 06) and YF-S201 water flow sensors were used with an Arduino mega 2560 microcontroller to monitor the temperature and the water flow rate of the cooling system. The KY-028 temperature sensor can measure temperatures between a range of -55°C to 125°C with an accuracy of ±0.5°C. For this experimental setup, 500W halogen lamps were selected as the light sources due to several reasons. These include their identical to natural sunlight in many aspects, low cost, high reliability, and commonly available in markets [27]-[29]. Also, the halogen bulbs emit considerably higher heat energy when operating which support to increase the operating temperature of the solar PV panel in a shorter time period.

Table 01: Specifications of the solar panel

Specifications	
Maximum Power (P_{max})	260 W
Maximum Power Voltage (V_{mp})	30.6 V
Maximum Power Current (I_{mp})	8.50 A
Open Circuit Voltage (V_{OC})	38.2 V

Short Circuit Current (I_{SC})	9.00 A

Four 500W halogen lamps (230V, 50 Hz) were placed 60 cm above the solar photovoltaic panel which was mounted horizontally. A water tank and a copper tube coil were used as the heat exchanger to absorb the heat of the photovoltaic panel through the cooling system as shown in Figure 06. The complete experimental setup is shown in Fig 08 which is located in a fully sealed chamber ensuring minimal exposure of the photovoltaic panel to external influences. The LUX-29 lux meter was used to measure the average luminous intensity on the solar panel.

Fig 05: Diaphragm water pump (TAIYOU TY-44520)

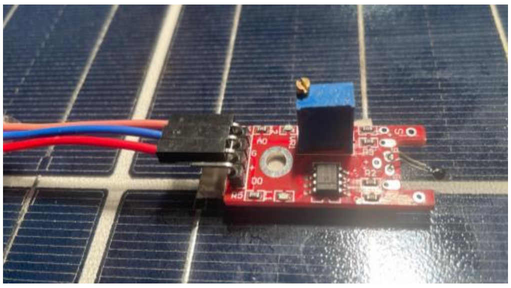

Fig 06: KY-028 digital temperature sensor

The measurements of the system were obtained to observe the performance of the polycrystalline solar panel under two main operating conditions, with and without the closed- loop water cooling system. The main parameters measured were open circuit voltage and short circuit current of the solar panel, panel top, panel bottom and aluminium frame temperature (T_{Frame}) of the solar panel, input water flow temperature ($T_{In\text{-}water}$) and luminous intensity (I_x). The average panel top temperature (T_{Top}) and panel bottom temperature (T_{Bottom}) values of the solar panel were obtained using multiple temperature sensors placed on random locations of the panel. The data was collected for a period of 75 minutes (1 hour and 15 minutes) at 5-minute intervals with and without the water-cooling system. Table 02 presents the data received for above parameters without the cooling system (Test 01) and Table 03 presents the data received with the water-cooling system (Test 02). All-data were obtained during night time for two consecutive days. Output water flow temperature ($T_{out\text{-}water}$), flow rate of the cooling system, temperature of heat exchanger, flow rate (Q_{water}), ambient temperature ($T_{ambient}$) and luminous intensity (I_x). The average panel top temperature (T_{Top}) and panel bottom temperature (T_{Bottom}) values of the solar panel were obtained using multiple temperature sensors placed on random locations of the panel. Table 02 presents the data received for the above parameters without the cooling system (Test 01) and Table 03 presents the data received with the water-cooling system (Test 02). All-data were obtained during night time for two consecutive days.

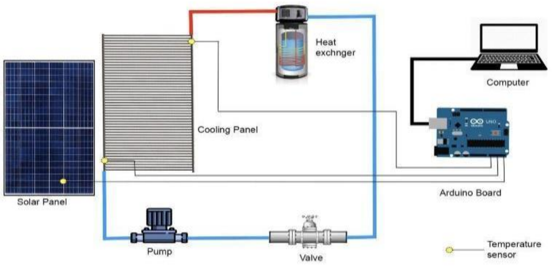

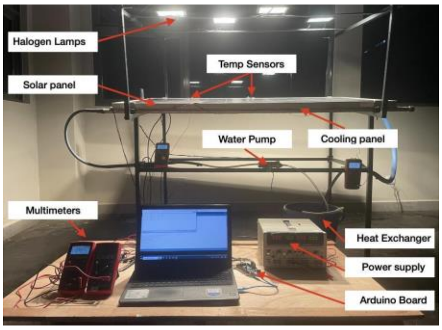

Figure 07: Schematic of the experimental setup

Figure 08: Indoor experimental setup

The average flow rate, ambient temperature and the luminous intensity during the two tests were as follows.

Table 02: Measurements of Q_{Water}, $T_{Ambient}$ and I_X

Measurement	Test 01	Test 02
Q_{water}	-	619.18 ml/min
$T_{ambient}$	27 ^{0}C	29 ^{0}C
I_x	704.20 lm/m2	674.2 lm/m2

3. Results and Discussion

The temperature variations of the solar panel during the two experiments are presented in Fig 09. Even there is a slightly different ambient temperature measured at the initial point of two experiments, it can be observed that the cooling system has reduced the operating temperature of the solar panel. The average bottom temperature of the panel decreased from 6.3% even with the 2°C ambient temperature difference. The average temperature increment of cooling water by absorbing the energy from the solar panel is 0.69 °C. It was observed that the bottom temperature was comparatively higher than the top temperature of the panel during the experiments. The temperature reading from the water inlet and the water outlet of the cooling panel, presented in Fig 10 confirms the heat transfer between the solar panel and the cooling system. Fig 11, Fig 12 and Fig 12 presents the behavior of I_{SC}, P_{out}, V_{OC} with the increase of operating temperature of the solar PV panel.

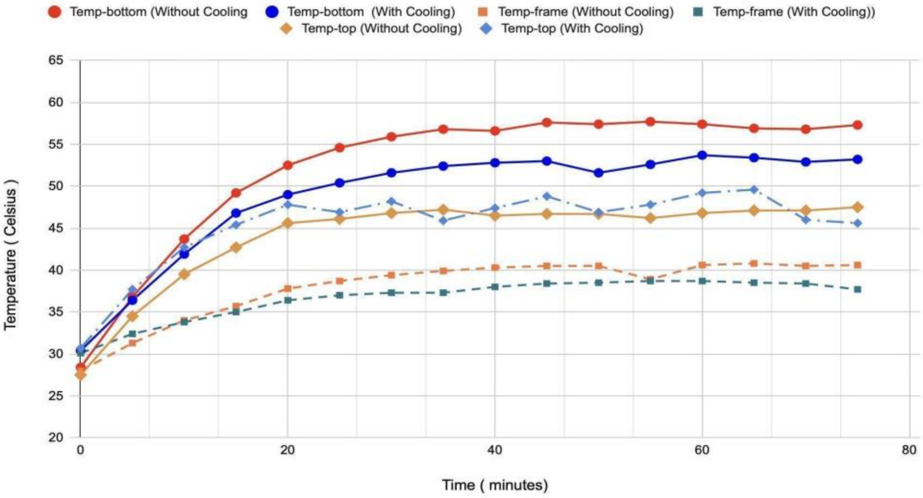

Figure 09: Temperature variation of the solar panel

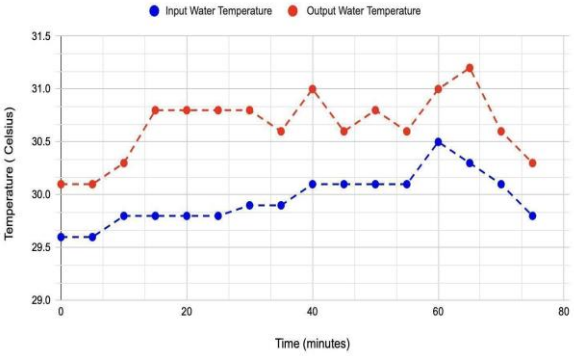

Figure 10: Temperature variation of water

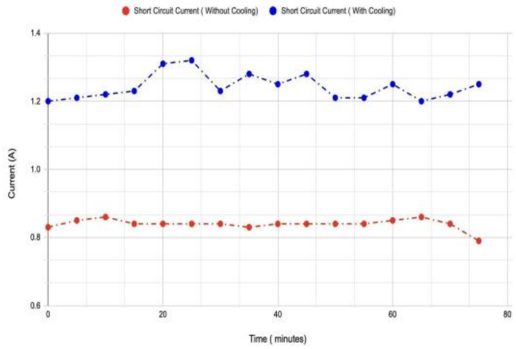

Figure 11: Variation of short circuit current (I_{SC})

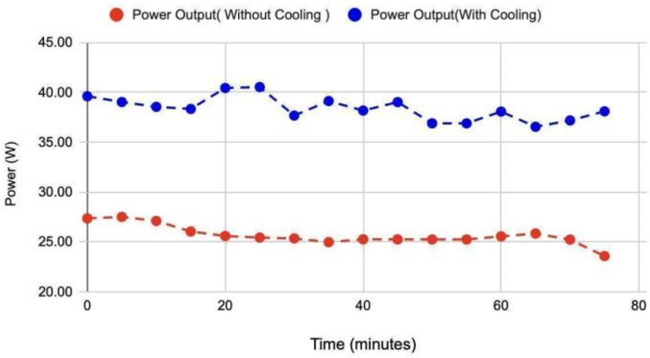

Figure 12: Variation of the power output (P_{out})

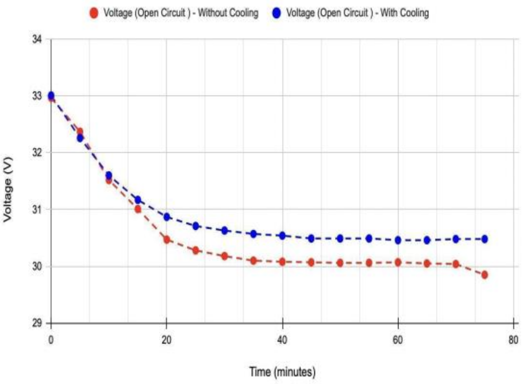

Figure 13: Variation of open circuit voltage (V_{OC})

It also confirms the temperature drop of the solar PV system. The power output of the solar panel can be calculated using the voltage and current measurements. There is a considerable increase in the V_{OC} and I_{SC} when the operating temperature of the solar panel is decreased using the closed-loop water cooling system. The average value of I_{SC} increased from 0.40 A and the average V_{OC} increased from 0.35V when the system is operated with the cooling system. The maximum improvements of V_{OC} and I_{SC} were 0.63 V and 0.48 A respectively. Figure 10 shows a significant increase in output power. The average electrical power output increased by 12.72W and the maximum improvement was 15.10 W. It was observed that the power output and the V_{OC} of the solar panel continuously decreased with the increase of the operating temperature of the solar panel while I_{SC} slightly increased. These observations agree with the conclusions of some of the recent studies, which conclude that the decreasing operating temperature of the solar panel increases the efficiency. When the solar panel operated with the cooling system, there was a considerable increase in I_{SC}, and with the increase of the operating temperature V_{OC} slightly increased and did not show a significant variation. This observation of the behavior of I_{SC} confirms the observations of some of the recent studies. This phenomenon occurs as the energy band-gap of the module decreases with the temperature increase which results in the rise of the band-to-band absorption coefficient, which is discussed in [30].

4. Conclusion

In this study, the performance of a commercially used polycrystalline solar panel operated with a closed-loop water cooling system was studied using an indoor experimental setup. Based on the results obtained the following conclusions can be made.

- The experimental results obtained conclude that the polycrystalline PV panel decreases its electrical efficiency by 0.69% for each 1°C temperature increase between 27.5 °C – 47.5 °C panel top surface temperature range.
- The overall electrical power output of commercially used polycrystalline PV panels decreases with an operating temperature increase.
- The operating temperature of the PV panel can be controlled through closed-loop water cooling systems leading to an increase in the electrical power output of the solar panel
- The water absorbs the heat energy from the solar panel, but there are practical limitations to utilize the amount of energy absorbed for an external application.
- The top surface, bottom surface and the frame of the solar panel have different temperature levels during operation and the panel surface temperature is not effectively controlled by the cooling panel in contrast to the bottom temperature.

Closed loop water cooling systems can be identified as promising technology among a number of other options used for solar PV cooling, that answer several practical limitations in other PV cooling technologies such as water wastage, design complexity, and installation limitations, etc.

5. Acknowledgments

This research was supported by the Science and Technology Human Resource Development Project, Ministry of Education, Sri Lanka, funded by the Asian Development Bank (Grant No: CRG-R2-SB-1).

References

1. Yang, C. *et al.* (2024) ‘Dew-point evaporative cooling of PV panels for improved performance’, *Applied thermal engineering*. Elsevier BV, 236(121695), p. 121695.
2. Parthiban, R. and Ponnambalam, P. (2022) ‘An enhancement of the solar panel efficiency: A comprehensive review’, Frontiers in energy research. Frontiers Media SA, 10.
3. Kumari, S. *et al.* (2023) ‘Efficiency enhancement of photovoltaic panel by heat harvesting techniques’, *Energy for sustainable development: the journal of the International Energy Initiative*. Elsevier BV, 73, pp. 303–314.
4. Shaik, F., Lingala, S. S. and Veeraboina, P. (2023) ‘Effect of various parameters on the performance of solar PV power plant: a review and the experimental study’, *Sustainable Energy Research*. Springer Science and Business Media LLC, 10(1).
5. Sarmah, P. *et al.* (2023) ‘Comprehensive analysis of solar panel performance and correlations with meteorological parameters’, *ACS omega*, 8(50), pp. 47897–47904.
6. Dhass, A. D. *et al.* (2022) ‘A review on factors influencing the mismatch losses in solar photovoltaic system’, *International journal of photoenergy*. Hindawi Limited, pp.1–27.
7. Krstic, M. *et al.* (2023) ‘Passive cooling of photovoltaic panel by aluminum heat sinks and numerical simulation’, *Ain Shams Engineering Journal*. Elsevier BV, (102330), p. 102330.

8. Govindasamy, D. and Kumar, A. (2023) ‘Experimental analysis of solar panel efficiency improvement with composite phase change materials’, *Renewable energy*. Elsevier BV, 212, pp. 175–184.
9. Khanegah, M. R. *et al.* (2023) ‘Performance evaluation of a concentrated Photovoltaic/thermal system based on water and phase change Material: Numerical study and experimental validation’, *Applied thermal engineering*. Elsevier BV, p. 120936.
10. Maghrabie, H. M. *et al.* (2023) ‘Performance enhancement of PV panels using phase change material (PCM): An experimental implementation’, *Case studies in thermal engineering*. Elsevier BV, 42(102741), p. 102741.
11. Hussien, A., Eltayesh, A. and El-Batsh, H. M. (2023) ‘Experimental and numerical investigation for PV cooling by forced convection’, Alexandria Engineering Journal. Elsevier BV, 64, pp. 427–440.
12. Arifin, Z. *et al.* (2020) ‘Numerical and experimental investigation of air cooling for photovoltaic panels using aluminum heat sinks’, *International journal of photoenergy*. Hindawi Limited, 2020, pp. 1–9.
13. Benato, A. *et al.* (2021) ‘Spraying cooling system for PV modules: Experimental measurements for temperature trends assessment and system design feasibility’, *Designs*. MDPI AG, 5(2), p. 25.
14. Sivakumar, B. *et al.* (2021) ‘Experimental study on the electrical performance of a solar photovoltaic panel by water immersion’, *Environmental science and pollution research international*. Springer Science and Business Media LLC, 28(31), pp. 42981–42989.
15. Sasmanto, A. A., Dewi, T. and Rusdianasari (2020) ‘Eligibility study on floating solar panel installation over brackish water in sungsang, South Sumatra’, EMITTER International Journal of Engineering Technology. EMITTER International Journal of Engineering Technology, 8(1), pp. 240–255.
16. Deivakumaran, S., Chua, Y. L. and Koh, Y. Y. (2023) ‘Active cooling system for solar panels with silver nanofluid and water’, IOP conference series. Earth and environmental science. IOP Publishing, 1205(1), p. 012012.
17. Alizadeh, H. *et al.* (2018) ‘Numerical simulation of PV cooling by using single turn pulsating heat pipe’, *International journal of heat and mass transfer*. Elsevier BV, 127, pp. 203–208.
18. Fu, Z. *et al.* (2024) ‘Performance evaluation of a novel vacuum-tube PV/T system with inserted PV module and heat pipe’, *Renewable energy*. Elsevier BV, 223(120027), p. 120027.
19. Shojaeefard, M. H. et al. (2023) ‘Experimental and numerical investigation of the effect of water cooling on the temperature distribution of photovoltaic modules using copper pipes, Energies. MDPI AG, 16(10), p. 4102.
20. Sohani, A. *et al.* (2021) ‘Energy and exergy analyses on seasonal comparative evaluation of water flow cooling for improving the performance of monocrystalline PV module in hot-arid climate’, *Sustainability*. MDPI AG, 13(11), p. 6084.
21. Younas, M. F. et al. (2020). Effect of active water cooling on the performance of PV module using steel channels. VW Applied Sciences.
22. Roslan, E. and Hassim, I. (2019) ‘Solar pv system with pulsating heat pipe cooling’, Indonesian journal of electrical engineering and computer science. Institute of Advanced Engineering and Science, 14(1), p. 311.
23. Habeeb, L. J et al. (2017). Cooling Photovoltaic Thermal Solar Panel by Using Heat Pipe at Baghdad Climate. International Journal of Mechanical & Mechatronics Engineering (IJMME-IJENS), 17(061J)

24. Meng, W. W. L. et al. (2021). Solar PV cell cooling with cool water circulation system: Design of closed-loop cool water re-circulatory system. Global Scientific Journal, 9(4), 3111.
25. Rasool, I. N. and Abdullah, R. S. (2023) ‘Experimental study of PV panel performance using backside water cooling chamber’, International journal of energy production and management. International Information and Engineering Technology Association, 8(2), pp. 89–95.
26. Rehman, A. U. (2023) ‘Solar panel cooling system evaluation: Visual PROMETHEE multi-criteria decision-making approach’, *Sustainability*. MDPI AG, 15(17), p. 12947.
27. Arifin, Z., Kuncoro, I. W. and Hijriawan, M. (2021) ‘Solar simulator development for 50 WP solar photovoltaic experimental design using halogen lamp’, *Heat and technology*. International Information and Engineering Technology Association, 39(6), pp. 1741–1747.
28. Al Mansur, A. *et al.* (2020) ‘Investigation of PV modules electrical characteristics for laboratory experiments using halogen solar simulator’, in *2020 2nd International Conference on Sustainable Technologies for Industry 4.0 (STI)*.
29. Enaganti, P. K. *et al.* (2020) ‘Analysis of submerged amorphous, mono-and poly-crystalline silicon solar cells using halogen lamp and comparison with xenon solar simulator’, *Solar energy (Phoenix, Ariz.)*. Elsevier BV, 211, pp. 744–752.
30. Paudyal, B. R. and Imenes, A. G. (2021) ‘Investigation of temperature coefficients of PV modules through field measured data’, *Solar energy (Phoenix, Ariz.)*. Elsevier BV, 224, pp. 425–439.

Implementation of programmable logic controller in machine operations with product sorting based on metal detection

Robinson Donald Franklin[1]* and Vadivel Hiroshaan[1]

[1] *Department of Mechatronics Technology, University College of Jaffna, University of Vocational Technology, Sri Lanka.*

* casrobinrobinson@gmail.com

Abstract

Every aspect of production has automated more and more in the last few decades. The food and apparel industries had to mandate that none of the hazardous metals be present in whatever product they made. In any case, the industry reduced any potential metal presence in the product to address the issue. Therefore, lowering the amount of money, time, and effort that people invest is one of our main goals. One of the most frequently employed automation devices in the industry is the Programmable Logic Controller (PLC), which allows for the programming of machine functions. This paper describes the development of an Omron PLC with ladder diagram programming using CX-One to control product sorting and packaging depending on metal and non-metal products. The design and implementation of an advanced PLC-based conveyor system, which integrates electro-pneumatic components to automate the sorting and separation of metal and non-metal objects. The system utilizes a PLC to precisely monitor and control the sorting process, ensuring high levels of accuracy and efficiency. To achieve effective object detection, the conveyor is equipped with a combination of inductive sensors, which are specifically used to detect metallic objects, and infrared (IR) sensors, which are employed to identify objects in the initial point. As objects move along the conveyor, the sensors detect their material composition in real-time. Upon detection, the PLC processes the sensor data and triggers the appropriate electro-pneumatic actuators to sort the objects into their respective bins. This automated sorting mechanism significantly enhances operational productivity by minimizing the need for manual intervention and reducing sorting errors. Based on the experimental results, this system can accurately and precisely classify objects into metal and non-metal categories and separate them in various pre-defined positions.

Keywords: metal, PLC, inductive, conveyor, automation

1. Introduction

The country is seeing a sharp rise in the industrial revolution, which needs to be appropriately managed, as a result of the fast development of urbanization, industrialization, and economic expansion. As globalization progresses, there is an increasing demand for superior products, more efficiency, and automated machinery (Ali and Ali, 2017). We require a tool that can operate a variety of universal work tool types in order to meet these needs. An increasing amount of manufactured goods, commercialized commodities, and transferred goods necessitates the use of automated machinery for packaging, sorting, manufacturing, handling, and shipping. To do this, some modifications to the size and complexity of automatic control systems and drivers were required. It is preferred in the industrial sector for fabrication to be as less "hands-on" as feasible as a technological process. For instance, severely hazardous, totally sterile, or vacuum- sealed environments are needed for the manufacturing of medicine, food scraps, metallic treatment, chemical disposal services, and advanced integrated circuits and microprocessors. Automated processing plants that operate without human intervention minimize human error while increasing productivity and profit margins and decreasing workplace accidents.

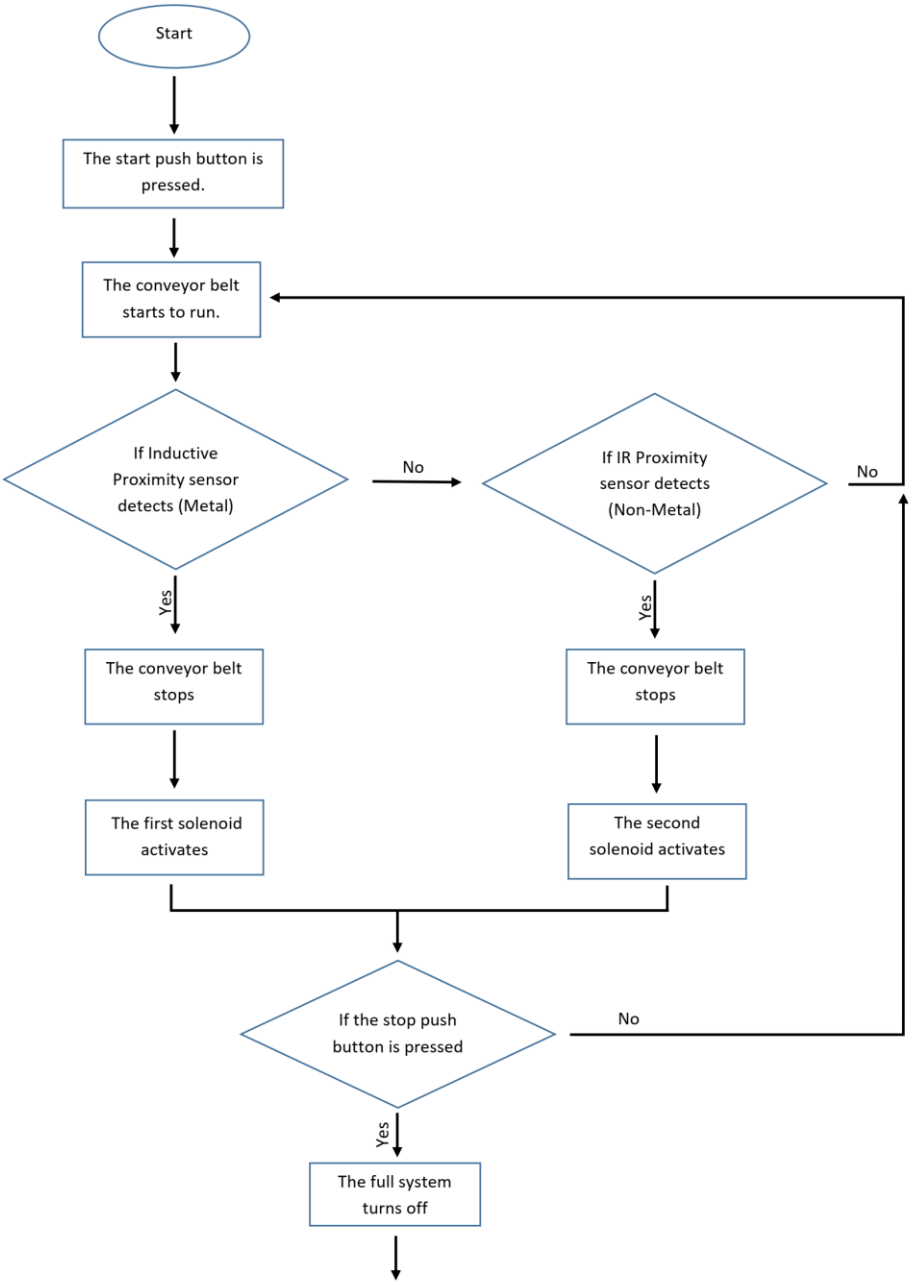

Figure 1. Process flow diagram

Industrial automation frequently uses Programmable Logic Controllers (PLCs) as system controllers (Basile *et al.*, 2012). PLCs are industrial devices that use logic algorithms in their operation (Otto and Hellmann, 2009). By integrating software, controllers extensively used in the industrial world replace conventional relays with simpler alternatives. (Sanver *et al.*, 2018). Because PLCs are so effective and efficient at installing, funding, and modifying circuits, they are widely employed in the industrial world.

The term "automation" describes a technological approach to production that reduces the need for human intervention (Smeu, 2013). In the process, manufacturing automation innovation in the industry is growing. Among them is the employment of sophisticated automated equipment to sort items more accurately and efficiently (Peilin *et al.*, 2017). Even for the food industry, the main goal of industrial standards is to keep foodstuffs free of metals and other pollutants that are harmful to the absorption of nutrients.. As a result, innovative methods for detecting metal elements in food have been developed recently (Liu and Zhou, 2011).

Sorting components based on sizes and materials is a task that an automatic sorting machine can complete independently, concurrently, with or without human intervention, depending on the application. Prior sorting methods that were put out relied mostly on PLC (Peilin *et al.*, 2017), machine vision (Pourdarbani *et al.*, 2015), hyper spectral imaging (Zhang *et al.*, 2014), and/or a variety of sensors (Oladapo *et al.*, 2016). However, there are a number of issues with these suggested methods, including low sorting efficiency, a lengthy time lag between inputs, inaccurate object identification, machine limitation for a particular task, the implementation of distinct programming for each task (which increases machine complexity), and manual operation.

The only material handling device in the design is a conveyor, which is highly adaptable in its use. We have created a low-cost automated system in this research project for the purpose of filtering for any metallic contaminant. With the aid of a PLC, the entire process is automated. The object is pushed into the box from the conveyor belt using pneumatic cylinders. The article begins with a quick overview of automation, sorting and PLCs and ends with a review of the literature. Section 2 discusses the materials and procedures. Section 3 covers the results and analysis, while Section 4 covers the conclusion and next steps.

2. Material and methods

The study discussed here proposes a semi-automated PLC-based sensory metal and non-metal sorting system. Figure 1 depicts the proposed way to operate the system. The proposed concept of the system makes use of proximity and inductive sensors to distinguish between metallic and non-metallic items on the conveyor and displays the contents of each kind of container. Utilizing ultrasonic sensors, the system determines the bin's level and adjourns when one or both of the bins are full. The bin's current status is shown on the LCD display. Nine different types of materials are needed to make this proposed design. Fig. 2 shows the schematic diagram of the proposed research. Table 1 illustrates the lists of components required to assemble this machine.

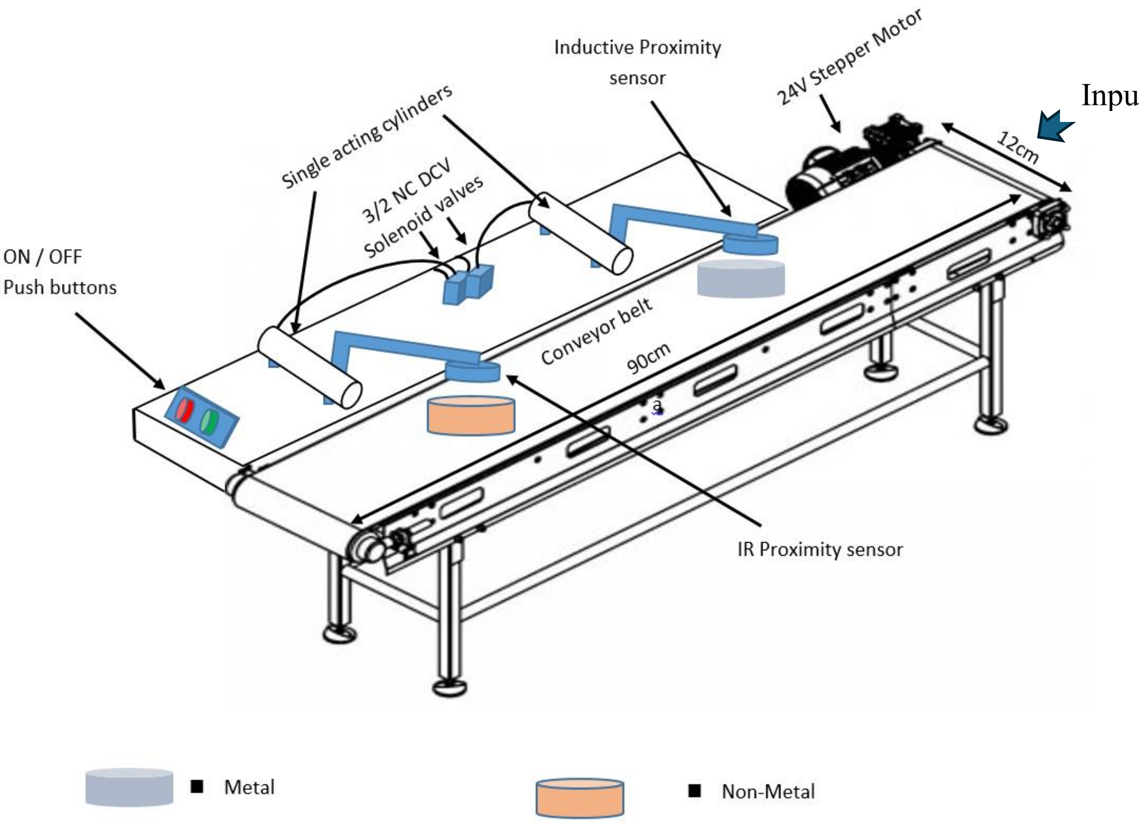

Table 1. Components list with specification and quantity.

Figure 2. Proposed design

Components	**Specification**	**PLC Address**	**Quantity**
PLC	Omron CP1E N40	-	1
Inductive sensor	8 mm range, NPN three cables, normally open type	X0.02	1
Proximity sensor	10 mm range, NPN three cables, normally open type	X0.03	2
Push buttons	Up to 24V DC	X0.01 & X0.02	2
3/2 Solenoid valve	3/2 Way 24V DC with spring return	Y100.02 & Y100.03	2
Single acting cylinder	Spring return	-	2
Stepper motor	24V DC	Y100.01	1
Ultrasonic sensor	3.3V – 5V, 8mA	-	2
Power supply	24V DC, 5A	-	1

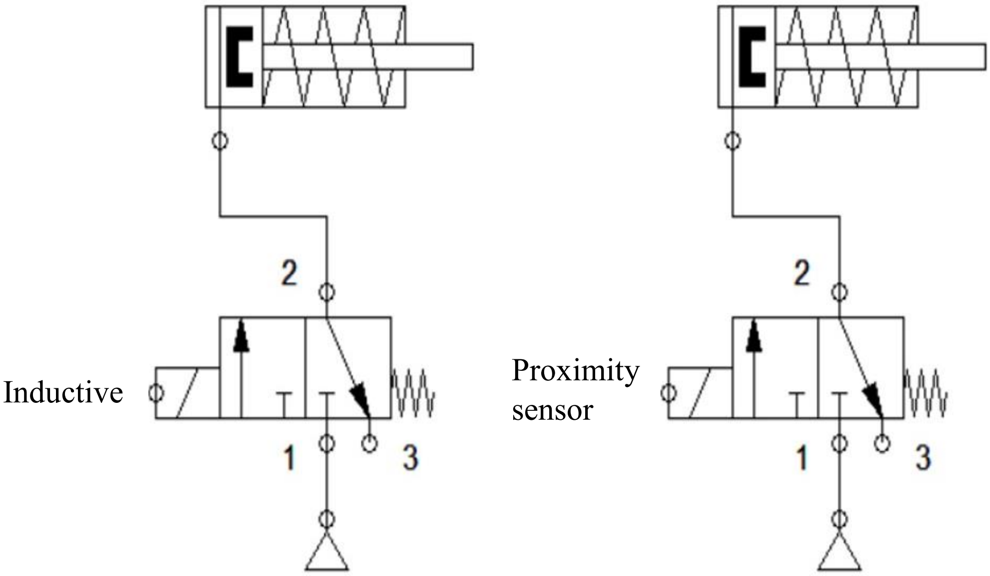

Figure 3. pneumatic design

According to the suggested design, the entire process starts when a proximity sensor on the conveyor picks up an object. When it detects something, the conveyor starts moving forward. As the object approaches, an inductive sensor is employed to distinguish between metallic and non-metallic objects. The conveyor stops and a pneumatic cylinder is triggered to advance based on the design in Figure 3, ejecting the metal object into a designated metal object bin if the inductive sensor detects the object as metal. An ultrasonic sensor is built into this bin to track the buildup of items.

Things made of non-metal require a slightly different procedure. When a non-metal object enters the detecting region of the inductive sensor and is later recognized by the proximity sensor, the conveyor halts and the non-metal object is expelled by the pneumatic cylinder into a different bin that is reserved for collecting non-metals.

The system additionally has an emergency stop function. The process instantly stops if the stop push button is pressed at any point while it is in operation, guaranteeing safety and averting any accidental activities. This methodology describes an organized process for handling and classifying items according to their material composition, complete with integrated safety and monitoring elements.

This system's automation technique makes use of a PLC, which designs and implements control logic using the ladder programming language. A popular tool in industrial automation for programming Omron PLCs is CX-Programmer software, which is used to create the ladder diagram that shows the control process visually. The above-described process is implemented and controlled through a ladder diagram, as illustrated in Figure 4. The ladder diagram serves as the foundational logic for automating the sequence of operations, ensuring precise coordination between sensors, actuators, and the conveyor system. The automation system's wire connections are set up in accordance with the schematic shown in Figure 5. This figure, which shows how each component is electrically connected to the PLC and other peripheral devices, is an essential reference. It takes proper

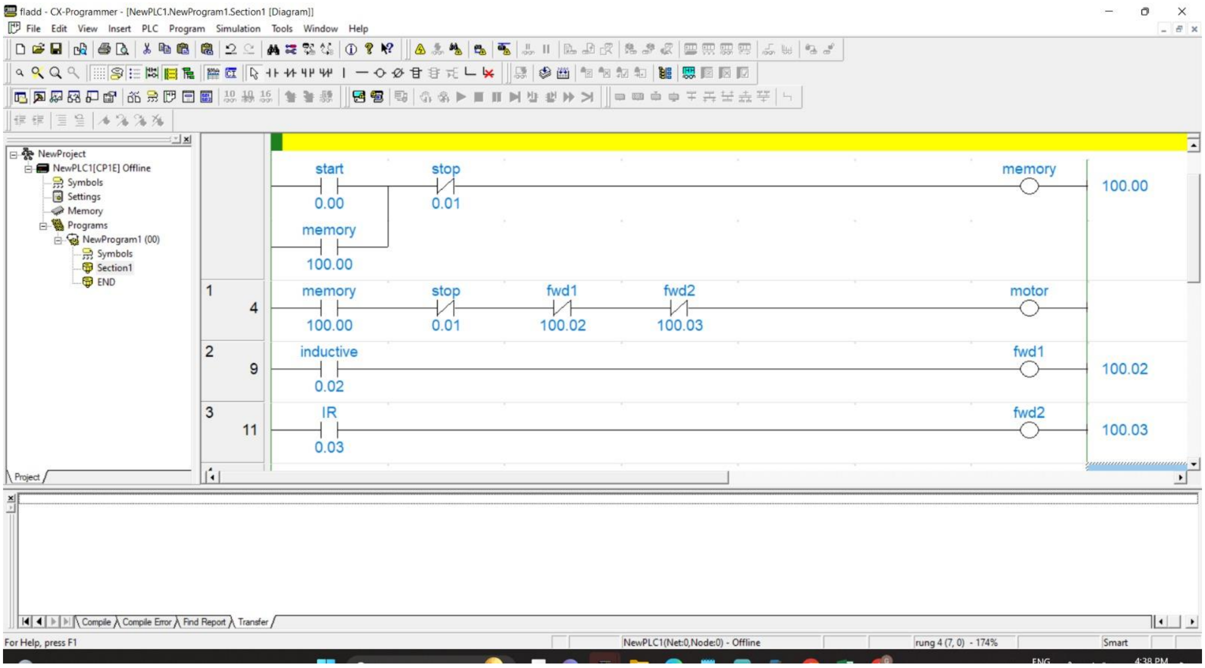

wiring to guarantee the system operates safely and dependably.

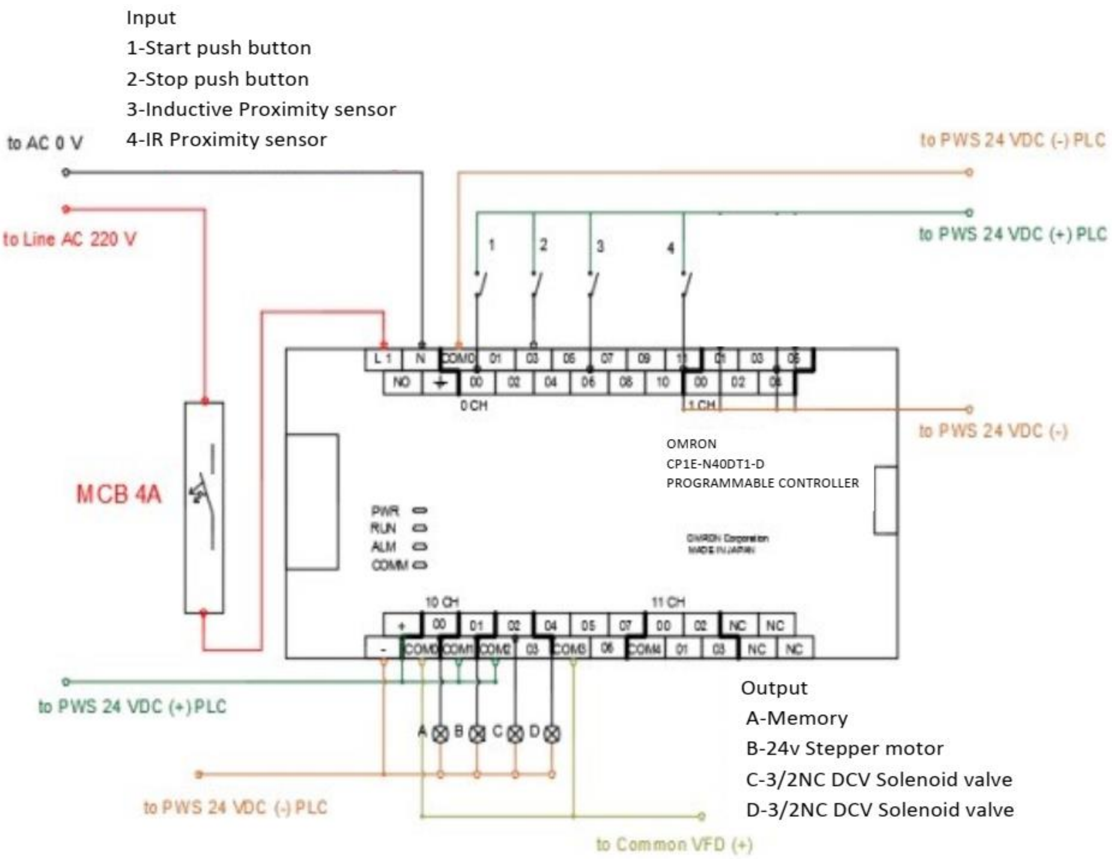

Figure 5. Wire connection diagram

3. Results and Analysis

After the automated object sorting system was developed and put into use, extensive testing was carried out to assess the tool's dependability and efficacy across a number of important electrical criteria. The testing comprised confirming that every system component sensor, the conveyor mechanism, and the pneumatic ejection system, among others performed as expected under a range of operating circumstances. Twenty distinct types of items were used in a series of tests to verify the system's functionality. These items were chosen to reflect a variety of materials and sizes that fall into the operational parameters that the design standards set forth. The system correctly distinguished between metal and non-metal objects and accurately sorted them into their appropriate bins during the testing phase, demonstrating full operational efficiency based on the Table 2. The system provided complete support for the height restriction of 18 to 23 mm, guaranteeing that objects falling inside this range are processed effectively. This setting is essential to make sure the objects are ejected by the pneumatic system and are positioned correctly for sensor detection. An actual representation of the project is given in Figure 6 of the outcomes section, which graphically illustrates the system's operational status and capacity to satisfy the requirements. This graphic depiction offers a thorough confirmation of the system's capabilities along with the recorded testing outcomes.

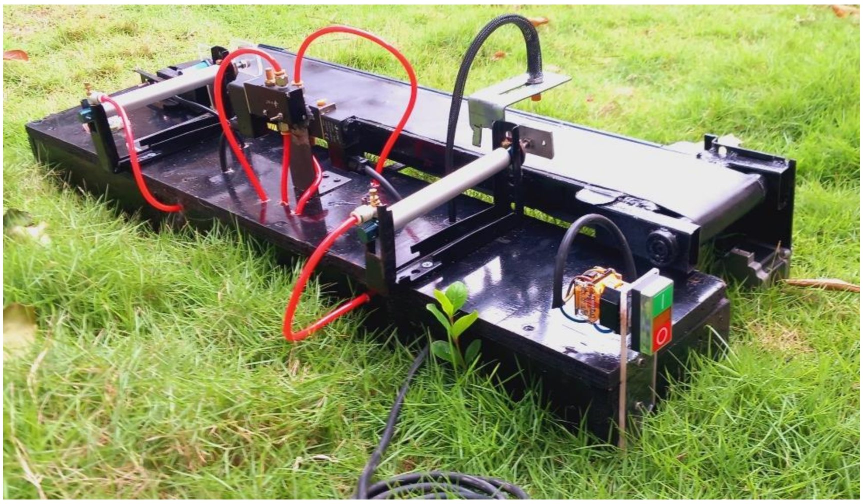

Figure 6. Actual representation of the project

Table 2. Experiment results

Height Range	Material	Count	Trails	Detected/Not detected
18 to 20 mm	Non metal	5	10	Detected
18 to 20 mm	Metal	5	10	Detected
21 to 23 mm	Non metal	5	10	Detected
21 to 23 mm	Metal	5	10	Detected

4. Conclusion and Future works

Managing the inputs that go through the input module, processing them using the configured program, and delivering the output to the output module are the steps in a PLC's operation. PLC usage is far more space-efficient and requires less room in the panel. The program has undergone multiple revisions by the author in order to adapt I/O as anticipated work principles. However, the author did not incur additional fees or lose money as a result of these modifications. The usage of traditional relays is adversely correlated with this. Typical relays need additional cables for testing, and something may go wrong with their installation. On the other hand, the PLC can be emulated prior to the installation being finished. Use a different type of sensor in the future in conjunction with the other adoptions for this project.

5. Reference

Ali, M.S. and Ali, M.S.R., 2017, September. Automatic multi machine operation with product sorting and packaging by their colour and dimension with speed control of motors. In *2017 international conference on advances in electrical technology for green energy (ICAETGT)* (pp. 88-92). IEEE.

Basile, F., Chiacchio, P. and Gerbasio, D., 2012. On the implementation of industrial automation systems based on PLC. *IEEE Transactions on Automation Science and Engineering*, *10*(4), pp.990-1003.

Liu, B. and Zhou, W., 2011, July. The research of metal detectors using in food industry. In *Proceedings of 2011 International Conference on Electronics and Optoelectronics* (Vol. 4, pp. V4-43). IEEE.

Oladapo, B.I., Balogun, V.A., Adeoye, A.O.M., Ijagbemi, C.O., Oluwole, A.S., Daniyan, I.A., Aghor, A.E. and Simeon, A.P., 2016. Model design and simulation of automatic sorting machine using proximity sensor. *Engineering science and technology, an international journal*, *19*(3), pp.1452-1456.

Otto, A. and Hellmann, K., 2009. IEC 61131: A general overview and emerging trends. *IEEE Industrial Electronics Magazine*, *3*(4), pp.27-31.

Peilin, L., Zhen, Y., Wenlong, Z. and Hong, L., 2017, December. An automatic sorting system for sorting metal cylindrical workpiece based on machine vision and PLC technology. In *2017 2nd International Conference on Robotics and Automation Engineering (ICRAE)* (pp. 446-450). IEEE.

Pourdarbani, R., Ghassemzadeh, H.R., Seyedarabi, H., Nahandi, F.Z. and Vahed, M.M., 2015. Study on an automatic sorting system for Date fruits. *Journal of the Saudi Society of Agricultural Sciences*, *14*(1), pp.83-90.

Sanver, U., Yavuz, E., Eyupoglu, C. and Uzun, T., 2018, January. Design and implementation of a programmable logic controller using PIC18F4580. In *2018 IEEE Conference of Russian Young Researchers in Electrical and Electronic Engineering (EIConRus)* (pp. 231-235). IEEE.

Smeu, G.A., 2013, May. Automatic conveyor belt driving and sorting using SIEMENS step 7-200 programmable logic controller. In *2013 8th international symposium on advanced topics in electrical engineering (ATEE)* (pp. 1-4). IEEE.

Zhang, Y., Du, B. and Zhang, L., 2014. A sparse representation-based binary hypothesis model for target detection in hyperspectral images. *IEEE Transactions on Geoscience and Remote Sensing*, *53*(3), pp.1346-1354.

Investigation of the electronic structure and interactions at the interface between L-cysteine and silver surfaces

Kaveenga Rasika Koswattage [1]*, Garage Don Kaveendra Virajith Maduwantha [1], Hewa Dewage Chandima Niroshan Gunawardana [1], Galpayage Don Chanaka Pradeep Galpaya [1], Happawana Vithanage Vimukthi Priyadarshana [1], Dingiriappu Kankanamlage Ashan Induranga [1], Samarathunga Vidana Arachchilage Amalka Indupama [1], Ekiriyagala Pallewaththe Ralalage Helitha Hiranya Wijethilake Nilmalgoda [1], Amarasinghe Mudiyanselage Prasad Chamara Amarasinghe [1] and Ekanayaka Rathnayaka Jayasundara Mudiyanselage Dasith Diyal Priyamal Wijesekara [1]

[1] *Centre for Nanodevices Fabrication and Characterization, Faculty of Technology, Sabaragamuwa University of Sri Lanka, Belihuloya, Sri Lanka.*

* koswattagekr@appsc.sab.ac.lk

Abstract

L-cysteine, a sulfur-containing amino acid, is known for forming bioactive surfaces through its strong interactions with metallic surfaces via its SH group. Among all noble metals, its bond with silver is considered unique and stronger. Although L-cysteine demonstrates a strong and distinctive interaction with silver, the electronic structure of their interface remains incompletely understood. In this research, ultraviolet photoelectron spectroscopy (UPS) and x-ray photoelectron spectroscopy (XPS) are utilized to investigate the electronic structure and interactions at the L-cysteine-silver interface. UPS revealed a spectral feature between the Fermi level of silver and the HOMO of L-cysteine, indicating an interaction between sulfur 3p and silver d orbitals. XPS displayed two peaks in monolayer films but only one in multilayer films. These findings enhance our understanding of the L-cysteine-silver electronic interaction and its potential applications in bioactive surface development and future bioelectronic devices.

Keywords: L-cysteine, Silver, Interface, UPS, XPS

1. Introduction

The advancement of bioelectronics, an interdisciplinary field that merges biology, electronics, and nanotechnology, hinges on the creation of bioactive surfaces and devices. A key challenge in this area is the effective interfacing of biomolecules with inorganic metallic substrates to construct functional bioelectronic devices such as biosensors. Sulfur-containing amino acids, particularly L-cysteine ($HS–CH_2–CH(NH_2)–COOH$), have attracted significant attention due to their robust affinity for noble metal surfaces like silver, gold, and copper (Koswattage and Ishii, 2020), (Lee *et al.*, 2008) Among these, silver is particularly notable for its distinctive characteristics, which are considered the best candidate to form bioactive surfaces.

L-cysteine interacts strongly with silver through its thiol group (-SH), as well as its amino (-NH2) and carboxyl (-COOH) groups, resulting in the formation of self-assembled monolayers (SAMs) (Chen *et al.*, 2021). This interaction can significantly alter the electronic structure at the L-cysteine-silver interface can significantly modify the electronic structure at the L-cysteine-silver interface, giving rise to new electronic states that hold promise for bioelectronic applications. Studies have demonstrated that L-cysteine forms densely packed layers on silver surfaces, with sulfur atoms playing a pivotal role in anchoring the molecules (Musarraf Hussain *et al.*, 2022). Theoretical studies suggest that increasing L-cysteine coverage might weaken the silver-sulfur bond (Luque *et al.*, 2012), but this phenomenon has not yet been thoroughly investigated experimentally.

In this study, we utilize ultraviolet photoelectron spectroscopy (UPS) and x-ray photoelectron spectroscopy (XPS) to provide a comprehensive investigation of the L-cysteine-silver interface. UPS provides valuable insights into the electronic states near the Fermi level, while XPS uncovers details regarding the chemical bonding and local structure around the sulfur atom. By the combination of these two surface-sensitive photoemission measurements, we aim to elucidate the formation of Ag-S bonds, interface electronic states, and the effects of L-cysteine coverage on the interaction with silver surfaces. This comprehensive approach enhances our understanding of the electronic structure and interactions at the L-cysteine-silver interface, with implications for the advancement of bioelectronic devices.

2. Experimental

Ultraviolet photoelectron spectroscopy (UPS) measurements were carried out at beamline BL8B of the Ultraviolet Synchrotron Orbital Radiation (UVSOR) facility at the Institute for Molecular Science in Japan. The spectra were acquired using a VGARUPS10 analyzer equipped with a multichannel detector system. The incident photon angle was set at 45° relative to the normal of the substrate surface, while the photoelectron detection angle was 0° (Koswattage *et al.*, 2015). Secondary electron cutoffs (SECO) were recorded with the sample biased at −5.00 V. All thickness-dependent UPS measurements were performed with a photon energy of 28 eV. The experiments were performed at room temperature. To mitigate beam damage, adjustments were made to the photon energy of the synchrotron beam, and acquisition was performed in brief intervals across different regions of the sample. For thicker films, charge accumulation was monitored by comparing consecutive UPS measurements under the same conditions. All XPS experiments were conducted at the BL 27A soft X-ray station in the Photon Factory of the High Energy Accelerator Research Organization (KEK-PF), Japan. The double crystals of InSb (111) were used as a monochromator. The energy resolution of the monochromator was 1.1 eV at 2.5 keV (sulfur K-edge). This beamline has the end station consisting of two ultra-high vacuum systems (UHV system), i.e., the main analyzing chamber and the sample preparation chamber. The base pressure of both chambers was in the order of 10^{-7} Pa. The main analyzing chamber consists of a hemispherical electron energy analyzer (VSW Co. Class-100) for conducting XPS measurements.

L-cysteine, sourced from Sigma Aldrich (purity: 99%), was placed in a quartz cylindrical tube wrapped with tungsten wire for heating. A single crystal Ag(111) surface was used for UPS measurements, while a silver plate was used for XPS measurements. Before the deposition of L-cysteine films, the gold surface was cleaned with acetone and introduced into the vacuum chamber, where it was subsequently sputtered using 1 keV Ar+ ions (Koswattage *et al.*, 2015). L-cysteine was evaporated at a controlled rate of 0.3 Å/s, as monitored by a crystal detector. The film thickness of the L-cysteine was estimated based on nominal values and adjusted according to previous evaporation rates and durations. Once the desired evaporation rate was achieved, the sample was transferred from the preparation chamber to the deposition area, positioned to face the evaporator for the specified duration, then repositioned and moved into the measurement chamber. Three different types of films were prepared by adjusting the evaporation times: monolayer (nominal thickness 0.4 nm), two-layered (nominal thickness 0.8 nm), and multilayer films (nominal thickness 5 nm). XPS measurements were then conducted for each film type to analyze the thickness at each stage of film formation.

3. Results and discussions

Figure 1 displays the UPS spectra of L-cysteine on Ag(111) across various film thicknesses, illustrating the thickness-dependent UPS analysis. Each thickness is represented by a different color, and each spectrum is labeled with the nominal thickness of the L-cysteine layer in Å. The x-axis of the figure denotes the binding energy of the photoemitted electrons, with BE = 0 eV corresponding to the Fermi level.

The spectrum at the bottom represents the UPS data for clean Ag(111), where the Ag 4d5/2 and Ag 4d3/2 peaks appear at approximately 4.8 eV and 6.1 eV, respectively. The work function of clean Ag(111) is estimated to be 4.5 eV, derived from the high binding energy cutoff of 23.5 eV.

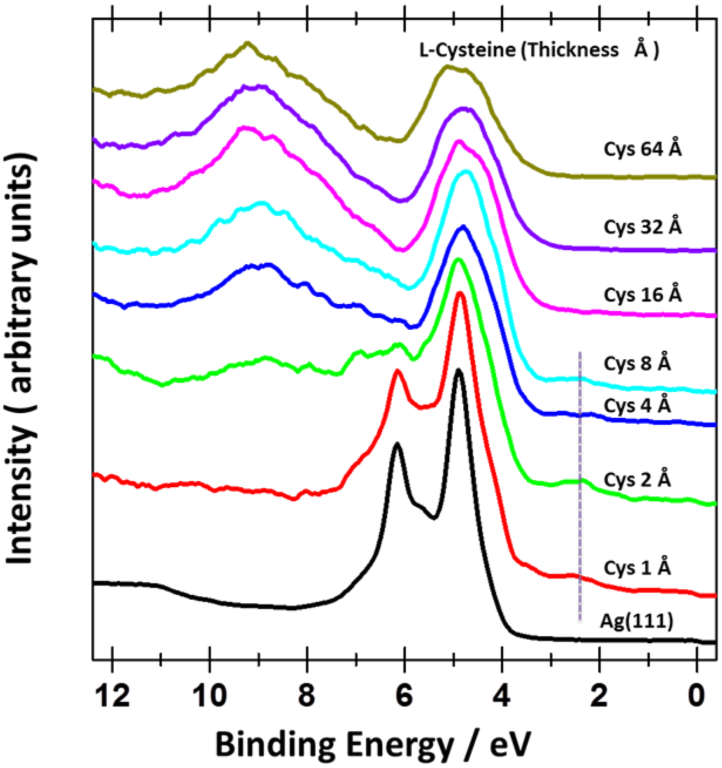

Figure 1. UPS spectra of a clean Ag(111) and subsequently evaporated L-cysteine films on the clean Ag(111).

The spectra for thin films clearly indicate that the spectra for thin films differ notably from those for thicker films, likely due to interactions between L-cysteine and Ag(111). In the thin film spectra, a distinct feature emerges around 2.5 eV, marked by a dotted line in the figure. Additionally, the intensity in the Ag d band region shows a partial reduction and a change in shape. As the L-cysteine layer thickness increases, the Fermi level of Ag(111) progressively diminishes and is completely absent at a thickness of 64 Å. Consequently, the UPS spectrum for 64 Å of L-cysteine is considered to reflect only the electronic structure of L-cysteine. The feature centered at approximately 4.8 eV binding energy for this thickness is attributed to the HOMO of L-cysteine. The HOMO cutoff is estimated to be 3.2 eV by fitting a straight line to the HOMO edge and determining its intersection with the binding energy axis.

Figure 2 shows XPS S 1s spectra of L-cysteine on a silver surface. Spectra with three colors correspond to monolayer, two-layered, and multi-layered films, respectively. It is clear from the figure that the main peak and a prominent shoulder can be observed in the monolayer in contrast to the thick layers. The main peak position of all three layers are nearly the same. It is deduced that the lower binding energy shoulder at 2473 eV may originate due to an interaction of Ag with L-cysteine. It is also attributed to the higher binding energy peak as the electrons are donated from the sulfur atom to the silver, and the sulfur can be positively charged. Such a positive charge may apply an additional coulomb repulsion on photoelectron which implies photoelectrons loss kinetic energy and as a result there should be a peak in the high binding energy side. However, any spectral change apart from the main peak cannot be observed in the case two-layered and multi-layered films. A slight difference of 0.3 eV in peak position between the two-layered and multi-layered films may be due to surface charge accumulation, which can contribute to the loss of photoelectron kinetic energy.

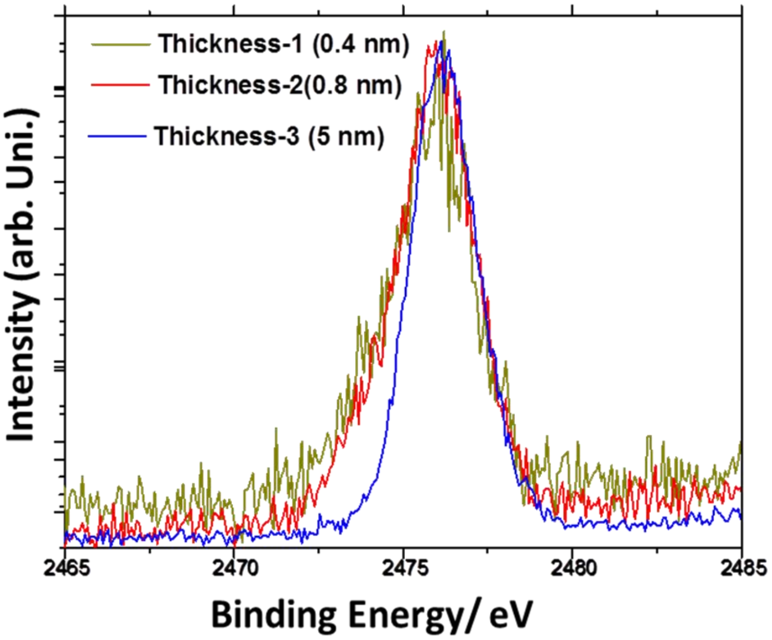

Figure 2. Thickness-dependent XPS S 1s spectra of L-cysteine on Ag.

The UPS spectra shown in Figure 1 provide detailed insights into the electronic interactions between L-cysteine and Ag(111) as a function of film thickness. The clear spectral feature centered around 2.5 eV for thin films suggests the presence of a sulfur-originated state from L-cysteine interacting with Ag d orbitals. According to the Anderson–Newns model, this interaction can lead to the formation of bonding and antibonding states due to the coupling between S 3p orbitals and Ag 4d orbitals (De Renzi, 2009). This interpretation is supported by previous studies where similar bonding and antibonding states were observed, indicating that the feature around 2.5 eV can be attributed to these states. The reduction in intensity in the Ag d band region further corroborates this interaction, highlighting that L-cysteine modifies the electronic structure of the Ag(111) surface.

Renzi et al. have described how such interactions result in the formation of bonding and antibonding states between sulfur and metal, with these states appearing below and above the metal's d band, respectively. The spectral feature around 2.5 eV, along with the observed changes in the d-band region, can be attributed to these bonding and antibonding interactions. Additionally, the presence of an interface state, or gap state, enhances charge transfer between L-cysteine and the silver substrate. Luque et al (Luque *et al.*, 2012). Also noted that these interactions are more complex than a simple bonding/antibonding view due to additional interactions with the sulfur-carbon bond, suggesting that the sulfur might be pushed closer to the surface than the equilibrium position, forming these states.

The peak shifts observed around 5 eV and 9 eV in the UPS spectra indicate interactions involving states originated from O, C, and N atoms. This observation is supported by DFT studies and previous experiments on the valence electronic structure of L-cysteine. These shifts likely result from interactions of O 2sp and N 2sp orbitals with the metal surface, which could push the adsorbate closer to the surface and support the formation of bonding and antibonding states, as suggested by Luque et al. The presence of the zwitterionic form of L-cysteine at higher coverages supports this view. The first layer is chemisorbed in a neutral form, while subsequent layers may form zwitterionic structures.

The UPS results show spectral changes between nominal thicknesses of 8 Å and 16 Å, including a 0.3 eV shift of the SECO to lower binding energies, a shift of the peak around 9 eV to higher binding energies, and the disappearance of the peak around 2.5 eV. These changes suggest that a second layer or more is forming on top of the chemisorbed first layer, weakening the interaction between the first layer and Ag(111). The formation of overlayers in a zwitterionic form aligns with these observations. Alternatively, the nominal thickness of 8 Å might correspond to a monolayer, as the SECO reaches its maximum value at this thickness and then decreases.

In their XPS studies, Honda et al. identified two distinct peaks at 2472.2 eV and 2480.4 eV for thin L-cysteine layers on gold, with the higher-energy peak attributed to Au-S interactions (Honda *et al.*, 2009). Our XPS results corroborate these findings, showing a primary peak and a higher-energy shoulder that we attribute to Ag-S interactions. The shoulder observed in the S 1s spectra of thin films suggests the formation of Ag-S bonds. This observation is in agreement with previous UPS results, which indicated that sulfur-originated states from the L-cysteine HOMO interact with Ag d orbitals, leading to the formation of bonding and antibonding states.

Our UPS results support the observed weakening of the silver-sulfur bond with increasing L-cysteine coverage. The behavior of SECO indicates a reduction in the interface dipole moment as coverage increases. This observation is consistent with Luque et al.'s findings, which suggest that silver-sulfur bonds weaken at higher coverages. Additionally, our XPS results reinforce this interpretation by showing the absence of a higher-energy peak in two-layered films, likely due to the weakening of the Ag-S bond caused by the additional L-cysteine layer.

In summary, the integration of UPS and XPS data delivers a thorough understanding of the electronic structure and chemical interactions at the L-cysteine/Ag(111) interface. The data reveal insights into bonding and antibonding states, charge transfer dynamics, and changes in work function. These observations enhance our understanding of the nature of the interactions and the influence of film thickness on these interactions.

4. Conclusions

This study further elucidates the interaction between L-cysteine and silver surfaces by combining UPS and XPS data, enhancing our previous findings on this system. UPS results reveal that as L-cysteine coverage increases, the interaction between L-cysteine and the silver surface results in the weakening of the Ag-S bond. The spectra reveal a distinct peak between the HOMO of L-cysteine and the Fermi level of Ag(111), which is attributed to an antibonding state resulting from the coupling of L-cysteine's S 3p orbital with Ag(111)'s 4d orbital. This finding corroborates the estimated charge injection barrier of 3.2 eV and an ionization energy of 7.24 eV for the chemisorbed L-cysteine layer on Ag(111).

XPS data further support these findings, highlighting a notable spectral change in the S 1s region. Specifically, a higher-energy shoulder appears in monolayer films, which is attributed to the formation of Ag-S bonds. The complete disappearance of this feature in multilayer films strengthens the hypothesis that the Ag-S bond weakens with increased L-cysteine coverage.

The combined UPS and XPS results reveal that the L-cysteine/Ag system undergoes notable changes in electronic structure and bonding characteristics with increasing coverage. These observations imply that using L-cysteine to anchor biomolecules to metal surfaces might be suboptimal for bioelectronic applications. The weakening of the Ag-S bond with higher L-cysteine coverage poses challenges for maintaining effective charge transfer.

5. Acknowledgments

The authors gratefully acknowledge the support provided by the Research Grant: Competitive Research Grant Round 2 (Grant No CRG-R2-SB-1), Science and Technology Human Resource Development Project (STHRDP). XPS was performed with the approval of KEK-PF (Proposal No. G068). The UPS experiments were performed under the approval of the Joint Studies Program (25-562) of the Institute for Molecular Science, Japan.

6. Reference

Chen, M., Fu, X., Chen, Z., Liu, J. and Zhong, W. (2021), "3 - Protein-Engineered Functional Materials for Bioelectronics", *Advanced Functional Materials*, Vol. 31 No. 4, p. 2006744, doi: 10.1002/adfm.202006744.

De Renzi, V. (2009), "6 - Understanding the electronic properties of molecule/metal junctions: The case study of thiols on gold", *Surface Science*, Vol. 603 No. 10–12, pp. 1518–1525, doi: 10.1016/j.susc.2008.10.063.

Honda, M., Baba, Y., Hirao, N. and Sekiguchi, T. (2009), "7 - Observation of Au-S Interface of L-Cysteine on Gold Surface", *E-Journal of Surface Science and Nanotechnology*, Vol. 7, pp. 110–114, doi: 10.1380/ejssnt.2009.110.

Koswattage, K.R. and Ishii, H. (2020), "1 - Photoemission investigation of interaction between L-cysteine and silver surface", *Surface and Interface Analysis*, Vol. 52 No. 8, pp. 513–517, doi: 10.1002/sia.6771.

Koswattage, K.R., Kinjo, H., Nakayama, Y., Ishii, H. (2015), "Interface electronic structures of the L-cysteine on noble metal surfaces studied by ultraviolet photoelectron spectroscopy", *E-Journal of Surface Science and Nanotechnology, Vol. 13, pp. 373–379, doi:10.1380/ejssnt.2015.373.*

Lee, J.-S., Ulmann, P.A., Han, M.S. and Mirkin, C.A. (2008), "2 - A DNA−Gold Nanoparticle-Based Colorimetric Competition Assay for the Detection of Cysteine", *Nano Letters*, Vol. 8 No. 2, pp. 529–533, doi: 10.1021/nl0727563.

Luque, N.B., Vélez, P., Pötting, K. and Santos, E. (2012), "5 - Ab Initio Studies of the Electronic Structure of L -Cysteine Adsorbed on Ag(111)", *Langmuir*, Vol. 28 No. 21, pp. 8084–8099, doi: 10.1021/la301107k.

Musarraf Hussain, M., Asiri, A.M., Uddin, J., Marwani, H.M. and Rahman, M.M. (2022), "4-Development of a L-cysteine Sensor Based on Thallium Oxide Coupled Multi-walled Carbon Nanotube Nanocomposites with Electrochemical Approach", *Chemistry – An Asian Journal*, Vol. 17 No. 3, p. e202101117, doi: 10.1002/asia.202101117.

Thermo-physical characteristics of reduced graphene oxide incorporated enhanced transformer oil nanofluids

Dingirappu Kankanamalage Ashan Induranga[1,2], Galpayage Don Chanaka Pradeep Galpaya[2], Happawana Vithanage Vimukthi Priyadarshana[1,2,3] Samarathunga Vidana Arachchige Amalka Indupama[1,2,3] and Kaveenga Rasika Koswattage[1,2,*]

[1]*Department of Engineering Technology, Faculty of Technology, Sabaragamuwa University of Sri Lanka, Belihuloya, Sri Lanka.*
[2]*Centre for Nanodevices Fabrication and Characterization, Faculty of Technology, Sabaragamuwa University of Sri Lanka, Belihuloya, Sri Lanka.*
[3]*Faculty of Graduate Studies, Sabaragamuwa University of Sri Lanka, Belihuloya, Sri Lanka.*

* koswattagekr@appsc.sab.ac.lk

Abstract

Nanofluids have emerged as a trending topic in various engineering disciplines since the early 21st century. These fluids, containing metallic, metal-oxide, or carbon nanoparticles with sizes smaller than 100 nm, significantly enhance thermo-physical properties such as thermal conductivity, thermal diffusivity, kinematic viscosity, dynamic viscosity, and specific heat capacity. This study focuses on transformer oil, a crucial insulation material that maintains proper insulation and operating temperature in power transformers. Reduced Graphene Oxide (rGO) was selected as the nanoparticles for this research after a comparative study with several other carbon nanomaterials. In this research work, rGO nanoparticles were used to improve the thermal properties of transformer oil at different weight fractions (0.01, 0.025, and 0.05 wt.%). The nanofluids were prepared using the two-step method without applying any surfactants. Thermo-physical measurements were conducted using the LAMBDA Thermal Conductivity Meter, SVM 3001 Viscometer, and Litesizer 500 Particle Size Analyzer. The data were analyzed based on weight fractions and temperature variations. Heat transfer coefficients, including the Prandtl number, Reynolds number, and Nusselt number, were calculated from the measured data of thermal conductivity, thermal diffusivity, kinematic and dynamic viscosity, and density to observe the cumulative heat transfer ability of nanofluids. The Prandtl and Nusselt numbers increased with higher rGO weight percentages and decreased with rising temperatures, while the Reynolds number exhibited the opposite trend. Notably, the Nusselt number showed the greatest increase at the highest weight percentage (0.05 wt.%), indicating that rGO is a promising additive for enhancing the heat transfer capabilities of transformer oils.

Keywords: Carbon nanoparticles, Heat transfer efficiency, Nano-enhanced Transformer Oil, Nanomaterials, Nanotechnology, reduced Graphene Oxide

1. Introduction

'Nanofluid' has been a developing section in different engineering and scientific disciplines in the previous decades. There are numerous applications of nanofluids in mechanical, automobile, electrical, process, biomedical, and electronic engineering fields specially focused on improving the thermos-physical properties (Saidur *et al.*, 2011).

The 'nanofluid' term was first introduced by Professor Choi in 1995 (Choi and Eastman, 1995). Nanofluids can be basically understood as a fluid that contains particles which has a size lesser than 100 nm.

The development of nanofluids helps to enhance the thermal properties such as thermal conductivity, viscosity, specific heat capacity, and flash point in basefluids such as water, mineral oil, transformer oil, engine oil, and coolants. There are different kinds of nanoparticles are used for preparing nanofluids, such as metallics (Cu, Ag, Au), metal oxides (TiO_2, Al_2O_3, CuO, Fe_2O_3), and carbon-based nanoparticles (Graphene, Fullerene, Carbon Nano Tubes). There are different kinds of factors affecting these enhancements, such as particle size, particle shape, Brownian motion, and interfacial layers of nanoparticles (Jama *et al.*, 2016).

Both theoretical and experimental research have been conducted on nanofluids. Theoretical studies have primarily focused on developing models to predict the thermal properties of nanofluids, such as thermal conductivity, viscosity, and specific heat capacity. Meanwhile, experimental research has explored how varying concentrations of nanoparticles influence the thermal behavior of different base fluids.

In this study, researchers have focused on improving the important thermal properties of transformer oils using Reduced Graphene Oxide (rGO) nanoparticles. In most of the research, the improvement of dielectric properties has been taken into account by the researchers, but a few studies have focused on the thermal properties of transformer oil (Fal *et al.*, 2018), (Amin *et al.*, 2019). Also, the studies that have been conducted to investigate the thermal properties have also focused on the individual thermal properties without calculating heat transfer coefficients, such as Prandtl, Reynol, and Nusselt numbers (Ramirez-Tijerina *et al.*, 2018),(Induranga *et al.*, 2023).

The Prandtl number represents the ratio of momentum diffusivity to thermal diffusivity, indicating the relative thickness of the fluid's velocity and thermal boundary layers (Eq. 01). The Reynolds number characterizes the flow pattern of the fluid, distinguishing between laminar and turbulent flow (Eq. 02). The Nusselt number measures the ratio of convective to conductive heat transfer across a boundary, serving as an indicator of the heat transfer rate from the solid surface to the fluid (Eq. 03).

$$\text{Prandtl number} = \frac{\text{Kinematic Viscosity}}{\text{Thermal Diffusivity}} \qquad (1)$$

$$\text{Reynolds number} = \frac{\text{Density x Velcoity x Characteristic Length}}{\text{Dynamic Viscosity}} \qquad (2)$$

$$\text{Nusselt number} = 0.023 \times Re^{0.8} \times Pr^{0.3} \qquad (3)$$

This study selected Reduced Graphene as the nanoparticle to enhance thermophysical properties due to their comparatively high dispersion rate in mineral oils. The samples were prepared at different weight ratios, and their thermophysical properties, such as thermal conductivity, thermal diffusivity, density, and kinematic and dynamic viscosity values, were measured. The zeta potential value was also measured to predict the stability of the nanofluid samples. Apart from measuring the thermal properties, heat transfer coefficients such as Reynolds, Prandtl, and Nusselt numbers are also calculated.

2. Methodology

rGO was purchased from Ceylon Graphene Technologies (CGT), and transformer oil (Nytro Libra) was received from Samanalawewa Hydro Power Station. The properties of rGO are mentioned in Table 1.

First, the weights of the reduced graphene oxide (rGO) and transformer oil were measured separately using an analytical balance to prepare nanofluid samples at different weight fractions (0.01, 0.025, and 0.05 wt.%). The rGO was then dispersed in the transformer oil using a magnetic stirrer for 30 minutes at 60°C. Following this, the samples were ultrasonicated for 3 hours at 60°C to enhance the dispersion of nanoparticles within the transformer oil. Surfactants were not used due to the inherent stability of carbon nanoparticles in mineral oils.

Table 1. Properties of rGO nanoparticles

Characteristic	**Value**
BET	521 (m^2/g)
Graphite source	Sri Lankan - Kahatagaha graphite
Appearance	Soft black powder
I_D/I_G rating	1.037

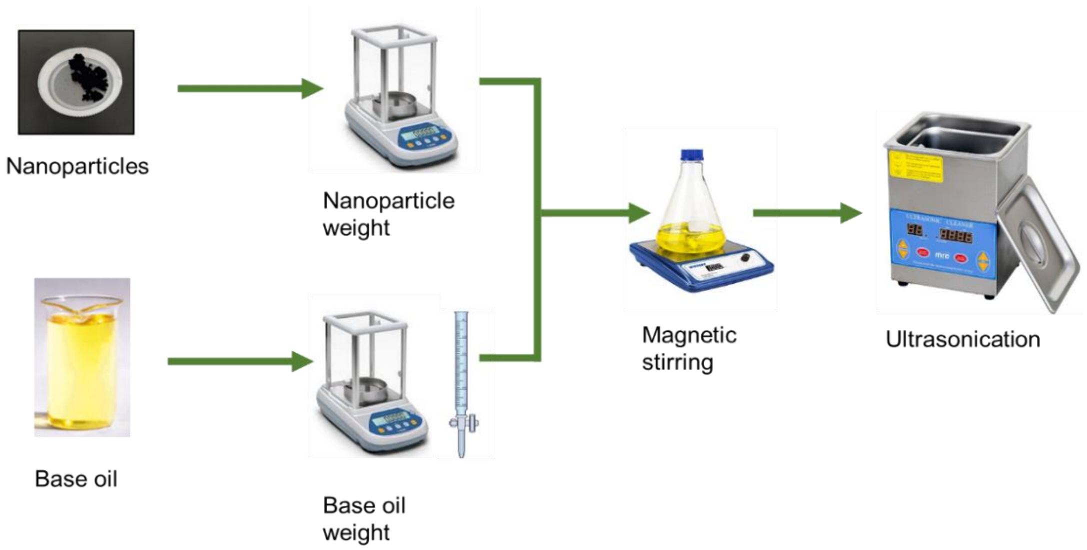

Figure 1. Nanofluid preparation

After the preparation, thermo-physical measurements were conducted using standard equipment, as given in Table 2.

Table 2. Thermo-physical measurements of the nanofluid

Physical property	**Instrument**
Thermal conductivity	LAMDA thermal conductivity meter
Thermal diffusivity	LAMDA thermal conductivity meter
Viscosity (Dynamic, Kinematic)	SVM 3001 Viscometer
Density	SVM 3001 Viscometer

Zeta potential	Litesizer 500 Particle Size Analyzer

LAMDA thermal conductivity meter uses the hot wire transient method to measure the thermal conductivity and thermal diffusivity. These values have been used for calculating the volumetric heat capacity. SVM 3001 viscometer uses the ASTM D7042 standard to measure the dynamic viscosity values. This instrument can measure dynamic viscosity and density simultaneously, which can be used to calculate the kinematic viscosity value. The measurement of zeta potential is also critical in nanofluids since it is a measurement of the stability of the nanofluids. Litesizer 500 particle size analyzer measures the zeta potential value by the Electrophoretic Light Scattering (ELS) method.

These thermo-physical values were used to calculate the Prandtl number, Reynold number, and the Nusselt number, which help to understand the cumulative heat transfer ability of nanofluids.

3. Results and Discussion

3.1 Nanoparticle characterization

Nanoparticle characterization was done using a ZEISS Scanning Electron Microscope (SEM), as given in Figure 2.

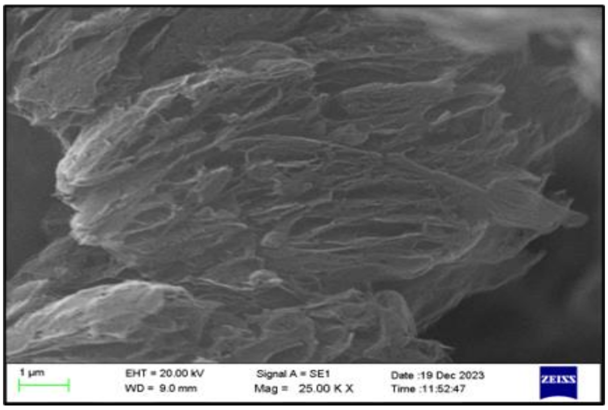

Figure 2. SEM image of rGO nanoparticles

3.2 Zeta Potential

Figure 3 presents the zeta potential measurements for all nanofluid samples taken on days 1, 2, 5, and 10 following sample preparation. The figure demonstrates the high stability of the rGO-based nanofluid samples. However, a decrease in zeta potential is observed with increasing rGO nanoparticle concentration. This decline can be attributed to particle agglomeration; as the concentration increases, nanoparticles are more likely to agglomerate and sediment. After 10 days, most nanofluid samples become unstable, except for the 0.01 wt.% sample, which maintained a zeta potential value close to 50 mV even after 10 days.

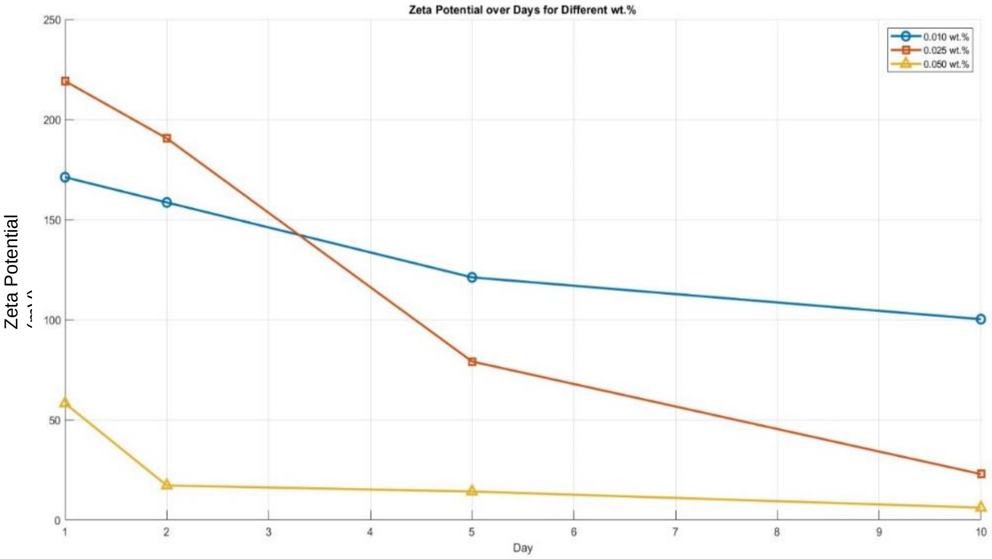

Figure 3. Zeta potential change with preparation day

3.3 Thermo-physical properties and heat transfer coefficients

As detailed in the methodology, key thermophysical properties were measured and calculated for all nanofluid samples, as shown in Tables 3 to 6. The results indicate that kinematic viscosity increases with higher nanoparticle concentrations but decreases with rising temperature. A similar trend is observed with thermal diffusivity. As previously noted, the Prandtl number, calculated from these properties, also increases with nanoparticle concentration and decreases with temperature, as demonstrated by the data in Table 3 and can be understood through Eq. 01.

Table 3. Kinematic viscosity, Thermal diffusivity, and Prandtl number values of samples

Temperature	**Weight Percentage (wt.%)**	**Thermal Conductivity (mW/K.m)**	**Kinematic Viscosity (mm^2/s)**	**Thermal Diffusivity (x 10^{-3} mm^2/s)**	**Prandtl Number**
20 °C	0.000	110.0	20.008	80.966	0.247
	0.001	110.40	20.370	81.025	0.251
	0.025	110.86	20.532	81.069	0.253
	0.050	111.05	21.195	81.083	0.261
40 °C	0.000	108.30	9.295	77.997	0.119
	0.001	108.84	9.434	78.042	0.121
	0.025	109.06	10.432	78.059	0.134
	0.050	109.31	10.890	78.083	0.139
60 °C	0.000	107.00	5.242	75.053	0.070
	0.001	107.33	5.304	75.069	0.071
	0.025	107.35	5.340	75.073	0.071
	0.050	107.45	5.515	75.080	0.073
80 °C	0.000	105.40	3.374	72.090	0.047
	0.001	105.21	3.418	72.060	0.047
	0.025	105.33	3.420	72.069	0.047
	0.050	105.52	3.678	72.085	0.051
100 °C	0.000	103.80	2.377	69.128	0.034
	0.001	104.05	2.410	69.137	0.035
	0.025	104.12	2.401	69.140	0.035
	0.050	104.66	2.693	69.138	0.039

Reynolds number values have been calculated using these two sets of values. It can be seen that both the density and the dynamic viscosity have decreased with the decreased temperature but increased with the nanoparticle concentration. According to these values, it can be understood that nanoparticles have a negative effect on the Reynolds number, and temperature has a positive effect since the rate of change of dynamic viscosity is much higher than the density. This observation is an important one since, at higher temperatures, the transformer oil becomes more suitable for heat transferring within the transformer.

Table 4. Density, Dynamic viscosity, and Reynolds number of samples

Temperature	**Weight Percentage (wt.%)**	**Density (kgm^{-3})**	**Dynamic Viscosity (mPas)**	**Reynolds Number**
20 ℃	0.000	0.87471	17.501	0.04998
	0.001	0.87545	17.833	0.04909
	0.025	0.87549	17.976	0.04870
	0.050	0.87571	18.203	0.04811
40 ℃	0.000	0.86135	8.0063	0.10758
	0.001	0.86207	8.1329	0.10600
	0.025	0.86212	8.8911	0.09696
	0.050	0.86286	8.9852	0.09603
60 ℃	0.000	0.84816	4.4460	0.19077
	0.001	0.84869	4.5017	0.18853
	0.025	0.84903	4.5337	0.18727
	0.050	0.85069	4.5969	0.18506
80 ℃	0.000	0.83497	2.8169	0.29641
	0.001	0.83493	2.8535	0.29260
	0.025	0.83589	2.8589	0.29238
	0.050	0.83766	2.9063	0.28822
100 ℃	0.000	0.82193	1.9539	0.42066
	0.001	0.82036	1.9773	0.41489
	0.025	0.82283	1.9752	0.41658
	0.050	0.82454	2.0452	0.40316

From the calculated values from Tables 4 and 5, the Nusselt number can be calculated as given in Table 5. Nusselt number values display a complex pattern compared to Prandtl and Reynold numbers with nanoparticle concentration and temperature. According to Table 5 data, it can be understood that Nusselt number values are lower compared to base oils at lower temperatures; however, at higher temperatures (80 ℃ and above) it can be observed a slight increment of the Nusselt number. The complex behavior of the Nusselt number can be understood by Eq. 03 as the effect of the Reynolds number is much higher than the Prandtl number.

Mainly, this observation can happen due to the rGO’s positive effect on the thermal properties and the negative effect on the Rheological properties. The higher surface area improves the thermal conductivity of the nanoparticles, but in the other hand it reduces the viscosity values due to their rough surface.

Table 5. Prandtl number, Reynolds number, and Nusselt number of nanofluid samples

Temperature	Weight Percentage (wt.%)	Prandtl Number	Reynolds Number	Nusselt Number
20 °C	0.000	0.247	0.04998	0.00138
	0.001	0.251	0.04909	0.00136
	0.025	0.253	0.04870	0.00136
	0.050	0.261	0.04811	0.00136
40 °C	0.000	0.119	0.10758	0.00204
	0.001	0.121	0.10600	0.00203
	0.025	0.134	0.09696	0.00194
	0.050	0.139	0.09603	0.00195
60 °C	0.000	0.070	0.19077	0.00275
	0.001	0.071	0.18853	0.00273
	0.025	0.071	0.18727	0.00272
	0.050	0.073	0.18506	0.00273
80 °C	0.000	0.047	0.29641	0.00347
	0.001	0.047	0.29260	0.00345
	0.025	0.047	0.29238	0.00345
	0.050	0.051	0.28822	0.00348
100 °C	0.000	0.034	0.42066	0.00419
	0.001	0.035	0.41489	0.00416
	0.025	0.035	0.41658	0.00417
	0.050	0.039	0.40316	0.00420

4. Conclusion

The incorporation of nanoparticles to enhance the thermal properties of heat transfer fluids has become a widely adopted approach across various engineering disciplines. In this study, the research team prepared several nanofluid samples by dispersing rGO nanoparticles in transformer oil. These nanofluids exhibited significant improvements in thermal conductivity, thermal diffusivity, and density. However, they also showed adverse effects on properties such as kinematic viscosity and dynamic viscosity.

To evaluate the overall heat transfer performance, the Prandtl, Reynolds, and Nusselt numbers were calculated. The Prandtl number increased with rising nanoparticle concentrations but decreased with higher temperatures.

In contrast, the Reynolds number exhibited the opposite trend. The behavior of the Nusselt number was more complex and did not follow a straightforward pattern like the other two coefficients.

As a future work, it is recommended to use nanoparticles with a smooth surface and a higher surface area, which can improve both the thermal properties as well as the rheological properties.

6. Acknowledgement

This work was supported by the Science and Technology Human Resource Development Project, Ministry of Education, Sri Lanka, funded by the Asian Development Bank (Grant number CRG-R3-SB-4).

7. Reference

Amin, D., Walvekar, R., Khalid, M., Vaka, M., Mubarak, N.M. and Gupta, T.C.S.M. (2019), “Recent Progress and Challenges in Transformer Oil Nanofluid Development: A Review on Thermal and Electrical Properties”, *IEEE Access*, Vol. 7, pp. 151422–151438, doi: 10.1109/ACCESS.2019.2946633.

Choi, S.U.S. and Eastman, J.A. (1995), “1- Enhancing Thermal Conductivity of Fluids with Nanoparticles”, presented at the ASME International Mechanical Engineering Congress and Exposition, San Francisco.

Fal, J., Mahian, O. and Żyła, G. (2018), “Nanofluids in the Service of High Voltage Transformers: Breakdown Properties of Transformer Oils with Nanoparticles, a Review”, *Energies*, Vol. 11 No. 11, p. 2942, doi: 10.3390/en11112942.

Induranga, A., Galpaya, C., Vithanage, V. and Koswattage, K.R. (2023), “Thermal Properties of TiO_2 Nanoparticle-Treated Transformer Oil and Coconut Oil”, *Energies*, Vol. 17 No. 1, p. 49, doi: 10.3390/en17010049.

Jama, M., Singh, T., Gamaleldin, S.M., Koc, M., Samara, A., Isaifan, R.J. and Atieh, M.A. (2016), “Critical Review on Nanofluids: Preparation, Characterization, and Applications”, *Journal of Nanomaterials*, Vol. 2016, pp. 1–22, doi: 10.1155/2016/6717624.

Ramirez-Tijerina, R., Rivera-Solorio, C.I., Singh, J. and Nigam, K.D.P. (2018), “Numerical Study of Heat Transfer Enhancement for Laminar Nanofluids Flow”, *Applied Sciences*, Vol. 8 No. 12, p. 2661, doi: 10.3390/app8122661.

Saidur, R., Leong, K.Y. and Mohammed, H.A. (2011), “2- A review on applications and challenges of nanofluids”, *Renewable and Sustainable Energy Reviews*, Vol. 15 No. 3, pp. 1646–1668, doi: 10.1016/j.rser.2010.11.035.

Low Cost IoT-Based Home Remote Monitoring and Controlling System

Marudhapulle Rukshanth* and Vadivel Hiroshaan

Department of Mechatronics Technology, University College of Jaffna, University of Vocational Technology, Sri Lanka.

* djshanth308@gmail.com

Abstract

The rapid advancement of technology has made life easier, which has led to a surge in popularity for home automation in recent years. Nearly everything is now automated and computerized. One application of the Internet of Things (IoT) that makes it easier to control home appliances online with an automation system is the "smart home." Numerous current systems have experimented in home automation, but it appears that they have not been able to offer affordable solutions for the same. This study suggested a low-cost, real-world-installable, user-friendly Smart Home automation system that uses voice commands and the Blynk app to remotely monitor and manage household appliances. In a smart, networked home, the goal of a Wi-Fi based Wireless Sensor Network (WSN) is to monitor and control electrical, safety, and environmental factors. The system is based on an ESP32-MCU node with an Internet connection that allows remote control of the device. The purpose of this system is to help satisfy the requirements of the elderly and disabled in their homes by offering support and assistance. Additionally, the system's smart home idea raises the standard of life at home. The Android application-based Graphical User Interface (GUI) on a smartphone allows the user to effortlessly operate the gadgets in a smart home. Consequently, the technology provides a completely automated solution that is inexpensive and simple to integrate with the actual electrical wiring configuration of the house.

Keywords: *Home automation system, IoT, ESP32, Wireless Communication, Voice Control*

1. Introduction

These days, connecting several smart devices together has become essential due to the widespread use of smart gadgets and our growing reliance on their luxurious features. Multiple devices can be connected to a single network using the great Wireless Fidelity (Wi-Fi) technology. 2.4GHz is the frequency band that has been certified worldwide for use by Wi-Fi. This study examines the many options for connecting these smart gadgets together while sparingly utilizing Wi-Fi technology.

One advantage of this interconnection is the ability to simultaneously monitor and operate smart devices. A concept known as "home automation" entails the real-time monitoring and control of numerous household appliances. There are several ways to define home automation; (Atzori *et al.*, 2010) defines it as a strategy to improve people's quality of life by introducing technology into the home. The X10 industry standard was created in 1975, and the inventor claims that it is the earliest standard for electronic device communication. Advances in communication technology have led to an increase in the use of Home Automation Systems (HAS). By utilizing the technology of the Internet of Things, a home automation system can raise people's quality of life, particularly for the elderly and disabled. The analysis and implementation of home automation have also increased on average. Linking and remotely monitoring objects over the Internet is made feasible by a technology called the Internet of Things (IoT). In recent decades, the objective of the Internet of Things has seen substantial development and is currently utilized in several domains such as smart homes, telemedicine, and industrial environments (El-Hajj *et al.*, 2019). The majority of processes in the current world, including those in households, businesses, and industries, are automated. This is the automation of the modern world. Systems for home automation are created in mechanization procedures where various loads in houses are operated by machinery equipment that needs human labor. It involves utilizing a variety of technologies and controllers to automatically operate household appliances from desktops, laptops, tablets, or smartphones. Smart homes improve comfort and simplify living. Remote controls are available for home equipment such as air conditioning, washing machines, refrigerators, and lighting. Smart homes notify you of events while you are at work or on vacation, and security systems offer support in the event of an emergency (Maqbool *et al*., 2020).

1.1. Limitations of the existing home automation systems

The majority of customers are unable to pay the implementation and maintenance costs of most existing HAS, which is one of their primary issues according to the research done. Furthermore, certain existing systems offer a view of the house via a web application, which causes trouble for users who need to log on to the internet each time they wish to monitor or operate their homes (Algoiare, 2014). Furthermore, some home automation systems' interfaces for managing and monitoring appliances are not user-friendly.

Furthermore, the automation systems that are currently in place have specific restrictions related to the communication technologies that have been employed. For instance, automation based on Bluetooth (Asadullah and Ullah, 2017) was quick and inexpensive, but its range is limited. The user will not be able to use the household appliances if the distance exceeds a certain threshold since the connection will be lost.

Additionally, ZigBee's 250 Kb/s data rate—which is inadequate for high-speed wireless personal networks—was the reason behind its design. GSM is an additional communication technology that is accessible globally, albeit it comes with high costs, slow transmission speeds, and restricted coverage in remote regions (Kazi and Tiwari, 2015). It was suggested in Shafana and Aridharshan (2017), to use Arduino boards for home automation. Arduino is affordable, open source, very flexible, and simple to program. Having a substantial and active user base is a huge advantage. However, Arduino cannot handle the high level of complexity that comes with sophisticated projects.

According to Danbatta and Varol (2019), there are a number of important drawbacks to the Zigbee-based communication network, such as poor product interoperability between manufacturers, a high switching time, and limited connection over short distances. Despite Z-wave technologies. The primary weakness of the system is its implementation of GSM components, which are susceptible to system failure if the GSM is misplaced in Chaurasia and Jain (2019), Azis (2018), and other sources. Pau and Salerno (2019) created a webApp-based cordless automated home system using an embedded Wi-Fi ESP 2866 device and an Arduino AT Mega board along with NodeMCU. A web application was developed using HTML and PHP to let users inspect and control appliances. Additional features on the website, such as passwords and usernames, enable data authentication. Users can access an advanced user interaction developed by Ajagbe *et al.* (2022) on a web server, where the Node controller can acquire actuated signals and pass them to a web server system, with the aid of the Android Blynk App. One of the system's drawbacks is that multiple users cannot connect at the same time. Data authentication and data user identity security were not taken into account during design.

Thus, we presented a novel system in this study that gets beyond the drawbacks of the current system of home automation. This can be done by using an Android smartphone and a NodeMCU microcontroller to design and build an affordable cost Wi-Fi-based automated system for an intelligent home prototype. Approximately four thousand Sri Lankan Rupees was spent on developing the prototype model. The system was designed to provide simple and effective control over a range of household appliances. It also facilitates remote control by supporting the Internet of Things idea.

2. Methodology

Today's low-cost IoT-based smart home systems are made possible by the availability of microcontrollers like the ESP32. The NodeMCU microcontroller, sensors, and actuators will enable the more effective and efficient design and implementation of an inexpensive, user-friendly smart home environment. This paper will offer a user-friendly, cost-effective IoT basis smart house model with implementation that will satisfy home users' needs and be dependable and reasonably priced. This solution just integrates with our panelboard to handle the electrical appliances manually and via a remote control.

2.1. Protype design

Figure 1 shows the layout design of the SOLIDWORKS developed home automation prototype, which includes all the tools and supplies needed to construct a smart house prototype.

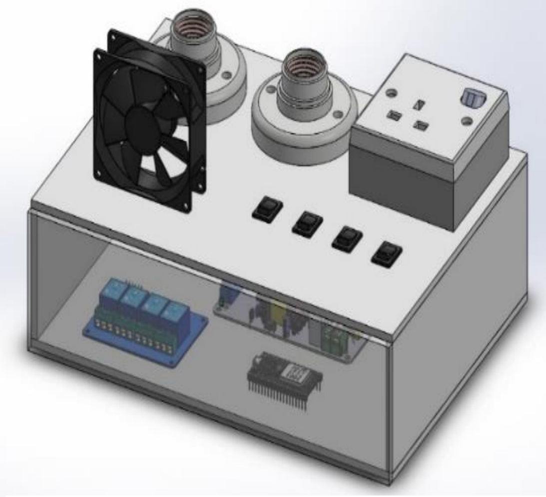

Figure 1. 3D view of Prototype design

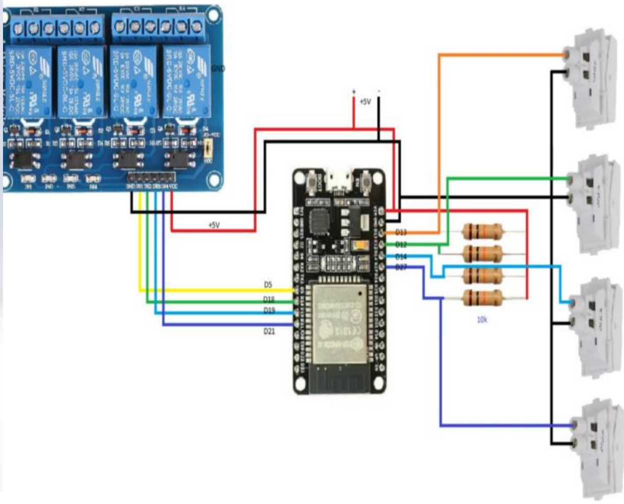

Figure 2. Wire connection of the prototype

As seen in Figures 3 and 4, the smart house prototype is constructed out of wood. After that, hardware implementation and wiring are finished according to the Fig.2. At that point, the software's programming process is finished. In order to optimize and improve the design, each issue that comes up during project construction is found and fixed at the experiment and testing stage. Error prevention also receives some improvement.

Figure 3. Front view of Actual Prototype

Figure 4. Front view of Actual Prototype

2.2. System Architecture and Implementation

This study focuses on controlling home appliances with the ESP32 WI-FI module in a HAS. Based on IoT, a local control system with Wi-Fi and remote control is set up. Blynk, an appropriate Android app with Wi-Fi capabilities, is used because it works well with ESP32 and allows for smartphone control and monitoring. It's a great option because of its intuitive UI. The ESP32 controller is intended to be in communication with the Blynk application.

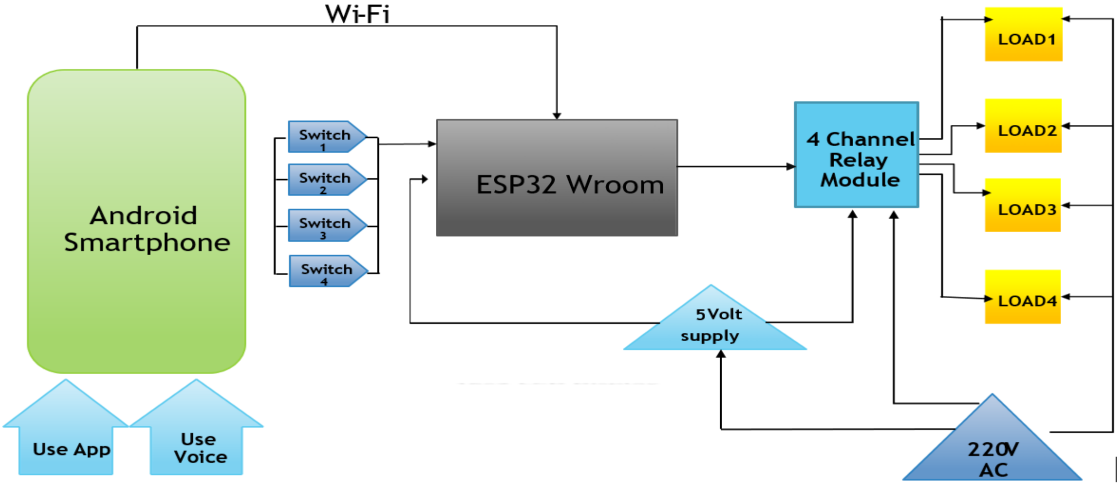

Figure 5. The proposed system architecture

The relay components receive its input electrical signals from the ESP32 module, and the relay outlets are connected to the lightbulbs and fan since these are replicas of real household appliances. The specific architecture for the suggested protype design is illustrated in Fig. 5.

Figure 6 shows the steps to use Blynk to operate the electrical appliances. This process allows mobile phone management and monitoring of the electrical equipment and house conditions under consideration. Using smartphone apps like Google Assistant and IFTTT to enable voice control. "If This Then That," or IFTTT, is an interface that offers web-based services for devices that are linked to a mobile application. The voice command method for operating the household appliance is demonstrated in Fig. 7.

2.3. Experimental Design

Four scenarios were used to test the algorithm: voice mode, switch mode via the Blynk, timer function mode, and manual switch mode. Our smartphones are installed with the Blynk app, which is set up using the authentication code from our sketch. The Blynk app uses our voice commands or switch mode to operate the electrical devices we request. The mobile and web applications display updates for the other two modes. The NodeMCU controller was linked to the router. The NodeMCU was configured so that when a user taps the ON/OFF button in the Blynk app or manual or voice command or timer function, the relay is triggered, which then causes the home appliances to switch on or off according to pin configuration in Table 1.

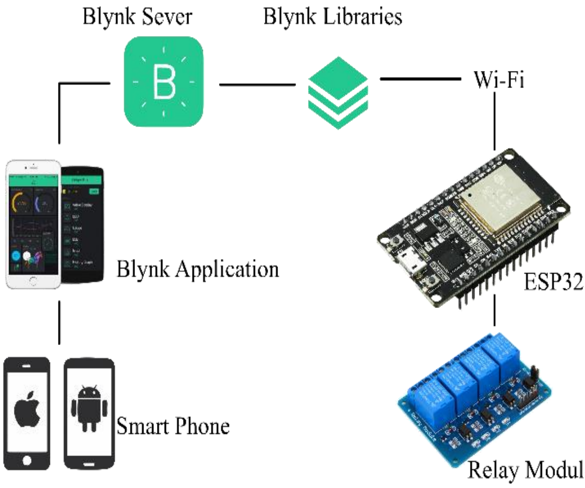

Figure 6. Working principle of Blynk application

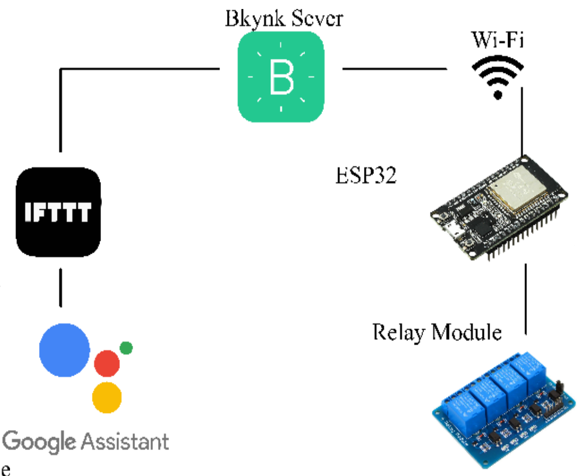

Figure 7. Working principle of Voice command

Table 1. Digital circuit connection configuration.

NodeMCU pin configuration	Relay pins
GND	GND
3 V	VCC
D1	IN 1
D2	IN 2
D3	IN 3
D4	IN 4

3. Results and Discussion

Safety and security systems, as well as remotely operated household appliances, have yielded results following successful testing and experimentation. Our proposed system was verified and tested using the scenarios listed in section 2.3. Using a Wi-Fi network, the following scenarios could be utilized to remotely switch the household appliances. Switch mode: In Blynk mode, the radio buttons that were formerly used to control home appliances are employed. The radio button relayed the condition of the switch. Voice Mode made it possible to control domestic appliances with voice instructions. The application created an intent using the microphone built into the smartphone to ask the Google server for voice data; the Google server responds with string data. The string data is processed following additional analysis. With the timer function mode, you can select a specific time to turn on and off, and the device will turn on and off automatically at that point. To manually operate the household appliances, utilize the manual switch mode. It is not dependent on the smartphone. As per Table 2, all the outcomes are successfully completed, with the symbol "√" indicating successful completion.

Figure 8 displays the suggested electrical equipment control scheme on the Blynk app. Naturally, one of its primary benefits is that it is comfortable and simple to use, making it suitable for anyone to connect with a home panel board system. Without question, smart home equipment may simplify our daily lives. Energy conservation is the subject of another benefit. Large homes with many rooms can waste a lot of energy just by idling the lights, fans, and other equipment while not in use. Furthermore, whether going to bed or leaving the house, a lot of individuals forget to turn off the fans or lights somewhere in the house. In these situations, it's simple to use the mobile device to manage the fans or lights and to monitor where they are on. When a button is pressed via the Blynk app, the user's smart home's lights and fans will turn on, and they will successfully switch off when they hit the opposite button or utilize other modes like voice mode, timing function mode, or manual mode. Furthermore, by enhancing security, a smart lighting control system contributes to home security. This implies, for instance, that the lighting system might occasionally turn on and off the lights in the house while you're away on vacation, just like if someone was home. This project makes use of nearly six commands, including those that turn on and off lights, fans, and plugs using the Blynk app on Google Assistant. It is suitable for usage as a real-world project interface with a panel board. Once the power source is connected to the AC input slot in Figure 9, the device can be controlled using the method described in the previous section. The outcomes demonstrate that every experiment was completed satisfactorily and provide us with reliable data. The entire system met the requirements of every experiment pertaining to every scenario, and the plug point in our system linked to a range of appliances, including radios, refrigerators, and televisions, to verify control and functionality.

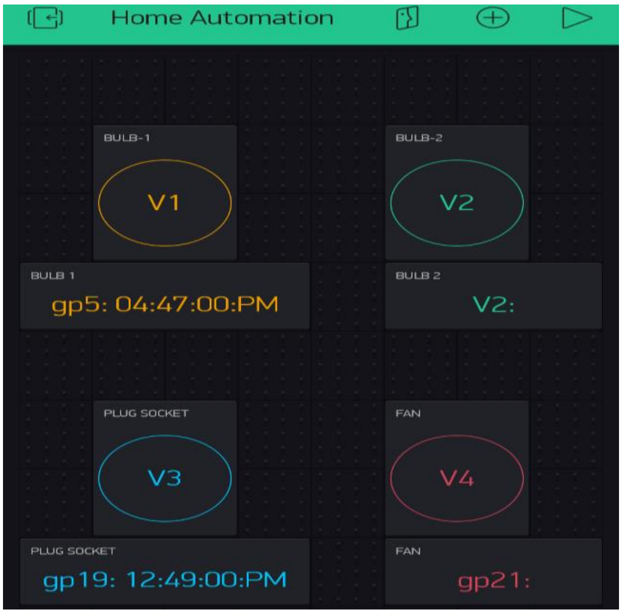

Figure 8. Blynk app user interface

Figure 9. Plug point for the panel board connection

Table 2. Experiment results based on scenarios.

Electrical components	Manual mode	Voice mode	Timer function mode	Switch mode via Blynk app
Light 1	√	√	√	√
Light 2	√	√	√	√
Fan	√	√	√	√
Plug point	√	√	√	√
D3	√	√	√	√
D4	√	√	√	√

4. Conclusion and Future works

A huge network of interconnected objects, services, and devices that may link, collaborate, and interact with one another is known as the Internet of Things (IoT). Numerous industries, including transportation, energy production and distribution, healthcare, agriculture, and smart homes and cities, are using and implementing IoT. The smart home system is one of the most significant IOT domains. Our lives are made more comfortable and easier by smart houses. Typically, mobile devices are used to control smart home functions. Users can operate a home appliance more efficiently with a user-friendly interface than with a complicated one. Many interactive smart home devices are abused when a system is sophisticated because they can be challenging to use and comprehend. The cost of the smart home systems now on the market is prohibitive for middle-class and lower-middle-class families. As a result, it's important to identify the users of smart home systems and create systems that are user-friendly, affordable, versatile, and suitable for people of all ages. This project offers a reasonably priced smart home system with the help of sensors, relays, and an NodeMCU controller. Many possible experiments are successfully carried out, including remotely operating fans, electrical devices, safety and security systems, and so on. There is no need to exert additional effort when controlling home appliances remotely. This demonstrated smart home concept effectively implements and uses safety and security systems. This prototype model has the ability to wirelessly operate the appliances and establish a direct connection with our main power supply unit. The proposed solution is cost-effective, user-friendly, and enhances quality of life. In the future, this system can be integrated into the main breaker, allowing control of all appliances through a wireless IoT network. This integration offers a sustainable and scalable approach to resource management while maintaining affordability. By leveraging IoT technology, the system enables efficient control of electrical devices, contributing to energy conservation and improved automation. The solution supports both economic and environmental sustainability for long-term usage.

5. References

Ajagbe, S. A., Misra, S., Afe, O. F., & Okesola, K. I. (2022, October). Internet of Things (IoT) for Secure and Sustainable Healthcare Intelligence: Analysis and Challenges. In *International Conference on Applied Informatics* (pp. 45-59). Cham: Springer International Publishing.

Algoiare, O.T., 2014. *Design and implementation of intelligent home using gsm network* (Doctoral dissertation).

Asadullah, M. and Ullah, K., 2017, April. Smart home automation system using Bluetooth technology. In *2017 International Conference on Innovations in Electrical Engineering and Computational Technologies (ICIEECT)* (pp. 1-6). IEEE.

Atzori, L., Iera, A., & Morabito, G. (2010). The internet of things: A survey. *Computer*

networks, *54*(15), 2787-2805.
Aziz, D. A. (2018). Webserver based smart monitoring system using ESP8266 node MCU module. *International Journal of Scientific & Engineering Research*, *9*(6), 801-808.

Chaurasia, T., & Jain, P. K. (2019, December). Enhanced smart home automation system based on Internet of Things. In *2019 Third International conference on I-SMAC (IoT in Social, Mobile, Analytics and Cloud) (I-SMAC)* (pp. 709-713). IEEE.

Danbatta, S. J., & Varol, A. (2019, June). Comparison of Zigbee, Z-Wave, Wi-Fi, and bluetooth wireless technologies used in home automation. In 2019 7th International Symposium on Digital Forensics and Security (ISDFS) (pp. 1-5). IEEE.

El-Hajj, M., Fadlallah, A., Chamoun, M. and Serhrouchni, A., 2019. A survey of internet of things (IoT) authentication schemes. *Sensors*, *19*(5), p.1141.

Imran, S.S., Vignesh, J., Singh, V.K. and Prasath, D.A., 2016, October. Smart Home automation based on IoT using Arduino mega. In *Proc. Int. Conf. Current Res. Eng. Sci. Technol. (ICCREST)* (pp. 2348-8379).

Kazi, R. and Tiwari, G., 2015. IoT based Interactive Industrial Home wireless system, Energy management system and embedded data acquisition system to display on web page using GPRS, SMS & E-mail alert. In *2015 International Conference on Energy Systems and Applications* (pp. 290-295). IEEE.

Maqbool, S., Iqbal, M. W., Naqvi, M. R., Arif, K. S., Ahmed, M., & Arif, M. (2020, November). IoT based remote patient monitoring system. In *2020 International Conference on Decision Aid Sciences and Application (DASA)* (pp. 1255-1260). IEEE.

Pau, G., & Salerno, V. M. (2019). Wireless sensor networks for smart homes: A fuzzy-based solution for an energy-effective duty cycle. *Electronics*, *8*(2), 131.

Shafana, A.R.F. and Aridharshan, A., 2017. Android based automation and security system for smart homes. *International Journal of Computer Science and Information Technology Research*, *5*(3), pp.26-30.

Helmet and Mask Detection for ATM's Surveillance via Deep Learning for Entrance Verification

Gnanapragasam Shanthoes*[1] and Vadivel Hiroshaan[1]
[1] *Department of Mechatronics Technology, University College of Jaffna, University of Vocational Technology, Sri Lanka.*

* gnanapragasamshanthoes@gmail.com

Abstract

The automated teller machine (ATM) is a crucial component of contemporary economic activity. It offers a quick and easy method for processing cost-effective transactions between banks and their clients. Regrettably, it also gives crooks an easy way to obtain cash without authorization. Every ATM has a camera system to capture the faces of people using it for security purposes. To prevent the surveillance system from recording their facial information, thieves typically cover their faces when using the ATM to take out illicit cash (such as by wearing masks or safety helmets). The surveillance system's effectiveness will suffer as a result. This study focuses on the use of automatic face detection tools to enforce security protocols at ATMs by identifying the absence of helmets and masks. The method employed in this research is based on Convolutional Neural Networks (CNNs) for face detection and classification. The implementation was carried out using Visual Studio and Python, leveraging the OpenCV library for image processing tasks. The CNN-based model operates through several stages. Initially, it detects faces in real-time from input images. The model then processes these detected faces to classify them into two categories: those wearing helmets and masks, and those without. The classification process involves several layers of convolution, pooling, and activation functions, which enable the model to learn complex patterns associated with the presence or absence of helmets and masks. The dataset used for training and testing the model consisted of 980 facial images. Each image was labeled based on whether the person was wearing a helmet and mask or not. During testing, the system correctly detected 190 out of 200 images, achieving an impressive accuracy rate of 95%. Future work will involve collecting a wider variety of images under different lighting conditions, angles, and resolutions to enhance the model's performance.

Keywords: helmet, mask detection, deep learning, CNN model

1. Introduction

Criminal activity in ATM square footage is regularly reported in Asian and international news sources. These well-known occurrences are not limited to developing nations; developed nations such as the United States, the United Kingdom, etc. also experience these problems. Similar to what has been reported recently, criminals are looking for novel ways to carry out their actions. They don't take any action to avoid ATM robberies, thus they don't care about video investigation techniques or footage square measures utilized for the spoken analysis of the robbery's impact. In order to confirm that an ATM is secure, the discovery of the victimization investigation camera during an ATM heist is a serious concern. Like other banking services, ATMs are a straightforward way to withdraw cash, but they also carry a high-security risk. To prevent ATM robberies, an automated surveillance system must be used to safeguard ATMs and offer security. Each camera scene's video recording, which is sent into the main server, causes memory to be misused and causes a delayed response to emergency situations. Therefore, it's critical to recognize unusual activities in order to take proactive precautions against theft. The burglars fool the security system even after the surveillance mechanism is installed by wearing helmets to cover their faces. In order to detect anomalous situations within ATM locations and alert relevant authorities, or stop the machine from releasing currency, the security system must to be effectively mechanized.

When someone comes into an ATM and covers their face using a cloth or other type of mask, our proposed system can identify aberrant activity and extract their features. The ATM's technology gathers data and electrical signals for the controller to lock or release the door, even if the user wears a helmet. The article begins with a quick overview of ATM crimes and ends with a review of the literature. The methodology is covered in Section 3; results and analysis are covered in Section 4; the conclusion and future work are covered in Section 5.

1.2 Existing study

Numerous scholars have devised diverse approaches to address the challenge of identifying an individual, such as a criminal wearing a helmet while driving—with reference to the unit of measurement. Ji *et al.* (2016) suggested a Helmet detection technique to handle faces that are arbitrary obscured for ATM surveillance. Here, the helmet in the ATM place is identified using CNN. Devi *et al.* (2019) presented a framework for determining if someone is donning a mask or helmet. After removing extraneous elements from the video using Background Subtraction, regions of interest (ROI) are performed. The head is identified, the skin-color ratio is extracted, and the LBP feature is found using a descriptor called Histogram of Oriented Gradients (HOG). Lastly, LBP feature can be used to train support vector machine (SVM) for the categorization of masks and helmets.

An algorithm has been developed by the authors Mathew *et al.* (2017) to address the issue of identifying bikers in traffic-recorded footage. In order to track the riders, heads, and helmets, this algorithm uses a probability-based method to split up each movie video frame. This solves the barrier issue, but it can't handle the minuscule variations brought on by light and noise. It also uses a fixed-size search window and on-observe head cranny edge detection. To identify motorcycle riders, the authors employed decisions based on edge histograms (Chiu *et al.,* 2007; Chiverton, 2012). The key benefit of this method is that, by using edge histograms close to the head instead of determining which region to select, it performs well even with low-resolution films. Because the sting histograms match and classify helmets using circular Hough transforms, there is often misclassification of bikers wearing helmets, and occasionally, items that resemble helmets are all grouped together and identified as helmets. Because they were all so different from one another, the helmets weren't considered to be helmets.

Some researchers suggested that the ability to identify unusual sounds—such as breaking an ATM machine with a rod, a customer yelling, or a gun blasting inside an ATM center—could alert bank employees to ongoing criminal activity and aid in apprehending the perpetrators (Kajendran and Pravin, 2017; Ray *et al.,* 2015). The aberrant sounds are identified using the HOG detection and cascade classifier. In order to determine if someone is wearing a mask in ATM machines Devi *et al.* (2019) presented a face mask based on a state model. The Gaussian Mixture Model (GMM) is used for foreground identification and to extract the ROI or human beings. By using the Viola-Jones technique in this search space and the torso partitioning, the face region is extracted from the foreground region. To identify the mask, certain facial features—such as the mouth, nose, and eyes—are cut out. A state model is then created. Mathew *et al.* (2017) introduced a Deep Convolutional Neural Network, which is the state of the art in object detection and localization. To achieve more precision, the data from the inception model has been sent to several fully linked layers with dropouts. The

Google Inception model is trained on a limited ATM surveillance dataset in order to enable automatic helmet identification.

2. Methodology

The research presented here suggests an automated surveillance system based on computer vision. The prototype design is as follows, and Fig. 1 displays the research project's schematic. Figure 2 depicts the system's suggested method. Our technology prompts a user to click the "Click me" button when they approach the ATM door. Following that, a camera will take visualizations to verify if the helmet is wearing or not. In order to identify and identify an object in a picture, we must first locate the loaded image's blob image, which is a grouping of binary data saved as a one file. The network will receive this image in order to determine the bounding boxes. A bounding box is utilized to define the target position in order to detect an object in an image.

The shape of the rectangular box may be resolved applying the X and Y coordinates, which are located at the upper-left and bottom-right corners of the rectangular box, respectively. This will be analyzed to the threshold limit once we have it. If the value is less than the threshold limit value, the image will be rejected because no item was found. In any other case, bounding box coordinates are computed. A crucial subsequent processing stage for the applications of computer vison is non-maximum suppression. This is used to produce several erroneous object window hypotheses from a smooth response map, ideally one bounding-box per item observed. The method was used using bounding boxes. The thing inside the bounding box shall be marked if there are at least one bounding box. The procedure will be terminated otherwise. The items can be detected and classified using convolutional neural networks.

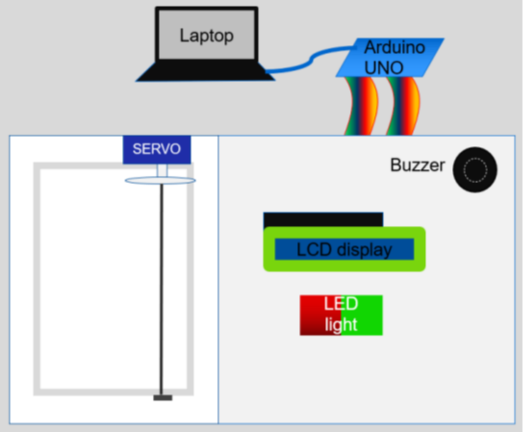

Figure 1. Prototype design

To create broader objects that could potentially find many object classes. An effective way to start would be to improve image categorization since object detectors are designed to measure certain item categories, such as facial identification. The primary unit of measurement in image classification is the convolutional neural network (CNN); the outcomes have a significant impact on this unit of measurement. Classification tools such as VGGnet and Inception were employed.

In image classification, we will supply an image as an input that, in the rare event of multi-label classification, yields an output that predicts one or more pre-trained categories. But it lacks any information regarding location. The classifiers are employed to locate both the related degree and the object associated with the finding across the entire image; a sliding window approach is typically used. Because the window sizes vary throughout this phase, the object sizes which are distinct will be measured using overlapping component scaling. Split up certain visual elements, which need to be treated with caution.

In the future system, a bounding box will identify and distinguish any linked items that the classifier occurs to recognize in the window. The result unit makes an estimate of a collection of bounding boxes and associated class names. That being said, with further research and the installation of a tone of suitable hardware, the result will have an associated degree of spare overlapping predictions. Finding familiar objects and object restrictions is the unit of measurement for CNN-based algorithms. R-CNN, an abbreviation for "region," is an effort to enhance the window approach. Region proposals, or bouncing boxes, are shown by R-CNN prior to the convolutional network extracting features. Selective search strategies are employed once region proposals have been obtained. While R-CNN does a regression on area suggestions using relevance-determined object categories to produce lower bounding box coordinates, some of them are support vector machines (SVM).

To cut down on the quantity of sending passes and achieve independent image features (CNN), classification (SVM), and bounding box modification, Fast R-CNN drifts Region of Interest Pooling (RoIPool). By using CNN findings for region suggestions rather than repeating them for selective search approaches, Faster R-CNN improves the selective search strategy. The faster R-CNN associate degree supplement known as "masked R-CNN" summarizes a parallel branch for segmentation mask prediction for every Region of Interest (RoI). It is an additional extension to the current branches among the networks that generate bounding box offsets and class labels. Applied to every ROI, a fully connected network (FCN) can be the outcome of the mask branch.

Masked R-CNN is based on the two phases of Faster R-CNN. A region proposal network (RPN) using prospective object box boundaries could be the first stage. A deep convolutional network analyzes a picture input and creates a feature map in the second stage of RPN. It starts with a smaller network that analyzes a feature map's spatial window, reduces the feature dimension, and feeds the results to two fully connected layers. The bounding box coordinates for the designated area will be given; by using these lines of difference, each rectangle's associate degree objectless "score" can be produced. This would be committing to the line of object category vs. backdrop for each spatial window. The reference boxes, often referred to as "anchors," support the organization of the k regions unit of estimation at a dependable time. They represent generic item shapes and have fixed sizes

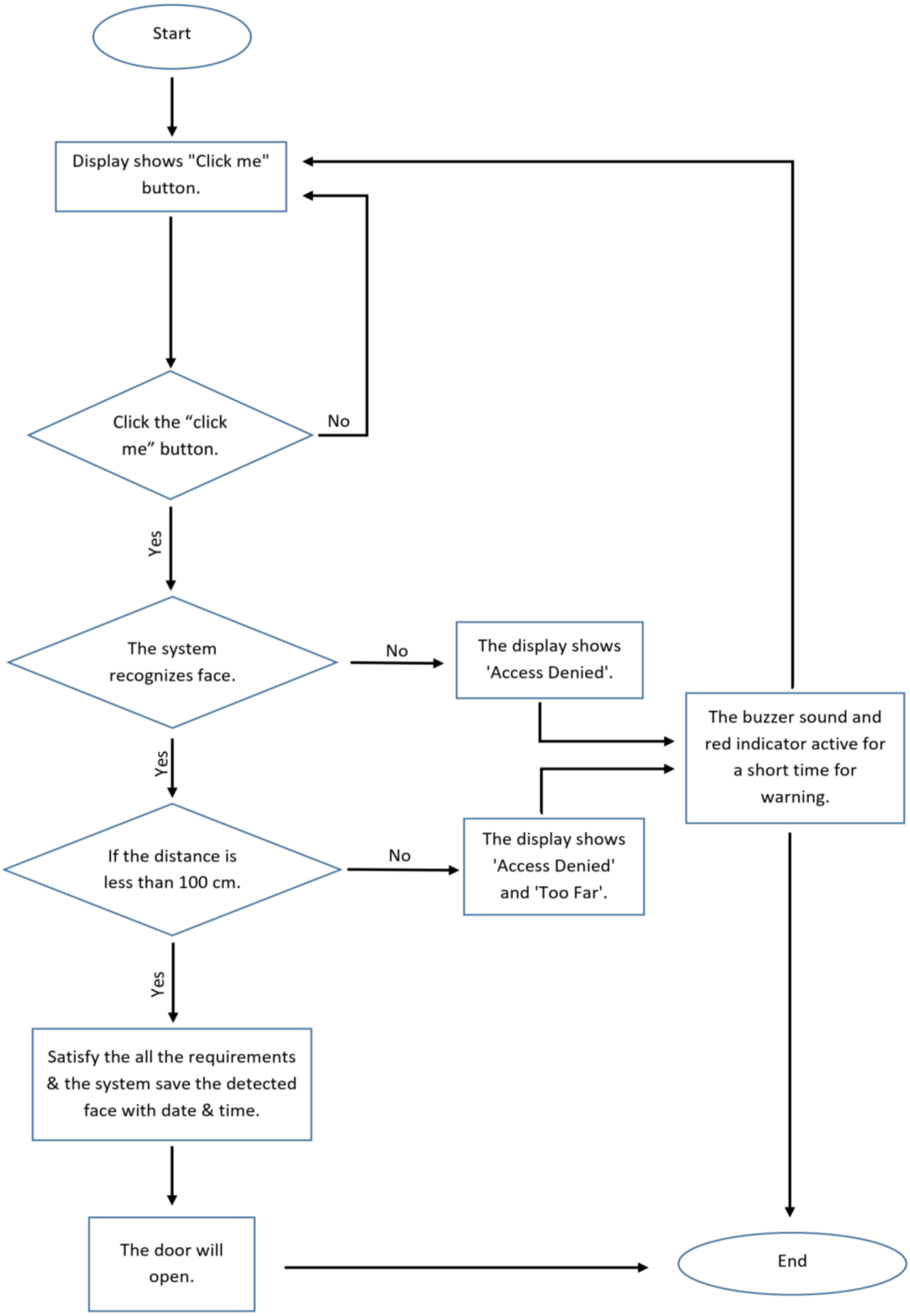

Figure 2. Flow diagram of the proposed research

and aspect ratios. The ROI picture's labeled ground truth data is utilized to generate training data for the RPN unit of measurement. When a ground truth box overlaps the Intersection-over-Union (IOU) by more than 0.5, the visible tag unit of measurement is selected to anchor with the IOU. This strategy makes use of several anchors, some of which could even be considered positive ones. The RPNs unit of measurement is taught from start to finish using random gradient descent and backpropagation. The image has been downsized to 800 pixels by square. To prevent negative samples from predominating in the data, a random sample of ROIs with a 1:3 ratio between positive and negative magnitudes is taken from each training image. Masked R-CNN finally produces bounding boxes and masks for every class that is available, based on the findings of the classification branch that is used to generate the box and mask selection.

2.1 Dataset

Image databases are the primary source of dependence for vision-based methods. Analyzing object attributes and evaluating detection algorithms' performance are crucial. There are databases accessible for the recognition of objects, characters, and scenes. However, there is no information available for the person using the ATM who is wearing a helmet. Thus, via the internet, over 980 pictures of people wearing and not wearing helmets were gathered.

3. Results and Analysis

Figure 3. Without helmet scenario

Previously indicated outcomes are tested in a real-world environment, where they can recognize the helmet wearer based on the bounding boxes. The odds of the objects we used to train the model will be shown. The testing for the scenarios with and without helmets is displayed in Figures 3 and 4, respectively. The images show that the door will be open if the individual is not wearing a helmet and that an alarm and red indication will sound if the person is wearing a helmet or face covered by mask or any clothes according to the Figure 5. Additionally, based on Figure 6, the system determined that there was too much space between the person's location and the camera. It displayed the message "Your distance is too far and come closer" on a display that was fixed to the ATM door. In order to determine the bounding boxes of a picture, the input picture will first be transformed to a Blob, after which it shall be sent to a convolution network and compared to a threshold value. We will determine the bounding box coordinates if they exceed a specified threshold. These bounding boxes will then undergo the non-maximum suppression technique to refine detection. Each object within the box will be compared with pre-trained classes, proceeding only if at least one bounding box remains; otherwise, the operation will terminate. If a person is detected wearing a mask or other obstructive clothing, the facial detection system will classify them as rejected, and the door will automatically close. During testing, the algorithm demonstrated impressive accuracy, achieving a 95% success rate by correctly identifying 190 out of 200 images, highlighting its reliability in detecting unobstructed faces.

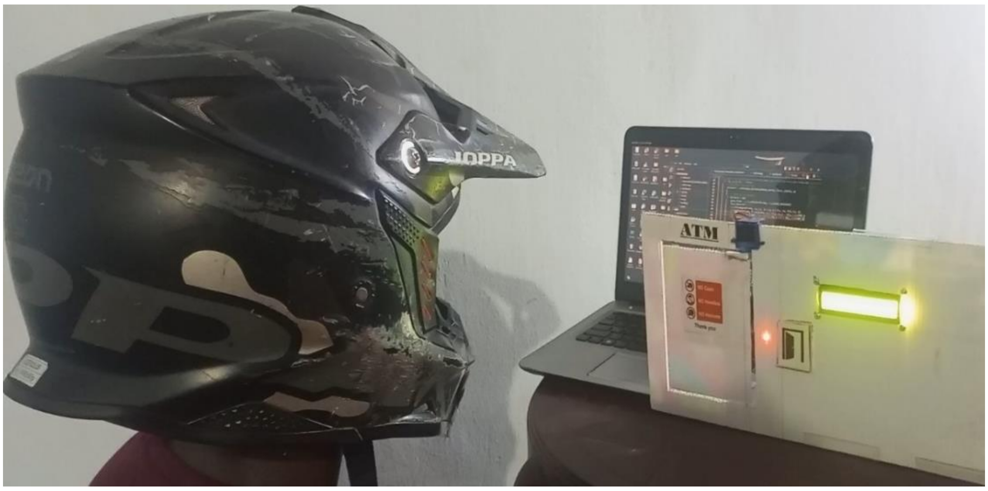

Figure 4. With helmet scenario

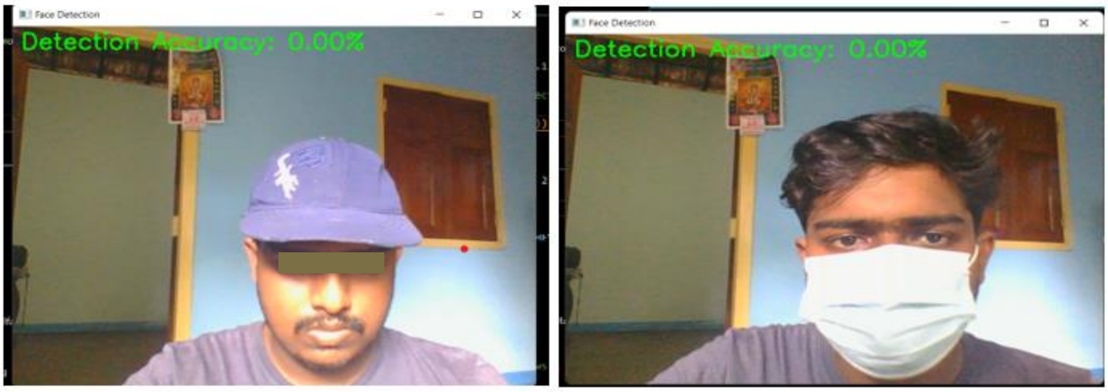

Figure 5. Abnormal conditions

Figure 6. Distance is too far scenario

4. Conclusion and Future works

This alert system needs human intervention at critical moments. While we observed some detection errors in the environment, we were able to get high accuracy for violations and non-violations; by providing additional data to train the network, we can improve this. By examining their behavior, this can be made simpler and better in the future, eventually becoming a completely automated system with various theft and crime footage. To improve the model's performance, more varied image collections with varying lighting, perspectives, and resolutions will be gathered in subsequent work.

5. References

Chiu, C.C., Ku, M.Y. and Chen, H.T., 2007, June. Motorcycle detection and tracking system with occlusion segmentation. In *Eighth International Workshop on Image Analysis for Multimedia Interactive Services (WIAMIS'07)* (pp. 32-32). IEEE.

Chiverton, J., 2012. Helmet presence classification with motorcycle detection and tracking. *IET Intelligent Transport Systems*, *6*(3), pp.259-269.

Devi, K.B., Roomi, S.M.M., Meena, M. and Meghana, S., 2019, March. Deep learn helmets-enhancing security at ATMs. In *2019 5th International Conference on Advanced Computing & Communication Systems (ICACCS)* (pp. 1111-1116). IEEE.

Ji, P., Kim, Y., Yang, Y. and Kim, Y.S., 2016, September. Face occlusion detection using skin color ratio and LBP features for intelligent video surveillance systems. In *2016 Federated Conference on Computer Science and Information Systems (FedCSIS)* (pp. 253-259). IEEE.

Kajendran, P. and Pravin, A., 2017. Enhancement of security related to ATM installations to detect misbehavior activity of unknown person using video analytics. *ARPN Journal of Engineering and Applied Science*, *12*, p.21.

Mathew, A., Mathew, J., Govind, M. and Mooppan, A., 2017. An improved transfer learning approach for intrusion detection. *Procedia computer science*, *115*, pp.251-257.

Ray, S., Das, S. and Sen, A., 2015, December. An intelligent vision system for monitoring security and surveillance of ATM. In *2015 Annual IEEE India Conference (INDICON)* (pp. 1-5). IEEE.

Silva, R., Aires, K., Santos, T., Abdala, K., Veras, R. and Soares, A., 2013, October. Automatic detection of motorcyclists without helmet. In *2013 XXXIX Latin american computing conference (CLEI)* (pp. 1-7). IEEE.

Detecting of Tomato Leaf Diseases using Machine Learning

Vimalanathan Dinesh[1*], Saikrisha Kaneswaran[1]

[1] *Department of Engineering Technology, Faculty of Technology, University of Jaffna, Kilinochchi, Sri Lanka.*

*2019et017@tech.jfn.ac.lk

Abstract

Plant diseases are a significant problem in global food security and productivity. Fungal, viral, and bacterial diseases commonly affect Tomato plants. It is a big challenge to farmers and decreases the quality and quantity of production. Early identification and perfect detection require a fast and accurate diagnosis to prevent a decline in productivity and increase the profit of the cultivator. Traditional methods are ineffective and time-consuming; unaware farmers require more experts to identify these diseases. However, the on-site prediction rate could be more accurate. Prompt detection of diseases requires an accurate system that supports vital stages of the food chain. Tomatoes are a plant of the Solanaceae family, which is not only cultivated by farmers but also commonly grown at home. So, this research developed an efficient Convolutional Neural Network (CNN) model and compared it with the DenseNet201 model to identify diseases on Tomato leaves. The existing Plant Village Dataset, with 13880 Tomato Leaf images, was used for both models with 50 epochs. The dataset is split into 80% training, 10% validation, and 10% testing. The Training and Validation accuracy of the DenseNet201 is 99.64% and 94.66%, respectively. However, the proposed CNN model performed with a training accuracy of 98.14% and a validation accuracy of 97.73%. The proposed CNN model can classify the Healthy Leaves, Early Blight, Late Blight, Bacterial Spot, Septoria Leaf Spot, and Yellow Leaf Curl Virus of 6 classes with 96.42% accuracy. This paper's findings show that the proposed model can be used for real-time crop disease detection, even in resource-constrained environments using a hand-held device or a mobile application. It could reduce the farmers' workload and thus make early treatment and curing of disease feasible for them and increase yield.

Keywords: *Plant disease detection; CNN; Machine learning; DenseNet201 algorithm; Tomato plant diseases*

1. Introduction

Agriculture is an important economic sector for developing and developed countries. It has been the future for many years. Agriculture also defines the country's wealth. Tomato, a member of the Solanaceae family, is a common household plant. These are also affected by pests, bacteria, parasites, viruses, and fungi. In fungi, viruses and bacterial infections are significant diseases that affect tomato plants (Mishra, Sachan and Rajpal, 2020).

Machine learning has emerged as a promising solution to the challenges faced by farmers in detecting plant diseases. Traditional disease detection methods often rely on visual inspection, which is time-consuming and may not be sufficiently accurate for early detection (Dhanalakshmi *et al.*, 2023). Integrating machine learning into disease detection processes offers a promising solution to address these challenges.

Machine learning algorithms can process diverse data sources (images) to identify subtle patterns indicative of plant diseases, allowing farmers to take proactive measures. Early detection reduces crop losses and minimizes the need for extensive pesticide use, contributing to more sustainable and environmentally friendly agricultural practices. Precision agriculture optimizes resource use, improves efficiency, and reduces environmental impact. It extends to global food security, as disease outbreaks can lead to shortages in tomato supply, affecting local markets and escalating prices.

The economic implications of this project are substantial for farmers, as crop losses due to diseases can result in financial setbacks, especially for small-scale farmers who may lack the resources to recover from significant yield reductions (FAO, 2017). By adopting machine learning for disease detection, farmers can mitigate these losses, protect their livelihoods, and increase their overall income.

2. Methods and Material

2.1. Dataset

Data is a crucial element of a machine-learning project. So, it can be buying the data from vendors, manual collection, web scraping, and readymade data. For our model, we collect the readymade data from Kaggle. We have 13880 images belonging to 6 model building classes: Bacterial Spot, Early Blight, Healthy, Late Blight, Septoria Leaf Spot, and Yellow Leaf Curl Virus (Urbieta *et al.*, 2024). The Jupyter Notebook platform with TensorFlow, CNN (Krishnan and Julie, 2023), data augmentation, and tf dataset were used. The dataset was divided into an 80:20 ratio (Singh and Yogi, 2023), where 80% was used for training, 10% for validation and 10% for testing. Here, 50 epochs were used with a batch size of 32.

Figure 1. Dataset

Table 1. Data Types

Types	No of Images
Bacterial Spot	2127
Early Blight	2400
Healthy	2407
Late Blight	2314
Septoria Leaf Spot	2181
Yellow Leaf Curl Virus	2451
Total	**13880**

2.2. Convolutional Neural Network

Convolutional Neural Network (CNN) is a deep learning architecture designed for processing structured grid data, such as images. It consists of multiple layers, including convolutional, pooling, and fully connected layers that automatically and adaptively learn spatial hierarchies of features from input data.

2.3. Pre-processing

Pre-processing is a crucial step in data analysis that involves preparing raw data for further processing by cleaning, transforming, and organizing it. This stage includes handling missing values, normalizing data, and converting data into a format suitable for analysis. The pre-processing layer for our dataset, resizing, and rescaling were done as 256 by 256 pixels. The data augmentation was done to make our model robust. Because the input images can be different, we contrasted, flipped, rotated, and zoomed to understand them. We did the Random Flip and Random Rotation (Sareen et al., 2022).

2.4. Convolution Layer

The convolutional layer is a core component of CNNs that detects local features in input images. In 2-dimensional convolution calculation, a 2-D image can be mapped into a convolution window, which slides continuously to obtain the corresponding convolution value. The activation function does the non-linear mapping between layers of the network, making it capable of learning and performing more complex tasks. We have chosen a Rectified Linear Unit (ReLU) as an activation function in each layer except at the output layer, where softmax activation is used (Mishra, Sachan and Rajpal, 2020).

2.5. Max-Pooling Layer

The max-pooling layer is a down-sampling technique used in CNNs to reduce the spatial dimensions of feature maps. Selecting the maximum value from each region of the feature map preserves the most significant features while reducing computational complexity and helping to prevent overfitting (Dhanalakshmi *et al.*, 2023).

2.6. Flatten Layer

A CNN's Flatten layer transforms the previous layers' multi-dimensional output into a one-dimensional vector. This step is essential for connecting the convolutional and pooling layers to the fully connected layers, enabling the network to process and make final classifications or predictions (Mishra, Sachan and Rajpal, 2020).

2.7. Dense Layer

The dense, fully connected layer is a fundamental component of neural networks, including CNN. It connects every neuron from the previous layer to each neuron in the current layer, allowing for complex combinations of features learned in earlier layers to make final decisions or predictions (Mahum *et al.*, 2023).

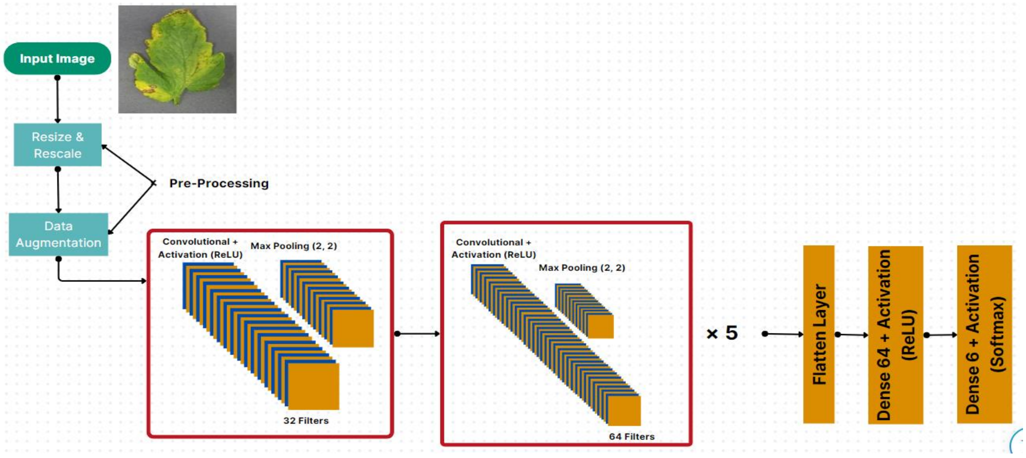

Figure 2.Architecture of the developed CNN model

3. Results & Discussion

3.1. Training & Validation Accuracy and Loss

Training accuracy is the percentage of correct predictions made by a machine learning model on the dataset on which it was trained. It indicates how well the model has learned the patterns in the training data. A high training accuracy suggests that the model has effectively captured the underlying relationships within the dataset. However, it may also indicate overfitting if significantly higher than the validation accuracy.

Validation accuracy measures the model's performance on a separate dataset not used during training. It serves as an indicator of the model's ability to generalize to unseen data. Consistent validation accuracy close to the training accuracy suggests a well-generalized model. At the same time, a significant drop may indicate overfitting, where the model performs well on the training data but poorly on new data.

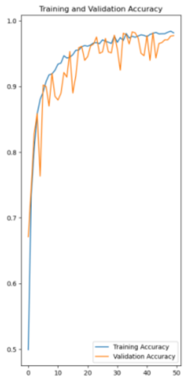

Figure 1: Accuracy Graph

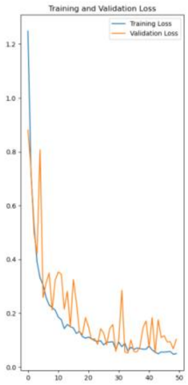

Figure 2: Loss Graph

Table 2. Training & Validation Accuracy Table

	Developed CNN	**DenseNet201**
Training Accuracy	0.9814	0.9964
Validation Accuracy	0.9773	0.9466
Training Loss	0.0504	0.0158
Validation Loss	0.1036	0.2078

The model was developed with 50 epochs (Mahum *et al.*, 2023) with training and validation curves for accuracy and loss. The accuracy increases with several epochs. A higher number of epochs will give a higher epoch. However, with enough datasets, models will be highly accurate. The loss curve of the developed CNN model is in the opposite direction to the accuracy. It also depends on the number of epochs.

3.2. Confusion Matrix

The confusion matrix (Nath, Mitra and Kumar, 2023) of developed CNN and DenseNet201 models, Figure 6, Figure 7 describes the correct predicted number of images. The array method is used to indicate the labels. 0, 1, 2, 3, 4, and 5 indicate the Bacterial Spot, Early Blight, Healthy, Late Blight, Septoria Leaf Spot, and Yellow Leaf Curl Virus. Using Figures 6 and 7, calculate the accuracy of the models. Accuracy obtained from the models is shown in below Table 3.

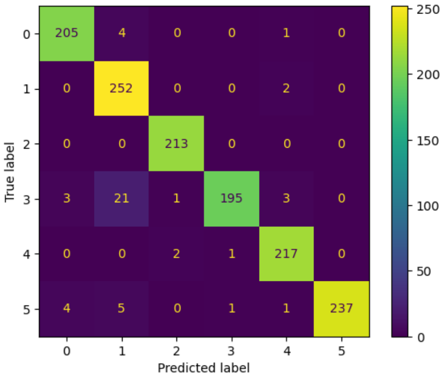

Figure 3: Developed CNN model

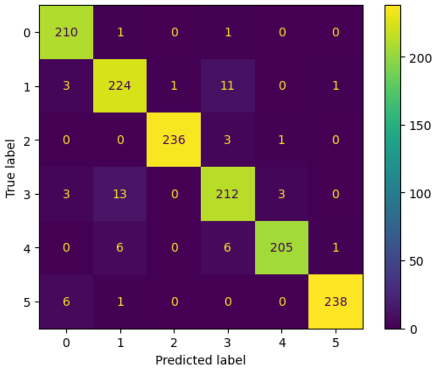

Figure 4: DenseNet201 model

$$Accuracy = \frac{Total\ Number\ of\ Correctly\ Predicted\ Samples}{Total\ Number\ of\ Samples} \quad (1)$$

Table 3. Accuracy of Models

	Testing Accuracy
Developed CNN	96.42%
DenseNet201	95.60%

3.3. Classification Report

Accuracy and recall depend on their shared focus on correctly identifying positive instances in a classification model. Accuracy measures the overall correctness of predictions, considering both True Positives and True Negatives. At the same time, recall evaluates explicitly the model's ability to capture all relevant positive instances, emphasizing the avoidance of false negatives.

$$Recall = \frac{True\ Positives\ (TP)}{True\ Positives\ (TP) + False\ Negatives\ (FN)} \quad (2)$$

As accuracy increases, it suggests an improvement in the overall correctness of predictions, including True Positives, True Negatives, False Positives, and False Negatives. However, changes in accuracy may not necessarily reflect changes in recall, as the latter is susceptible to the model's performance in identifying Positive instances. In scenarios where the cost of missing Positive instances is high, prioritizing recall over accuracy becomes crucial to ensure comprehensive coverage of relevant cases. The relationship between these metrics underscores the need for a balanced assessment of overall correctness and the model's effectiveness in capturing Positive instances (Verma, Kumar and Singh, 2024).

Precision and the F1 score share a complementary relationship in evaluating the performance of a classification model, especially in situations where False Positives have significant consequences. Precision focuses on the accuracy of Positive predictions and is calculated as the ratio of True Positives to the sum of True Positives and False Positives.

$$Precision = \frac{True\ Positives\ (TP)}{True\ Positives\ (TP) + False\ Positives\ (FP)} \quad (3)$$

On the other hand, the F1 score is the harmonic mean of precision and recall, providing a balanced measure that considers both False Positives and False Negatives. In instances where precision is high, indicating fewer False Positives, the F1 score also tends to be higher. However, the F1 score penalizes models that overly prioritize precision or recall individually, encouraging a balanced trade-off between the two. This interdependence reinforces the need for a comprehensive assessment of a model's precision and recall to ensure a suitable balance between accurate Positive predictions and a minimized risk of false positives.

$$F1\ Score = \frac{2 \times Precision \times Recall}{Precision + Recall} \quad (4)$$

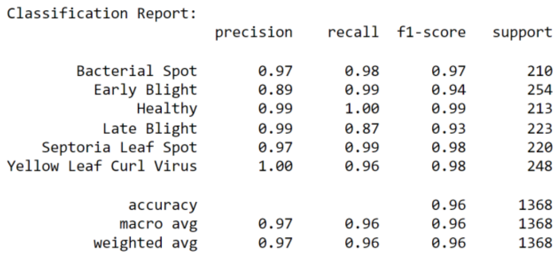

```
Classification Report:
                      precision    recall  f1-score   support

      Bacterial Spot       0.97      0.98      0.97       210
        Early Blight       0.89      0.99      0.94       254
             Healthy       0.99      1.00      0.99       213
         Late Blight       0.99      0.87      0.93       223
  Septoria Leaf Spot       0.97      0.99      0.98       220
Yellow Leaf Curl Virus     1.00      0.96      0.98       248

            accuracy                           0.96      1368
           macro avg       0.97      0.96      0.96      1368
        weighted avg       0.97      0.96      0.96      1368
```

Figure 5: Classification Report of developed CNN model

The developed CNN model reached an accuracy of 96%, precision of 97%, recall of 96%, and f1-score of 96% based on the classification report. This report is generated from the model training coding. These values are based on the tested images, and 1368 images were used for testing purposes, which is 10% of the overall dataset.

4. Conclusion

In the pursuit of enhancing the accuracy of tomato disease classification models, this research undertook the development and evaluation of a Convolutional Neural Network (CNN) model. The primary objective was to compare the performance of the proposed model against the widely recognized DenseNet201 architecture in the context of predicting five common tomato diseases along with a category for healthy leaves, encompassing a total of six distinct classes.

The development and evaluation of the Developed CNN model for tomato disease classification have yielded promising results, surpassing the benchmark established by DenseNet201. The model's superior accuracy of 96.42%, particularly in distinguishing between various diseases and healthy leaves, positions it as a valuable asset in the arsenal of tools available for precision agriculture. As we move forward, the lessons learned from this research can guide the development of more tailored and efficient models for diverse agricultural applications, ultimately contributing to sustainable and resilient food production systems.

5. References

Dhanalakshmi, R. *et al.* (2023) 'Tomato leaf disease identification by modified inception based sequential convolution neural networks', *The Imaging Science Journal*, 71(5), pp. 408–424. Available at: https://doi.org/10.1080/13682199.2023.2183318.

FAO (2017) *The future of food and agriculture: trends and challenges*. Rome: Food and Agriculture Organization of the United Nations.

Krishnan, R.S. and Julie, E.G. (2023) 'Computer aided detection of leaf disease in agriculture using convolution neural network based squeeze and excitation network', *Automatika*, 64(4), pp. 1038–1053. Available at: https://doi.org/10.1080/00051144.2023.2241792.

Mahum, R. *et al.* (2023) 'A novel framework for potato leaf disease detection using an efficient deep learning model', *Human and Ecological Risk Assessment: An International Journal*, 29(2), pp. 303–326. Available at: https://doi.org/10.1080/10807039.2022.2064814.

Mishra, S., Sachan, R. and Rajpal, D. (2020) 'Deep Convolutional Neural Network based Detection System for Real-time Corn Plant Disease Recognition', *Procedia Computer Science*, 167, pp. 2003–2010. Available at: https://doi.org/10.1016/j.procs.2020.03.236.

Nath, M., Mitra, P. and Kumar, D. (2023) 'A novel residual learning-based deep learning model integrated with attention mechanism and SVM for identifying tea plant diseases', *International Journal of Computers and Applications*, 45(6), pp. 471–484. Available at: https://doi.org/10.1080/1206212X.2023.2235750.

Sareen, N., Chug, A. and Singh, A.P. (2022) 'An image based prediction system for early blight disease in tomato plants using deep learning algorithm', *Journal of Information and Optimization Sciences*, 43(4), pp. 761–779. Available at: https://doi.org/10.1080/02522667.2021.2000167.

Singh, G. and Yogi, K.K. (2023) 'Performance evaluation of plant leaf disease detection using deep learning models', *Archives of Phytopathology and Plant Protection*, 56(3), pp. 209–233. Available at: https://doi.org/10.1080/03235408.2023.2183792.

Urbieta, Matias *et al.* (2024) 'A scalable offline AI-based solution to assist the diseases and plague detection in agriculture', *Journal of Decision Systems*, 33(3), pp. 459–476. Available at: https://doi.org/10.1080/12460125.2023.2226381.

Verma, S., Kumar, P. and Singh, J.P. (2024) 'A Unified Lightweight CNN-based Model for Disease Detection and Identification in Corn, Rice, and Wheat', *IETE Journal of Research*, 70(3), pp. 2481–2492. Available at: https://doi.org/10.1080/03772063.2023.2181229.

IoT Based Underground Power Cable Fault Monitoring System

Ketheeswaran, G.[1*], Rusilan, S.[1], Senthuran, M.[1], Jayasooriya, L.T.[1], Kugaranan, T.[1], Thilakarathne, M.R.D.P.[1]

[1]*Department of Electrical and Electronic Technology, Faculty of Technology, Rajarata University of Sri Lanka.*

*ent1718042@tec.rjt.ac.lk

Abstract

This study proposes a fault detection method for *Underground cables* using a *Microcontroller* and software. The *Microcontroller* calculates the fault distance and notifies the user through software with the location of the fault in the *Underground cable*. The system is able to identify the location of faults by measuring the capacitance and resistance of the cable and applying the principles of Ohm's law. The system includes an oled display device that shows the fault distance from the *Base station*. If a fault is detected, the system provides details to the user. These details can be entered and viewed using an *Android application*. Overall, the proposed system is designed to improve the efficiency and performance of *Electrical systems* by quickly identifying the location of faults in *Underground cables*. By reducing the time required to find faults, the system can help prevent damage to transformers and other electrical equipment, while also improving safety and reducing operating expenses.

Keywords: *Microcontroller; Android application; Base station; Underground cables; Electrical system*

1. Introduction

The transmission of electrical power can be done through overhead electrical cables or underground ones. In the past, overhead cables were commonly used, but they had several drawbacks such as the risk of electrocution and damages due to weather conditions, which made them less reliable. The proposal of underground wires for power transmission has led to significant advancements in this field over the past two decades.

Underground cables play a crucial role in modern electricity transmission systems, providing efficient and reliable electricity transportation from power plants to homes and businesses. They are protected from weather, pollution, and physical damage, making them more durable and longer-lasting than overhead cables. Additionally, underground cables are less visible, making them suitable for areas where overhead cables may be unsightly or pose a safety hazard. However, like all electrical systems, underground cables can experience problems or failures over time, such as corrosion, physical damage, age-related issues, poor installation, and inadequate maintenance. These problems can disrupt electricity transmission and result in power outages, and it's important to address them promptly to minimize their impact. Pinpointing the location of the fault can be challenging, and it may require excavation of the surrounding area to access the cable and make repairs, which can be time-consuming and costly.

With the advancement of digitalization, this project aims to detect the location of faults in underground cable systems using digital methods. Underground cable systems are commonly used in urban areas, and when faults occur, repairing the cable becomes challenging due to the lack of precise fault location information. In this project, we will explore the potential of digital fault detection methods for underground cable systems and their advantages in improving the reliability and efficiency of cable maintenance and repair processes.

The proposed system is an Internet of Things (IoT) enabled underground cable fault detection system, that use Ohm's law, as a fundamental principle in electricity, to calculate the distance to the fault and determine the location within the cable once a fault has been detected. The IoT technology enables location tracking on a map and retrieval of historical data for analysis. This system has the potential to provide a cost-effective and efficient way to maintain and repair underground cables, improving the reliability and longevity of electricity transmission systems. By accurately identifying and locating faults, the system can help minimize downtime, reduce repair costs, and ensure uninterrupted power supply.

2. Materials and Methods

Based on the Case studies, the proposed system is an IoT enabled underground cable fault detection system. The basic principle behind the system is Ohm’s law, once a fault has been detected, the system can use Ohm's law to calculate the distance to the fault and determine the location of the fault within the cable. IoT technology can able to pinpoint the location in the map and retrieve the history and analyze the data, this system could provide a cost-effective and efficient way to maintain and repair underground cable.

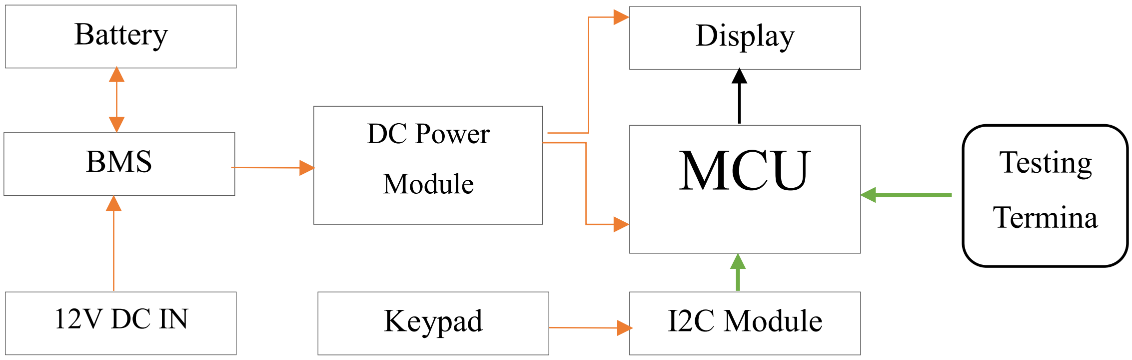

Figure 1. Block diagram of IoT based underground fault detector

To achieve the goal of the proposed system, several components and technologies are involved. The system consists of a 12V power input that goes into a battery management system (BMS) which is connected to a DC power module. The DC power module supplies power to the microcontroller and display. The testing probes are used to input the signals into the system.

The system uses a microcontroller to process the data and perform calculations. The display module is used to show the results of the calculations, and we manually enter the data to the software to track the location of the fault. The information that is transferred from the Arduino to the relay driver and ultimately to the appropriate relays is crucial. With the aid of switches, the relays attempt to locate the defect, and the Arduino board receives this information. The necessary information will be displayed since this data will be delivered to both the GSM module and the LCD display.

The methodology used in this project involves designing and building a prototype system, testing the system using open and short circuit fault conditions. The prototype system will be built using off-the-shelf components and assembled according to a design specification.

Table 4. Required software

Software	Hardware	Equipment
• Easy EDA • Proteus • AutoCAD • MS office • MIT App inventor • Arduino IDE • Think Speak Cloud Database	• Microcontroller • BMS(HX-35) • OLED display • Buck converter • I2C Expander module • Keypad (4x4 matrix) • Resistance • Capacitance • Diode • Transistor • Relay • Voltage regulator • Sliding Switches	• Multi meter • PCB printing machine • LRC meter • Arduino • Soldering ion • Variable DC power Source

2.1 Software used for Designing of the project

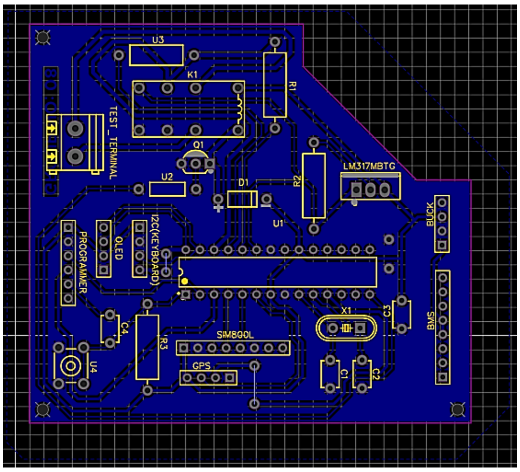

Figure 2. PCB Layout of the design

AutoCAD Electrical was utilized in the design and drafting phase of the project. This software provided a comprehensive set of features and capabilities that were essential for the creation of accurate and detailed electrical schematics and wiring diagrams.

Easy EDA is a popular web application tool used for designing printed circuit boards (PCBs). It provides an easy-to-use interface for designing schematics and PCB layouts. Easy EDA includes a vast library of electronic components, which makes it easy to create custom PCB layouts quickly. It also includes an auto-router tool that can route connections automatically, although manual routing is usually preferred for better control over the layout. One of the key advantages of using Easy EDA is its compatibility with various PCB manufacturers, making it easier to transfer the design files to a manufacturer for fabrication. It also allows for 3D visualization of the PCB design, which can help identify and resolve any potential layout issues before fabrication. Proteus is a popular software tool used in the electronics industry for simulation, design, and testing of electronic circuits. It offers a virtual environment where designers can simulate and test their electronic designs, providing a cost-effective and time-efficient way to prototype and refine electronic circuits.

Arduino IDE is an open-source software platform used for programming microcontrollers. It has several features that make it an ideal choice for programming microcontrollers, such as a simplified language, real-time serial communication, and debugging capabilities. It also includes a vast library of pre-written codes that can be used for various purposes, including interfacing with sensors, controlling motors, and communicating with other devices.

MIT App Inventor is a web-based integrated development environment (IDE) used to develop mobile applications for Android devices. It is a visual programming language that allows users to drag and drop graphical objects to create an application. MIT App Inventor is designed to be an easy-to-use tool for beginners who have no prior coding experience. It includes a variety of components and features, such as buttons, labels, textboxes, and sensors that can be used to create interactive mobile applications.

In the underground cable fault detection system project, MIT App Inventor was used to create a mobile application that allows the user to view the location of the fault on a map.

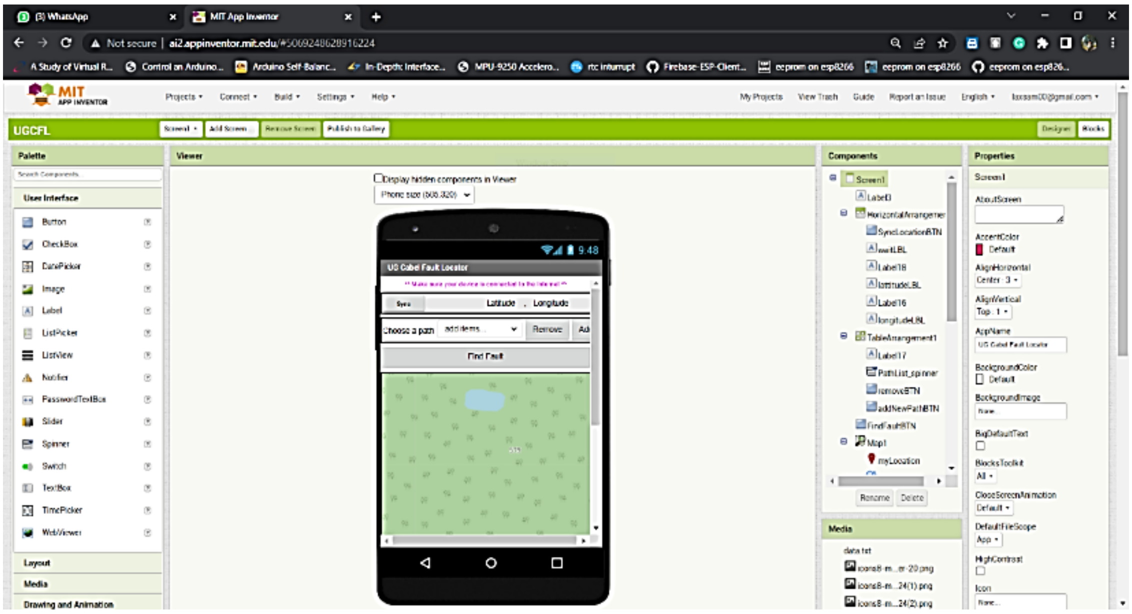

Figure 3. MIT App inverter screenshot – UG Cable Fault Locator

2.2 Proposed System Working Principle and Calculations

2.2.1 Measuring Capacitance

An RC circuit is an electric circuit that contains resistances and capacitors, the time constant (T) in an RC circuit is given by the product of the total resistance and the total capacitance

$$T = RC$$

An RC circuit's time constant is defined as the time it takes for the voltage across the capacitor to reach 63.2% of its full charge voltage.

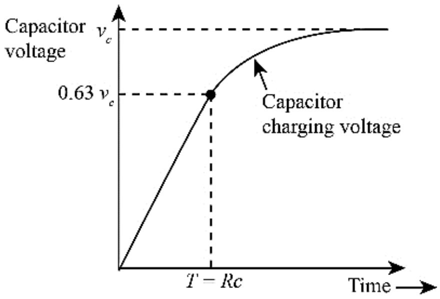

Figure 4. Raising Voltage (V) vs RC Time Constant (s)

Underground fault detector has two probe to measure capacitance. The time constant of an RC circuit can be defined as the time when it takes for the voltage across the capacitor to reach 63.2% of its voltage when it fully charged. Following equation provide technique to measure capacitance.

Capacitance = Time constant of capacitor/resistance of circuit

This capacitance meter has an RC circuit with known resistor values and an unknown capacitor value. The AVR will measure the voltage at the capacitor and record the time it takes to reach 63.2% of its voltage when fully charged (the time constant).

Since the resistance value is already known, that meter probes connected to AVR two analog pins then we can use the formula above in a program that will calculate the unknown capacitance.

Fault location = Total capacitance/ Unit capacitance

2.2.2 Measuring Resistance

Measuring the resistance of an unknown resistor involves setting up a voltage divider circuit with a known resistor and an unknown resistor in series. The voltage divider circuit provides a voltage output between the two resistors, which can be measured using an AVR analog pin.

Using Ohm's Law and the voltage divider formula, we can calculate the value of the unknown resistor. The voltage divider formula is $V_1/V_2 = R_1/R_2$, where V_1 is the voltage across the known resistor, V_2 is the voltage across the unknown resistor, R_1 is the known resistance, and R_2 is the unknown resistance.

By measuring the voltage across the unknown resistor and knowing the voltage across the known resistor and the resistance value of the known resistor, we can calculate the resistance of the unknown resistor using the formula $R_2 = R_1 * (V_2/V_1)$.

This technique can be used to locate a fault in a circuit by measuring the resistance of the portion of the circuit before and after the fault. By measuring the resistance between two points in the circuit and calculating the resistance of the portion of the circuit between those points, we can determine the location of the fault within the circuit.

2.2.3 Short circuit fault calculations

The short circuit can be determined by measuring the resistance between two wires at one end (base station). The value of the resistance tells us the exact distance of the short circuit.

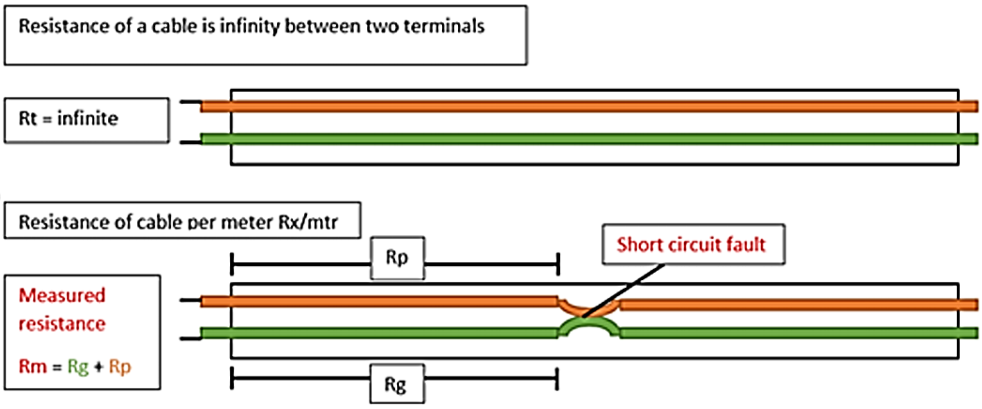

Figure 5. Short circuit calculations (https://circuits4you.com/2016/05/17/arduino-based-underground-cable-fault-detection/)

2.2.4 Open circuit fault calculations

The Open circuit can be detected by measuring capacitance between two wires. The capacitance of the cable changes according to the length. The length of the wire varies depending on the location of the cut (open) wire. As the cable is open, the capacitance of the parallel cable is reduced based on this, we can calculate the location of the fault.

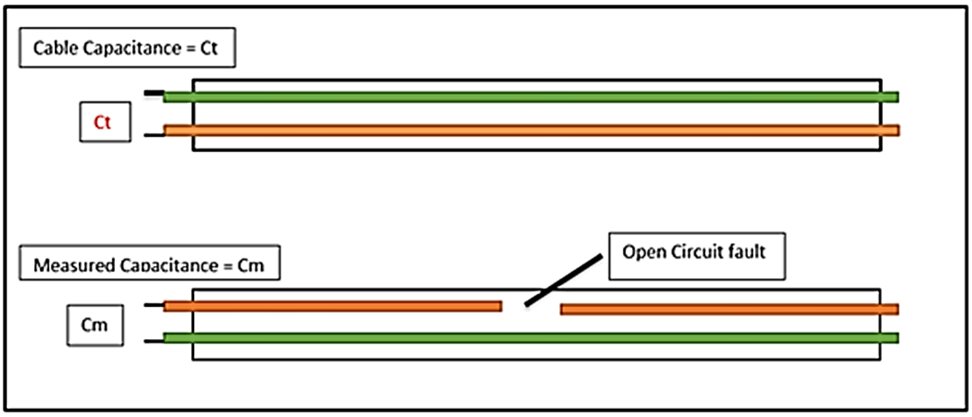

Figure 6. Open circuit calculations (https://circuits4you.com/2016/05/17/arduino-based-underground-cable-fault-detection

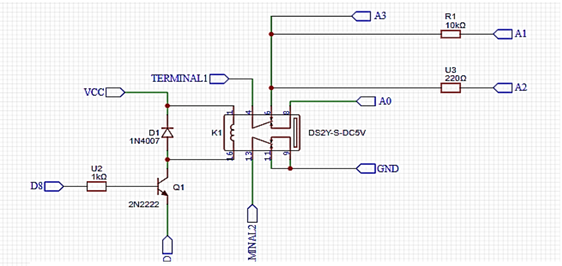

Figure 7. Selection of capacitance and resistance

K1: Measurement selection relay. Used to select open circuit or short circuit.

A3: Pin for capacitance read (Open circuit measurement).

3. Results

After switching ON and the device comes to its operation condition, we connect the faulty cable through terminal 1 and terminal 2. Then select one option of both short and open circuit faults. If we select Option 1 (short circuit fault) it will display the resistance value and distance at which the fault occurs in the cable, but faulty cable with a short circuit, the device will display infinite resistance value. According to this result, we can decide that the measured cable has no short circuit fault and that the measured cable with short circuit fault. After identifying types of faults, we can choose another option (Option 2 – open circuit fault) and carry out measurement again.

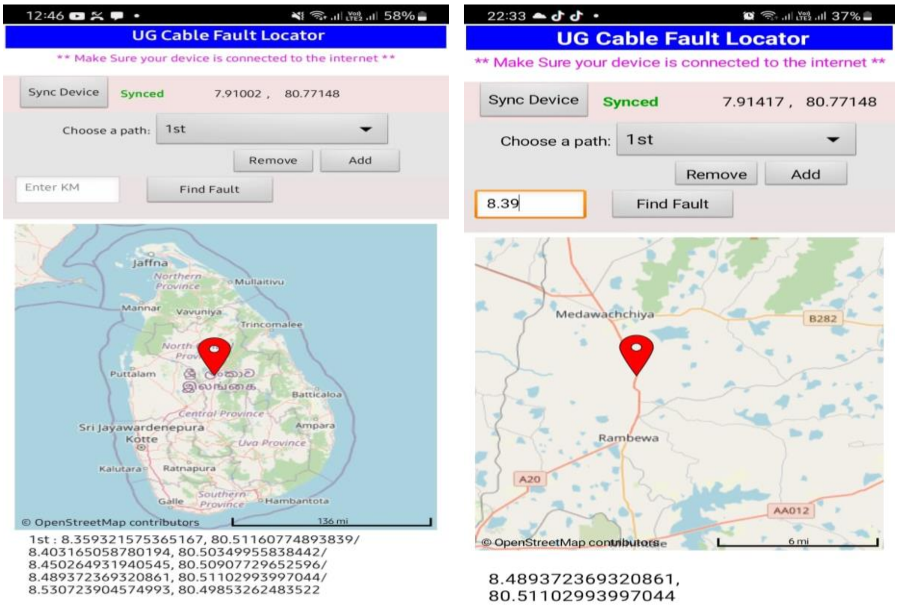

** Make Sure your device is connected to the internet **

Synced 7.91002 , 80.77148

Choose a path: 1st

Enter KM

1st : 8.359321575365167, 80.51160774893839/
8.403165058780194, 80.50349955838442/
8.450264931940545, 80.50907729652596/
8.489372369320861, 80.51102993997044/
8.530723904574993, 80.49853262483522

** Make Sure your device is connected to the internet **

Synced 7.91417 , 80.77148

Choose a path: 1st

8.39

8.489372369320861,
80.51102993997044

Figure 8. Fault location output – UG Cable Fault Locator Android App

During the testing process, the device was able to successfully detect and locate faults in underground cables. The capacitance and resistance measurements were found to be accurate and reliable. The device was able to distinguish between open circuit and short circuit faults and provided the appropriate readings for each. Overall, the device met the project requirements and demonstrated its potential for use in the field of cable fault detection and location.

4. Discussions and Conclusions

In conclusion, the developed prototype has shown promising results in detecting the location of faults in underground cable lines. The system's hardware and software were tested and validated using simulation software and actual testing probes to simulate different fault conditions. The system was able to accurately identify the type of fault (open circuit or short circuit) and calculate the location of the fault from the base point. The system is also IoT enabled, allowing data to be uploaded to a cloud database for future analysis and management. The system has the potential to revolutionize the way faults are identified and repaired in the future, offering faster repair times, improved system performance, and reduced operating expenses. The system's low-cost solution makes it an attractive option for both underground and overhead cable systems, and its implementation can lead to increased efficiency and safety in electrical systems.

In future development, the proposed system can be extended to identify earth faults in underground cable lines. An earth fault is a common type of fault that occurs when the insulation of the cable is damaged, causing a short circuit to the earth. The proposed system can be enhanced by adding a feature to detect earth faults by measuring the leakage current to the earth. This feature can be implemented by adding an earth leakage sensor to the system. By identifying earth faults, the system can provide more accurate and comprehensive fault detection capabilities, allowing for faster repairs and improved system performance. Additionally, the system can be further improved by incorporating artificial intelligence and machine learning algorithms to enhance the accuracy and reliability of fault detection. With the integration of these advanced technologies, the system can provide real-time monitoring and predictive maintenance capabilities, reducing downtime and improving overall system efficiency.

The design and development of the prototype device for detecting and locating underground cable faults involved several technical and scientific factors, such as the selection of appropriate hardware components and software programs, as well as the consideration of power supply and voltage regulation. The use of the ATmega 328p AVR as the microcontroller was suitable for this project, given its ability to handle the three analog inputs and 15 digital input outputs required for the device. In terms of software, programs such as Proteus, Arduino IDE, and MIT App Inventor were used for designing and testing the device, demonstrating the importance of software in the development process.

The basic principle behind the system is Ohm’s law, could measure the Capacitance and resistance of the cable, detect faults, and calculate the location of the fault from the base point and the measured values manually entered and could be viewed using an android application. The benefits of quickly locating faults include faster repair times, improved system performance, and reduced operating expenses.

Overall, the successful testing and validation of the device's ability to detect and locate cable faults highlights the potential for similar devices to be used in the industry for efficient and accurate fault detection.

5. Reference

CDFI Publications (no date) NEETRAC. Available at: https://www.neetrac.gatech.edu/cdfi-publications.html (Accessed: April 17, 2023). [1]

Farade, Rizwan A., et al. “Design and Implementation of GSM Based Underground Fault Detector.” 2022 Third International Conference on Intelligent Computing Instrumentation and Control Technologies (ICICICT), 11 Aug. 2022, 10.1109/icicict54557.2022.9917993. Accessed 13 Jan. 2023.

K. S. Md. Khairuddin , A. Subbarayudu , G. Lokesh , N. Pramod, R. V. Manoj, Dr. A. Venkateswara Reddy, 2022, Underground Cable Fault Detection using IOT, INTERNATIONAL JOURNAL OF ENGINEERING RESEARCH & TECHNOLOGY (IJERT) Volume 11, Issue 06 (June 2022), Kavitha, K, et al. “IOT BASED UNDERGROUND FAULT DETECTOR.” Journal of Complementary Medicine Research, vol. 11, no. 1, 2020, p. 265, www.ejmanager.com / mnstemps /55/55-1595160368.pdf?t=1659286709, 10.5455/jcmr.2020.11.01.29. Accessed 1 Aug. 2022.

N. Sampathraja et al. (2017) IOT BASED UNDERGROUND CABLE FAULT DETECTOR, http://iaeme.com/Home/issue/IJMET?Volume=8& Issue=8. International Journal of Mechanical Engineering and Technology (IJMET).

R. A. Farade, F. M. Umair, K. M. Faisal, S. Ibrahim, P. Zaid and M. E. M. Soudagar, "Design and Implementation of GSM Based Underground Fault Detector," 2022 Third International Conference on Intelligent Computing Instrumentation and Control Technologies (ICICICT), Kannur, India, 2022, pp. 377-380, doi: 10.1109/ICICICT54557.2022.9917993.

IoT-Based LPG Leakage Alert System

Balenthira Thanusanth[1]

[1] *Department of Information communication Technology, Faculty of Technology, Sri Lanka – German Training Institute, Kilinochchi, Sri Lanka.*

* thanusanthbala@gmail.com

Abstract

Liquefied Petroleum Gas (LPG) is a popular fuel choice in many households due to its affordability and efficiency, but its flammable nature presents significant safety hazards. This paper discusses the development of a low-cost wireless sensor network using the MQ6 gas sensor and Arduino Nano to detect LPG leaks and alert users. The system is composed of a detection and transmission module and a receiving module. The MQ6 sensor, with its high sensitivity and detection range of 100-10,000 ppm, monitors LPG concentrations and triggers an audiovisual alarm upon detecting a leak. The system then transmits a wireless signal to the receiving module, which promptly notifies the user via a mobile alert, ensuring timely responses to potential hazards. This real-time alert system helps prevent accidents caused by unnoticed gas leaks, such as those from faulty tubing or regulator issues. The system is powered by a rechargeable lithium battery, making it both mobile and reliable. With an Arduino Nano at its core, the entire setup is affordable, costing under 10,000 Rs. Real-world testing demonstrated 100% accuracy in detecting LPG leaks. This system offers an efficient and practical solution for enhancing household safety by providing proactive alerts to mitigate the dangers associated with LPG use

Keywords: *LPG leakage, wireless sensor network, gas sensor, audiovisual alarm, safety notification, real-time alert*

1. Introduction

The abbreviation of LPG is liquefied petroleum gas, the prime fuel used in kitchens to cook food. It has a lot of facilities than other sources of fuel for the kitchen. The only caveat is that we need to handle it with care. The mishandling can lead to life-threatening accidents. Worldwide, so much research is carried out to prevent the accident from LPG leakage. The problem is that we often forget to consider the practical scenario, so the project or product fails to comply in a natural environment. There many ways to identify LPG leakage in manually such as” soapy water test”. But people do not prefer the doing same thing again and again. Human Error: LPG has an added odorant to facilitate leak detection, but human olfactory senses can be unreliable, especially in low concentration leaks.Lack of Continuous Monitoring: Most traditional systems are passive, relying on individuals to recognize the smell of LPG or check sensor readings intermittently.

Limited Sensitivity: Older systems often lack the sensitivity to detect leaks at lower levels, allowing minor leaks to go unnoticed until they escalate. Widely used in households for cooking and heating purposes, presents a risk of leakage due to its highly flammable nature. Mexico City Gas Explosion (2015): An LPG truck explosion in a maternity hospital caused over 20 deaths and injured more than 70 people. Investigations later revealed a slow leak that could have been detected earlier with proper monitoring systems. Istanbul LPG Leak (2020): An explosion caused by a gas leak in a residential building led to 2 fatalities and multiple injuries. Again, insufficient leakage detection measures played a role in the delayed response.

Focusing on that the device is intended for use in household and industry or plants that depend on LPG and natural gas in their operations safety. This system is mainly used for the detection of LPG gas. If gas leakage happens when no one identified at the certain place, the system detects the LPG gas alerts the peoples by buzzing and sending SMS on users' mobile phone using Arduino Nano GSM shield compatible to the Arduino Nano board. It is portable and can fix in small space enough. The main advantage is the gas sensor can work with the battery. Battery operated device is designed to operate up to six months with two AA-size alkaline batteries. Thereby people can buy the system at a lower cost.

1.1 Literature Review

There are some scientific studies going on which had just recently quite a big break through. If you have a closer look at the already proposed system for prevent the LPG leakage. A research is deal with the detection, monitoring and control system of LPG leakage. Using relay DC motor the stove knob is automatically controlled. Along with safety measures the system has additional advantage of automatic rebooking of cylinder when the level of gas goes below the normal weight of cylinder (Soundarya *et al.,* 2014*).*A system design consists of two main module, which are the detection and transmission module, and the receiving module. The detection and transmission module detects the changes of gas concentration using a special sensing circuit (Premalatha *et al*., 2018).If the sensor detects a change in gas concentration, it activates and audio visual alarm and sends a signal to the receiver module which acts as a mobile alarm devices to allow the mobility within the house premises (Luay *et al*., 2018*)*. The development of wireless sensor network for LPG gas leakage detection. The sensor node will detect a minute concentration of the gas according to the voltage output of a sensor and also collects the gas leakage data thereby locating the specific area of the sensor node. XBee sends the data from gas sensor to the monitoring system that is displayed on LabVIEW GUI. The system could be installed at any remote place and could be controlled by any mobile phone supporting the SMS service (Mujawar *et al*., 2014). A system which they used in a highly sensitive gas sensor with a portable C-16 gas detector which can detect more than 30 different gases or vapours. Also system includes GSM SIM 900 module which can send message so as to take useful cautions. Noteworthy part of this system is that it not only alerts or warns people but the accommodating factor is to provide a runtime safety by evacuating the leaked particles of combustible gas present in air on immediate basis, in case a custodian is not at home to take care of handicapped and disabled one's (Sunil *et al*., 2016*)*.

2. Methodology & Experiment Design

Gas sensor was selected from market based on the need of sensitivity and accuracy range of our system. A GSM sensor was also used to send an alert SMS to the operator in case of micro controller receiving positive signals from Gas sensor. A Buzzer system was used to create an alarming signal to alert all workers and people inside the premises. Arduino Nano mega was selected as the Control platform for the project. The Arduino Nano board was tested first for the success of its functionality. Then the Gas sensor was interfaced with Arduino Nano system as an input. The GSM sensor module and the Buzzer was connected as the output of the system. Arduino Nano board was programmed such that the positive signals from Gas sensor triggers GSM module and Buzzer system to produce SMS signals and sound signals respectively. The system was then checked for its errors and the errors were corrected.

Here, I used the wood material for the body so no any chances to electrical passes and electrical accidents and also the system is light weight because of wood material.

Figure1. Final system

Figure 2. Check the suitable place

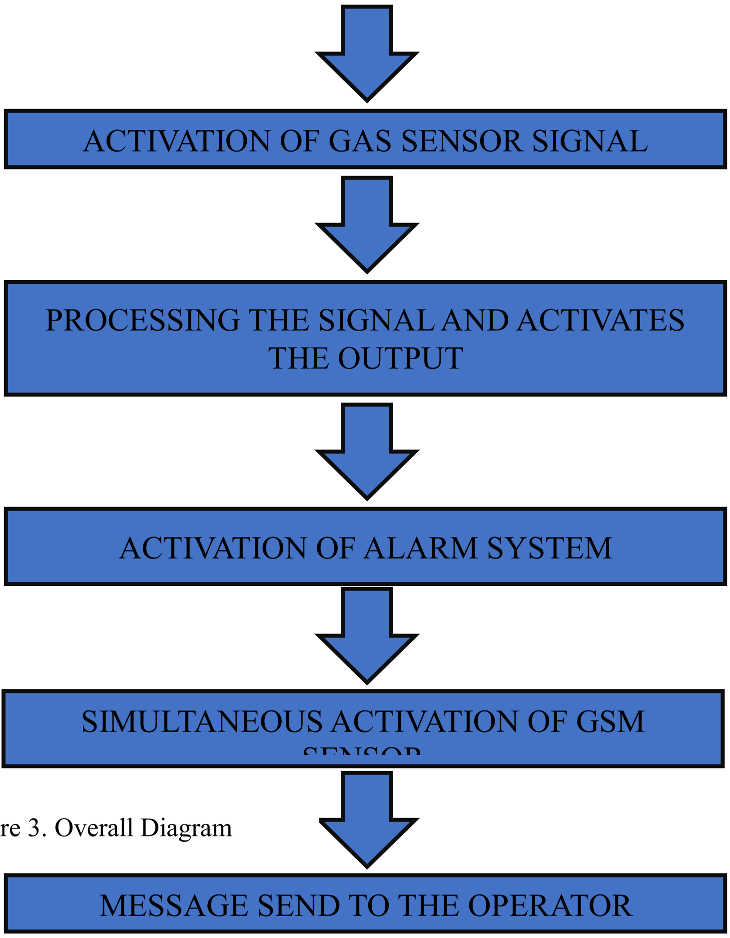

Figure 3. Overall Diagram

3. Results

Traditional systems often have a higher false alarm rate, as they can be sensitive to other gases or environmental factors like humidity and temperature. This leads to unnecessary alerts, which can cause users to become desensitized to alarms. The new system could be designed to have **greater specificity**, reducing false alarms by using advanced sensors or filtering out noise from non-LPG gases. Additionally, **temperature- and humidity-compensating sensors** ensure that the system remains accurate even in varying environmental conditions. The Alert message is received with in one minute. Message is appear as what written for alert message in code. Result is given by figure 2. The proposed system was tested by small amount of LPG into a bottle of 1Litters filled with air. The sensor was configured to detect small amounts of gases and the alarm was activated. As per expect, the alert message was received within predefined meters of area.We can ensure from the figure 04 that the performance is high accuracy when the system is within 40cm to 60cm. figure 05 is the proof to get the alert from mobile.

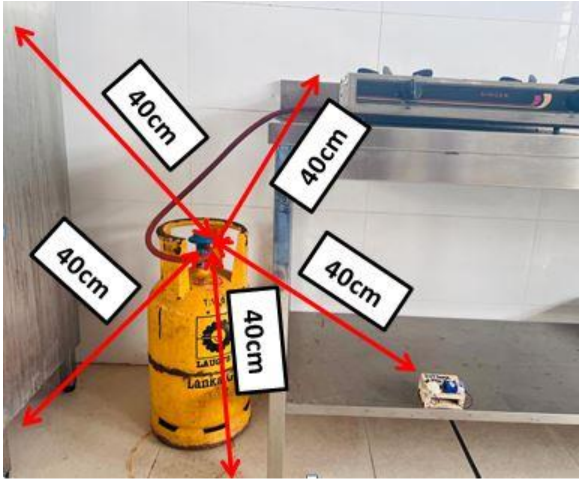

Figure 4. Suitable Position

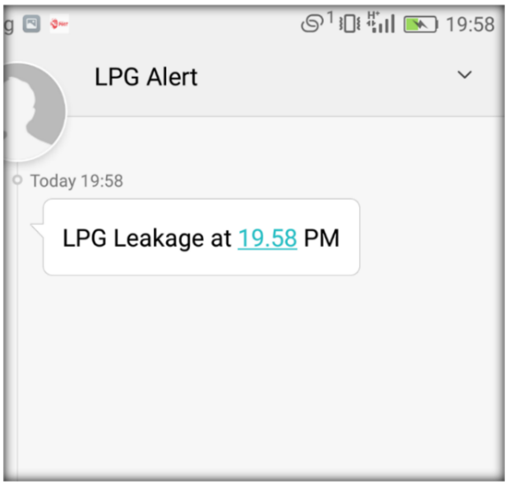

LPG Alert

Today 19:58

LPG Leakage at 19.58 PM

Figure 5. Final Mobile output

4. Discussion, Conclusion & future works

4.1 Discussion & Conclusion

This system has more advantageous function than the existing system. This wireless gas leakage system can be used mainly in household safety and many other applications in the industry and environment. This can be used in factories where gas cylinders are stored. The sensor used in the system may be affected by the surrounding temperature and humidity, it will cause major issues the whole system, and therefore, calibrating the system at the start-up of operation was done to determine the zero set point. The sensitivity of the entire system can be adjusted by changing the load resistor of the sensor which provides the flexibility to externally calibrate the system to avoid any false alarms. Human safety is the most critical concern when dealing with LPG leaks. Inhalation of LPG in enclosed spaces can lead to asphyxiation as the gas displaces oxygen in the air, potentially causing unconsciousness or death. A reliable LPG leakage alert system provides early warnings, allowing occupants to evacuate the premises before the gas concentration becomes life-threatening. In addition to posing a threat to lives, LPG leaks can cause significant damage to **property**. Fires and explosions resulting from gas leaks can destroy homes, commercial establishments, and industrial sites. By alerting users to a leak in real-time, these systems can prevent costly destruction and help protect valuable assets. In industrial environments, where LPG is often used in bulk, the risks are even higher. A leakage in an industrial setting can result in large-scale explosions, endangering workers and causing significant business disruption. Having a comprehensive LPG alert system helps ensure industrial safety by monitoring gas concentrations continuously and alerting workers or safety personnel before a disaster occurs. However, it is important to note that the testing was conducted under **specific laboratory conditions** and with a **limited sample size**. The controlled environment may not fully capture the complexities and variability of **real-world conditions**, such as diverse environmental factors, varying gas compositions, and potential external interferences. To fully validate the system's performance and reliability, **further testing** in **real-world environments** across different settings (e.g., industrial, commercial, and residential) with a **larger sample size** is necessary. This would help ensure that the system performs effectively in practical applications and under varied conditions.

4.2 Future Works

The current system has enough to detect and alert the user via message. Further in the future, this is should be changed as controlling gas leakage by itself. And the system's timeframe can be configured by users via mobile. Further, the system should be consistent with practical application in the large scale petrochemical industry. This will improve the system efficiency and effectiveness.

5. References

Luay Fraiwan, Khaldon Lweesy, Aya Bani-Salma, Nour Mani (March-2018). A Wireless Home Safety Gas Leakage Detection System. Jordan University of Science & Technology Department Biomedical Engineering.

R. Premalatha, B.Aswini, R.Haritha, A.Ajitha (Mar. 2018). A WIRELESS HOME SAFETY GAS LEAKAGE DETECTION SYSTEM USING GSM TECHNOLOGY. International Research Journal of Engineering and Technology (IRJET). Vol. 05

Sunil Pervaiz, Ali Waqar (Apr-Jun 2016). GSM Based Gas Leakage Detection & Prevention System for Disabled and Handicapped. International Journal of System Modelling and Simulation Vol. 1

T.H.Mujawar, V.D.Bachuwar, M.S. Kasbe, A.D. Shaligram and L.P. Deshmukh (April.2015). Development of wireless sensor network system for LPG gas leakage detection system. International Journal of Scientific & Engineering Research. Vol. 6

T.Soundarya, J.V. Anchitaalagammai, G. Deepa Priya, S.S. Karthick kumar (Feb. 2014). C-Leakage: Cylinder LPG Gas Leakage Detection for Home Safety. IOSR Journal of Electronics and Communication Engineering (IOSR-JECE).Vol. 9

Evaluate the effect of edible coating and packaging to improve the shelf-life of sugarcane jaggery

Sureshkumar Sudharshan[1], S.M.T. Aloka Maralanda [2*], L. Panoshan Sinthuja[1], Shanmuganeson Mirunadharani[1]
[1] *Department of Biosystems Technology, Faculty of Technology, University of Jaffna, Kilinochchi, Sri Lanka.*
[2] *Process Technology Division, Sugarcane Research Institute, Udawalawa, Sri Lanka.*

* alokamaralanda@gmail.com

Abstract

Jaggery is a natural, traditional sweetener made by concentrating sugarcane juice. Jaggery can become hygroscopic due to incorrect packaging, which reduces its quality and shelf life. The present study was conducted to increase the quality and shelf life of jaggery by *Aloe vera* gel and sago starch as edible coating along with low-density polyethylene (LDPE) and vacuum packages. The parameters such as reducing sugar, moisture content, viable cell count, total soluble solids, pol value, purity, pH, ash and sensory quality were analyzed at the two-week interval from the initial to 8th weeks and responses were analyzed statistically to determine the quality of the coated jaggery with uncoated non-packed sugarcane jaggery. The results were the reducing sugar, moisture content, viable cell count, purity, pH, and ash were successfully controlled in the sugarcane jaggery coated with *Aloe vera* gel and sago before the storage to enhance the shelf-life and maintain the quality, While low-density polyethylene (LDPE) and vacuum package method also had significant results in moisture, pH and Brix value over the non-packed sugarcane jaggery without alter the sensory characteristics.

Keywords: *Aloe vera*, Edible coating, Jaggery, Sago, Sugarcane

1. Introduction

The growing consumer demand for confectionery with improved shelf life and strong sensory appeal necessitates research to provide an innovative method for preserving food's original characteristics while maintaining safety standards. When it comes to better protecting the product from processing to customer tables, packaging is a crucial strategy and instrument. Since synthetic materials cannot degrade organically, the majority of today's packaging contributes to environmental pollution. This issue with synthetic packaging has led to the development of edible coating and packaging. Because they are created from natural materials or agricultural waste products and have naturally degradable qualities, edible coatings are regarded as non-polluting (Maftoon Azad, 2007).

Sugarcane jaggery quality was significantly influenced by atmospheric conditions. During the wet season, jaggery melts down due to increased humidity because jaggery contains hygroscopic properties, resulting in loss of composition and texture. Moisture absorption also creates an ideal environment for developing various bacteria and fungi contamination. It is challenging to preserve jaggery for a longer period. Applying a semi-permeable protective layer and barrier to gas and water vapor serves as an edible coating that can prolong jaggery shelf life and preserve its quality while it is being stored.

Additionally, *Aloe vera* gel is naturally occurring antimicrobial properties due to the presence of emodin and aloin provide good protection against moisture and gas. Sago starch is an excellent barrier to gases, and can stop the migration of moisture from the atmosphere to jaggery. It also stops the enzymatic oxidation of the jaggery. As a result, the edible covering made of *Aloe vera* and sago starch can prolong the jaggery shelf life and preserve its quality while it is being stored.

2. Materials and Methods

2.1.Materials

Matured sugarcane from SL 96 128 varieties
Matured *Aloe vera* leaves
Sago Starch

2.2.Methods

The filtered sugarcane juice had been boiled to the endpoint at 118ºc (75ºbrix). Scum on the surface of the juice had been removed and concentrated to 118ºc (75ºbrix), it was taken from the fire and filled into the mold and cooled until it had been set. Finally, jaggery had been stored in a dry and cool place.

First the impurities from *Aloe vera* were removed by washing. Then the outer skin of the *Aloe vera* leaves was peeled out. The *Aloe vera* gel was washed with slightly warm water. Next, the gel was crushed and filtered. Then, the gel was heated at 80ºc for 5min and cooled to room temperature. After cooling, the jaggery was dipped in the gel for 5-10 seconds and kept in the tray at room temperature to dry out the gel coating and stored in a cooled and dry place of low-density polyethylene (LDPE), vacuum packages and without a package.

First, the 200g sago was taken with 1000ml drinking water and heated at 80ºc to dissolve well in the water. After that all the sago was dissolved, and the sago solution was allowed to cool to 40ºc. The jaggery was dipped in a sago solution for 2-3 seconds and kept in a tray at room temperature to dry out the coating. The coated jaggery was stored in a cooled and dry place with low-density polyethylene (LDPE) and vacuum packages without a package. The proximate analysis was carried out in two weeks of intervals and the results were statistically analyzed through Analyze of Variance (ANOVA) method using Minitab.

3. Results and Discussion

Table 1. Proximate analysis results of the sugarcane jaggery test samples after 8th week of storage.

Sample	Reducing Sugar (%)	Moisture (%)	Brix (%)	Pol Value	Purity (%)	pH	Ash (%)
Uncoated non pack	8.23	9.81	69.6	17.32	74.65	5.325	1.5
Uncoated LDPE pack	9.91	9.76	70.8	17.21	72.92	5.326	1.45
Uncoated vacuum pack	7.04	9.61	71.1	17.29	72.95	5.332	1.53
Aloe vera coated non pack	5.99	9.43	70.2	18.53	79.18	5.398	1.72
Aloe vera coated LDPE pack	5.72	8.32	71.7	18.86	78.91	5.412	1.8
Aloe vera coated vacuum pack	5.31	8.63	71.1	18.53	78.18	5.425	1.86
Sago coated non pack	6.64	8.78	72.0	18.71	77.95	5.428	1.98

Sago coated LDPE pack	5.59	8.32	71.7	18.47	77.28	5.409	2.09
Sago coated vacuum pack	6.2	8.17	73.8	19.03	77.35	5.427	2.12

Sucrose in the jaggery was converted into invert sugars during the storage period by yeast, bacteria and fungi. The results of the samples were significantly different ($p<0.05$). Compared to the coated samples, uncoated samples had higher mean values. The maximum reducing sugar value was observed to be 9.91% for the uncoated LDPE packed sugarcane jaggery from the initial of 5.79% preceded by uncoated non-packed Sugarcane jaggery had 8.23% from the initial of 5.79%, and uncoated vacuum-packed sugarcane jaggery had 7.04% from the initial of 5.79%. In coated samples after the 8th week, *Aloe vera* coated vacuum packed sugarcane jaggery was shown the lowest values of 5.31% from the initial of 5.86% preceded by sago coated LDPE packed had 5.59% from the initial of 6.10%, and *Aloe vera* coated LDPE packed had 5.72% from initial of 5.86%. These three samples had lower reducing sugar % compared to the initial, this could be due to the increased moisture content of these samples in the 8th week. Coated sugarcane jaggery had higher mean values compared to the uncoated. Also, non-packed Jaggery had higher reducing sugar value than LDPE and vacuum packed Jaggery.

After the storage of 8th week maximum moisture content was observed to be 9.81% for the uncoated non-packed Sugarcane jaggery preceded by 9.76% for the uncoated LDPE packed Sugarcane jaggery, and 9.61% for the uncoated vacuum-packed sugarcane jaggery from the initial of 8.15% and minimum moisture content was observed to be 8.17% sago coated vacuum packed sugarcane jaggery, 8.32% for the sago coated LDPE packed sugarcane jaggery from the initial of 7.66%, and 8.32% for the *Aloe vera* coated LDPE packed sugarcane jaggery from the initial of 8.36%.

Also, *Aloe vera*-coated non-packed and sago-coated non-packed sugarcane jaggery had increased moisture content that of 9.43% from the initial of 8.36% and 8.78% from the initial of 7.66%, respectively. Between the storage of the 4th and 6th week, *Aloe vera* coated Sugarcane jaggery had significantly decreased moisture content in both LDPE and vacuum packaged (from 8.54% to 8.17% and from 8.88% to 8.59%, respectively) and again increased after the 6th week of storage. In sago coated sugarcane jaggery, LDPE packed had significantly decreased moisture content after the 4th week (from 8.61% to 8.32%) and also, vacuum packed had significantly decreased moisture content after the 6th week (from 8.27% to 8.17%). The decreased moisture content in the coated samples could be due to the surface dryness of the coated material on the jaggery. Overall compared to the coated Jaggery, Uncoated Jaggery had continuously increased moisture content and also had higher moisture content values. Also, LDPE and Vacuum-packed sugarcane jaggery had lower moisture content value than non-packed sugarcane jaggery.

The coating materials of *Aloe vera* gel and sago and also low-density polyethylene (LDPE) and vacuum package had successfully controlled the bacterial attack compared to uncoated sugarcane jaggery due to the natural anti-microbial activity of *Aloe vera* gel. Also, the maximum yeast and mold count after the 8th week was observed to be $7.90*10^{13}$ for the sago-coated non-packed sugarcane jaggery. Also, the minimum yeast and mold count after the 8th week was observed to be $9.00*10^{9}$ *Aloe vera* coated low-density polyethylene (LDPE) packed sugarcane jaggery.

The decreased brix value indicated the loss of Jaggery quality, this could be due to the moisture absorption and fermentation of sugars by bacteria, yeast and Mold. The maximum value after the storage condition was observed to be 73.8% for the Sago coated vacuum packed sugarcane jaggery preceded by 72.0% for the sago coated non-packed, and 71.7% for the Sago coated LDPE packed Sugarcane jaggery from the initial of 67.8% and minimum value observed to be 69.6% for the uncoated non-packed sugarcane Jaggery preceded from the initial of 69.6% by 70.2% for the *Aloe vera* coated non-packed Jaggery from the initial of 68.7%, and 70.8% for the uncoated LDPE packed sugarcane jaggery from the initial of 69.6%. These values indicate the vacuum-packed sugarcane jaggery had higher brix values compared to non-packed and LDPE packed. Also, the coating material had successfully controlled brix values compared to the Uncoated Sugarcane jaggery.

Pol value gives the sucrose content in sugarcane jaggery. The decreased pol value indicated a loss of quality of sugarcane jaggery, this could be due to the conversion of sucrose into inverted sugars by bacteria, yeast and fungi at the same time reducing sugar was increased. The maximum value after the 8th week of storage was observed to be 19.03% for the sago coated vacuum packed sugarcane jaggery from the initial of 16.68% preceded by 18.86% for the *Aloe vera* coated LDPE packed sugarcane jaggery from the initial of 16.53%, and 18.71% for the sago coated non-packed sugarcane jaggery from the initial of 16.68% and minimum value observed to be 17.21% for the Uncoated LDPE packed sugarcane jaggery, preceded by 17.29% for vacuum packed, and 17.32% for the non-packed sago coated sugarcane jaggery from the initial of 17.42%. The results showed that the package method had no significant difference in pol value. However coated sugarcane jaggery had a significant difference compared to uncoated.

Purity indicates the sucrose purity in the jaggery, decreased purity due to the conversion of sucrose into inverted sugar by bacteria, yeast and fungi that led to the loss of quality of sugarcane jaggery. The maximum value after the 8th week of storage was observed to be 79.81% for the *Aloe vera* coated non-packed sugarcane jaggery preceded by 78.91% for the *Aloe vera* coated LDPE packed sugarcane jaggery, and 78.18% for the *Aloe vera* coated non-packed sugarcane jaggery from the initial of 72.18% and the minimum value observed to be 72.92% for the uncoated LDPE packed sugarcane jaggery preceded by 72.95% for the uncoated vacuum packed sugarcane jaggery, and 74.65% for the uncoated non-packed sugarcane jaggery from the initial of 75.08%. In overall, coated sugarcane jaggery had higher value compared to uncoated sugarcane jaggery, mainly *Aloe vera*-coated sugarcane jaggery. However the package system much not have an impact on purity values.

pH gives the acidity of sugarcane jaggery during the storage period, it also indicates the indicates the microbial activity during the storage period that decreases the pH of samples. The uncoated sugarcane jaggery had continuous decreased pH from the initial compared to coated sugarcane jaggery. The maximum pH was value observed to be 5.428 for the sago non-packed sugarcane jaggery from the initial of 5.382, the minimum value was observed to be 5.325 for the uncoated non-packed sugarcane jaggery from the initial of 5.583.In coated sugarcane jaggery, pH continuously increased from the initial to 6th week storage period, after 6th week of storage pH had decreased values but it remained higher than initial values, that could be due to the coating material loss its capacity to maintain pH. But compared to the sago-coated sugarcane jaggery, *Aloe vera* coated sugarcane jaggery had a low pH value that could be due to the *Aloe vera* gel naturally having low pH value. Also, the package system much not had an impact on pH values.

Ash values indicate the mineral content of the jaggery. After the 8th week of storage compared to uncoated sugarcane jaggery, the coated Sugarcane jaggery had higher ash values, because sago and *Aloe vera* gel naturally had mineral content that also added to the total mineral content of the Sugarcane jaggery. Also, LDPE and vacuum package systems had no significant difference in Ash value from the initial to 8th week of storage.

4. Conclusion

Compared to uncoated sugarcane jaggery, coated sugarcane jaggery had lower moisture content, reducing sugar content, delaying bacteria, yeast, and mold growth, and successfully regulated brix and pH values. Also, edible-coated sugarcane jaggery had higher sugar purity. While low-density polyethylene (LDPE) and vacuum packaging showed no effect on pol, purity, pH, and ash, but had a considerable influence on sugar, moisture content, total soluble solids, and microbial growth. On the other hand, the retention of ash content during storage indicates the use of edible coatings (*Aloe vera* gel and sago) preserves mineral content in sugarcane jaggery, hence increasing the nutritional value of jaggery. Shelf-life and quality of sugarcane jaggery were increased, where jaggery was coated with the edible coatings of *Aloe vera* gel and sago. Additionally, the low-density polyethylene (LDPE) and vacuum used for the storage influenced the extension of sugarcane jaggery shelf life. These results show that *Aloe vera* and sago-based edible coatings were promising alternatives for post-harvest handling of fresh sugarcane jaggery, maintaining their quality and extend the shelf life of sugarcane jaggery.

5. References

Armghan Khalid, M., Niaz, B., Saeed, F., Afzaal, M., Islam, F., Hussain, M., Mahwish, Muhammad Salman Khalid, H., Siddeeg, A., & Al-Farga, A. (2022). Edible coatings for enhancing safety and quality attributes of fresh produce: A comprehensive review. *International Journal of Food Properties*, *25*(1), pp. 1817–1847. https://doi.org/10.1080/10942912.2022.2107005

Hirpara, P., Thakare, N., Kele, V., & Patel, D. (2020). Jaggery: A natural sweetener. *Journal of Pharmacognosy and Phytochemistry*, *9*, pp. 3145–3148.

Kumar, A., & Singh, S. (2020). The benefit of Indian jaggery over sugar on human health. In *Dietary Sugar, Salt and Fat in Human Health*, pp. 347–359. Elsevier. https://doi.org/10.1016/b978-0-12-816918-6.00016-0

Madhu, B., Patel, S., Jagannadha Rao, P. V. K., & Sreedevi, P. (2018). Use of Edible Coatings to Increase the Shelf Life of Jaggery: A Review. *International Journal of Current Microbiology and Applied Sciences*, *7*(06), pp. 2466–2479. https://doi.org/10.20546/ijcmas.2018.706.293

Maftoon Azad, N. (2007). *Evaluation of edible films and coatings for extending the postharvest shelf life of avocado.* Library and Archives Canada = Bibliothèque et Archives Canada.

Incorporation of sesame flour as a substitute for chicken fat in the manufacturing of chicken sausages

Madushika. E.A.H[1]., Gunaratne. A[1], Rajapaksha K.K.B.S[1], and Senanayake, M.P.[2]

[1] The Department of Livestock Production, Faculty of Agricultural Sciences, Sabaragamuwa University of Sri Lanka.
[2] Quality Assurance Manager, LG Farm (Pvt) Ltd, CP Pura, Minneriya.

** bawanthi.rajapaksha96@gmail.com*

Abstract

Chicken skin is widely used as a source of fat for chicken sausages but a high concentration of saturated fat in chicken skin generates a health risk. Studies reveal that sesame seed flour with polyunsaturated fat is a perfect fat alternative for meat products. Four types of chicken sausages were prepared substituting chicken fat by 0% (control), 5% (T1), 10% (T2) and 15% (T3) with sesame flour. The treatments were tested for proximate composition, total phenolic content, water holding capacity (WHC), cooking loss, emulsion stability and sensory properties. With the incorporation of sesame flour, protein (18–24%), fat (25–30%) and ash content (2-3%) were increased. The WHC and cooking loss were in the range of 6.9-8.9% and 25-16% respectively. The addition of sesame flour significantly($p<0.05$) increased WHC while decreasing the cooking loss. The emulsion stability was significantly improved with the addition of sesame flour. The total phenolic content increased with increase of sesame flour content and in T3, total phenolic content was increased by two-fold. Sensory analysis revealed that incorporation of sesame flour had no significant ($p>0.05$) influences on odor, flavour and overall acceptability. Compared with other treatments, there was a significant difference ($p<0.05$) in color and juiciness of T3. The study has led to a conclusion that the chicken sausages incorporated with sesame flour, particularly, at the level of 10% and 15% improve the total protein, fat, ash, phenolic content and physicochemical properties with consumer acceptable sensory attributes.

Keywords: Chicken sausage, Physiochemical properties, Sesame flour, Sensory properties, chicken fat

1. Introduction

Sausage is ground pork, ground beef, or other meat combined with various additional ingredients and spices and is usually stuffed into prepared intestines or other casings, often made of links. The industry is using new technology to process sausages. There are various types of sausages and cooked chicken sausages are one of them. Chicken fat (skin and loose meat), rich in fats (30%-40%) is widely used as a source of fat for chicken sausages. However, high concentrations of cholesterol and saturated fatty acids contained in animal fat (Anam et al., 2023) pose a health risk for sausage consumers and therefore, there is a growing interest in healthy substances that can be used as alternatives for animal fat. Due to its high polyunsaturated fat content, sesame flour makes a perfect potential fat alternative for processed meat products (Indumathi et al., 2020). Further, proteins and starch present in sesame seeds may also have similar roles that animal fat plays in sausage manufacturing because starch and proteins are well known potential fat replacers. Sesame seeds have 40–50% oil, 20–25% protein, 20–25% carbohydrate, and 5-6% ash by chemical composition (Indumathi et al., 2020). Additionally, bioactive substances like lignans, sesamine, sesamoline, and sesamol found in sesame seeds have been reported to have health beneficial properties. Currently there is a growing consumer demand for health beneficial food products. Though sesame has high potential to be used as a healthy fat replacer its application is still not comprehensively investigated.

Therefore, the objective of the present study is to evaluate the suitability of sesame flour as a fat replacer for chicken skin (chicken fat) in chicken sausage while evaluating nutritional quality and health beneficial properties of chicken sausage.

2. Materials and methods

2.1 Experiment design

Sesame flour incorporated chicken sausages were prepared replacing chicken fat (loose meat andchicken skin) with 5%, 10% and 15% of sesame flour appropriately (Table 1).

2.2 Preparation of sesame flour

High quality sesame seeds were purchased from local super market. Sesame seeds were dried in a roasting 100 ^{0}C for 20 minutes and dried seeds were ground to make sesame flour. Then sesame flour was packedin to polythene bags and sealed properly until used in the sausage making.

2.3 Production flow chart of sausage

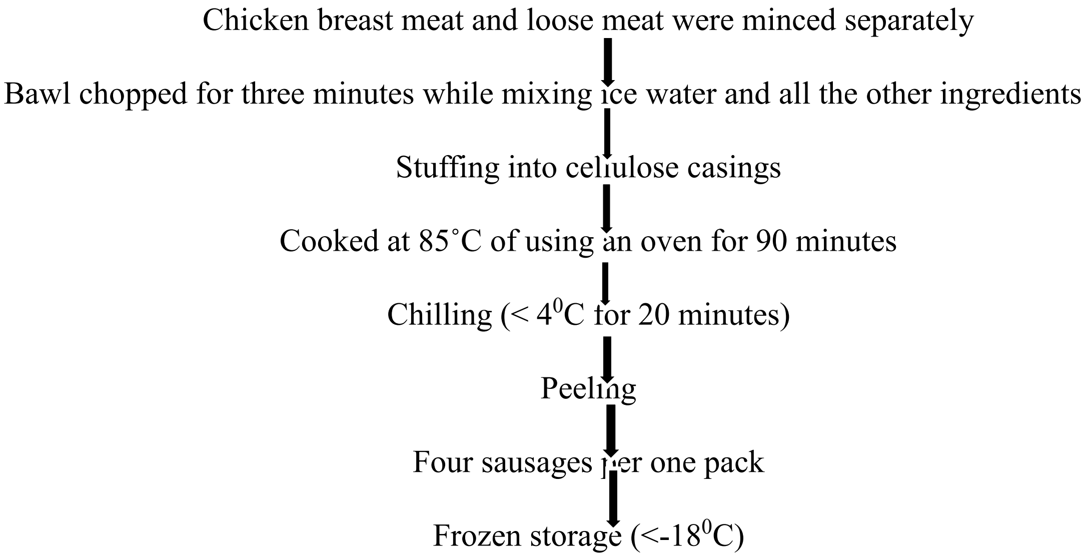

Figure 01: Flow chart of sausage production

Table 01. Formulation of ingredients for sausage

Ingredient (%)	Control	T1	T2	T3
Boneless meat	65	65	65	65
Chicken fat (skin and loose meat)	15	10	5	0
Sesame flour	0	5	10	15
Water	10	10	10	10
Spices	2	2	2	2
Table salt	2	2	2	2
Sodium phosphate	0.5	0.5	0.5	0.5
Sugar	0.3	0.3	0.3	0.3

Ascorbic acid	0.1	0.1	0.1	0.1
Rusk	5.09	5.09	5.09	5.09
Coloring	0.01	0.01	0.01	0.01

2.4 Proximate analysis

Moisture content was determined as described in AOAC (2001) using an oven dry method. Protein content was analyzed according to the procedure described in Kjeldahl method. Crude fat content of sausage samples was estimated using Soxhlet extraction method (AOAC 2001). In the estimation of ash, dried material obtained from moisture determination was ignited in a muffle furnace at 600^0C for 24 hours. (Wise Therm Korean) (AOAC 2012).

2.5 Determination of physicochemical properties

2.5.1 Water Holding Capacity

Water holding capacity was measured as described by Purohit et al. (2016).

2.5.2 Cooking loss

Cooking loss was measured as described by Tafadzwa et al. (2021)

2.5.3 Emulsion stability

Emulsion stability was measured as described by Hughes et al. (1997)

2.5.4 Total phenolic content

The Folin-Ciocalteu method was employed to determine the total phenolic content (Sharma et al.2017).

2.6 Sensory evaluation

Sensory evaluation was conducted using 30 semi-trained panelists. Four types of sausages were marked by using three digits numbers. Sensory evaluation was conducted according to five-pointhedonic scale (Wichchukit and Mahony, 2015).

2.7 Data analysis

Data analysis was done by using statistical analysis software 9.0 version. One-way ANOVA was conducted to determine the proximate composition. Sensory data was analyzed by using Friedman test. Graphically illustration was done by Microsoft Excel.

3. Results and discussion

3.1 Proximate analysis

Table 02. Proximate composition and total phenolic content of sesame flour-incorporated sausages

	C	T1	T2	T3
Protein	18.53± 0.125^a	19.91± 0.178^a	21.15 ±0.556^{ab}	24.1±2.377^b
Fat	24.61± 6.038^a	25.82 ± 5.527^a	27 ± 6.512^{ab}	30.25±6.241^b
Moisture	52.46± 0.377^a	56.2 ± 1.329^{ab}	58.16±0.979^b	60.36±0.316^c
Ash	2.47± 0.887^a	3.44 ± 0.953^b	3.61 ± 0.150^b	3.84 ±0.785^b
Total Phenolic mg (GAE)/g	7.42 ± 3.857^b	8.51 ± 3.818^b	15.06 ± 3.741^a	15.7 ± 3.608^a

Values are mean ± Standard deviation values with different superscript under the same column are significantly different ($p< 0.05$), C=control, T1 5% sesame flour, T2= 10% sesame flour t3= 15% sesame flour.

The addition of sesame flour increased protein, fat, and moisture content and this was more prominent at the level 15% addition. Sesame raw seeds have a unique nutritional composition containing 22 % protein, 41% fat, 4.3% ash/minerals and 24% nitrogen free extract such as watersoluble sugar and starch (Sibt-e- Abbas et al. 2020; Matthaus and Ozcan, 2018). Animal fat often contains more saturated fatty acids and cholesterols and it is widely accepted that the regular consumptionof these fats could pose a greater health risk. By reducing saturated fat with healthy mono and poly unsaturated fatty acids could be a good strategy in reducing the fatty diet related diseases. It has been reported that sesame oil is rich in unsaturated fatty acids (Indumathi et al., 2020).

Increased moisture content in sesame flour added samples suggests that sesame flour can enhance the moisture retention ability of sausages. The addition of sesame flours significantly increased the total phenolic content and at the 15% level addition it was increased by two - fold. It has been well documented sesame as a bioactive polyphenol (ex: lignans) rich plant source having various noticeable health benefits such as reduction in high blood pressure, anti-oxidant activities, and anticancer property and showed hypocholesterolemic effects (Elleuch et al. 2011). Indumathi et al. (2020) suggest sesame incorporated sausage as functional sausage owing to its nutraceutical and health beneficial properties.

3.2 Water holding capacity

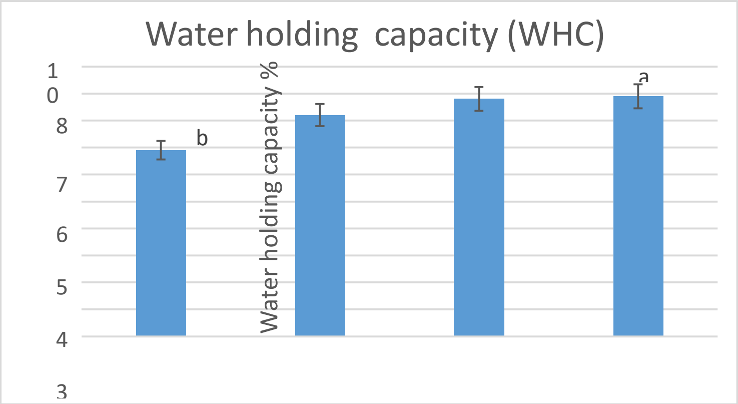

Figure 02: Water holding capacity of formulated sausages with sesame flour

Water holding capacity (WHC) was significantly increased when chicken fat was replaced with sesame flour but no significant differences were noted among sesame flour treated samples. High WHC reflects improved water binding capacity. Tafadzwa et al (2021) mentioned improved WHC could attribute to the increased protein content in beef sausage. According to proximate analysis it was observed that protein content significantly increased with the addition of sesame flour and therefore it can be speculated that improved WHC of sesame added samples could relate to the enhanced protein content. Further same authors revealed that starch-protein interaction has more impact on WHC in which the arrangement of starch granules with protein molecules provides more space to hold more water molecules. Sesame flour has both protein and starch and thus there can be a starch-protein interaction improving WHC.

It has been reported that macroscopic properties such as the water- and fat-holding capacity and the texture of gel-type emulsified meat products depend on various factors such as the nature andamount of the lean meat fraction, fat characteristics, water amount, additives, and processing conditions (Santhi et al. 2017). It is very obvious that the replacement of chicken fat by sesame flour alters the fat characteristics affecting the WHC. Furthermore, seeds of sesame flour may enhance the soluble dietary fiber content of formulated sausages. Soluble dietary fiber has been shown to improve the water retention ability in meat products.

3.4 Cooking loss

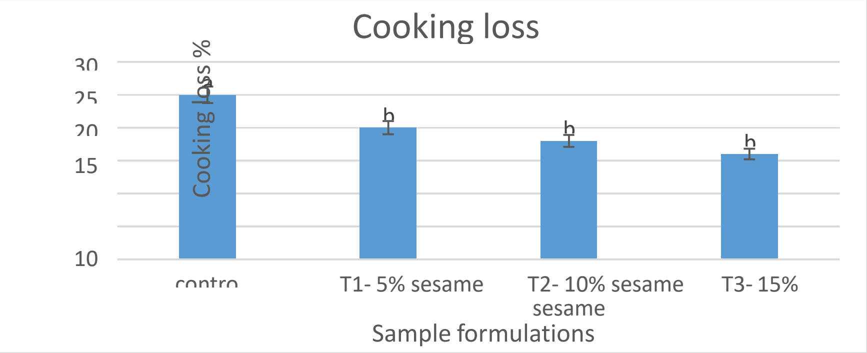

Figure 03: Cooking loss of sesame flour incorporated sausages

The cooking loss significantly reduced with the addition of sesame flour but no significant differences were noted among the all sesame flour treated samples. The reduction of cooking loss might be due to better moisture retention by ground sesame seed flour. This is in agreement with finding of Indumathi et al. (2020). It is apparent that WHC had an inverse correlation with cooking loss whereas WHC had a positive correlation with moisture content of formulated sausage samples (Anam et al., 2023).

3.6 Emulsion stability

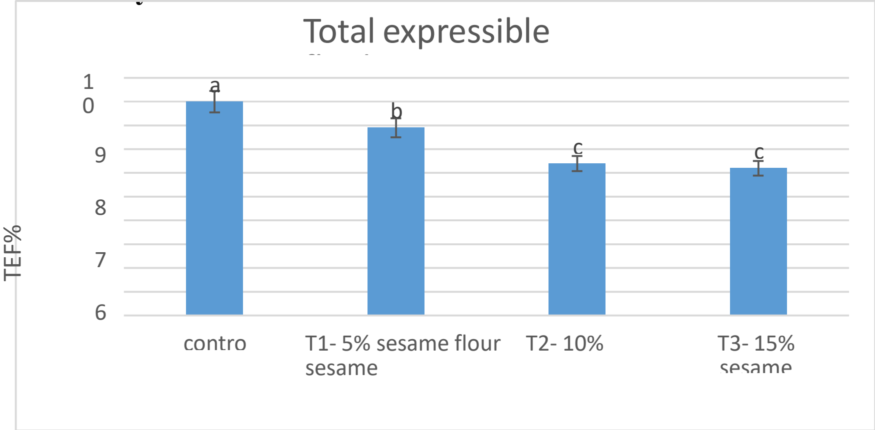

Figure 04: Emulsion stability of sesame flour incorporated sausages

The emulsion stability significantly improved with the addition of sesame flour where 10 and 15% sesame flour substitution showed the highest improvement (Fig 3). Moisture retention and better emulsifying property of sesame flour may be the reason for this improvement (Indumathi et al.2020). Zhuang, et al (2016) also reported the similar results for sesame oil added meat batter. An emulsion-type sausage is a mixture of meat, fat, water, spices, and additives in which fat is dispersed more or less uniformly in a continuous, highly hydrated protein matrix. Therefore, the improved emulsion stability suggests that high integrity of highly hydrated proteinmatrix with the replacement chicken fat with sesame flour.

3.7 Sensory analysis

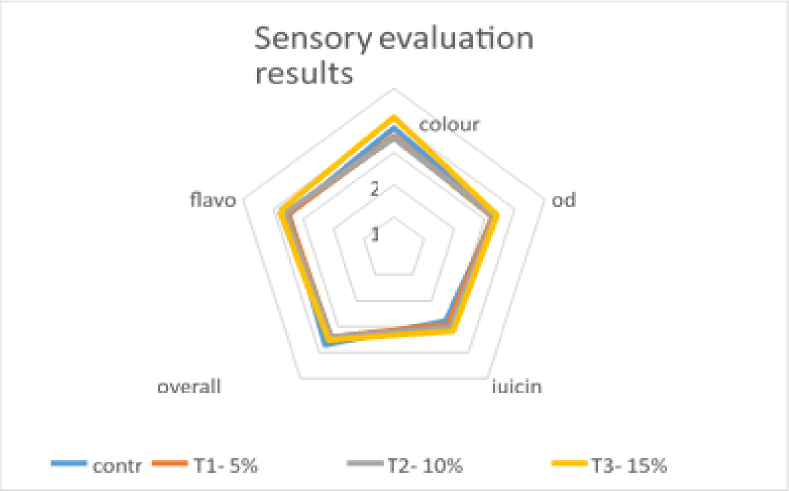

Figure 05: Sensory attributes of chicken sausage prepared by incorporating sesame flour. Data expressed as means spss 26.0 version

There was no significance difference in odor, flavour and overall acceptability of sesame seeds flour incorporated sausages and control. When compared with other treatments, there was a significance difference in color and juiciness of T3. The improved juiciness in 15 % sesame flour added sample indicates that higher water retention with in the protein matrix which is consistent with the high WHC noticed for the same sample

.

4. Conclusion

The replacement of chicken fat with sesame flour significantly increased the protein, fat and ash content. Moisture retention and better emulsion property of sesame flour could improve the WHC, emulsion stability while reducing the cooking loss. Greatly enhanced total phenolic content suggest that sesame added sausages can be considered as a functional food. This study has demonstrated that sesame seed flour (10-15%) can be incorporated by replacing chicken fat which in turn improve the physicochemical properties of chicken sausage with consumer acceptable sensory properties. Further studies are needed to investigate the quality of fat with respect to the fatty acid profile of sesame flour incorporated sausages.

5. References

Anam, M., Tuseef, M., Gull, T., Saleem, A., Jamil, A., Khan, M.Y., and Ashraf, J.Z. (2023). Addition of Sweet Potato Powder and Olive Oil as Fat Replacer in Chicken Sausages Coated with Carom Essential Oil. RADS Journal of Food Biosciences, 2: 2959-3182.

Anam, M., Tuseef, M., Gull, T., Saleem, A., Jamil, A., Khan, M.Y., and Ashraf, J.Z. (2023). Addition of Sweet Potato Powder and Olive Oil as Fat Replacer in Chicken Sausages Coated with Carom Essential Oil. RADS Journal of Food Biosciences, 2: 2959-3182.

Association of Official Analytical Chemists (AOAC). (2012). Official method of analysis,18th ed. Association of official analytical chemists, Washington.

Association of Official Analytical Chemists (AOAC). (2001). Methods of analysis of AOAC international.17 ed. Journal of AOAC international ,Gaithersburg,MD,USA.

Elleuch, M., Bedigian,D., and A. Zitoun, (2011) "Sesame (Sesamum indicum L.) seeds in food, nutrition, and health, In Nuts and Seeds in Health and Disease Prevention, W.R.Preedy,

R.R.Watson, and V.B. Patel (eds) pp. 1029–1036, Academic Press, Cambridge, MA, USA.

Hughes, E., Cofrades, S. and Troy, D.J. (1997). Effect of fat level, oat fiber, and carrageenan on frankfurters formulated with 5, 12 and 30% fat, Meat Science, 45: 273-281.

Indumathi, J., Shashikumar, M., Reddy, G.V.B., Babu, A.J., and Prakash, M.G. (2020). Influence of incorporation of ground sesame seed as fat replacer on the functionality of spent broiler chicken hen sausages, Journal of Pharmacognosy and Phytochemistry , 9(5): 676-682.

Matthaus, B., and M. M. ̈Ozcan, (2018). Fatty acid composition and tocopherol contents of some sesame seed oils," Iranian Journal of Chemistry and Chemical Engineering, 37: 151–155,

Purohit, A.S., Reed, C. and Mohan, A. (2016) Development and evaluation of quail breakfast sausage, LWT-Food Science and Technology, , 69, 447–453.

Santhi, D., Kalaikannan, A. and Sureshkumar, S., 2017. Factors influencing meat emulsion properties and product texture: A review. Critical reviews in food science and nutrition, 57(10), 2021-2027.

Sharma, H., Mendiratta, S.K., Agarwal, R.K., Kumar, S. (2017). Evaluation of anti-oxidant ant anti-microbial activity of various essential oils in fresh chiken sausages, Food science and Technology, 2: 279-292.

Sibt-e-Abbas, M., Butt, M.S., Khan, M. R. Sultan, M. T.. Saddique, M. S and. Shahid, M. (2020) "Nutritional and functional characterization of defatted oilseed protein isolates," Pakistan Journal of Agricultural Sciences, vol. 57:. 219–228

Tafadzwa MJ, Zvamaziva JT, Charles M, Amiel M, Pepukai M and Shepherd, M 2021 Proximate , physico-chemical , functional and sensory properties OF quinoa and amaranth flour as potential binders in beef sausages, Food Chemistry, 365, 130619.

Wichchukit, S. and O'Mahony, M. (2015). The 5-point hedonic scale and hedonic ranking in food science: Some reappraisals and alternatives, Journal of the Science of Food and Agriculture, 95(11). 2167–2178.

Zhuang X, Han, M, Kang, Z.L, Wang, K, Bai Y, Xu, X.L, and Zhou G.H. (2016). Effects of the sugarcane dietary fiber and pre- emulsified sesame oil on low-fat meat batter physicochemical property, texture, and microstructure. Meat Science 2016; 113:107-115

Study the effect of post-harvest quality of sugarcane juice in the jaggery production

Shanmuganeson Mirunadharani[1], S.M.T. Aloka Maralanda [2*], L. Panoshan Sinthuja[1], Sureshkumar Sudharshan[1]

[1] *Department of Biosystems Technology, Faculty of Technology, University of Jaffna, Kilinochchi, Sri Lanka.*
[2] *Process Technology Division, Sugarcane Research Institute, Udawalawa, Sri Lanka.*

* alokamaralanda@gmail.com

ABSTRACT

Jaggery production is an economically valued cottage business in Sri Lanka. Because Sri Lanka had good climatic conditions for sugarcane cultivation. The lack of knowledge among farmers and producers regarding the optimum storage duration for sugarcane has an impact on the quality of jaggery. The study was to examine the impact of post-harvest quality of sugarcane juice on the quality of jaggery through the experimental methods and create awareness among the farmers and manufacturer. For this study, SL 96 128, SL 04 010, and SL 88 116 Sugarcane varieties were chosen. The Sugarcanes were harvested at the appropriate maturity stage, and samples were taken at intervals of 1st, 3rd, 5th, and 7th days. The stems of each variety on each day were crushed to extract the juice, and the weight of crushed juice, volume of juice, and weight of bagasse were recorded. Brix value, pol, purity, pH, and POCS of crushed juice were analyzed. The crushed juice was then used for jaggery production, and samples of jaggery from each variety were analyzed for moisture, ash, reducing sugar, viable cell count, brix, pol, purity, and pH. The findings revealed that after the third day of cane harvesting, there was minimal fluctuation in pol, purity, pH of sugarcane juice, while the standard plate count, yeast mold count, and total reducing sugar level increased. Similar changes were observed in the jaggery processed from the sugarcane juice. On the seventh day, jaggery was not produced by obtained juice because of high brix value and low sucrose content of juice, which was due to the dextran formation. However, the SL 88 116 variety was possible in the jaggery production until 9th day from harvesting, this variety exhibited the highest sugar levels and mineral content compared to the other two varieties.

Keywords: Deterioration, Jaggery, Post-harvest, Sugarcane, Variety

1. Introduction

The product created by condensing to a solid or semi-solid condition is known as jaggery. Its sweet fluids of sugarcane can be used to make any number of sweet meals that are well-known worldwide. It has distinct qualities that make it people's choice over white sugar when making some sweet foods and processing juice extracted from sugarcane. It has a sweet, wine-like aroma and flavor and is a natural sweetener (Kele *et al.*, 2020).

In addition to adding nutrients to our food, jaggery preparation increases the farmers' overall revenue, improving their standard of living. The majority of farmers make jaggery using little to no financial outlay and without considering cultivars of sugarcane or scientific methods for preparing jaggery without post-harvest losses. Additionally, it is vital to safeguard farmers' earnings by raising the amount and caliber of their jaggery units (Bhatt, Kashyap and Sharma,).

Several meteorological factors frequently affect the process of sucrose accumulation in sugarcane stalks, known as ripening. Temperature, air, and water deficiencies come to mind.

When making jaggery, the sugar content of the liquid from the sugar cane is usually used to gauge the product's quality. The delay between sugarcane harvest and crushing will affect the jaggery's quality. Without taking into account these factors, jaggery is of poor quality and has poor product characteristics, including a short shelf life, unsatisfactory color, bad texture, and terrible flavor. Lower demand and manufacturer reluctance are the results of these issues. The development of the confectionery business and providing revenue for rural entrepreneurs depend on the length of time between the harvest and the crushing of sugar cane stalks for the production of high-quality jaggery. The proper information on the time interval between sugarcane harvest and crushing is obtained by this study using post-harvest analysis of sugar cane, sugar cane juice, and jaggery. Here is the recommended sugarcane storage time for obtaining high-quality jaggery. The possibilities of this study may lead to increased jaggery commerce in Sri Lanka. Aside from that, Sri Lanka is often a tourist destination with distinctive traditional cuisine and a wide range of eating customs. In particular, jaggery holds a special place in Sri Lankan cuisine, therefore maintaining its quality can assist Sri Lanka's image among tourists. Additionally, can execute the jaggery production and locate sugarcane types for quality jaggery production by studying the impact of post-harvest on the production of quality jaggery.

3. Materials and Methods

3.1 Materials

Commercial sugarcane varieties namely SL 96 128, SL 04 010 and SL 88 116.

3.2 Methods

Before being crushed, the 120kg of harvested bundles of each variety of sugarcane were weighed at intervals of 1, 3, 5, and 7 days using a hanging balance. A crusher was used to perform the crushing. Juice extraction rates from each bundle of each cultivar were calculated and recorded. The weight of each bundle of bagasse from each variety was measured using a balance and data were recorded.

At the first, third, fifth-, and seventh-day intervals, crushed cane juice from each variety was used to prepare sugarcane jaggery for each bundle of sugarcane. Juice that had been crushed was filtered using a filter, and it was heated on a boiling pan by burning bagasse and wood. During the boiling process, all contaminants that rose to the surface were scrubbed away. Since almost all of the water and thick, golden-brown color syrup is evaporated during the boiling, up to 118°C sugarcane juice's concentration process, remained in the pan. Once the juice reached a concentration of 72° brix, it was taken off the heat. After stirring the syrup for a while, it was allowed to cool down. Subsequently, the syrup was poured into an aluminum mold and left to solidify. The jaggery cubes were then carefully separated from the mold and let it cool at room temperature for a few hours before being packaged in polypropylene.

Samples of sugarcane juice from three bundles were analyzed for brix percent, pol percent, purity percent, Pure Obtainable Cane Sugar (POCS), and pH of the first, third, fifth and seventh days of each variety. Each parameter was assessed using three replicates. Brix and pol values of the sugarcane juice were measured using a refractometer and polarimeter, respectively, the pH was determined using a pH meter. The following calculation was utilized to determine the quantities of pol, purity, and POCS. The results were statistically analyzed through Analyze of Variance (ANOVA) test using Minitab.

4 Results and discussion

Table 01. Proximate analysis of sugarcane juice after 7th day of harvesting

Variety	Brix (%)	Pol	Purity (%)	POCS	pH (%)	Reducing Sugar (%)
SL 96 128	17.45	12.185	69.565	7.28	5.21	1.97
SL04 010	16.5	10.93	66.24	6.47	5.07	4.21
SL 88 116	20.6	13.49	65.5	7.53	4.68	2.13

In general, sugarcane's brix value increased throughout the post-harvest period of storage because a bacterium called *Leuconostoc mesenteroides* produced dextran. Additionally, the brix value decreased once more at the same time that *Leuconostoc mesenteroides* activity had stopped and the texture of the jaggery had changed. The maximum brix value for the variety of SL 88 116 was seen to be 22.5 percent after the 11th day of harvesting from the initial of 19.75, while the minimum value brix for the variety of SL 04 010 was found to be 16.5 after the 7th days of harvesting from the initial of 15.2.

The sucrose concentration in sugarcane juice is indicated by its pol value. In general, pol values decline over time. When pol value reduced, reducing sugar level should rise concurrently. In this study, there were some variations in the pol value caused by the rains since the water content lowers temperature, delaying bacterial activity. After the first day of harvesting, it was discovered that the greatest pol value for the SL 88 116 variety was 17.95 percent, and the minimum pol value for the SL 04 010 variety was 12.72 percent. Overall, SL 88 116 had a higher mean value than SL 96 128 and SL 04 010, in that order.

The degree of purity of sugar is indicated by purity. Because bacteria, yeast, and mold convert sucrose into invert sugar during the post-harvest period, sugarcane purity levels should be lowered. The value of the figure varied; this could be the result of the recent, intense rains, due to variations in brix. The variety of SL 88 116 was found to have a maximum purity value of 90.94 percent on the first day of harvesting, and the variety of SL 96 128 was found to have a minimum purity value of 83.56 on the same day. Overall, the mean value of SL 88 116 was higher than that of SL 04 010 and SL 96 128.

POCS is for Pure Obtainable Cane Sugar, which refers to the juice's sugar concentration. Due to the sugarcane's post-harvest storage period, POCS value gradually declined. On the first day of harvesting, the variety SL 88 116's POCS value was seen to be 13.66 percent, while on the next day, the variety SL 04 010's POCS value was noted to be 9.24 percent. Overall, SL 88 116 had a higher mean value than SL 96 128 and SL 04 010, in that order.

In general, pH decreased throughout the interval between harvest and storage. Due to bacterial activity, the pH in this investigation decreased over time from the beginning level. Three types were mildly acidic when their pH values were first measured. Bacterial activity began in this situation with the aid of time and storage temperature. in order to subject the juice to an acidic condition. Due to the acidic environment at that time, bacterial activity gradually increased; however, when the pH increased slightly, bacterial activity decreased. The most caustic situation After 11 days of harvesting from the initial of 5. 20 and minimum value acidic condition, the variety SL 88 116's pH value was found to be 4.68. After seven days of harvesting, the variety SL 96 128's pH value was found to be 5.21, down from its initial value of 5.23. SL 88 116 had a higher mean value overall, followed by SL 04 010 and SL 96 128.

In this study the total reducing sugar level of juice was gradually increased, due to the conversion of sucrose into invert sugars, this happened because of bacterial activity. The low value of total reducing sugar meant that high sucrose level that aids high pol value and purity value. When reduction of pol and purity value, can explain in other words that increasing of reducing sugar level. The minimum value of total reducing sugar was observed to be 0.33 for the variety of SL 88 116 after the 1st day of harvesting and maximum total reducing sugar value was observed to be 2.06 for the variety of SL 04 010 after the 1st day of harvesting. The maximum value of total reducing sugar was observed to be 4.78 for the variety of SL 88 116 after the 11st day of harvesting and minimum total reducing sugar value was observed to be1.97 for the variety of SL96 128 after the 7st day of harvesting. In overall, SL 88 116 had higher mean value preceded by SL 04 010 and SL 96 128.

Table 02. Proximate analysis of sugarcane jaggery after 5th day of harvesting

Variety	**Jaggery recovery juice based (%)**	**Moisture (%)**	**Pol (%)**	**Purity (%)**	**Brix (%)**	**pH**	**Reducing Sugar (%)**
SL 96 128	15.82	5.2	15.25	67.05	67.20	5.33	13.20
SL04 010	15.07	7.7	11.82	67.92	70.70	5.40	13.33
SL 88 116	18.65	8.9	18.51	78.28	71.40	5.29	8.52

Recovering jaggery from juice was dependent on the number of total solids in the cane. Jaggery recovery is typically calculated using the sugarcane juice's brix value. Jaggery recovery rose along with the rise in brix value. On the 11th day after harvest, under the brix of 22.5, the variety SL 88 116's maximum jaggery recovery value was found to be 18.47. After the seventh day of harvesting, which was under the 16.5 of brix, the minimum jaggery recovery value was found to be 14.53 for the variety of SL 04 010. Overall, SL 88 116 had a higher jaggery recovery than SL 96 128 and SL 04 010, in that order.

Generally jaggery containing low levels of reducing sugars has lower equilibrium moisture content (EMC). For this reason, moisture could be reduced, but in these results some fluctuations were observed, due to the high rates of reducing sugar level because of inversion of sucrose. The 3rd variety, SL 88 116 is maintaining the moisture content appropriately. Other than 2 varieties were faced vast fluctuations in values.

Pol value of sugarcane jaggery indicates the sucrose content of jaggery. When pol value sugarcane juice was decreased at the same time the pol value of jaggery was reduced. Due to the high temperature that gave during heating process, the reason behind was high temperature was breakdown the sucrose into invert sugars, at this study some fluctuations were happened in pol value, due to the rainfall because the water content reduces the temperature it was delays the bacterial activity. The maximum pol value was observed to be 18.36% for the variety of SL 88 116 after the 1st day of harvesting and minimum value pol was observed to be17.41% for the variety of SL 04 010 after the 1st day of harvesting. In overall, SL 88 116 had higher mean value preceded by SL 96 128 and SL 04 010.

Purity indicates the level of sugar purity in jaggery. During the post-harvest period, the purity level of sugarcane should be reduced due to the conversion of invert sugar from sucrose by bacteria, yeast and mold, due to this reason the purity level of jaggery also reduced. The maximum jaggery purity value was observed to be 77.31% which is obtain from juice of the variety of SL 88 116 at the 1st day of harvesting and minimum value purity of jaggery was observed to be 74.51% which was obtain from the juice of the variety of SL 04 010 after the 1st day of harvesting. In overall, SL 88 116 had higher mean value preceded by SL 96 128 and SL 04 010.

The brix value of sugarcane jaggery was decreasing due to time lagging between harvesting and crushing. The maximum brix value was observed to be 71.70% for the variety of SL 88 116 after the 9th day of harvesting and minimum value brix was observed to be 67.20 for the variety of SL 96 128 after the 7th days of harvesting. In overall, SL 88 116 had higher mean value preceded by SL 04 010and SL 96 128.

Brix indicates the amount total soluble solids of Sugarcane juice, which Includes sugars, minerals and other solid particles in juice. Generally the brix value of sugarcane jaggery was decreasing due to time lagging between harvesting and crushing. The maximum brix value was observed to be 71.70% for the variety of SL 88 116 after the 9th day of harvesting and minimum value brix was observed to be 67.20 for the variety of SL 96 128 after the 7th days of harvesting. In overall, SL 88 116 had higher mean value preceded by SL 04 010and SL 96 128.

5 Conclusion

Three different sugarcane varieties were tested, and the results showed that the storage period after the third day was unsuitable for producing jaggery of high quality. The first day's sugarcane juice had the right amount of brix, pol, and purity, which helped to make high-quality jaggery. The total reducing sugar level and brix were higher in the juice after three days, and after five days of cane storage, the brix and total reducing sugar were higher but the pol and purity were lower. On the seventh day had higher brix and lowering sugar levels, making it impossible for the juice to build a framework for jaggery. From the results, SL 88 116 sugarcane variety was more suitable and produced high quality jaggery than the other two varieties.

6 References

A Bhatt, R., Kashyap, L. and Sharma, A. (no date) *Sugarcane Jaggery: An alternative of sugar for healthy living*. Available at: https://www.researchgate.net/publication/361323820

B.D.S.K. Ariyawansha (2014) ‘Adaptability of some sugarcane varieties in different environments in SL’, *Sugarcane Sri Lanka*, 01. Available at: http://sugarres.lk/wp-content/uploads/2020/07/Journal-Vol-01-2014.pdf (Accessed: 2 April 2023).

Kele, V. *et al.* (2020) ‘Jaggery: A natural sweetener Application of IOT in Dairy Industry View Project Goat milk View project Parth Hirpara 2 PUBLICATIONS 12 CITATIONS SEE PROFILE Jaggery: A natural

Misra, V. *et al.* (2016) ‘ Post-harvest Sugarcane Deterioration: Leuconostoc and Its Effect ’, *Journal of Functional And Environmental Botany*, 6(1), p. 1. Available at: https://doi.org/10.5958/2231-1750.2016.00001.9

Study on synbiotic salad dressing based on the addition of *Lacticaseibacillus rhamnosus*.

W.L.P.U.S. Wijesinghe[1*], K.M.G.M.M Kariyawasam[1]

Department of Biosystems Technology, Faculty of Technological studies, Uva Wellasssa University, Badulla, Sri Lanka.
[*]bbst19016@std.uwu.ac.lk

Abstract

In recent years, salad dressing products have received growing attention in the food industry due to increased consumer demand for salads as a healthy food option. This research aimed to develop a synbiotic salad dressing inoculated with *Lacticaseibacillus rhamnosus* and Fructo-oligosaccharides. Salad dressing was prepared by blending with sunflower oil, acetic acid, N-creamer starch, egg white and yolk powder, mustard cream, black pepper powder, onion powder, garlic powder, salt, sugar, and potassium sorbate. The best recipe was selected from developed three salad dressing recipes by conducting a sensory evaluation using a seven-point hedonic scale and sensory parameters, including color, aroma, taste, texture, and overall acceptability, were evaluated using 30 semi-trained panelists. Selected best recipe of salad dressing was inoculated with *Lacticaseibacillus rhamnosus* and fructo-oligosaccharide as prebiotic (T). The control sample was prepared without adding probiotic and prebiotic (C). The proximate composition, physio-chemical properties and microbiological properties were analyzed for C and T samples. The C sample had moisture (40.83±0.37%), crude fat (53.04±0.53%), crude fiber (0.12±0.03%), crude ash (2.09±0.03%). The T sample had moisture (40.31±0.02%), crude fat (52.90±1.04%), crude fiber (0.15±0.01%) and crude ash (2.19±0.01%). In physio-chemical properties analysis, Total soluble solids (TSS), percentage titratable acidity (%TA), pH of C and T samples were 16.6, 0.36%, 3.74 and 18.5, 0.35%, 3.68, respectively. Microbial counts of C were less than the standard minimum limits and T was shown 2.4×10^5 cfu/g under total plate count. In evaluating the shelf-life evaluation tests for variations of physicochemical properties of both C and T samples were conducted weekly for four weeks. This synbiotic salad dressing is a healthier alternative compared to the control salad dressing sample.

Keywords: Salad dressing; synbiotic; *Lactobacillus;* physio-chemical; healthy foods

1. Introduction

In recent years, Consumers have become increasingly interested in their health and expect food to be healthy and prevent disease. Modern developments in food science and technology make the public aware of the importance of embracing a healthy diet and improving one's lifestyle. Salad dressing is a popular food item that contains vegetable flavoring elements (sweetener, salt, garlic), emulsifying agents (crystal inhibitors, texture enhancers, and stabilizers), and acidic constituents (maleic acid, acetic acid, and citric acid). Salad dressings have recently gained popularity among consumers (Avci *et al.*, 2023).

Synbiotic foods are defined as foodstuffs that have the potential to enhance human health by containing both probiotics and prebiotics. Probiotic has been defined as “Live microorganisms (bacteria or yeasts), which when ingested or locally applied in sufficient numbers confer one or more specified demonstrated health benefits for the host” (FAO/WHO, 2001) (Lieu, Dang and Nguyen, 2017). Prebiotics are nondigestible food components that benefit the customer by selectively boosting bacterial growth and activity in the colon. Inulin and its hydrolysates, resistant starch, lutein, fructo-oligosaccharides, and galacto-oligosaccharides are examples of prebiotics that are typically found in human diets (Shafiei, 2018).

Synbiotic salad dressing is a functional food product. when the probiotics are added to the salad dressing, it can give more nutrient value to the consumer's diet while consuming salads. In addition, lactose intolerance consumers can assume probiotics nutrients with other nutrients. The present work aims to develop synbiotic salad dressing inoculated with *Lacticaseibacillus rhamnosus* with acceptable physicochemical, nutritional composition and microbial properties.

2. Materials and methods

2.1 Materials

Ingredients used to prepare the salad dressing formulation: Sunflower oil, salt, sugar, black pepper powder, garlic powder, onion powder and mustard cream were purchased from a local market in Colombo Fort, Sri Lanka. Acetic acid and Potassium Sorbate were purchased from Glorchem Enterprises in Colombo, Sri Lanka. All the ingredients used were food grade. The *Lacticaseibacillus rhamnosus* bacterial strains packet was obtained from the Biosystem Department at Uva Wellassa University, Badulla, Sri Lanka.

2.2 Methods

2.2.1 Preparation of salad dressing

Salad dressing was prepared according to the method described by Ma *et al.*, 2013 with slight modifications. Three salad dressing formulations were developed as shown table 1. Ingredients were measured accurately according to the recipes. First, water, salt, sugar, mustard cream, garlic powder, onion powder, black pepper powder, and potassium sorbate were added into the blender cup and mixed well. Next, Whole egg powder was added to the mixture and blended well. After, Sunflower oil and modified tapioca starch were added and blended the mixture until the mixture taking creamy body. Then, Acetic acid was added and grinned one minute. Finally, the mixture was poured in to sterilized glass bottles, sealed, labelled and kept at room temperature. The best salad dressing recipe was selected through a sensory evaluation using trained panellists. The selected salad dressing was used to develop as the synbiotic salad dressing.

Table 1: The three salad dressing formulations

Ingredients	Recipe with different amount of ingredients as a percentage by mass (w/w)		
	Recipe 1	Recipe 2	Recipe 3
Sunflower Oil	35.7%	43.8%	50.0%
Water	51.0%	43.8%	38.0%
Sugar	2.4%	2.0%	2.0%
Salt	4.0%	2.0%	2.0%
Egg Powder	1.2%	1.2%	1.2%
Modified Tapioca Starch	2.6%	3.0%	3.0%

Mustard Cream	2.0%	2.1%	2.1%
Onion Powder	-	0.3%	0.3%
Garlic Powder	-	0.3%	0.3%
Black Pepper powder	-	0.3%	0.3%
Acetic Acid	1.0%	1.0%	1.0%
Potassium Sorbate	0.1%	0.1%	0.1%

2.2.1 Preparation of synbiotic salad dressing

Salad dressing was prepared according to the selected best recipe using the above procedure and added 1% fructo-oligosaccharide. Then, *Lacticaseibacillus rhamnosus* stain included packet (1% w/w) was added to the salad dressing mixture under aseptic conditions and mixed using a blender. Finally, the mixture was poured into sterilized glass bottles, sealed, labelled under aseptic conditions and stored in a refrigerator (4±1°C).

2.2.2 Determination of proximate composition

Moisture, fat, fiber and ash contents of the control salad dressing and synbiotic salad dressing were determined in accordance with AOAC methods 934.01, 920.39, 962.09 and 942.05, respectively.

2.2.4 Determination of physicochemical properties

Standard AOAC methods were used to examine the physicochemical parameters of control salad dressing (C) and synbiotic salad dressing (T). pH, percentage titratable acidity (%TA), and Total soluble solids (TSS) were evaluated as physicochemical properties of both samples in weekly for four weeks. pH was measured using a pH meter (MM-42DP, Tokyo, Japan). Total soluble solids (TSS) was measured using a digital refractometer (MA871, Colorado, USA).

2.2.5 Sensory analysis of salad dressing

Sensory analysis for the salad dressing formulations was performed using effective acceptance and preference test with 30 semi-trained panelists to select the best recipe out of three formulations. The selected salad dressing was used to develop as synbiotic salad dressing by inoculating *Lacticaseibacillus rhamnosus* strain. Each panelist received three samples with an unsweet biscuit. They were served on disposable white cups coded with random three-digit numbers. The panelists were asked to drink water between the samples to avoid aftertaste. Colour, body/texture, flavor, aroma/odor and overall acceptability were evaluated using, a seven-point structured hedonic scale where 1 – like extremely and 7 – dislike extremely.

2.2.6 Microbial analysis

Total plate count was performed with both control salad dressing sample and synbiotic salad dressing sample.

2.2.7 Statistical analysis

All statistical data were analyzed using MINITAB 20 statistical software. Physicochemical properties and proximate composition of both salad dressing samples were analyzed using one- way ANOVA to determine the statistical differences between both salad dressing. Means were compared using the Tukey method at a 95% confidence interval. Each experiment were replicated three times, and the standard deviations were calculated. Sensory

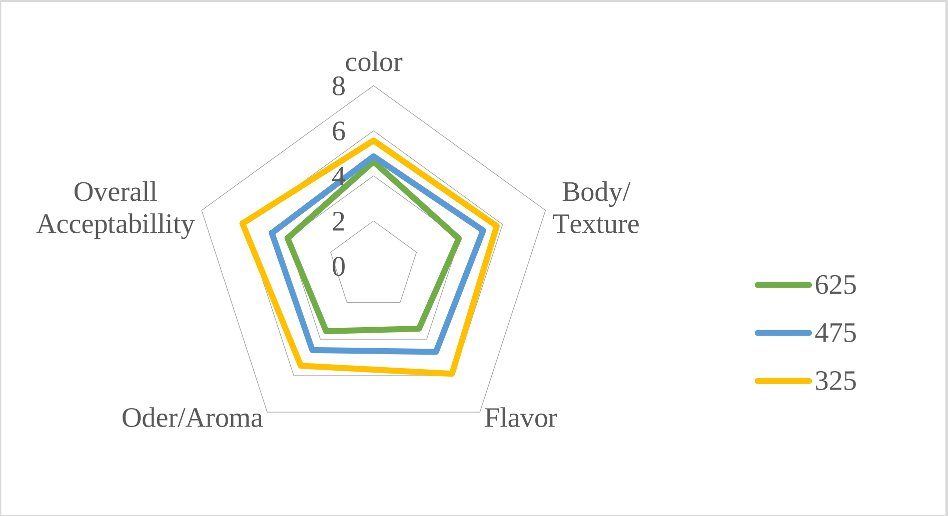

Figure 1: Overall sensory profile for three salad dressing formulations. 625: Recipe 01 which 35% sunflower oil incorporated salad dressing. 475: Recipe 02 which 40% sunflower oil incorporated salad dressing. 325: Recipe 03 which 50% sunflower oil incorporated sample

evaluation data were analyzed a using nonparametric test, the Friedman test with a 95% confidence level.

3. Results and discussion

3.1 Selection of the best recipe

The best salad dressing recipe was selected after conducting a sensory evaluation for use as a control sample. This selected salad dressing recipe was used to incorporate probiotics for development as the synbiotic salad dressing. Figure 1 shows the results of the sensory evaluation.

Based on the results of Friedman test (Table 2) since the P≤α=0.05 for each attribute, it can be concluded that there were significant differences between the three salad dressing recipes. Recipe 03 (325) emerged out to be the best salad dressing recipe with the highest sum of ranks for all attributes. Recipe 03 sample has contained 50% sunflower oil content than other both recipes and is incorporated with spices. Sample of recipe 01(625) has gained the least estimated median values for virtually all attributes than recipe 02 (475) and recipe 03 (325). Recipe 01 has contained 35% sunflower oil content, a smaller amount than the other two recipes, and has not incorporated spices. Overall, the estimated median values suggest that recipe 03 is the most preferred salad dressing recipe and offers a better sensory result across all sensory attributes. The salad dressing recipe 03 which incorporated with 50% sunflower oil and spices was selected for further studies.

Table 2: Mean and standard deviation of sensory characteristics of different recipe samples

Sensory characteristics	625 (SDR 01)	475 (SDR 02)	325 (SDR 03)
Color	4.633 ± 1.450^{b}	4.867 ± 0.860^{b}	5.567 ± 0.817^{a}
Body/ Texture	3.967 ± 1.245^{b}	5.100 ± 1.213^{a}	5.733 ± 0.868^{a}
Flavor	3.400 ± 1.354^{c}	4.700 ± 1.236^{b}	5.900 ± 0.995^{a}
Odor/Aroma	3.567 ± 1.251^{c}	4.600 ± 1.248^{b}	5.467 ± 1.252^{a}

Overall Acceptability	4.000±1.232^{c}	4.733±0.907^{b}	6.100±0.759^{a}

Different letters in the same row indicate the values are significantly different ($p<0.05$)

3.2 Proximate analysis

The proximate analysis was carried out for both the control salad dressing sample and the synbiotic salad dressing sample.

Table 3: Proximate composition of C and T salad dressing samples

Composition (%)	Control salad dressing (C)	Synbiotic salad dressing (T)
Moisture	40.83±0.37^{a}	40.31±0.02^{a}
Crude fat	53.04±0.53^{a}	52.90±1.04^{a}
Crude fiber	0.12±0.03^{a}	0.15±0.01^{a}
Crude ash	2.09±0.03^{b}	2.19±0.01^{a}

Values are mean ± standard deviation of three determinations

Based on observations of the proximate composition of both samples, there is no drastic difference observed in the synbiotic salad dressing sample (T) compared to the control sample (C). This could be clearly shown by very minimal differences in moisture content, crude fat, crude fiber, and crude ash, all of which have a close range, thereby indicating that the synbiotic dressing (T) has maintained almost the same nutritional profile when compared to the control salad dressing (C). Additionally, this combined with slight improvements in fiber content and the added advantages of a probiotic, could be made this synbiotic dressing (T) a healthier alternative compared to the control sample.

3.3 Physicochemical properties

pH, percentage titratable acidity (TA%), and Total soluble solids (TSS) were evaluated as physicochemical properties of both the control sample (C) and synbiotic salad dressing (T) in weekly for four weeks. As shown in the Figure 2, pH and Figure 3, percentage titratable acidity (TA%) of both salad dressing samples was shown slight changes during the storage period. Additionally, As shown in Figure 4, the Total soluble solids (TSS) of both salad dressing samples remained the same during the storage period.

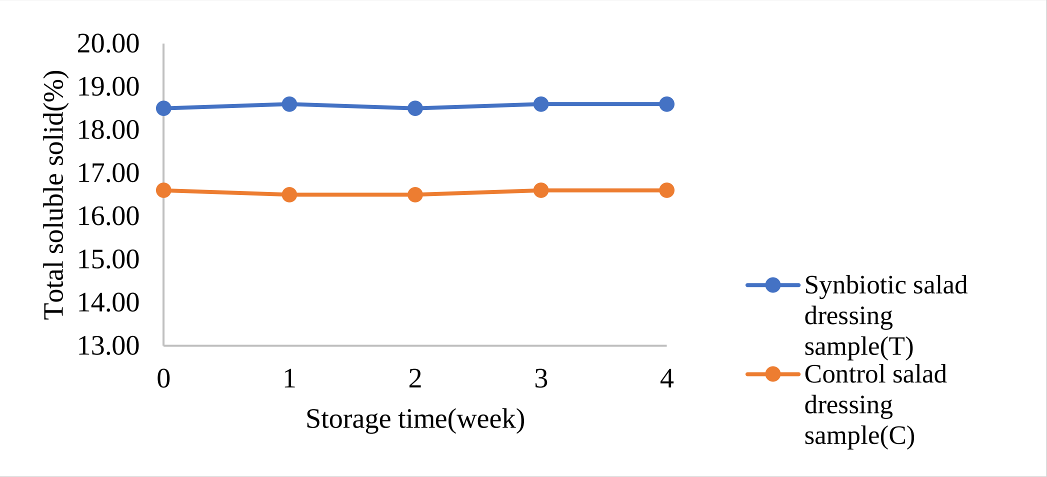

Figure 4:Change in pH value of synbiotic (T) and control (C) salad dressing samples during in a refrigerated (4±1℃) storage period . Values are mean ± standard deviation of three determinations.

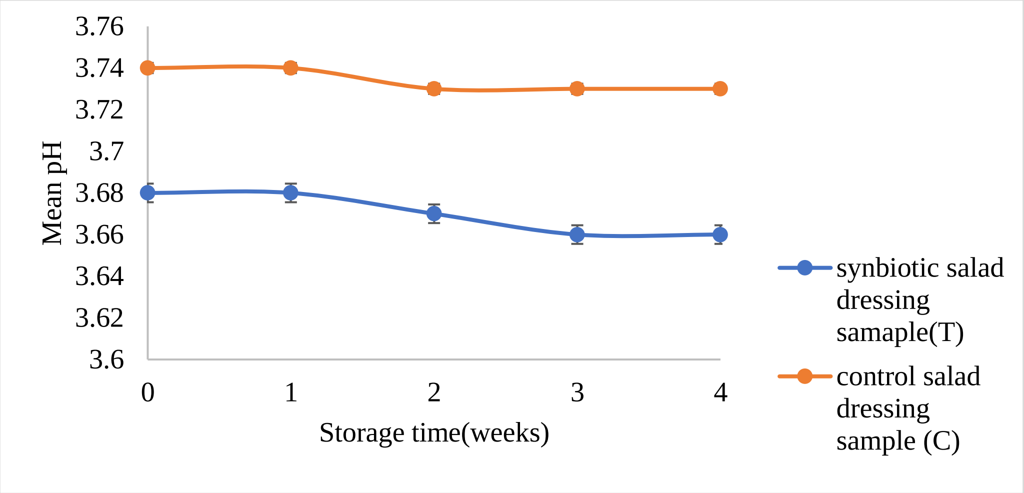

Figure 3:Change in titratable acidity value of synbiotic (T) and control (C) salad dressing samples during in a refrigerated (4±1℃) storage period. Values are mean ± standard deviation of three determinations.

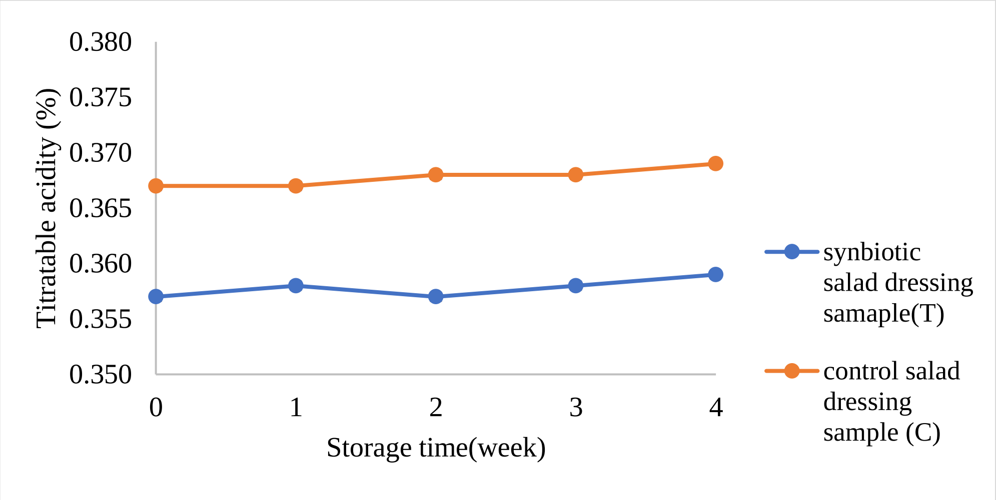

Figure 2: Change in total soluble solid value of synbiotic (T) and control (C) salad dressing samples during in a refrigerated (4±1℃) storage period.

3.4 Microbial properties

According to the total plate count results, initial date of control sample (C) was given 2 colonies in per gram. As well as, synbiotic salad dressing sample (T) was given 24 colonies in per gram at initial date. Synbiotic salad dressing (T) sample was shown 3.68 pH value. Pourable dressings have a pH in the range of 3.5 to 3.9. salad dressings with a pH less than 4.0 are very safe due to pathogenic bacteria cannot survival at this pH range (Fracis F Busta, D.T Bernard, R.B Gravani, 2018). Synbiotic salad dressing (T) product was shown better survival results under total plate count method.

4. Conclusion

Salad dressing which is incorporated 50% oil is the best out of three salad dressing recipes. Selected recipe was used for inoculated with *Lacticaseibacillus rhamnoses* and fructo-oligosaccharide as prebiotic (T). The control sample was prepared without adding probiotic and prebiotic (C). The proximate composition of both samples, T has maintained almost the same nutritional profile when compared to the control salad dressing C. Shelf life of the T and C salad dressing samples in a refrigerator (4±1°C) is four weeks, pH and percentage titratable acidity (%TA) have remained same during the storage period. Microbial counts of C were less than the standard minimum limits and T was shown 2.4×10^5 cfu/g under total plate count. This synbiotic dressing (T) a healthier alternative compared to the control sample.

5. Acknowledgement

I would like to thank Dr. Menaka Kariyawasam, Senior Lecturer, Department of Biosystems Technology, Uva Wellassa University, for her great inspection and intellectual contribution to this research work and thank Faculty of Technological Studies, Department of Biosystems Technology, Uva Wellassa University of Sri Lanka for facilities provided for the successful accomplishment of this work.

6. References

Avci, E. *et al.* (2023) 'Capsaicin Rich Low-Fat Salad Dressing: Improvement of Rheological and Sensory Properties and Emulsion and Oxidative Stability', *Foods*, 12(7). Available at: https://doi.org/10.3390/foods12071529.

Fracis F Busta, D.T Bernard, R.B Gravani, P.H. (2018) 'Evaluation and Definition of Potentially Hazardous Foods - Full Report', *Evaluation and Definition of Potentially Hazardous Foods*, 2(223), pp. 1–109. Available at: http://www.fda.gov/.

Lieu, M.D., Dang, T.K.T. and Nguyen, T.H. (2017) 'Viability of microencapsulated lactobacillus casei in synbiotic mayonnaise', *Food Research*, 1(6), pp. 234–239. Available at: https://doi.org/10.26656/fr.2017.6.103.

Ma, Z. *et al.* (2013) 'Rheological, physical stability, microstructural and sensory properties of salad dressings supplemented with raw and thermally treated lentil flours', *Journal of Food Engineering*, 116(4), pp. 862–872. Available at: https://doi.org/10.1016/j.jfoodeng.2013.01.024.

Shafiei, Y. (2018) *Probiotic and Synbiotic Yogurt Production Using Free or Alginate/Resistant Starch Microencapsulated Lactobacillus plantarum*, *Role of Materials Science in Food Bioengineering*. Elsevier Inc. Available at: https://doi.org/10.1016/B978-0-12-811448-3.00009-

Detection of GMOs in some imported seed consignments to Sri Lanka

K.A.S.T. Madusanka[1*], M.H.A.D. Subhashini[2] and N.M.C. Nayanakantha[1]

[1]*Department of Biosystems Technology, Faculty of Technological Studies, Uva Wellassa University of Sri Lanka,*
[2] *National Plant Quarantine Service, Canada Friendship Road, Katunayake.*

[*]*Suresh1112madusanka@gmail.com*

Abstract

Genetically modified organisms (GMOs) are organisms in which foreign DNA segments including transgenes have been purposefully incorporated into the organism. Still, society has not yet accepted this technology due to the adverse impacts it may have on the environment and health. Sri Lanka enforces strict regulations on the import of genetically modified (GM) seeds to protect local agriculture and the environment. Concerns are being raised about the possibility of GM seeds entering the country without proper labeling, posing risks to biodiversity and traditional farming practices as well as consumer safety. This research aims to assess the prevalence of GM seeds in imported seed commodities such as maize, groundnut, seed potato, mung bean, finger millet, dhal, orid, jumbo peanut, carrot, onion, and beetroot, which are cultivated. in Sri Lanka. Seed samples collected from different access points in Sri Lanka were analyzed using a PCR-based method. DNA was extracted from both test and positive samples using CTAB method, and purity and quantity were assessed by spectrophotometry. PCR was performed with P-35S, Cry1Ab, and HA-nos118 primers, targeting common GMO elements with optimized PCR conditions for each primer. The results indicated no contamination of GMOs in the test samples, with only positive control samples displaying the expected bands; DNA purity was confirmed with 260/230 nm and 260/280 nm values between 1.8 and 2.2, PCR amplified bands were resolved at 204 bp for Cry1Ab, 123 bp for P-35S, and 118 bp for the Nos terminator in positive samples.

Keywords: Genetically Modified Organisms (GMOs), Imported Seed Commodities, PCR Analysis, Sri Lanka, DNA extraction.

1. Introduction

The development of genetically modified organisms (GMOs) represents a significant advancement in agricultural biotechnology, with GM crops now cultivated on millions of hectares worldwide. These crops are engineered to express traits such as resistance to pests and diseases, tolerance to herbicides, and improved nutritional profiles (Innes, 2006). The first genetically modified plant, a tomato with delayed ripening properties, was introduced in 1994, marking the beginning of a new era in crop production (Gou *et al.*, 2016). Despite their potential benefits, GMOs have been the subject of intense scrutiny due to concerns about their environmental impact, potential risks to human health, and the ethical implications of altering the genetic makeup of living organisms (Domingo and Giné Bordonaba, 2011)

In response to these concerns, many countries, including Sri Lanka, have implemented strict regulations to control the importation and cultivation of GMOs. Sri Lanka’s regulatory framework is rooted in the precautionary principle, which emphasizes the need to avoid harm to the environment and public health, even in the face of scientific uncertainty (Wimalasiri and Ranasinghe, 2010)The importation of genetically modified seeds into Sri

Lanka is subject to rigorous testing and documentation to ensure that GMOs do not enter the country's agricultural system without proper oversight. However, there remains a risk that unlabeled GM seeds could be imported, either unintentionally or through illegal trade, posing a threat to the country's biodiversity and traditional farming practices.

This study aimed to detect the presence of GMOs in various seed varieties imported into Sri Lanka. These varieties, which include maize, groundnut, seed potato, mung bean, finger millet, dhal, orid, jumbo peanut, carrot, onion, and beetroot, are widely used in Sri Lankan agriculture. Given the global prevalence of GM crops, particularly in maize, which has been extensively modified to express traits such as insect resistance (e.g., Bt maize), it is critical to monitor these imports to prevent the introduction of GMOs into Sri Lanka's agricultural system (Wimalasiri and Ranasinghe, 2010)

The detection of GMOs was performed using polymerase chain reaction (PCR), a highly sensitive and specific technique for amplifying DNA sequences associated with genetic modifications. The PCR method was selected because of its ability to detect even minute amounts of transgenic DNA, making it ideal for screening imported seeds for GMO contamination. This study focused on detecting the 35S promoter, Cry1Ab gene, and Nos terminator—genetic elements commonly found in GM crops (Schreiber, 1999)

2. Materials and methods

2.1 Materials

The materials used included a thermal cycler, micropipettes, microcentrifuge, submarine agarose gel electrophoresis system, gel documentation system, vortex mixer, 1.5 mL microcentrifuge tubes, autoclavable PCR tubes (0.2 mL), and a laminar flow hood. Key reagents comprised dNTPs, Taq DNA polymerase, 10x PCR buffer, 25 mM $MgCl_2$, sterile nuclease-free water, 2% agarose gel, 5x TBE buffer, a 100 bp DNA ladder, ethidium bromide (10 mg/mL), CTAB extraction and precipitation buffers, sodium chloride solution, 70% ethanol, TE buffer, Proteinase K solution, and RNase-A solution. The primers used for PCR amplification were Cry1Ab (F: 5'-ATG GAC AAC AAC CCC AAC ATC-3', R: 5'-AAA GAT ACC CCA GAT GAT GTC-3'), p35S (F: 5'-CCA CGT CTT CAA AGC AAG TGG-3', R: 5'-TCC TCT CCA AAT GAA ATG AAC TTC C-3'), and HA-nos118 (F: 5'-GCA TGA CGT TAT TTA TGA GAT GGG-3', R: 5'-GAC ACC GCG CGC GAT AAT TTA TCC-3').

2.2 Methods

2.2.1 Sample collection and registration

Eleven types of seed varieties were collected from the Colombo airport and seaport, representing the primary entry points for agricultural imports into Sri Lanka. These commodities were selected based on their economic importance and potential for genetic modification. Each sample was carefully labeled, registered, and prepared for genetic testing. The labeling process included assigning unique identifiers to each sample, ensuring traceability throughout the testing procedure.

2.2.2 DNA extraction

DNA was extracted using the cetyltrimethylammonium bromide (CTAB) method, which is effective for plant materials rich in polysaccharides and polyphenols (Doyle and Doyle, no date)Approximately 200-300 mg of each seed sample was ground and mixed with pre-warmed CTAB extraction buffer (2.0 g/L CTAB, 1.4 mol/L NaCl, 0.1 mol/L Tris-HCl, 0.02 mol/L Na_2 EDTA, pH 8.0). The mixture was incubated at 65°C for 30 minutes to lyse the cells. Proteinase K was then added, followed by a second incubation at 65°C for 30 minutes. After centrifugation at 12,000 x g, the supernatant was subjected to chloroform-isoamyl alcohol extraction to remove proteins and contaminants. The DNA was precipitated with isopropanol, washed with 70% ethanol, and air-dried. Finally, the DNA pellet was dissolved in 100 µL of TE buffer (pH 8.0). DNA quality and quantity were assessed using a NanoDrop spectrophotometer. Purity was confirmed with absorbance ratios of 260/280 nm between 1.8 and 2.0, indicating high-quality DNA suitable for PCR analysis (Gómez *et al.*, 1998)

2.2.3 PCR amplification

PCR amplification was carried out for the P-35S, Cry1Ab, and HA-nos118 sequences using a 50 µL reaction volume. For P-35S, the mix included 2 µL of DNA, 10 µL of Flexi buffer, 5 µL of $MgCl_2$, 2.5 µL of dNTPs, 1.25 µL each of primers, 0.25 µL of Taq polymerase, and 27.15 µL of water, with cycling conditions of 95°C for 3 minutes, followed by 50 cycles of 95°C for 20 seconds, 62°C for 30 seconds, and 72°C for 45 seconds, finishing with 72°C for 3 minutes. For **Cry1Ab**, the reaction contained 2 µL of DNA, 5 µL of Flexi buffer, 5 µL of $MgCl_2$, 2.5 µL of dNTPs, 1.25 µL of primers, 0.25 µL of Taq polymerase, and 32.75 µL of water, with cycling conditions of 95°C for 3 minutes, followed by 30 cycles of 95°C for 1 minute, 62°C for 1 minute, and 72°C for 3.5 minutes, ending with 72°C for 10 minutes. For HA-nos118, the mix included 1.5 µL of DNA, 10 µL of Flexi buffer, 2 µL of $MgCl_2$, 1 µL of dNTPs, 1 µL of primers, 0.25 µL of Taq polymerase, and 33.25 µL of water, with cycling conditions of 95°C for 3 minutes, followed by 50 cycles of 95°C for 25 seconds, 62°C for 30 seconds, and 72°C for 45 seconds, finishing with 72°C for 7 minutes.

2.2.4 Gel electrophoresis

Following amplification, PCR products were analyzed by agarose gel electrophoresis to confirm the presence and size of the amplified DNA fragments. A 1.5% agarose gel was prepared, and 8 µL of each PCR reaction was mixed with 2 µL of loading buffer before being loaded into the gel wells. Electrophoresis was performed at 100 volts for 60 minutes. A 100 bp DNA ladder (15 µL) was loaded in adjacent wells to accurately determine the size of the amplicons. After electrophoresis, the gel was stained with ethidium bromide and visualized under UV light. The specific bands corresponding to the expected sizes for the GMO target sequences (204 bp for Cry1Ab, 123 bp for P-35S, and 118 bp for the Nos terminator) indicated successful amplification. Positive control samples (Bt11, Bt176 and, NK603) were included in each run to validate the accuracy of the PCR and electrophoresis procedures, and the gel was documented for a permanent record of the results.

2.2.5 Control samples

Positive control samples of Bt maize (Bt11, Bt176, and NK603) were used to optimize PCR conditions and confirm the reliability of the assay. These controls are well-characterized GM varieties known to contain the genetic elements targeted in this study. Additionally, negative controls (non-GM maize) were used to ensure that there was no contamination during the DNA extraction or PCR amplification processes.

3. Results and discussion

3.1 DNA Extraction and quality assessment

High-quality DNA extraction is a prerequisite for successful PCR amplification and subsequent detection of genetically modified organisms (GMOs). In this study, DNA was extracted using the CTAB method, which is widely recognized for its ability to efficiently isolate DNA from plant materials that are often rich in polysaccharides and polyphenols

(Doyle, 1990)These substances can inhibit downstream applications such as PCR; however, the spectrophotometric analysis of the extracted DNA showed absorbance ratios at 260/280 nm and 260/230 nm ranging between 1.8 and 2.2, indicating that the DNA was of high purity and free of significant contaminants. This high-quality DNA was necessary to ensure accurate and reproducible PCR results, which is critical in molecular diagnostics, especially when detecting GMOs in food and agricultural products. (Abdel-Latif and Osman, 2017)

The DNA concentrations across the samples varied, with the highest concentrations observed in maize (up to 119.3 ng/µL) and somewhat lower values in groundnut and other commodities. The yield was sufficient for all subsequent PCR analyses, confirming that the extraction protocol was robust and suitable for a range of plant species.

3.2 PCR amplification and GMO detection

The PCR assays were conducted using primers designed to detect specific genetic elements frequently found in GMOs: Cry1Ab, HA-nos118, and P-35S. Each of these genetic elements is integral to many genetically modified crops, which have been engineered to exhibit desirable agronomic traits such as pest resistance, herbicide tolerance, and improved yield (Innes, 2006)

3.2.1 Cry1Ab primer results

Figure 5 : Agarose Gel Electrophoresis of PCR Products for Cry1Ab Gene Detection (204 bp) in Maize, Groundnut, Seed Potato, and Other seed Samples: PCR amplification of the Cry1Ab gene targeting a 204 bp fragment. Lanes 1-5 represent maize test samples (M1, M2, M4, M5, M7), lanes 6-10 groundnut samples (G1, G2, G3, G8, G10), lanes 11-15 seed potato samples (S1, S5, S6, S7, S10), and lanes 16-23 other commodity samples (Other 01 - Mung bean, Other 02 - Finger millet, Other 03 - Dhal, Other 04 - Orid, Other 05 - Jumbo peanut, Other 06 - Carrot, Other 07 - Onion, Other 08 - Beetroot). Lane P is the positive control, showing a clear 204 bp band, while the negative control (Lane N) shows no amplification. Ladder (L) indicates molecular

The Cry1Ab gene encodes the Cry1Ab protein, an insecticidal protein derived from *Bacillus thuringiensis* (Bt). This gene is commonly incorporated into genetically modified maize to provide resistance to lepidopteran pests such as the European corn borer (*Ostrinia nubilalis*) (Bravo *et al.*, 2011)The presence of the Cry1Ab gene in a sample indicates that the crop has been genetically modified to express this insecticidal trait. In this study, as shown in the Figure 5 , the Cry1Ab-specific PCR amplification yielded a clear band at 204 bp in the positive control samples, which were known to contain genetically modified maize. None of the tested samples, including those of maize, groundnut, seed potato, and other commodities, showed any amplification at this locus. This result indicates that none of these samples contained the Cry1Ab transgene. The absence of amplification in the test samples suggests that the imported seed commodities were free from Cry1Ab-containing GMOs.

3.2.2 HA-nos118 primer results:

Figure 6 : Agarose Gel Electrophoresis of PCR Products for HA-nos118 Terminator Sequence Detection (118 bp) in Maize, Groundnut, Seed Potato, and Other Commodity Samples**-** PCR amplification results for the HA-nos118 terminator sequence targeting a 118 bp fragment. Lanes 1-5 represent maize test samples (M1, M2, M4, M5, M7), lanes 6-10 groundnut samples (G1, G2, G3, G8, G10), lanes 11-15 seed potato samples (S1, S5, S6, S7, S10), and lanes 16-23 other commodity samples (Other 01 - Mung bean, Other 02 - Finger millet, Other 03 - Dhal, Other 04 - Orid, Other 05 - Jumbo peanut, Other 06 - Carrot, Other 07 - Onion, Other 08 - Beetroot). The positive control (Lane P) exhibits a 118 bp band corresponding to the HA-nos118 sequence, while the negative control (Lane N) and test sample lanes show no visible amplification. Ladder (L) indicates molecular weight markers.

The HA-nos118 primer targets the nopaline synthase (Nos) terminator, which is a commonly used genetic element derived from *Agrobacterium tumefaciens*. This terminator sequence is typically employed to ensure proper transcriptional termination in transgenic constructs (Bevan *et al.*, 1983)The Nos terminator is a reliable indicator of genetic modification, as it is often used in conjunction with other transgenes in GM crops. In this study, Figure 6 shows a clear band at 118 bp was observed in the positive control lanes, confirming the presence of the NOS terminator in the known GMO samples. However, none of the seed samples under investigation exhibited amplification at this locus. This finding further confirms the absence of GM elements in the tested seed lots.

3.2.3 P-35S primer results

Figure 7 : PCR amplification of the CaMV 35S promoter sequence, showing a 123 bp fragment. Lanes 1-5 represent maize test samples (M1, M2, M4, M5, M7), lanes 6-10 groundnut samples (G1, G2, G3, G8, G10), lanes 11-15 seed potato samples (S1, S5, S6, S7, S10), and lanes 16-23 other commodity samples (Other 01 - Mung bean, Other 02 - Finger millet, Other 03 - Dhal, Other 04 - Orid, Other 05 - Jumbo peanut, Other 06 - Carrot, Other 07 - Onion, Other 08 - Beetroot). The positive control (Lane P) displays a distinct 123 bp band, while the negative control (Lane N) and test sample lanes show no amplification. Ladder (L) indicates molecular weight markers.

The Cauliflower Mosaic Virus 35S (CaMV 35S) promoter is one of the most frequently used promoters in plant genetic engineering due to its ability to drive high levels of transgene expression in a wide range of plant species (Odell, Nagy and Chua, 1985). The P-35S primer amplifies a region of this promoter, and its presence is a strong indicator of genetic modification in crops. As shown in **Figure 7**, the positive control samples of this study showed a distinct band at 123 bp, confirming the presence of the CaMV 35S promoter. None of the test samples showed amplification, suggesting that these seed commodities do not contain the CaMV 35S promoter or associated transgenes.

3.3 Implications of findings

The absence of detectable GMO elements in the tested seed samples highlights the effectiveness of Sri Lanka's stringent import regulations in preventing unauthorized genetically modified seeds from entering the country. This finding reinforces Sri Lanka's commitment to maintaining a GMO-free agricultural sector, which is essential for both biodiversity conservation and food security (McGeoch *et al.*, 2010). Ecologically, it helps protect the genetic diversity of local crops, reducing the risk of gene flow between GM and non-GM species that could disrupt ecosystems. Additionally, by ensuring that imported seeds are GMO-free, Sri Lanka maintains consumer trust and meets market preferences for non-GMO products, which is increasingly important in the global market.

3.4 Robustness and sensitivity of detection methods

The successful detection of Cry1Ab, HA-nos118, and P-35S elements in positive controls validates the high sensitivity and specificity of the PCR assays used, minimizing the risk of false negatives. The specificity of these primers, which target commonly used GM sequences, supports the reliability of the results. However, since the study focused on specific genetic elements, other modifications might not have been detected, indicating the need for broader GMO surveillance in future studies by incorporating additional primers (Heinemann, Agapito-Tenfen and Carman, 2013)

3.5 Global comparison and future prospects

Sri Lanka's regulatory approach is consistent with global practices in GMO detection, similar to those in the EU, Japan, and South Korea, which also employ PCR-based methods to monitor GMOs in imports. As genetically modified crops continue to diversify, the adoption of advanced detection technologies like digital PCR (dPCR) and next-generation sequencing (NGS) could enhance the sensitivity and scope of GMO detection, helping Sri Lanka and other nations better safeguard their agricultural sectors against GMO contamination (Cottenet *et al.*, 2013).

4. Conclusion

The results of this study indicate that the tested seed samples were free from genetically modified organisms, as evidenced by the absence of the Cry1Ab, HA-nos118, and P-35S sequences in the samples. This suggests that Sri Lanka's stringent GMO import regulations and monitoring mechanisms are effective in preventing the entry of unauthorized GM seeds into the country. The robustness of the PCR-based detection methods employed in this study was demonstrated by the successful amplification of target sequences in the positive controls, providing confidence in the accuracy and reliability of the results. These findings have significant implications for Sri Lanka's agricultural biodiversity, food security, and consumer confidence. By maintaining a GMO-free status, Sri Lanka can protect its unique ecosystems, support traditional farming practices, and meet the growing demand for non-GMO food products. Continued monitoring and the adoption of more advanced detection technologies are recommended to ensure that Sri Lanka remains at the forefront of GMO surveillance and biosafety.

5. Acknowledgement

I would like to express my sincere gratitude to Ms. M.H.A.D. Subhashini, Dr. N.M.C. Nayanakantha, and the National Plant Quarantine Service, Katunayake, Sri Lanka, for their support and for providing the necessary facilities for this research. We also extend our appreciation to Uva Wellassa University of Sri Lanka for their invaluable guidance throughout the study.

6. References

Abdel-Latif, A. and Osman, G. (2017) ‘Comparison of three genomic DNA extraction methods to obtain high DNA quality from maize’, *Plant Methods*, 13(1), pp. 1–9. Available at: https://doi.org/10.1186/s13007-016-0152-4.

Bevan, M. *et al.* (1983) ‘Nucleic Acids Research Downloaded from https://academic.oup.com/nar/article/11/2/369/2385022 by Uva Wellassa University user on 20 August 2024 Nucleic Acids Research’, 11(2), pp. 369–386.

Bravo, A. *et al.* (2011) ‘Bacillus thuringiensis: A story of a successful bioinsecticide’, *Insect Biochemistry and Molecular Biology*, 41(7), pp. 423–431. Available at: https://doi.org/10.1016/j.ibmb.2011.02.006.

Cottenet, G. *et al.* (2013) ‘Development and validation of a multiplex real-time PCR method to simultaneously detect 47 targets for the identification of genetically modified organisms’, *Analytical and Bioanalytical Chemistry*, 405(21), pp. 6831–6844. Available at: https://doi.org/10.1007/s00216-013-7125-5.

Domingo, J.L. and Giné Bordonaba, J. (2011) ‘A literature review on the safety assessment of genetically modified plants’, *Environment International*, 37(4), pp. 734–742. Available at: https://doi.org/10.1016/j.envint.2011.01.003.

Doyle, J.J. (1990) ‘Isolation of plant DNA from fresh tissue’, in. Available at: https://api.semanticscholar.org/CorpusID:85677467.

Doyle, J.J. and Doyle, J.L. (no date) ‘A rapid DNA isolation procedure for small quantities of fresh leaf tissue’, *PHYTOCHEMICAL BULLETIN* [Preprint], (RESEARCH). Available at: http://worldveg.tind.io/record/33886.

Gómez, C. *et al.* (1998) ‘Perception of mealiness in apples: A comparison of consumers and trained assessors’, *European Food Research and Technology*, 207(4), pp. 304–310. Available at: https://doi.org/10.1007/s002170050337.

Gou, L. *et al.* (2016) ‘Multigene synergism increases the isoflavone and proanthocyanidin contents of Medicago truncatula’, *Plant Biotechnology Journal*, 14(3), pp. 915–925. Available at: https://doi.org/10.1111/pbi.12445.

Heinemann, J.A., Agapito-Tenfen, S.Z. and Carman, J.A. (2013) ‘A comparative evaluation of the regulation of GM crops or products containing dsRNA and suggested improvements to risk assessments’, *Environment International*, 55, pp. 43–55. Available at: https://doi.org/10.1016/j.envint.2013.02.010.

Innes, N.L. (2006) ‘ Global Status of Commercialized Biotech/GM Crops: 2005. ISAAA Briefs No. 34 . By C. James. Ithaca, NY, USA: ISAAA (2005), pp. 46, US$50.00. ISBN 1-892456-38-9 ’, *Experimental Agriculture*, 42(3), pp. 372–372. Available at: https://doi.org/10.1017/s0014479706343797.

McGeoch, M.A. *et al.* (2010) ‘Global indicators of biological invasion: Species numbers, biodiversity impact and policy responses’, *Diversity and Distributions*, 16(1), pp. 95–108. Available at: https://doi.org/10.1111/j.1472-4642.2009.00633.x.

Odell, J.T., Nagy, F. and Chua, N.H. (1985) ‘Identification of DNA sequences required for activity of the cauliflower mosaic virus 35S promoter’, *Nature*, 313(6005), pp. 810–812. Available at: https://doi.org/10.1038/313810a0.

Schreiber, G.A. (1999) 'Challenges for methods to detect genetically modified DNA in foods', *Food Control*, 10(6), pp. 351–352. Available at: https://doi.org/10.1016/s0956-7135(99)00073-0.

Wimalasiri, J.D. and Ranasinghe, R.S. (2010) 'A Study on Strengthening the Laws on Genetically Modified Organisms in Sri Lanka with Special Reference to the Proposed Regulatory Mechanism'.

Formulation and evaluation of natural hair dyeing cream

G.G.C.P.Karunananda[1]*, J.M.K.M.Jambugaswaththa[1] and T.D.C.M.K.Wijayasiriwardena[2]

[1]*Department of Bio systems Technology, Faculty of Technology, Sabaragamuwa University of Sri Lanka*
[2]*Department of Techno Entrepreneurship Development, Manufacturing and Logistics, Industrial Technology Institute, Malabe, Sri Lanka*

* drchandima@iti.lk +94718609190

Abstract

Graying hair is a normal part of aging. However, due to the harmful effects of synthetic dyes, there is growing interest in using safer, eco-friendly natural alternatives, especially for covering gray hair. Many commercial synthetic hair dyes contain Para-Phenylenediamine (PPD), a chemical linked to health risks like respiratory issues and cancer. Additionally, these dyes can cause irritations such as skin and eye discomfort. The composition of the natural hair dye cream consisted of *Indigofera tinctoria* L, *Lawsonia inermis* L, *Murraya koenigii* L, *Tectona grandis* L plant leaves, and *Nigella sativa* L seeds. Coconut oil and olive oil were used to extract the color pigments from the above raw materials. A hair cream was developed using the above oil extract by using a synthetic polymer used in cosmetic formulations. Certain physicochemical parameters, such as pH value, peroxide value, water content, non-aqueous content and thermal stability, were evaluated according to the SLS 611:2021 standard. The pH value was 6.04, the peroxide value was 6.55, the water content was 68.59% (v/w), the non-aqueous content was 27.50% (w/w) and thermal stability was evaluated, that there was no layer separation. A Thin Layer Chromatography fingerprint profile was developed to highlight the herbal ingredients in the formulation. Premarketing consumer surveillance studies were evaluated on the prepared hair dyeing cream with 20 individuals. From the results, the formulations exhibited a better dyeing effect, were free from skin irritation, had great retention capacity, and promoted hair growth. In addition, eco-friendliness is a value addition in comparison with synthetic dye formulations. Further, herbal hair dye cream containing natural colorants has shown better dyeing ability without hair damage or scalp irritation, and hence this formulation proves to be an alternative for synthetic hair dyes. For future improvement of the natural hair dye cream, several aspects can be considered such as refining extraction methods, enhancing color range, improving longevity, ensuring broader consumer appeal through targeted formulations, and aligning the product with sustainable practices. It will help make the cream more effective and commercially successful.

Keywords: Hair dye, gray hair, natural ingredients, SLS 611:2021, physiochemical parameters, survey.

1. Introduction

Hair is an extension of the skin, consisting of the hair follicle and the hair shaft. Beauty treatments only affect the shaft, not the follicle. The hair has three layers; the cuticle, cortex, and medulla. It is made up of proteins, lipids, water, melanin, and trace elements. The shaft can reveal a person’s hair care habits and show signs of wear and tear from the root to the tip, with the tip being the most damaged. The root is usually less damaged and has different chemical properties, affecting how treatments work in this area. The hair shaft is flexible and can stretch significantly before breaking, which is important for cosmetic practices like applying hair extensions (A.Guerra-Tapia *et al*., 2014).

Hair beauty cosmetics are used to change the color or shape of hair. These include temporarily *products as well as permanent treatments. Hair dyes can either temporary or permanently* change hair color by removing some of the natural color or adding a new color. Both men and women use hair dyes to change their natural hair color, delay the appearance of gray hair, or bring back color to gray hair (Guerra-Tapia *et al.,* 2014).

Nowadays, people prefer natural hair dyes over synthetic ones because synthetic dyes can result in unpleasant side effects (Gonzalez, V *et al*., 2019). Synthetic hair dyes often contain harmful chemicals like Para-phenylenediamine (PPD), ammonia, hydrogen peroxide, resorcinol, and parabens. PPD is the main component of commercial synthetic hair dyes (Prabhu *et al*., 2012). These chemicals help to dye the hair but can have serious side effects. PPD, especially when used in darker dyes, can be dangerous if used too often, potentially leading to health problems like respiratory distress, skin and eye irritation, and cancer risk (Dominguez *et al.,* 2001). Ammonia helps the dye ton penetrate the hair but can damage the hair, cause lung irritation, and make the hair frizzy. Parabens, hydrogen peroxide and resorcinol can lead to hormonal issues, scalp irritation, hair loss and even increased the risk of cancer (Gupta *et al*., 2022).

Natural products, which are safe and free from side effects, are being used to keep hair healthy. Around 70% of people over 50 face issues like graying hair (Havalikar *et al*., 2023). Therefore, an attempt has been made to introduce a new hair dyeing cream to increase the use of natural ingredients from plant sources. Plant-based products have been used in traditional medicine for a long time. In this study, a natural black hair dye was developed using a combination of different plant materials. The demand for herbal-based natural medicines is rapidly increasing due to their natural benefits and minimal side effects. Before modern hair dyes were invented, various plant extracts were commonly used for hair dyeing (Vaidya *et al* ., 2007). The plant leaves of *Indigofera tinctoria* Linn, *Lawsonia inermis* Linn, *Murraya koenigii*, *Tectona grandis* and the seeds of *Nigella sativa* are well known Ayurvedic herbal medicines traditionally used as hair colorants and for hair growth. Drugs from plant sources are easily available, less expensive, safe and eco-friendly. Indigo, originally used as a hair dye, could be combined with henna to create different shades of brown to black hair dye.

2. Materials and methods

2.1 Plant sources

Indigofera tinctoria

Kingdom: Plantae
Order: Fabaceae
Family: Fabaceae
Genus: *Indigofera*
Species: *Indigofera tinctoria*

Indigo dye contains various chemical compounds like Flavonoids, Terpenoids, Alkaloids, Glycosides, Indigo tine, Indi Rubin and Rotenoids (Gupta et al.,2022).

Lawsonia inermis

Kingdom: Plantae
Order: Myrtales
Family: Lythraceae
Genus: *Lawsonia*

Species: *Lawsonia inermis*
Lawsone is the main active ingredients in Henna leaves, which has the ability to bond with protein. Henna also contains other substances like Gallic acid, White resin, Sugars, Tannins, Flavonoids and Xanthones (Gupta *et al.*,2022).

Murraya koenigii
Kingdom: Plantae
Order: Sapindales
Family: Rutaceae
Genus: *Murraya* J. Koenig ex L
Species: *Murraya koenigii* L.spreng
Chemical content of Murraya koenigii includes Alkaloids, Flavonoids, Essential oils, Phenylpropanoids, Alkanes and sesquiterpenes also xanthophyll (Nishan *et al*.,2015).

Tectona grandis
Kingdom: Plantae
Order: Lamiales
Family: Verbenaceae – Verbena family
Genus: *Tectona* L.
Species: *Tectona grandis* L.
Tectona grandis leave has revealed the presence of Flavonoids, Phenolic, Alkaloids, and certain Glycosides (Abubakar *et al*., 2014).

Nigella sativa
Kingdom: Plantae
Order: Ranunculales
Family: Ranunculaceae Juss
Genus: *Nigella* L.
Species: *Nigella sativa* L.
Thymoquinone is one of the most active constituent and contain Fixed oil, Proteins, Alkaloid, Saponin and Essential oil (Tavakkoli et al., 2017).

2.2 Collection of raw materials

Natural leaves of *Lawsonia inermis*, *Murraya koenigii* and *Tectona grandis* were collected from the home garden of Ruwanwella, Sri Lanka. *Indigofera tinctoria* was collected from the Ayurvedic medical center in Mawanella, Sri Lanka. *Nigella sativa*, coconut oil and olive oil were purchased from the local market in Sri Lanka.

2.3 Preparation of samples

The collected leaves and seeds were cleaned, rinsed, and shade dried in the room. The dried leaves and seeds were taken to a grinder machine and ground into a coarse powder.

2.4 Formulation of the herbal hair dye

45g of *Indigofera tinctoria*, 15g of *Lawsonia inermis*, 10g of *Murraya koenigii*, and 23g of *Nigella sativa* also 7g of *Tectona grandis* powder were taken separately. All samples were mixed together put into an aluminum container, and heated with 500ml of coconut oil and 500 ml of olive oil. Additionally, water was added to the container as the oil was frying. Heat was supplied until the water vaporized. Finally, the extract was filtered.

2.5 Preparation of the hair dye cream

A hair cream was developed using the above oil extract by using a synthetic polymer used in cosmetic formulations. Firstly, 45 ml of emulsifier 915(Polymer) was added to the container. 10 ml of vitamin E was added and mixed well and 5 ml of Phenoxyehanol (preservative) was added. After, 250 ml of extracted oil was added and 680 ml of distilled water was added and mixed well until homogeneous. Finally, fragrance was added to make it smell better.

2.6 Evaluation of the natural hair dyeing cream

Certain physicochemical parameters such as pH value, peroxide value, water content, total non-aqueous content and thermal stability were evaluated followed by SLS 611:2021 standard. Thin Layer Chromatography (TLC) fingerprint profile was developed to highlight the herbal ingredients in the formulation.

2.6.1 Determination of pH value

Approximately 5g of cream sample was weighed into 100ml beaker. 45ml of distilled water was added and dispersed cream in it. The pH was measured using calibrated pH meter.

2.6.2 Determination of peroxide value

25 g of cream sample was taken in round bottom flask. Petroleum ether and diethyl ether was added to the cream sample containing round bottom flask in 1:1 ratio. (50 ml in each) The mixture was refluxed using low temperature and 45 minutes. Sample was cold in room temperature. 20 ml saturated NaCl solution was added. Again the mixture was refluxed using low temperature at 1 and half hour. The mixture was added separating funnel. Oil containing ether layer was separated and put into the empty flask. The ether layer was evaporated using heating. The oil sample was taken. 5g of oil sample was weighed in a conical flask. 10 ml Chloroform was added and well mixed. 15ml of acetic acid was added. 1 ml of potassium iodide solution was added and shakes well. Dark cool place was allowed for 5 minutes. 75 ml of distilled water was added and mixed well. 2 drops of freshly prepared starch solution was added and mixed well.

Titration- 0.005M Sodium thiosulfate solution was filled to the burette. Sodium thiosulfate solution was added gradually while continuous swelling the flask. Blue color change was observed in oil sample. Blue color end point was recorded.

2.6.3 Determination of water content

5g of the material was weighted into the flask. 200 ml of toluene was added to the flask. A few pieces of dry pumice stone were added. The moisture arm and distillation apparatus was connected. The receiving end of the trap with the toluene was filled by pouring it through the top of the condenser. The flask was heated for 3 hours and 30 minutes. The heat source was removed and allowed the receiving tube to cool. Once the water and solvent have separated, read the volume of water collected.

2.6.4 Determination of total non-aqueous content

3 petri dishes were taken and the empty weight was taken. 5g of samples were added to each petri dish. The petri dish containing the samples was placed in water bath and heated until the volatile material evaporated. Then, these petri dishes were placed in an oven at 105 0c for 2 hours. After 2 hours, the petri dishes were placed in a desiccator and weighed after cooling.

2.6.5 Determination of thermal ability

A 20 mm broad and 5 mm thick strip of the cream was spread on the internal wall of a beaker. The beaker was placed in a humidity chamber. The chamber was maintained at a relative humidity of 60% to 70% and a temperature of 40°C. The beaker was kept in these conditions for 8 hours. After 8 hours, the beaker was removed from the humidity chamber. The cream was examined for any signs of oil separation.

2.6.6 Thin Layer Chromatography profile

Dichloromethane (DCM), Cyclohexane, Ethyl acetate (4:3.4:06v/v) mixture was used as a solvent. The plate was marked 1 cm from the bottom and spots were made with the only DCM solvent sample and water, DCM solvent samples. Then the plate was suspended lightly in the solvent and was allowed to run until it reaches a 8 cm position. Conc. Sulphuric acid was used as the spraying agent and it was sprayed all over the plate and was allowed to dry in the hot plate. The colored spots developed were noted.

3. Results and discussion

Table 1. Physicochemical properties of prepared hair dyeing cream compared with SLS 611:2021

Physicochemical properties	**SLS 611:2021 requirements**	**Results**
pH value at 27±2 0c	4.5 – 8.0	6.04
Peroxide value, mill equivalents/kg, max	10.0	6.55
Water content, per cent by mass, max	70.0	68.59
Total non-aqueous content, per cent by mass, min	15.0	27.50

The physicochemical analysis of the prepared hair dyeing cream using natural plant sources shows promising results for cosmetic use.

The produced natural hair dye has all of the benefits of natural components, this formulation, in addition to working as a hair color, also functions as a hair growth, hair nourisher, conditioner and anti-dandruff agent due to the optimal combination of herbals (Sri Bhuvaneswari *et al.*, 2021). Henna, as the basic powder, serves as a worldwide hair dye because it is utilized for its coloring capabilities all over the world. Henna helps balance the scalp's pH which can prevent premature hair fall and graying (Santhosham *et al.*, 2022), (Naishadham *et al*., 2013). It helps the color retain and bind the keratin to give conditioning effect (Brave *et al*., 2016).

Indigo dye gives a green color, works as an excellent conditioning property, promotes hair growth, prevents scalp itching and helps reduce dandruff (Surya et al., 2021). *Tectona* spp helps hair promoter and useful in scabies also give red color pigments to the product (Deepali *et al*., 2010). The combination of Indigo dye and Tectona dye gave the black color in the final product. Murraya leaves and their essential oil can be used both inside the body and on the hair to promote healthy, long, strong, and shiny hair also prevent hair loss and have high antioxidant capacity (Jain *et al.*,2017). Clinical research supports black seed oil is role in enhancing hair growth, showing it can significantly reduce hair fall, increase hair density and soothe scalp psoriasis without side effects also black seed were used to increase the black color of the final product (Gholamnezhad *et al*., 2016). The data shows that by mixing different amounts of henna and indigo (1:3 best) you can create a dye also natural alternative to synthetic dye (Rao *et al*., 2007). The color gets stronger with more applications, even with regular washing and sunlight. This long-lasting effect is likely due to tannins in the mix, which help the dye stick better and make the color more intense. Coconut oil and olive oil (1:1 ratio) have been utilized as vehicle to prepare hair dye. Coconut oil known as common hair oil acting strengthen hair (Dogan *et al*., 2017). In a survey of 20 volunteers, participants reported high satisfaction, conforming the effectiveness and user-friendliness of the herbal hair dyeing cream. The product met the SLS 611:2021 standards for pH value, peroxide value, water content, total non-aqueous content and thermal stability, ensuring its quality and safety for consumers.

4. Conclusion

The current study examines the formulation of natural hair dyeing cream made from a blend of powdered plant materials containing natural ingredients beneficial for coloring hair. The results clearly show that this formulation works well at a slightly alkaline pH, without causing any damage to the hair. An appropriate black color for hair may be obtained by varying the proportions of Henna and Indigo. As well, raw materials and the final product are biodegradable and theses compositions are stable at room temperature. In addition, eco-friendliness is a value addition in comparison with synthetic dye formulation. Further, herbal hair dye cream containing natural colorant has shown better dyeing ability without hair damage or scalp irritation and hence this formulation prove to be an alternative for synthetic hair dyes.

5. Acknowledgments

I would like to sincerely thank my supervisor, Dr.T.D.C.M.K.Wijayasiriwardena, for his continuous support throughout my research. His guidance and unwavering help have been invaluable in the completion of this study.

6. References

Barve, K. and Dighe, A., 2016. The Chemistry and Applications of Sustainable Natural Hair Products. Springer International Publishing.

Doğan, B., 2017. *Studies on herbal dye formulations* (Doctoral dissertation, Yüksek Lisans Tezi. Yeditepe Üniversitesi Sağlık Bilimleri Enstitüsü. İstanbul. 61s).

Gago-Dominguez, M., Castelao, J.E., Yuan, J.M., Yu, M.C. and Ross, R.K., 2001. Use of permanent hair dyes and bladder-cancer risk. *International journal of cancer*, *91*(4), pp.575-579.

Gholamnezhad, Z., Havakhah, S. and Boskabady, M.H., 2016. Preclinical and clinical effects of Nigella sativa and its constituent, thymoquinone: A review. Journal of ethnopharmacology, 190, pp.372-386.

Gonzalez, V., Wood, R., Lee, J., Taylor, S. and Bussemaker, M.J., 2019. Ultrasound-enhanced hair dye application for natural dyeing formulations. *Ultrasonics Sonochemistry*, *52*, pp.294-304.

Guerra-Tapia, A. and Gonzalez-Guerra, E. (2014). Hair Cosmetics: Dyes. *Actas Dermo-Sifiliográficas (English Edition)*, [online] 105(9), pp.833–839. doi:https://doi.org/10.1016/j.adengl.2014.02.003.

Jain, M., Gilhotra, R., Singh, R.P. and Mittal, J., 2017. Curry leaf (Murraya koenigii): A spice with medicinal property. *MOJ Biol Med*, *2*(3), pp.236-256.

Jaybhaye, D., Varma, S., Gagne, N., Gite, A. and Bhosle, D., 2010. Effect of Tectona grandis Linn. seeds on hair growth activity of albino mice. *International journal of Ayurveda research*, *1*(4), p.211.

Packianathan, N. and Karumbayaram, S., 2010. Formulation and evaluation of herbal hair dye: an ecofriendly process. *Journal of Pharmaceutical Sciences and Research*, *2*(10), p.648.

Prabhu, K.H. and Bhute, A.S., 2012. Plant based natural dyes and mordants: A Review. *J. Nat. Prod. Plant Resour*, *2*(6), pp.649-664.

Rao, Y.M. and Sujatha, P., 2008. Formulation and evaluation of commonly used natural hair colorants.

Santhosham, N., Jahnavi, J., Mounika, N., Vishnu, N., Bhargavi, R., Manjoorilhali, S.K., Vamsikrishna, S. and Aliya, S.D., 2022. Preparation and evaluation of herbal hair dye.

Surya, A., Deepan, T., Alekhya, V. and Dhanaraju, M.D., 2021. A comparative study of dyeing efficiency and retention capacity of formulated polyherbal hair dye. Int. J. Recent Sci. Res, 12(9), pp.43106-43109.

Vaidya, A.D. and Devasagayam, T.P., 2007. Current status of herbal drugs in India: an overview. Journal of clinical biochemistry and nutrition, 41(1), pp.1-11.

Formulation and quality assessment of herbal hair dyeing oil

W.W.D.D.Weedagama[1*], J.M.K.M. Jambugaswaththa[1] and T.D.C.M.K.Wijayasiriwardena.[2]

[1] *Department of Engineering Technology, Faculty of Technology, University of Jaffna, Kilinochchi, Sri Lanka.*
[2] *Department of Techno Entrepreneurship Development, Manufacturing and Logistics, Industrial Technology Institute, Malabe, Sri Lanka.*

* drchandima@iti.lk , +94718609190

Abstract

Hair dyeing oil has been used since ancient times by both males and females which has comparatively high demand among other cosmetics. Commercial synthetic dyes contain Paraphenylenediamine (PPD) as the main active ingredient and also, oxidative hair dyes contain Hydrogen peroxide and ammonia compounds that damage the hair and cause irritation such as eye irritation, skin irritation, etc. Further, respiratory issues, cancer, and chemical burns have been reported. In order to minimize such counter effects, a novel herbal hair dye oil has been developed based on use in the Traditional Medical system in Sri Lanka. For this leaves of *Indigofera tinctoria Linn, Lawsonia inermis Linn, Tectona grandis Linn, Murraya koenigii Linn,* and seeds of *Nigella sativa Linn* were used. Coconut oil and olive oil were used to extract the color pigment from the above raw materials. Physicochemical parameters, including acid value, peroxide value, and stability, were evaluated following the SLS 1341:2021 standard. Thin Layer Chromatography fingerprint was developed for the oil. The acid value was 0.51, the peroxide value was 5.94, and stability passed the test. Premarketing consumer surveillance studies were evaluated on the prepared hair-dyeing oil with 25 individuals. From the result, it can be concluded that the formulation is a safe alternative to synthetic hair dye, as it does not pose risks such as cancer, eye irritation, or hair damage even when combined with synthetic hair dyes. Its natural composition makes it an effective and non-toxic solution for individuals seeking safer options for hair dyes. Furthermore, the formulation developed was eco-friendly, low cost, easy to apply, secure, has a good dying effect, promotes hair growth, has great retention capacity, and people with catarrh or phlegm can also use it. In this formulation, herbal hair dye oil containing natural colorant has shown better dyeing efficiency; gray hair turns the darkest brown and black color. It is also stable in hair with no side effects.

Keywords: Herbal hair dyeing oil, SLS 1341:2021, *Tectona grandis, Indigofera tinctoria,* Survey

1. Introduction

The complex structure of human hair consists of multiple layers and components, each of which adds special properties and capabilities to the hair. The hair shaft consists of three layers: medulla, cortex, and cuticle. A protective barrier is provided by the cutter. Melanin and keratin, on the other hand, provide the cortex with its strength, elasticity, and texture. The strength and volume of the hair can be influenced by the medulla, a soft, porous substance. (Yang Yu , Wen Yang *et al.,* 2016). Beauty treatments only affect the shaft, not the follicle. The hair has three layers made up of proteins, lipids, water, melanin, and trace elements. The shaft can reveal a person's hair care habits and show signs of wear and tear from the root to the tip, with the tip becoming more damaged. The root is usually less damaged and has different chemical properties, affecting how treatments work in this area. Hair shafts are flexible and can stretch significantly before breaking, which is important for cosmetic procedures such as hair extensions. (Guerra-Tapia *el al.,* 2014).

Hair dyeing oil's formulation and quality evaluation represents a novel response to the harmful effects of synthetic hair dyes, which frequently contain para-phenylenediamine (PPD), a chemical with documented health hazards. (Abd-ElZaher *et al*., 2012) The common ingredient in synthetic hair dyes, PPD, has been linked to some unfavorable effects, such as skin irritation, allergic reactions, hair loss, in extreme situations, and long-term health issues. (Leena *et al*., 2021) As people become more aware of these hazards, there is a greater need for safe, natural alternatives to successfully color hair without endangering health. Natural hair dyes have a long history, spanning centuries across many cultures. In the past, various hair colors were produced from plants and other natural substances, which had both nutritional and cosmetic benefits. The main objective of this research is to create a herbal dye oil that can dye two of the most popular hair colors: gray hair, black, or dark brown.

The research investigates the color theory, which states that the combination of red and green colors produces the color black, to achieve this goal. In particular*, Indigofera tinctoria* was used because of its green color. *Tectona grandis* was selected because of its red color. (Abubakar *et al.,* 2014) Researchers used additional naturally occurring plants known for their ability to darken hair to overcome this problem. Black seed (*Nigella sativa), Murraya koenigii* leaves, and *Lawsonia inermis* leaves are some examples. *Murraya koenigii* leaves are used for additional quality. The leaves have high antioxidant content fight free radical damage, lessen hair damage, and encourage the growth of healthy hair. Antimicrobial qualities found in leaves help prevent dandruff and infections on the scalp. (Nishan *et al*., 2015)These leaves avoid dryness and flakiness by assisting in preserving the scalp's moisture balance. Improved blood flow to the scalp by regular application encourages the growth of hair. (Bangre *et al.,* 2022). *Lawsonia inermis* leaves have long been used for hair coloring because of their natural coloring properties. (Jallad *et al.,* 2008) Medicinal hair care products often include hair dye oil in them because it has several advantages when combined. These plants have been chosen for their combined ability to make natural black hair dye and provide other benefits such as strengthening hair and nourishing the scalp.

A natural pigment in plants called lawsone binds with the keratin in the hair to produce an orange-red stain.(Bhuiyan *et al.,* 2017) to naturally dye objects. This pigment *lawsonia inermis* leaves can transmit colors ranging from pale red to rich reddish-brown, contingent upon its processing and combination with other components.(Kannamarikani *et al.,* 2015)Black and brown are among the deeper colors that it may create furthermore dandruff and other scalp diseases can be avoided by using these leaves' inherent antifungal and antibacterial qualities, which can support the maintenance of healthy scalp tissue.(Kumar Singh *et al*., 2015).

2. Material and method

2.1. Materials –

Plant sources- (The following plant materials have been collected from the garden. The materials have been dried in shade and powdered) Leaves of *Indigofera tinctoria, Lawsinia* *inermis, Tectona grandis,Murraya koenigi* and *Nigella sativa* seed. Coconut oil, olive oil, and Distill water.

2.2. Preparation of plant sources powder

All the plants' sources were obtained from locally available sources in the kegalle district. Nigella sativa seeds were also available in the shop. The leaves were harvested from the plant and dried in shade under sunlight for 7-8 days. The leaves were then ground into a powder using a mechanical grinder.

2.3. Preparation of hair dye oil

The herbal hair coloring oil was made by separately weighing 45g of *Indigofera tinctoria*, 15g of *Lawsonia inermis*, 10g of *Murraya koenigii*, 23g of *Nigella sativa*, and 7g of *Tectona grandis* powder. To ensure a precise composition, each powder was carefully measured. To ensure a homogenous composition, these powders were then thoroughly mixed in an aluminum container. 500 ml of coconut oil and 500 ml of olive oil were heated with the mixed powders to form the extraction's foundation. Water was poured into the container gradually to help with the frying process. The oils were able to completely extract the active ingredients from the herbal powders by heating the mixture until all of the water evaporated. The mixture was allowed to cool following the heating process. A pure herbal oil extract was obtained by filtering the mixture after it had cooled to remove any solid leftovers. Lastly, the filtered oil has 5 milliliters of vitamin E added to it as an antioxidant and preservative. Once ready for usage, the produced herbal oil was carefully placed into bottles.

2.4. Evaluation of the physiochemical properties and other parameters of prepared hair-drying oil

The prepared hair dyeing oil was evaluated according to the SLS 1341:2021 standards for various parameters such as Acid value, Peroxide value, and Stability. Additionally, a Thin layer chromatography (TLC) fingerprint profile was developed to highlight the herbal ingredients in the formulation.

2.4.1. Determination of acid value - 5g of the hair oil was accurately weighed into a 250 ml conical flask. 100 ml of a mixed solvent compound of freshly neutralized hot ethyl alcohol was added to the flask. 1ml of phenolphthalein indicator was added to the flask ensuring that the solution remained colorless. The mixture was boiled for about 5 minutes. The solution was titrated with a 0.1M KOH solution while the flask was shaken constantly until a faint pink color. The reading was then taken.

2.4.2. Determination of peroxide value- 5g of hair oil sample was weighed in a conical flask. 10 ml of Chloroform was added and well mixed. 15ml of acetic acid was added. 1 ml of potassium iodide solution was added and shaken well. A dark cool place was allowed for 5 minutes. 75 ml of distilled water was added and mixed well. 2 drops of freshly prepared starch solution were added and mixed well. The solution 0.005M Sodium thiosulfate solution was filled to the burette. Sodium thiosulfate solution was added gradually while continuously swelling the flask. The blue color change was observed in the oil sample. A blue-colored endpoint was recorded.

2.4.3 Stability- A 50ml sample of the hair oil was taken and placed in a clean beaker. A beaker containing the sample was placed under an ultraviolet lamp. The sample was exposed to ultraviolet lamp light continuously for a total period of 6 hours.

2.4.4. Thin layer chromatography profile- Used as a solvent was a mixture of dichloromethane (DCM), cyclohexane, and ethanol (4: 3.4: 06 v/v). Spots were created using the single DCM solvent sample and water, with the plate being marked at a distance of 1 centimeter from the bottom. Once the plate reached an 8 cm position, it was allowed to run in the solvent while being gently suspended in it. Conc. Sulfuric acid served as the spraying agent; the plate was completely covered, and the heated plate was let to dry. The colored patches that appeared were observed.

3. Results and discussion

Table 1: Physiochemical properties of prepared hair dyeing oil compared with SLS 1341:2021.

Physiochemical properties	SLS 1341:2021 requirement	Results
Acid value	1	0.51
Peroxide value	10 max	5.94
Stability	Pass the test (no color change)	Pass the test (no color change)

3.1. Calculation of acid value

$$\text{Acid value}=\frac{56.1\times \text{KOH Consumed during the tiration}\times \text{molarity of KOH (0.1M)}}{\text{weight of the oil taken}}$$

$$=\frac{56.1\times 0.5\times 0.1}{5.50}$$

$$= 0.51$$

3.2. Calculation of peroxide value

$$\text{Peroxide value}=\frac{(V\times N)\times 1000}{W}$$

V= Volume of sodium thiosulfate solution used for the sample

N= Normality of sodium thiosulfate

W= weight of the Oil sample

$$=\frac{2.4\times 0.005\times 1000}{2.020}$$

$$=5.94$$

Tectona grandis L. and *Indigofera tinctoria L.*were used to create a concoction that was intended to convert gray and white hair from dark brown to black. The *Tectona grandis L.* leaves added a red color, and the *Indigofera tinctoria L.* contributed a deep green color. Despite the initial assumption that blending these two colors would produce the color black, *Tectona grandis L. the* leaves' red color took center stage and the desired black shade was not obtained. To this, more components were added to the mixture.To get the right shade of black, *Lawsonia inermis* leaves , *Murraya koenigii L.* leaves, and *Nigella sativa* were mixed into the oil. *Lawsonia inermis* L. acted as a binding agent, enabling the dye to stick to the hair. (Hongyan Cui *et al.,* 2022) and *Nigella sativa* successfully darkened the oil, furthermore, hair follicles and the scalp are nourished by the vital fatty acids, vitamins, and minerals found in black seed oil, which encourages hair development and anti-inflammatory properties contribute to lessening irritation on the scalp, which improves the conditions for hair development, oil's ingredients contribute to stronger hair strands, which lowers breaking and hair loss. (Begum *et al.,* 2020) . To preserve the oil's quality over time, vitamin E was added as a preservative. The components' ratios were changed to balance out the teak leaves' predominant red color. The ratio was 1:3 *Lawsonia inermis* L: and *Indigofera tinctoria L.* (Madhusudan Rao *et al.,* 2007) A survey was administered to twenty-five individuals who had used the specially-made hair dyeing oil. The majority of respondents recommended the product, indicating a high degree of satisfaction with the outcomes. Apart from its efficacy in hair coloring, there have been documented advantages like diminished dandruff and enhanced hair development, reduced hair loss, and reduced headache. Because *Murraya koenigii* leaves benefits are Beta-carotene and proteins found to stimulate hair follicles and encourage hair growth. (Bangre *et al.,* 2022).

They also include amino acids, which lessen hair loss and strengthen the hair shaft, and contain antioxidants and vitamins, including vitamin B, which can help stop hair from graying too soon. They replenish natural pigmentation by nourishing the hair and scalp. The proteins, vitamins, and minerals in curry leaves strengthen hair from the inside out, preventing breaking and shedding. (Nigam *et al.,* 2023). Apart from giving the red color of the *Tectona grandis L. leaves also gives other results.* Possess antimicrobial-active bioactive substances. These are beneficial for both treating and preventing fungal infections and scalp problems like dandruff. A healthier scalp can be encouraged by using hair oil enriched with *Tectona grandis L.* leaves regularly. The anti-inflammatory qualities of the leaf extract can help calm an irritated or swollen scalp. This is especially helpful for people who have sensitive skin or scalp issues like psoriasis or eczema. (Khera *et al.,* 2013).The plants included in this formulation are widely available in Sri Lanka and provide a safe, natural substitute for synthetic hair colors because they don't include potentially dangerous ingredients like hydrogen peroxide or PPD. In conclusion, the herbal hair dye oil successfully added extra health advantages to the hair while transforming gray hair into a dark color. According to survey data, people have reacted favorably to the product, and the results justify the usage of these natural substances for safe and effective hair coloring. Another reason to do this research is that it possible to find the ingredients contained in it and it is oil that can be made without much cost. It was also an environmentally friendly hair dyeing oil product. It can be applied more easily than synthetic hair dye, it safe and can make hair black without side effects. People with phlegm, running nose, sneeze, catarrh can also use it.

4. Conclusion

The designed herbal hair dye oil offers a safe way to color gray hair and white hair and has been used as a solution to synthetic hair dyes. Natural hair dyeing oil that successfully converted gray hair into dark brown or black without the negative side effects of commercial dyes were created by combining ingredients including leaves of *Tectona grandis, Indigofera tinctoria, Lawsonia inermis, Murraya koenigii, and* seed of *Nigella sativa*. The nourishing and antibacterial qualities of the substances in the oil not only provided coloration but also supplied a host of health benefits, such as increased hair growth, less dandruff, improved scalp health, reduced headache, and reduced phlegm. Participants in the survey, which involved 25 volunteers, expressed high levels of pleasure, further validating the formulation's efficacy and user happiness. The SLS 1341:2021 criteria for acid value, peroxide value, and stability was met by the herbal hair dyeing oil, proving its high quality and safety for consumer usage. This formulation was a low-cost, natural, easy-to-apply, eco-friendly, and safe alternative to synthetic hair dyes, making it a promising choice for wider commercial application. The plant ingredients utilized in its preparation are widely available.

5. Reference

Abd-ElZaher, M.A., Fawzy, I.A., Ahmed, H.M., Abd-Allah, A.M. and Gayyed, M.F., 2012. Some toxicological health hazards associated with subchronic dermal exposure to paraphenylene-diamine (PPD): An experimental study. *Egyptian journal of forensic sciences*, *2*(3), pp.105-111.

Abubakar, S., Usman, A.B., Nnadi, O., Alaku, C. and Etim, V.A., 2014. Perfection of organic dye from Tectona grandis (Linn) young leaves methanolic extract for mycological staining. *International Journal of Biological Sciences and Technology*, *6*(6), p.31.

Al-Snafi, A.E., 2019. A review on Lawsonia inermis: A potential medicinal plant. *International Journal of Current Pharmaceutical Research*, *11*(5), pp.1-13.

Bangre, P., Belge, A., Karande, N. and Urkude, M., 2022. A Study of Effect of Shirobhyanga (applying oil on hair and scalp) with Kaidarya siddha Narikela taila (Coconut oil medicated with Murraya koenigii (L.) Sprengel) in the Management of Khalitya (hair fall): A Randomized Controlled Trial. *International Journal of Ayurvedic Medicine*, *13*(3), pp.680-685.

Begum, S. and Mannan, A., 2020. A review on nigella sativa: a marvel herb. *Journal of Drug Delivery and Therapeutics*, *10*(2), pp.213-219.

Begum, S. and Mannan, A., 2020. A review on nigella sativa: a marvel herb. *Journal of Drug Delivery and Therapeutics*, *10*(2), pp.213-219.

Bhuiyan, M.R., Islam, A., Ali, A. and Islam, M.N., 2017. Color and chemical constitution of natural dye henna (Lawsonia inermis L) and its application in the coloration of textiles. *Journal of Cleaner Production*, *167*, pp.14-22.

Cui, H., Xie, W., Hua, Z., Cao, L., Xiong, Z., Tang, Y. and Yuan, Z., 2022. Recent advancements in natural plant colorants used for hair dye applications: a review. *Molecules*, *27*(22), p.8062.

Das, B.C., Reji, N. and Philip, R., 2021. Optical limiting behavior of the natural dye extract from Indigofera Tinctoria leaves. *Optical Materials*, *114*, p.110925.

Fachrunniza, Y., Srivilai, J., Wisuitiprot, V., Wisuitiprot, W., Suphrom, N., Temkitthawon, P., Waranuch, N. and Ingkaninan, K., 2020. Tectona grandis, a potential active ingredient for hair growth promotion. *Songklanakarin Journal of Science & Technology*, *42*(6).

Guerra-Tapia, A. and Gonzalez-Guerra, E., 2014. Hair cosmetics: dyes. *Actas Dermo-Sifiliográficas (English Edition)*, *105*(9), pp.833-839.

Hariprasad, D.L.P. and Anita, P., Effect of PPD on Human Health.

Ishida, W., Makino, T. and Shimizu, T., 2011. Severe hair loss of the scalp due to a hair dye containing para phenylenediamine. *International Scholarly Research Notices*, *2011*(1), p.947284.

Jallad, K.N. and Espada-Jallad, C., 2008. Lead exposure from the use of Lawsonia inermis (Henna) in temporary paint-on-tattooing and hair dying. *Science of the total environment*, *397*(1-3), pp.244-250.

Kalita, H., Mohanty, J.P. and Pokhrel, G., 2022. Formulation and evaluation of natural herbal hair dye gel using lawsonia inermis (henna leaves) and skin irritation studies in albino rats. *Journal of Pharmacy and Pharmacology*, *10*(1), pp.18-24.

Kanniappan, R., 2015. Assessment of dyeing properties and quality parameters of natural dye extracted from Lawsonia inermis. *European Journal of Experimental Biology*, *5*(7), pp.62-70.

Khera, N.E.H.A. and Bhargava, S.A.N.G.E.E.T.A., 2013. Phytochemical and pharmacological evaluation of Tectona grandis Linn. *International Journal of Pharmacy and Pharmaceutical Sciences*, *5*(3), pp.923-927.

Naishadham, P., Sushma, P.R., Dasika, R., Tangirala, S. and Tangirala, S., 2013. Evaluation of organic hair dye formulation by an environment friendly process. *International Journal of Pharmaceutical Sciences Review and Research*, *28*, pp.152-157.

Nishan, M. and Subramanian, P., 2015. Murraya koenigii (curry leave)-A review on its potential. *Int. J. PharmTech Res*, *7*(4), pp.566-572.

Purwal, L., Gupta, S.P.B. and Pande, S.M., 2008. Development and evaluation of herbal formulations for hair growth. *Journal of Chemistry*, *5*(1), pp.34-38.

Putri, P.G. and Warsiki, E., 2019, November. The stability of extract Indigofera tinctoria for color indicator. In *IOP Conference Series: Earth and Environmental Science* (Vol. 347, No. 1, p. 012070). IOP Publishing.

Singh, D.K., Luqman, S. and Mathur, A.K., 2015. Lawsonia inermis L.–A commercially important primaeval dying and medicinal plant with diverse pharmacological activity: A review. *Industrial Crops and Products*, *65*, pp.269-286.

Surya, A., Deepan, T., Alekhya, V. and Dhanaraju, M.D., 2021. A comparative study of dyeing efficiency and retention capacity of formulated polyherbal hair dye. *Int. J. Recent Sci. Res*, *12*(9), pp.43106-43109.

Investigation on impacts of mosquito fern (*Azolla pinnata*) liquid fertilizer on plant growth and yield performance of tomato (*Solanum Lycopersicum*) var. Thilina

Laksikaa Vijayendren[1*], Vijitha Vikneshwaran[1] and Somarathna, W.G.R.S.[2]

[1]*Department of Biosystems Technology, Faculty of Technology, University of Jaffna, Kilinochchi, Sri Lanka.*
[2]*Rice Research Station, Department of Agriculture, Samanthurei, Ampara. Sri Lanka.*

* laksikaa610@gmail.com

Abstract

Tomato, a member of the Solanaceae family, is one of the widely grown fruit crops all over Sri Lanka excluding up-country wet zone. Excessive usage of inorganic fertilizers to improve the yield negatively impacts both environment and human health. Therefore, the current study aimed to investigate the impacts of Azolla liquid fertiliser (ALF) on plant growth and yield performance of tomato var. Thilina. The experiment was arranged in a randomised complete block design with four treatments T1-100% of ALF, T2-50% of Department of Agriculture (DOA) recommended fertilizer+50% of ALF, T3-100% of DOA recommended fertiliser and T4-Control (water), each with three replicates. Foliar and ground application of fertilizers was carried out until pod formation at one-week intervals from one week after transplanting. The plant growth and yield parameters including mean plant height, number of leaves, number of branches, number of flowers, number of pods, and individual pod weight per plant were measured and recorded for statistical analysis. Based on the results, the highest performance of mean plant height (69 cm), number of leaves (30), number of branches (4), number of flowers (13), number of pods (11), individual pod weight per plant (43 g) and total yield (490 g) were recorded under application of 50% of DOA recommended fertilizer+50% of ALF whereas the lowest values for all the parameters studied were observed in control as 53 cm, 23, 3, 6, 3, 30 g, and 100 g respectively. In conclusion, application of 50% DOA recommended fertilizer with 50% Azolla liquid fertilizer improves plant growth and yield of tomatoes significantly. Further, it is expected to carry out the investigation in detail by changing the concentration of ALF and by incorporating some other organic nutrient sources in future to recommend a best organic fertilizer which would reduce the cost spend on chemical fertilizer while improving the plant growth and yield.

Keywords: Azolla, Foliar application, Ground application, Growth, Liquid fertilizer, Yield

1. Introduction

Tomato (*Solanum lycopersicum* L.) is a significant income crop for medium-scale commercial producers (Hanafy and El-Emary, 2018). Tomatoes contain vitamin C and carotenoids, which are beneficial for human health. Consumption of both tomato and tomato-based products reduces the risk of chronic health issues (Ali *et al.*, 2021). The application of organic fertilizers influences the quality and productivity of tomatoes (Gao *et al.,* 2023).

Most farmers apply several chemical fertilizers to enhance yield in intensive agriculture (Da Costa *et al.,* 2013), which may lead to various negative impacts like eutrophication due to nutrient leaching, greenhouse gas emission in the long-term (Blanco-Canqui and Schlegel, 2013). Furthermore, decreases soil health (Jayasinghe and Weerawansha, 2018) and causes several detrimental impacts on human health.

As a larger portion of applied inorganic fertilizers are lost to the environment, it is advantageous to switch to organic fertilizers that release nutrients at a slow rate (Guo *et al*., 2017). In addition, the physical and chemical properties of soil (Janusauskaite and Ciuberkis, 2010), soil fertility and water-holding capacity improve with organic fertilizer application (Beeby *et al*., 2020; Jumadi *et al*., 2014). These beneficial impacts on soil positively influence not only the plant growth but also the quality (Mohamed *et al*., 2018; Kimbonguila *et al*., 2019).

Nowadays, farmers are aware of the application of organic fertilizer to improve their production (Sarolkar, 2022) and organically produced agriculture commodities keep getting attention from consumers. Therefore, the current study intended to produce organic fertilizer from the nitrogen-rich plant *Azolla pinnata* (Lestari and Mutryarny, 2020) and investigate its efficacy in promoting plant growth and yield of tomato (Var.Thilina).

2. Materials and methods

2.1. Study location

The field experiment and laboratory analysis of this study were carried out in Rice Research Station, Department of Agriculture, Samanthurei, Ampara from February 2023 to May 2023.

2.2. Materials

Tomato seeds needed for the experiment were obtained from the local market in Kalmunai, and the Azolla ferns at the mature stage were collected from District Agriculture Training Center (DATC), Jaffna. Further, the poultry manure was collected from a poultry farm in Nintavur. In addition, 50 mL of 13%-15% sugar cane syrup and 5 L of water were used to prepare the liquid fertilizer. A single outlet aquarium air pump and a spray tank were used to homogenize the mixture and to apply the fertilizer respectively.

2.3. Azolla dry particle preparation

Azolla was cultivated in a cultivation bed with the dimension of 180 cm length, 120 cm width and 60 cm depth. A slurry with 2 kg of cow dung and 100 g of super phosphate mixed in 10 L of water was prepared to add to the Azolla bed. Additionally 4 L of water was poured to raise the water level to about 10 cm. Then, about 1 kg of fresh Azolla was introduced and allowed to grow to reach about 1.5 to 3 cm in length and 1 to 3 cm in breadth. After 15 days, matured Azolla was harvested and washed thoroughly to remove any dirt. Next, they were air dried in shaded area at temperature of 25℃ to 27℃ for five days. After that the fully dried Azolla was crushed and kept in sterilized aluminium foil bag with the dimension of 15 cm × 20 cm and thickness of 0.045-0.12mm. Finally, the sample was stored in airtight container at cool condition (below 24℃).

2.4. Preparation of Azolla liquid fertilizer

Dried Azolla particles of 100 g and 100 g of poultry manure were mixed well before tightened up using muslin cloth. After that, it was placed into the bucket (30 cm of diameter and 40 cm of height) filled with 5 L of water and 50 mL of sugar cane syrup in hanging position to avoid accumulation of particles at the bottom and to promote uniform nutrient release. The solution was stirred and homogenized using an aerator pump for 24 hours. The bucket was closed with a lid after making a hole on it to prevent nutrients loss due to evaporation and to facilitate disposal of unwanted gas produced during the process.

After 7 days, the solution was filtered using a mesh with 120 openings per inch. Then, 100 mL of filtered sample was dissolved in 1 L of water to obtain Azolla liquid fertilizer (ALF). Finally, pH, EC and available N were measured using pH meter, electrical conductivity meter and Kjeldahl method respectively whereas available P and K content of the ALF were measured using flame photometer.

2.5. Raising of seedlings and transplanting

Tomato (var.Thilina) seeds were sown in nursery beds. After 18 days, healthy disease-free good quality seedlings were transplanted in potting bags (16 inches × 14 inches) filled with topsoil and compost at 1:1 ratio.

2.6. Other cultural practices

As high temperature observed during the study period, watering was done two times per day after transplanting. Further, weeding and pest and disease control were practiced according to the Department of Agriculture recommendations (Jayasinghe and Weerawansha, 2018).

2.7. Treatments and experimental design

Tomato crops in the potting bags and soil were sprayed with different treatments (fertilizer) mentioned in the Table 1 using sprayer. Each treatment with three replicates was laid in a randomized complete block design.

Table 1. Treatments

Treatments	Components
Treatment 1 (T1)	100% of ALF
Treatment 2 (T2)	50% of DOA recommended fertilizer + 50% of ALF
Treatment 3 (T3)	100% of DOA recommended fertilizer
Treatment 4 (T4)	Water (Control)

2.8. Measurement of plant growth and yield parameters

Plant growth and yield parameters such as mean plant height (cm), number of leaves per plant, number of branches per plant, number of flowers per plant, number of pods per plant, individual pod weight (g) and total yield (g) were measured and recorded for data analysis.

2.9. Data analysis

Recorded data for each week was analyzed using ANOVA in SAS (9.4) package and mean separation was done by the Duncan multiple range test at $p=0.05$.

3. Results and discussion

The Table.2 below show the properties of soil used in the current study.

Table 2: Characterization of potting soil

Property	Value
pH	6.10
EC (µS/cm)	5.20
Organic carbon content (%)	0.24

Available phosphorous (ppm)	7.65
Available potassium (ppm)	109.30
Soil type	Non-calcic brown

Available N, P and K content along with EC and pH of Azolla liquid fertilizer are shown in the Table 3 below.

Table 3. Properties of Azolla liquid fertilizer

Property	Value
pH	4.80
EC (µS/cm)	3.02
Available nitrogen	5.0%
Available phosphorous	1.5%
Available potassium	1.8%

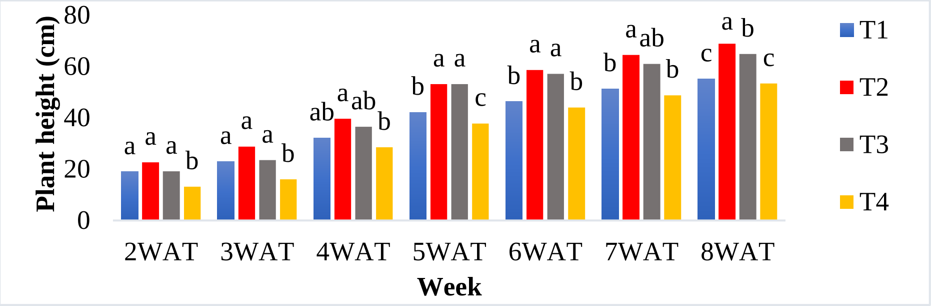

Figure 1: Mean plant height per plant at a week interval

There were significant differences observed among all the treatments for mean plant height at *p=0.05*. According to the Figure 1 above, significantly highest mean plant height was recorded under T2 (68.83[a]). A recent study of Rajeevan et al., 2024 revealed that Azolla solution increases the plant height of chili but as a combination with vermicompost.

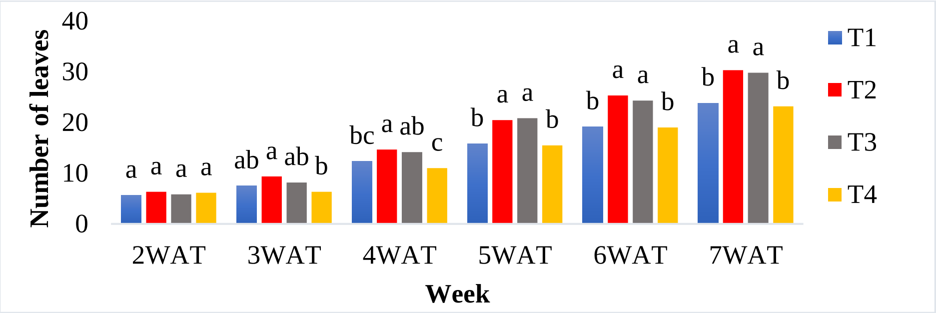

Figure 2: Mean number of leaves per plant at a week interval

Significant differences were recorded among all four treatments in terms of mean leave number per plant at *p=0.05*. Based on Figure 2, statistically similar responses were observed in T2 and T3 for leaf number per plant. However, T2 showed comparatively better performance (30.33[a]) than other all treatments. Gao *et al.,* 2023 also found the impact of

Azolla liquid organic fertilizer in the highest leaves number along with goat manure application.

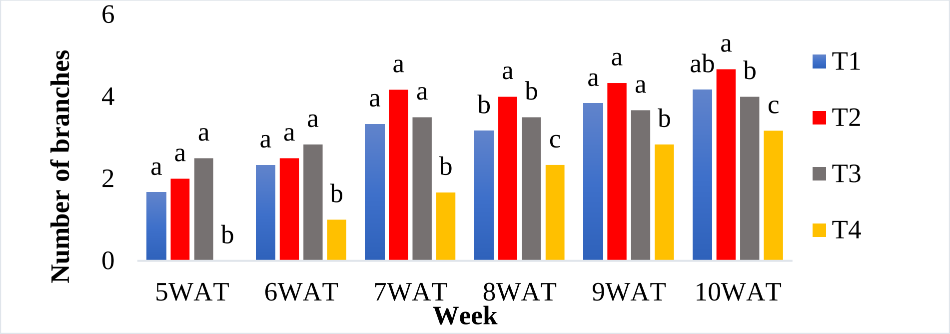

Figure 3: Mean number of branches per plant at a week interval

With a significant difference at *p=0.05*, the highest mean number of branches was observed under T2 (4.66^{a}) while T4 (3.16^{c}) produced the lowest number of branches. Dungga *et al.*, 2020 also revealed the positive impacts of Azolla liquid fertilizer on number of productive branches in chili crop.

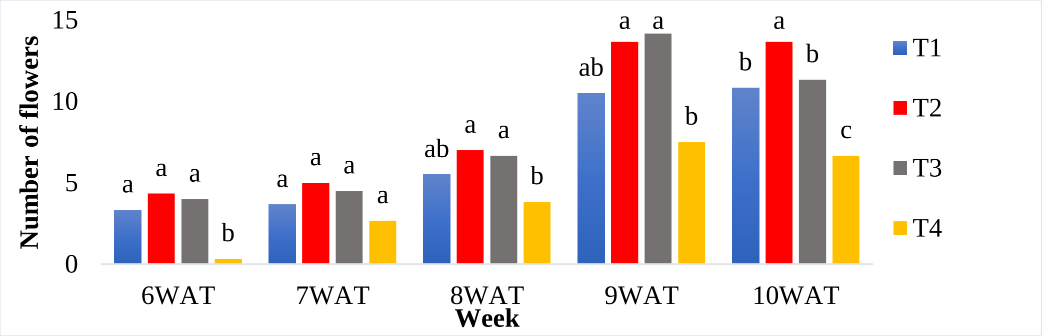

Figure 4: Mean number of flowers per plant at a week interval

Significant differences (*p=0.05*) were recorded among the treatments in terms of mean flower number per plant toward the end of the study period whereas T2 performed well (13.66^{a}) compare to other treatments.

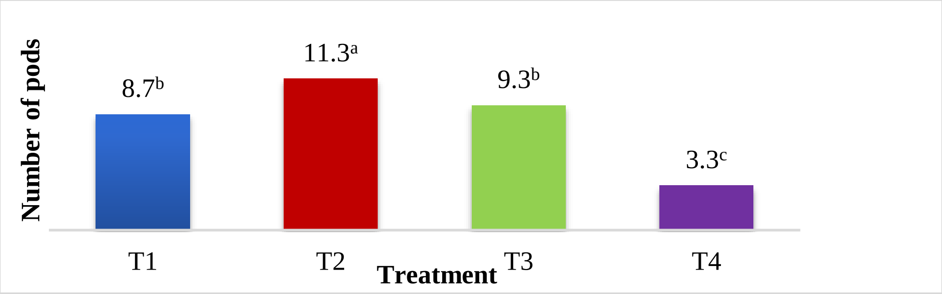

Figure 5: Number of pods per plant

Based on Figure 5 above, number of pods produced per plant under T2 statistically varies from all other treatments. In contrast, the lowest number of pods was observed in T4 (Control) while T1 and T4 did not show any statistical differences. Sarolkar, 2022 also studied the effectiveness of Azolla liquid fertilizer as high on tomato fruit development.

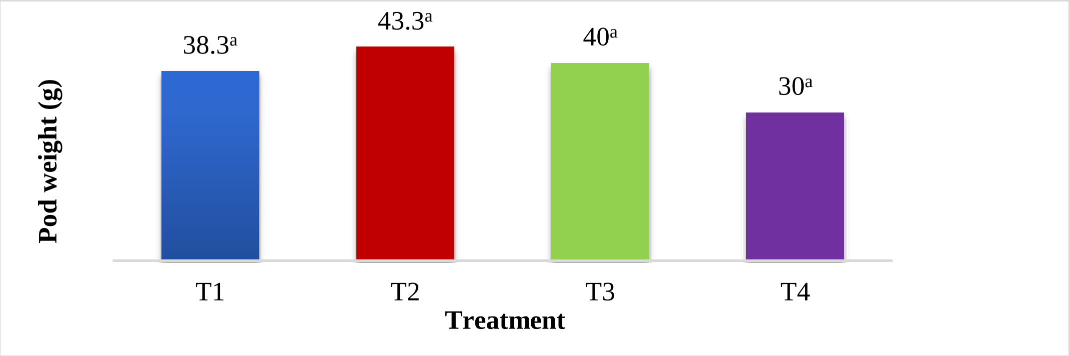

Figure 6: Mean individual pod weight (g)

At harvest, there was no significant difference at $p=0.05$ observed on pod weight among all four treatments. However, the highest mean weight of individual pod was observed in T2 followed by T3, T1, and T4 (control).

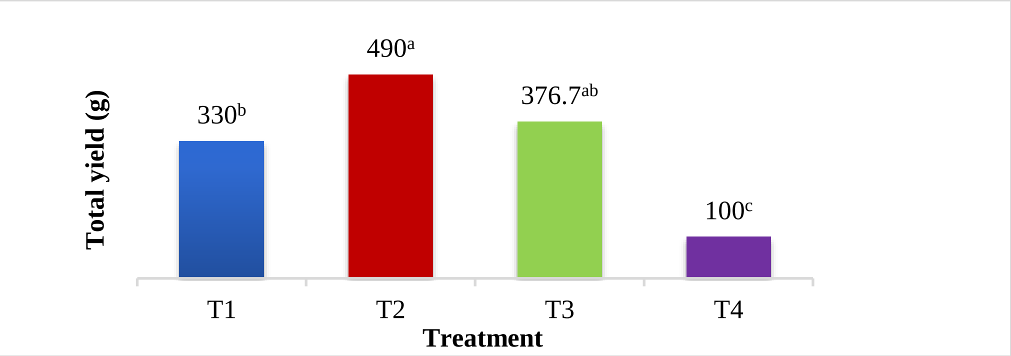

Figure 7: Total yield of tomato

With significant difference at $p=0.05$, there was a remarkable variation among all four treatments in terms of total yield. As for other parameters studied T2 led to the highest total weight at harvesting (490 g) whereas the minimum yield was noticed under T4 (100 g). Adhakary *et al.* (2016) found that the combination application of 50% organic fertilizer and inorganic fertilizer resulted in maximum tomato production.

4. Conclusion

The study revealed that application of 50% of the Department of Agriculture recommended fertilizer with 50% Azolla liquid fertilizer can improve the plant growth and development parameters such as plant height, number of leaves, number of branches, number of flowers, number of pods, individual pod weight and total yield in tomato (Var-Thilina). Hence, it can be concluded that the above-mentioned combination of fertilizers has greater potential to enhance the growth and development of tomato crop compared to the sole application of the Department of Agriculture recommended fertilizer and Azolla liquid fertilizer.

5. Reference

Adhakary, B., Dash, P.K., Sajid, K. and Mannan, M.A. (2016) 'Yield Response of Tomato under Different Combination of Manures and Fertilizers 2016', *Journal of Agriculture and Veterinary Sciences*, 9(1), pp. 6–16. DOI: 10.9790/2380-09110616

Ali, M.Y., Sina, A.I., Khandker, S.S., Neesa, L., Tanvir, E.M., Kabir, A., Khalil, M.I. and Gan, S.H. (2021). Nutritional Composition and Bioactive Compounds in Tomatoes and Their Impact on Human Health and Disease: A Review. *Foods*, *10*(1), 45. DOI: 10.3390/foods10010045

Beeby, J., Moore, S., Taylor, L. and Nderitu, S. (2020). Effects of a One-Time Organic Fertilizer Application on Long-Term Crop and Residue Yields, and Soil Quality Measurements Using Biointensive Agriculture. *Front. Sustain. Food Syst.*, *4*, 67. DOI: 10.3389/fsufs.2020.00067

Blanco-Canqui, H. and Schlegel, A.J. (2013). Implications of Inorganic Fertilization of Irrigated Corn on Soil Properties: Lessons Learned after 50 Years. *J. Environ. Qual.*, *42*, 861–871.

Da Costa, P.B., Beneduzi, A., de Souza, R., Schoenfeld, R., Vargas, L.K. and Passaglia, L.M.P. (2013). The effects of different fertilization conditions on bacterial plant growth promoting traits: Guidelines for directed bacterial prospection and testing. *Plant Soil*, *368*, 267–280.

Dungga, N.E. et al., (2020). Growth and production of chili (*Capsicum annuum* L.) on the application of Trichoderma sp. and Azolla liquid organic fertilizer, *IOP Conference Series: Earth and Environmental Science*, 486(1). DOI: 10.1088/1755-1315/486/1/012119

Gao, F., Li, H., Mu, X., Gao, H., Zhang, Y., Li, R., Cao, K. and Ye, L. (2023). Effects of Organic Fertilizer Application on Tomato Yield and Quality: A Meta-Analysis. *Appl. Sci.*, *13(4)*, 2184. DOI: 10.3390/app13042184

Guo, J.X., Hu, X.Y., Gao, L.M., Xie, K.L., Ling, N., Shen, Q.R., Hu, S.J. and Guo, S.W. (2017). The rice production practices of high yield and high nitrogen use efficiency in Jiangsu, China. *Sci. Rep.*, *7(1)*, 2101. DOI: 10.1038/s41598-017-02338-3

Hanafy, A. and El-Emary, G.A.E. (2018). Role of *Azolla Pinnata* Biofertilizer Extract in Producing Healthy Tomatoes, *Asian Journal of Research in Biochemistry*, *3(3)*, 1–8. DOI: 10.9734/AJRB/2018/46785

Janusauskaite, D. and Ciuberkis, S. (2010). Effect of different soil tillage and organic fertilizers on winter triticale and spring barley stem base diseases. *Crop Prot., 29,* 802–807.

Jayasinghe, H. and Weerawansha, A. (2018). Effect of Compost and Different NPK Levels on Growth and Yield of Three Tomato (*Solanum lycopersicum*) Varieties in Sri Lanka, *Journal of Advanced Agricultural Technologies*, *5(2),* 129–133.

Jumadi, O. (2014). Influence of Azolla (*Azolla microphylla* Kaulf.) compost on biogenic gas production, inorganic nitrogen and growth of upland kangkong (Ipomoea aquatica Forsk.) in a silt loam soil, *Soil Science and Plant Nutrition*, *60(5)*, 722–730.

Kimbonguila, A. et al., (2019). Effect of Physical Treatment on the Physicochemical, Rheological and Functional Properties of Yam Meal of the Cultivar “Ngumvu” From Dioscorea Alata L. of Congo, *International Journal of Recent Scientific Research*, *10(11 B)*, 30693–30695. DOI: 10.24327/IJRSR

Lestari, S.U. and Mutryarny, E. (2020). Using POC *Azolla Mycrophylla* and Urea Fertilizer: Lettuce Plant (Lactuca Sativa L) Context, *IOP Conference Series: Earth and Environmental Science*, 469(1). DOI: 10.1088/1755-1315/469/1/012115

Mohamed, A.S., Shohba, N.E.A., Abou-Taleb, S.A., Abbas, M.S. and Soliman, A.S. (2018). Beneficial effects of Bio-Organic fertilizers as a partial replacement of chemical fertilizers on productivity and fruit quality of Pomegranate trees. *Biosci. Res.*, *15*, 4603–4616.

Rajeevan, R., Vijitha, V. and Anchanadevi, S. (2024). Investigation on Efficacy of Azolla with Different Organic Fertilizers as Plant Growth Enhancer on Chili (Var.Super). *Proceedings of the 28th International Forestry and Environment Symposium 2024 of the Department of Forestry and Environmental Science, University of Sri Jayewardenepura, Sri Lanka,* pp. 216. DOI: 10.31357/fesympo.v28.7129

Sarolkar, P.S. (2022). Growth response and production of tomato plant with application of Azolla composting, *International Journal of Advances in Engineering and Management*, 4(2), 233–236.

Optimization of an RNA extraction method for *Aglaonema.* Spp for improving RNA yield and quality

R.A.S.T. Ranasinghe[1*], M.H.A.D. Subhashini[2], and N.M.C. Nayanakantha[1].

[1]*Department of Biosystems Technology, Faculty of Technological Studies, Uva Wellassa University of Sri Lanka.*
[2] *National Plant Quarantine Service, Canada Friendship Road, Katunayake.*

* senuriranasinghe2019@gmail.com

Abstract

Acquiring adequate amounts of high-quality RNA is critical in plant molecular biology and genetic investigations. Several methods for RNA extraction from plants are known in the literature, owing mostly to the high biochemical variety found in each species and tissue, which can complicate or impede extraction. *Aglaonema* spp. (Araceae: family) is an important ornamental foliage of great economic value and has a good export market in Sri Lanka. However, there are only a few molecular investigations available for the species, specifically for RNA isolation. Also, extracting RNA from *Aglaonema* is difficult due to plant tissue's fibrous, protein-rich structure, which can contain high levels of polysaccharides, polyphenols, and secondary metabolites that can interfere with RNA extraction and downstream uses. This research aims to develop an optimized RNA extraction protocol specifically tailored for the *Aglaonema* plant to improve RNA quantity and quality. Here, the quality and yields of RNA isolates were compared using three different extraction protocols: one protocol that uses the TRIzol reagent, one that applies LiCl lysis buffer, and one commercial kit (Biospin Total RNA Extraction KIT) and determines the most suitable protocol for maximum RNA yield and quality of *Aglaonema* plant by optimizing the selected method. The quality of RNA was evaluated through spectrophotometric techniques and formaldehyde-agarose gel electrophoresis. The Biospin Total RNA Extraction Kit produced the highest RNA yields and quality for *Aglaonema*. For the optimized protocol, the average RNA yield from *Aglaonema* tissues was 163.63 ng/µl, and the A260/A280 and A260/A230 ratios were 2.1 and 1.8, respectively. Further confirmation was done by formaldehyde-agarose gel electrophoresis. This protocol supports reliable downstream application

Keywords: RNA Extraction, *Aglaonema* spp., Araceae family, Biospin Total RNA Extraction KIT, Ornamental foliage plant

1. Introduction

RNA extraction is a procedure in plant molecular biology and genetic studies that is pivotal because it provides the basis for transcriptomic studies, gene expression analysis and functional genomics. The reliability and accuracy of these investigations depends on high quality RNA since extracted RNA integrity and purity implicates reverse transcription PCR (RT-PCR), RNA sequencing (RNA-Seq) and cDNA library construction (Ghawana *et al.*, 2011). Nevertheless, the extraction of RNA from plant tissues comes with unique challenges because of the biochemical complexity of plant cells; the presence of secondary metabolites, polysaccharides, and polyphenols that can co-purify with RNA may impede the extraction process. Isolating RNA from Araceae plants like *Aglaonema* spp., an important ornamental plant, is particularly challenging. Despite its horticultural and export significance, there is limited research on *Aglaonema*, including optimized RNA extraction protocols. The fibrous and protein-rich tissues of *Aglaonema* pose significant obstacles as they tend to bind nucleic acids and cause the degradation of RNA (Aarum *et al.*, 2020). Moreover, *Aglaonema* tissues are rich in polysaccharides, polyphenols, and secondary metabolites, which are well-known to interfere with RNA isolation by forming viscous solutions or precipitates that reduce yield and quality. Traditional RNA extraction methods, such as those utilizing the TRIzol reagent, have been widely used across various plant species. However, efficiency may be strongly dependent on plant tissue and species, often providing RNA of compromised quality or contaminated with secondary compounds (Ghawana *et al.*, 2011). LiCl-based lysis buffers have also been applied as an alternative for the selective precipitation of polysaccharides; however, this does not always provide a guarantee for high RNA integrity (Meier, 1988). Commercial RNA extraction kits, designed to streamline the process and reduce contamination, have increasingly gained popularity in plant molecular studies, with some kits specifically formulated to overcome plant-specific challenges (Schroeder *et al.*, 2006).

In this study, we aimed to develop and optimize an RNA extraction protocol for *Aglaonema* spp. by comparing the efficiency of three different extraction methods: a TRIzol reagent-based protocol, a LiCl-based lysis buffer method, and a commercial kit (Biospin Total RNA Extraction Kit). Our primary goal was to tailor the protocol that produces the highest RNA yield and purity suitable for downstream molecular applications. The optimization of RNA extraction from *Aglaonema* spp. is expected to advance molecular research and genetic studies in this ornamental species, facilitating further investigations into its physiology, stress responses, and potential for genetic improvement.

2. Materials and methods

2.1 Plant materials

Healthy *Aglaonema* spp. plants, exhibiting uniform morphological characteristics, were selected as the experimental subjects. These plants were cultivated under controlled conditions in the net house belonging to the Plant Pathology Division at the National Plant Quarantine Service (Katunayake, Sri Lanka) Leaf samples were harvested and immediately processed to ensure the preservation of RNA integrity.

2.2 Reagents and chemicals

The Analytical-grade chemicals were used, including TRIzol reagent, chloroform, isopropanol, ethanol, LiCl, and the BIOSPIN Plant Total RNA Extraction Kit. Mercaptoethanol, RNase-free water was used throughout the procedures. All the reagents were prepared with 0.1% diethylpyrocarbonate (DEPC) treated water.

2.3 RNA isolation protocols

To optimize RNA extraction, three methods were evaluated: the TRIzol reagent-based method, the LiCl lysis buffer-based method, and the BIOSPIN Plant Total RNA Extraction Kit. RNA yield, purity, and integrity were assessed using spectrophotometry and formaldehyde-agarose gel electrophoresis.

TRIzol Method: 200 mg of leaf tissue was homogenized in 1 mL TRIzol reagent. After adding 200 µL chloroform, the mixture was vortexed, incubated on ice, and centrifuged. The aqueous phase was extracted, RNA was precipitated with isopropanol, washed with ethanol, and resuspended in 50 µL RNase-free water (Allen and Allen, 2016).

LiCl precipitation Method: 100 mg of leaf tissue was homogenized in 1 mL LiCl lysis buffer, incubated on ice, and centrifuged. RNA was precipitated with 8M LiCl, washed with ethanol, air-dried, and resuspended in 50 µL RNase-free water (Meier, 1988).

Commercial Kit (BIOSPIN Plant Total RNA extraction Kit): Using the BIOSPIN Plant Total RNA Extraction Kit (Hangzhou Bioer Technology, China), RNA was extracted according to the manufacturer's protocol. The lysis buffer containing Mercaptoethanol and the plant RNA reagent were used for testing on all leaf samples. Ethanol was used for RNA washing, and RNase-free water was used for final RNA resuspension

Optimization of BIOSPIN KIT: The BIOSPIN Plant Total RNA Extraction Kit was optimized for RNA extraction from *Aglaonema* by comparing three different buffers (AG, BG, and BG+) provided by the kit. Approximately 100 mg of leaf tissue was processed with each buffer. The BIOSPIN Plant Total RNA Extraction Kit was optimized by varying leaf tissue amounts (100 mg vs. 200 mg) and elution methods (single 100 µL vs. two 50 µL elutions).

2.4 RNA quality and yield assessment

RNA concentration and purity were measured using a spectrophotometer, with A260/A280 and A260/A230 ratios used to assess contamination. RNA integrity was confirmed via formaldehyde-agarose gel electrophoresis, and the yield was recorded for each extraction method and condition.

3. Results and discussion

RNA isolation is crucial in plant molecular biology experiments, such as gene expression and transcriptomics. However, achieving high-quality and sufficient RNA can be challenging, particularly in plants, due to their biochemical composition, which can obstruct extraction. The diversity of plant cellular contents means no single RNA isolation method is universally applicable. Members of the Araceae family, for instance, contain fibrous, protein-rich tissues with high polysaccharides, polyphenols, and secondary metabolites that complicate nucleic acid extraction (Jaakola *et al.*, 2001). This highlights the need for optimized extraction methods to advance molecular studies for the species of this family.

3.1 Comparison of RNA extraction methods

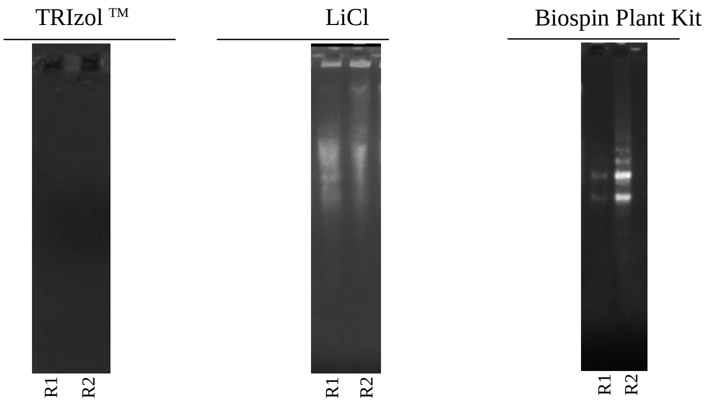

Figure *8*. Qualitative analysis of RNA by agarose gel electrophoresis. Denaturing agarose gel (1%) electrophoresis of total extracted RNA (2µL) stained with Diamond ™ Nucleic Acid Dye. For the total RNA was extracted from Aglaonema leaves were performed in duplicate (R1 and R2).

In this study, Firstly, three RNA isolation methods were compared, and the success of each protocol was judged by the quantity, purity, and integrity of the recovered RNA. Figure *8* shows the outcomes for RNA integrity, assessed by agarose gel electrophoresis.

In the TRIzol™ method, no RNA bands appeared, nor was a degradation smear observed. The LiCl-based extraction method produced smeared and faint bands, indicating RNA degradation and potential contamination, with no distinct 28S and 18S rRNA bands observed, suggesting suboptimal RNA integrity. In contrast, the Biospin Plant total RNA extraction Kit yielded the most distinct and intense 28S and 18S rRNA bands, indicating minimal degradation and superior RNA integrity and concentration. These results suggest that the Biospin Plant Kit is the most effective method based on the RNA quality assessment via gel electrophoresis

Table 4. Analysis of RNA yield and purity for different methods. spp.

Method	Concentrations (ng/µL)	A260/A280	A260/A230
Bio Spin Total RNA Extraction Kit	128.97 ± 15.98^b	1.81 ± 0.22^a	0.72 ± 0.08^a
LiCl Precipitation	230.83 ± 72.79^a	1.35 ± 0.13^b	0.37 ± 0.06^b
TRIzol	238.12 ± 0.07^a	1.41 ± 0.07^b	0.25 ± 0.03^c

Spectrophotometric analysis further quantified the differences in RNA yield and purity. Table 4 Shows the concentration of RNA extracted with the Biospin Plant Kit (128.97 ± 15.98 ng/µL) was lower compared to LiCl based method (230.83 ± 72.79 ng/µL) and TRIzol™ Method (238.12 ± 0.07 ng/µL). However, the purity ratios (A260/A280 and A260/A230) are critical for assessing contamination. The Biospin Plant Kit exhibited the highest A260/A280 ratio of 1.81 ± 0.22, indicating a high level of purity with minimal protein contamination. In contrast, the TRIzol™ and LiCl methods yielded lower A260/A280 ratios (1.41 ± 0.07 and 1.35 ± 0.13, respectively), suggesting the presence of protein or other contaminants. The A260/A230 ratio, which reflects contamination from organic compounds and chaotropic salts, was highest for the Biospin Plant Kit (0.72 ± 0.08), further confirming its superior purity. The significantly lower ratios for TRIzol™ (0.25 ± 0.03) and LiCl (0.37 ± 0.06) indicate substantial contamination, which could interfere with downstream applications such as RT-PCR.

In summary, while TRIzol™ and LiCl methods produce higher RNA concentrations, the Biospin Plant Kit provides superior RNA purity and minimal degradation, as demonstrated by clear gel bands and favorable spectrophotometric ratios. Thus, the Biospin Plant Kit is the preferred method for extracting high-quality RNA from *Aglaonema*, especially for applications requiring high purity.

3.2 Optimization of the selected RNA extraction method

After selecting Biospin Plant total RNA extraction Kit as the most effective RNA extraction method, we moved on to optimize the process by evaluating the performance of three different lysis buffers (AG, BG, and BG+). Lysis buffers are critical in the RNA extraction process as they influence the efficiency of cell disruption and RNA preservation (Wilfinger et al, 1997). Therefore, this stage of the study involved systematically testing each lysis buffer to determine its impact on RNA yield and purity in *Aglaonema*.

Table 5. Analysis of RNA yield and purity for different Lysis buffers.

Buffer	**Concentrations (ng/µL)**	**A260/A280**	**A260/A230**
AG	5.43 ± 1.23^{c}	0.67 ± 0.28^{b}	0.52 ± 0.15^{ab}
BG	151.43 ± 1.51^{a}	2.38 ± 0.03^{a}	1.12 ± 0.39^{a}
BG+	77.68 ± 13.43^{b}	2.00 ± 0.10^{a}	0.32 ± 0.15^{b}

The concentration and purity ratios (A260/A280 and A260/A230) obtained from the spectrophotometric analysis for RNA extracted using the three lysis buffers are presented in Table 9. Significant differences were observed in the RNA concentrations between the buffers, with BG yielding the highest concentration of RNA (151.43 ± 1.51 ng/µL), followed by BG+ and AG .The RNA concentration obtained from the BG buffer was significantly higher compared to the other buffers, indicating its superior efficiency in RNA extraction. The purity of the extracted RNA, as indicated by the A260/A280 ratio, showed that the BG and BG+ buffers produced RNA with acceptable purity (2.38 ± 0.03 and 2.00 ± 0.10, respectively), while the RNA extracted using the AG buffer showed a low purity (0.67 ± 0.28), which is indicative of protein contamination. The optimal A260/A280 ratio for RNA purity is generally considered to be around 2.0, which confirms that both BG and BG+ buffers yielded RNA of suitable purity for downstream applications (Wilfinger, Mackey and Chomczynski, 1997). Similarly, the A260/A230 ratios, which reflect the presence of contaminants such as phenols or other organic compounds, were highest for RNA extracted using the BG buffer (1.12 ± 0.39), while the AG buffer exhibited the lowest ratio (0.52 ± 0.15). The BG+ buffer produced RNA with a moderate A260/A230 ratio (0.32 ± 0.15). Typically, A260/A230 ratios between 2.0 and 2.2 are considered indicative of pure RNA (Xu *et al.*, 2009) . The suboptimal A260/A230 ratios for all buffers suggest the presence of some residual contaminants, although the RNA extracted using the BG buffer had a significantly better purity profile than the other buffers.

Figure 9. Qualitative analysis of RNA by agarose gel electrophoresis. Denaturing agarose gel (1%) electrophoresis of total extracted RNA (2µL) stained with Diamond $^{\text{TM}}$ Nucleic Acid Dye. For the total RNA was extracted from Aglaonema leaves were performed in duplicate (R1 and R2).

Formaldehyde agarose gel electrophoresis confirmed the RNA quality extracted with BG and BG+ buffers (Figure 2). Both buffers showed distinct 28S and 18S rRNA bands, indicating intact RNA with minimal degradation. The BG buffer produced slightly more intense rRNA bands than BG+, aligning with its higher RNA concentration in spectrophotometric analysis. Consistent banding patterns in BG buffer lanes (R1 and R2) confirmed reproducibility. Although BG+ buffer yielded intact RNA, the bands were less intense due to lower RNA concentration. However, it is noteworthy that RNA samples extracted using the AG buffer did not meet the necessary concentration criteria required for gel electrophoresis analysis. The results indicate that the BG buffer is the most suitable lysis buffer for extracting RNA from *Aglaonema* using the Biospin Total RNA Extraction Kit. This buffer yielded the highest RNA concentration, with acceptable purity and integrity, as confirmed by both spectrophotometric analysis and RNA gel electrophoresis.

Treatment	Concentrations (ng/µL)	A260/A280	A260/A230
T1	98.70 ± 42.64^{ab}	1.98 ± 0.63^{a}	0.63 ± 0.11^{b}
T2	102.93 ± 27.44^{ab}	2.07 ± 0.05^{a}	0.81 ± 0.11^{b}
T3	55.80 ± 15.10^{b}	2.27 ± 0.63^{a}	0.55 ± 0.18^{b}
T4	163.63 ± 10.17^{a}	2.13 ± 0.05^{a}	1.81 ± 0.04^{a}

Table 6. Analysis of RNA yield and purity for different Treatments.

After selecting the BG buffer as the most suitable lysis buffer for RNA extraction from *Aglaonema* using the Biospin plant Total RNA Extraction Kit, further optimizations were conducted to enhance RNA yield and quality. The optimization focused on varying the quantity of plant samples and the method of elution buffer application. In here, four treatments were evaluated:

T1: 100 mg of plant sample, elution buffer applied twice (50 µL + 50 µL).
T2: 100 mg of plant sample, elution buffer applied once (100 µL).
T3: 200 mg of plant sample, elution buffer applied twice (50 µL + 50 µL).
T4: 200 mg of plant sample, elution buffer applied once (100 µL)

The spectrophotometric data showed that the quantity and purity of RNA varied significantly depending on the treatment (as seen in Table 6). The RNA concentration was highest in T4 at 163.63 ± 10.17 ng/µL, which was statistically significant compared to the other treatments. T3 resulted in the lowest RNA concentration at 55.80 ± 15.10 ng/µL. The A260/A280 ratios, indicative of protein contamination, were consistent across the treatments, ranging from 1.98 ± 0.63 to 2.27 ± 0.63, all within the acceptable range of 1.8 to 2.0, suggesting low levels of protein contamination. The A260/A230 ratios, which assess contamination by organic solvents and other impurities, showed the highest purity in T4 (1.81 ± 0.04), followed by T2 (0.81 ± 0.11), indicating that the method of applying the elution buffer (single elution in T4) is more effective in reducing impurities.

The RNA integrity was assessed using formaldehyde agarose gel electrophoresis (Figure 10). The gel images showed that T4 produced the most intense and sharp bands with minimal smearing, indicating the highest integrity and quality of RNA. In contrast, T3 displayed fainter bands, reflecting the lower yield and purity observed in the spectrophotometric analysis.

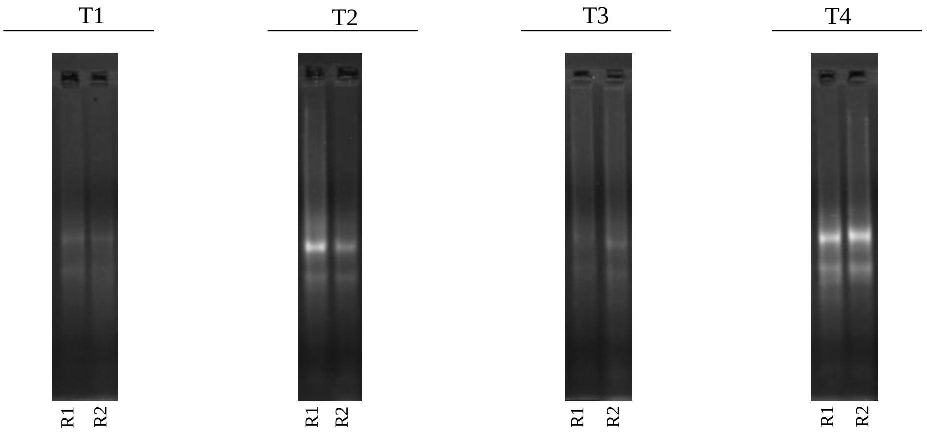

Figure 10. Qualitative analysis of RNA by agarose gel electrophoresis. Denaturing agarose gel (1%) electrophoresis of total extracted RNA (2µL) stained with Diamond ™ Nucleic Acid Dye. For the total RNA was extracted from Aglaonema leaves were performed in duplicate (R1 and R2).

The optimization trial results suggest that using 200 mg of plant material with a single 100 µL elution (T4) provides the best balance between RNA yield and purity. The two-step elution process (T1 and T3) led to lower RNA concentrations. In contrast, a single elution with 100 µL (T4) maximized RNA recovery and purity. Therefore, according to the results, the optimal protocol for *Aglaonema* RNA extraction is the BioSpin Total RNA Extraction Kit with BG buffer, using 200 mg of plant material and a single 100 µL elution. This method provides RNA suitable for qPCR and RNA-Seq.

4. Conclusion

The study successfully developed and optimized an RNA extraction protocol specifically tailored for *Aglaonema* spp., addressing the challenges posed by its fibrous, protein-rich tissues with high levels of polysaccharides, polyphenols, and secondary metabolites. Among the three evaluated methods -TRIzol reagent-based extraction, LiCl-based lysis buffer method, and the Biospin Total RNA Extraction Kit-the Biospin Kit, when used with the BG lysis buffer and incorporating the proposed modifications, demonstrated the highest efficacy. This optimized protocol reliably yields high-quality RNA suitable for cDNA synthesis and gene expression analysis, making it a valuable tool for molecular studies in *Aglaonema* spp. and potentially other plant species within the Araceae family. This method enhances the capability to perform advanced molecular research on *Aglaonema* and provides a robust foundation for future investigations in plant molecular biology.

5. Acknowledgement

I would like to express my sincere gratitude to the National Plant Quarantine Service, Katunayake, Sri Lanka, for providing the facilities and support necessary to conduct this research in their laboratories. I extend my deepest appreciation to Uva Wellassa University of Sri Lanka. Special thanks go to Ms. M.H.A.D. Subhashini and Dr. N.M.C. Nayanakantha for their invaluable support and guidance throughout the course of this study.

6. References

Aarum, J. *et al.* (2020) 'Enzymatic degradation of RNA causes widespread protein aggregation in cell and tissue lysates', *EMBO reports*, 21(10), p. e49585. Available at: https://doi.org/https://doi.org/10.15252/embr.201949585.

Allen, E. and Allen, E. (2016) 'RNA Extraction from Drosophila Tissues using TRIzol

Reagent V . 1 of Massachusetts Medical School', pp. 8–11.

Ghawana, S. *et al.* (2011) 'An RNA isolation system for plant tissues rich in secondary metabolites.', *BMC research notes*, 4, p. 85. Available at: https://doi.org/10.1186/1756-0500-4-85.

Jaakola, L. *et al.* (2001) 'Isolation of high quality RNA from bilberry (Vaccinium myrtillus L.) fruit.', *Molecular biotechnology*, 19(2), pp. 201–203. Available at: https://doi.org/10.1385/MB:19:2:201.

Meier, R. (1988) 'Volume 16 Number 5 1988 Nucleic Acids Research A universal and efficient protocol for the isolation of RNA from tissues and cultured cells Ronald Meier', 16(5), p. 5294.

Schroeder, A. *et al.* (2006) 'The RIN: an RNA integrity number for assigning integrity values to RNA measurements.', *BMC molecular biology*, 7, p. 3. Available at: https://doi.org/10.1186/1471-2199-7-3.

Wilfinger, W.W., Mackey, K. and Chomczynski, P. (1997) *Effect of pH and ionic strength on the spectrophotometric assessment of nucleic acid purity.*, *BioTechniques*. England. Available at: https://doi.org/10.2144/97223st01.

Xu, M. *et al.* (2009) 'Isolation of high quality RNA and molecular manipulations with various tissues of Populus', *Russian Journal of Plant Physiology*, 56(5), pp. 716–719. Available at: https://doi.org/10.1134/S1021443709050197.

Organizing Committee Tech*Inn* 2024

Conference General Chair: Dr.T.Ketheesan, Dean, Faculty of Technology

Convener: Dr. Hiranya Nawarathna

Joint Secretaries: Ms.E.Banusha, Mr.A.Kunaraj

Editorial Board

Chief Editor: Mr. S. Vinujan

Sub Editors: Ms. R. Nivetha, Ms. S. Thawsika

Financial Committee:

Treasurer: Dr. N. Shakthivelnathan

Assistant Treasurer: Dr. T. Ketheesan, Mrs. K. Nathiparan, Mr. S. Sayanthan, Ms. R. Nivetha, Mr. Sangeeth Khan, Mr. A. Canistus, Ms. S. Venuja, Mr. S. Niruparan

Publicity Committee

Dr. T. Ketheesan, Mr. T. Sajaruban, Ms. P. Vaishnavy, Ms. R. Nivetha , Mr.T. Luxman, Ms.V.Vijitha, , Mr. Yasitha Madusanka.

Technical Program Committee

Track coordinators

Construction technology – Eng. S.Venuja

Automobile technology –Eng. Joy Mathavan

Electro technology – Dr.(Eng) N.Sakthivelnathan

Food production technology – Mrs. J.Rajeetha

Commercial Green farming technology – Mrs.E.Banusha

Decoration Committee:

Mrs. J.Rajeetha, Ms.P.Priyatharshini, Ms.V.Vijitha, Mrs.K.Nathiparan, Ms. Thawshika, Ms. R. Nivetha, Ms. S. Prabakani, Mr. M. M. Khan

Food Committee:

Mr. M.M.Khan, Eng.K.Saikrisha, Ms.V.Vijitha, Ms. S. Prabakani, Ms.R.Nivetha, Mr. S. Nishanthan, Ms. Kirushanthi, , Mr.V.Y.Madhusanka, Mr.R.Athavan

Photos and Video/Audio visual arrangement:

VC media

Mr. T. Sajarupan

Reviewers Details – Tech*inn* 2024 Conference

Prof. Ajith Jayaweera (Faculty of Livestock Fisheries & Nutrition, University of Wayamba)

Prof. K.Pakeerathan (Faculty of Agriculture, University of Jaffna)
Prof. T. Thiruvaran (Faculty of Engineering, University of Jaffna)

Prof. N. Sathiparan (Faculty of Engineering, University of Jaffna)

Dr.(Mrs.) S. Piratheepan (Faculty of Agriculture, University of

Jaffna) Dr. N. Thiruchchelvan (Faculty of Agriculture, University of

Jaffna) Dr.J.Janarny (Faculty of Engineering, University of Jaffna)

Dr. D.M.B.P. Ariyasinghe (Faculty of Technology, University of Jaffna)

Dr.N. Sakthivelnathan (Faculty of Technology, University of Jaffna)

Eng.A. Kunaraj (Faculty of Technology, University of Jaffna)

Eng. Asad Munir (Mirpur University of Science & Technology, Mirpur, Azad Kashmir,

Pakistan) Eng. J. Joy Mathavan (Faculty of Technology, University of Jaffna)

Dr.S.Sukirtha (Faculty of Technology, University of Jaffna)

Dr. R. Sarathadevi (Faculty of Agriculture, University of Jaffna)

Ms.C. Priyanthi (Faculty of Technology, University of Jaffna)

Ms.J.Rajeetha (Faculty of Technology, University of Jaffna)

Dr. (Mrs). S. Subajiny (Faculty of Agriculture, University of

Jaffna) Dr.(Mrs).B. Mayurathan (Faculty of Science, University

of Jaffna) Dr.R.Nagulan (Faculty of Applied science, University of

Vavuniya) Dr.B.Janarthanan (Faculty of Engineering, University

of Jaffna) Dr.S.Gowthaman (Faculty of Engineering, Kyushu

University) Dr.H.G.S.Mayuranga (Faculty of Engineering,

University of Ruhuna)

JUICE - 2024
"Striving for Excellence"

www.juice.jfn.ac.lk

Under the Sphere of

50 Years of Academic Pursuits
University of Jaffna

Salford & Co.

Jaffna University International Research Conference - 2024

Dialog

BANK OF CEYLON

AURA
PRIME PVT LTD

Coco Lovers (Pvt) Ltd

Sponsors

JUICE - 2024

"Striving for Excellence"

www.juice.jfn.ac.lk

Under the Sphere of

50 Years of Academic Pursuits

University of Jaffna

Jaffna University International Research Conference - 2024

Faculty of Technology
University of Jaffna
Ariviyalnagar, Kilinochchi, Sri Lanka